High-pressure carbonation : a petrological and geochemical study of carbonated metasomatic rocks from Alpine Corsica

Francesca Piccoli

▶ **To cite this version:**

Francesca Piccoli. High-pressure carbonation : a petrological and geochemical study of carbonated metasomatic rocks from Alpine Corsica. Earth Sciences. Université Pierre et Marie Curie - Paris VI, 2017. English. NNT : 2017PA066448 . tel-02319440

HAL Id: tel-02319440

https://theses.hal.science/tel-02319440

Submitted on 18 Oct 2019

HAL is a multi-disciplinary open access archive for the deposit and dissemination of scientific research documents, whether they are published or not. The documents may come from teaching and research institutions in France or abroad, or from public or private research centers.

L'archive ouverte pluridisciplinaire **HAL**, est destinée au dépôt et à la diffusion de documents scientifiques de niveau recherche, publiés ou non, émanant des établissements d'enseignement et de recherche français ou étrangers, des laboratoires publics ou privés.

Université Pierre et Marie Curie

Ecole doctorale: Géoscience, Ressources Naturelles et Environnement

Laboratoire : IMPMC/Equipe : Géobiologie

High-Pressure carbonation: a petrological and geochemical study of carbonated metasomatic rocks from Alpine Corsica

Par Francesca Piccoli

Thèse de doctorat en Science de la Terre

Dirigée par Alberto Vitale Brovarone

Présentée et soutenue publiquement le 16 Octobre 2017

Devant un jury composé de :

M. Jörg Hermann	Professor - University of Bern	Rapporteur
M. Philippe Goncalves	Maître de conférences - Université de Franche-Comté	Rapporteur
M. Giovanni Aloisi	CNRS, DR - Université Pierre et Marie Curie	Examinateur
Mme. Anne Verlaguet	Maître de conférences - Université Pierre et Marie Curie	Examinateur
Mme. Isabelle Martinez	Maître de conférences - Université Paris Diderot	Examinateur
M. Benoit Dubacq	CNRS, CR - Université Pierre et Marie Curie	Examinateur
M. Alberto Vitale Brovarone	CNRS, CR - Université Pierre et Marie Curie	Directeur de thèse

Abstract

The balance between the carbon input in subduction zone, mainly by carbonate mineral-bearing rock subduction, and the output of CO_2 to the atmosphere by volcanic and metamorphic degassing is critical to the carbon cycle. At fore arc-subarc conditions (75-100 km), carbon is thought to be released from the subducting rocks by devolatilization reactions and by fluid-induced dissolution of carbonate minerals. All together, devolatilization, dissolution, coupled with other processes like decarbonation melting and diapirism, are thought to be responsible for the complete transfer of the subducted carbon into the crust and lithospheric mantle during subduction metamorphism.

Carbon-bearing fluids will form after devolatilization and dissolution reactions. The percolation of these fluids through the slab- and mantle-forming rocks is not only critical to carbon cycling, but also for non-volatile element mass transfer, slab and mantle RedOx conditions, as well as slab- and mantle-rock rheology. The evolution of such fluids through interactions with rocks at high-pressure conditions is, however, poorly constrained.

This study focuses on the petrological, geochemical and isotopic characteristic of carbonated-metasomatic rocks from the lawsonite-eclogite unit in Alpine Corsica (France). The study rocks are found along major, inherited lithospheric lithological boundaries of the subducted oceanic-to-transitional plate and can inform on the evolution of carbon-bearing high-pressure fluids during subduction. In this work, it will be demonstrated that the interaction of carbon-bearing fluids with slab lithologies can lead to high-pressure carbonation (modeled conditions: 2 to 2.3 GPa and 490-530°C), characterized by silicate dissolution and Ca-carbonate mineral precipitation. A detailed petrological and geochemical characterization of selected samples, coupled with oxygen, carbon and strontium, neodymium isotopic systematic will be used to infer composition and multi-source origin of the fluids involved. Geochemical fluid-rock interactions will be quantified by mass balance and time-integrated fluid fluxes estimations.

This study highlights the importance of carbonate-bearing fluids decompressing along down-T paths, such as along slab-parallel lithological boundaries, for the sequestration of carbon in subduction zones. Moreover, rock-carbonation by fluid-rock interactions may have an important impact on the residence time of carbon and oxygen in subduction zones and lithospheric mantle reservoirs as well as carbonate isotopic signatures in subduction zones. Lastly, carbonation may modulate the emission of CO_2 at volcanic arcs over geological time scales.

Resumé

Le cycle global du carbone est fortement lié au bilan entre l'enfouissement en profondeur du carbone dans les zones de subduction, et les émissions de CO_2 dans l'atmosphère par dégazage volcanique et métamorphique. Dans la zone d'avant arc (75-100 km en profondeur), les réactions de volatilisation et la dissolution des carbonates induite par l'infiltration des fluides aqueux sont les processus à l'origine de la production de fluides de composition C-O-H. Le carbone initialement piégé sous forme minéral dans les roches peut donc être mobilisé et transporté par ces fluides vers le manteau ou la croûte lithosphérique. Des estimations récentes prévoient que, compte tenu de l'ensemble des processus qui ont lieu dans les zones de subduction (volatilisation, dissolution, mais aussi bien le magmatisme et la formation de diapirs de metasediments), presque la totalité du carbone enfoui serait mobilisé et transféré en phase fluide dans la croûte ou dans le manteau.

La percolation de fluides COH à travers des roches de la plaque plongeante et du manteau n'est pas seulement critique pour le recyclage du carbone, mais elle joue aussi en rôle sur le contrôle de l'état d'oxydoréduction du manteau, sur la mobilisation des éléments non volatils, ainsi que sur la rhéologie de ces roches. Cependant, les connaissances sur l'évolution de ces fluides à hautes pressions sont très limitées. Cette étude est centrée sur la caractérisation pétrologique, géochimique et isotopique des échantillons naturels de roches métasomatiques carbonatées de l'unité en facies lawsonite-eclogite de la Corse Alpine (France). Ces roches métasomatiques se localisent sur plusieurs kilomètres le long des contacts lithosphériques majeurs hérités de la plaque océanique subductée, et peuvent révéler des informations importantes sur l'évolution des fluides COH en condition de haute pression pendant la subduction. Dans ce travail, il sera démontré que l'interaction des fluides COH avec des roches silicatées à hautes pressions (entre 2-2.3 GPa et 490-530 ° C) peut causer la dissolution des silicates et la précipitation de carbonates, processus défini comme carbonatation à haute pression. Une caractérisation pétrologique et géochimique détaillée des échantillons, couplée à une étude systématique des isotopes de l'oxygène, du carbone et du strontium-néodyme sera utilisée pour déduire la composition et l'origine *multi-source* des fluides impliqués. Les implications géochimiques des interactions fluide-roche seront quantifiées par des calculs de bilan de masse et de flux de fluides intégrés dans le temps. Cette étude met en évidence l'importance de la remonté des fluides COH le long des gradients en pression et température pour le stockage du carbone dans les zones de subduction.

Acknowledgements-Remerciements-Ringraziamenti

I would like to express my special appreciation and thanks to all the people who have been part of these 4 years project (including M.Sc), starting from my supervisor Alberto Vitale Brovarone, and Jay J. Ague, for the constructive discussions and advises they gave me during these years. Thank you, Alberto, for introducing me to this amazing world that is metasomatism and high-pressure fluid-rock interactions, for teaching me the accuracy and precision of scientific work, and for making me understand how long and complex evolution can be record in rocks. Thank you, Jay, for all your wise advices and motivating words, for how much you taught me in only five months, and for your enthusiasm for science and geology that is absolutely contagious.

I would like to thank Jörg Hermann and Philippe Goncalves for accepting to review this manuscript, as well as the others members of the committee Anne Verlaguet, Isabelle Martinez, Giovanni Aloisi and Benoit Dubacq.

The Deep Carbon Observatory and the Reservoir and Fluxes community are thanked for co-funding this Ph.D. project. The Deep Energy community is thanked for co-funding my visiting period in the Geology and Geophysics Department of Yale University.

I would like to particularly thank Olivier Beyssac for the useful scientific discussion about rocks, science and for all the good advices you gave me on how to find my way in this competitive, but exciting world that is the research in the academia.

Delphine Bosch and Isabelle Martinez are thanked for all the support during isotopic analyses and for the useful discussions. Olivier Alard and Olivier Bruguier are thanked for their assistance during the analyses with the LA-ICP-MS and the data treatment. Anne Verlaguet is thanked for the help with the microthermometry on fluid inclusions. I also would like to thank Jacques Touret for advising me during the fluid inclusions study and for everything he taught me about fluids and metamorphism.

Imène Estève and Benoit Baptiste (IMPMC) are thanked for their technical support at the SEM and XRD platforms. Michel Fialin and Nicolas Rividi (CAMPARIS service) are also thanked for their assistance during electron microprobe measurements.

I wish to express all my gratitude to the IMPMC people who shared with me most of the greatest moments of these 4 years. A special thanks to my office-mate Nina and all the other (crazy!) friends: David (Davidix), Mario (Mariolix), Guilherme, Guillaume, Ornella, Nicolas (Devaux), Johan, Sara L., Mélanie, Eric, Edo, Silvia, Carlos and Giulia. Francesca,

we shared the very beginning in Milan, sampling under the rain and snow, preparing exams and now, here in Paris, surviving our Ph.D! I am so glad you are here with me in this moment.

I also wish to thank Andrea for sharing with me that great experience that was mapping in Champorcher, for all the discussions about geology, books, life, and, above all, for being a good friend.

I cannot forget the amazing people of Yale G&G department: Elvira, Fabio, Jean, Nav, Jennifer, Matthiew, Xavier, and our favorite engineer-deejay-musicians Ad, Berk and Luca. Thanks for these great five months together!

How to do not mention, my Parisian family, my beloved housemates: Cyrille, Mario (again!), Silvio and Marianne! Thanks also to Matthieu, Thibault and Simon (and Luna of course) for hosting me when I needed it the most and always make me feel welcome.

Michele, thank you for your friendship and support, without you, this manuscript would not have been written.

Last but not the least, thank to my family that was, is and always will be by my side.

"*Je suis de ceux qui pensent que la science est d'une grande beauté. Un scientifique dans son laboratoire est non seulement un technicien: il est aussi un enfant placé devant des phénomènes naturels qui l'impressionnent comme des contes de fées. Nous ne devrions pas laisser croire que tout progrès scientifique peut être réduit a des mécanismes, des machines, des rouages, quand bien même de tels mécanismes ont eux aussi leur beauté. Je ne crois pas non plus que l'esprit d'aventure risque de disparaitre dans notre monde. Si je vois quelque chose de vital autour de moi, c'est précisément cet esprit d'aventure, qui semble qui me paraît indéracinable et s'apparente à la curiosité. Sans la curiosité de l'esprit, que serions-nous? Telle est bien la beauté et la noblesse de la science: désir sans fin de repousser les frontières du savoir, de traquer les secrets de la matière et de la vie sans idée préconçue des conséquences éventuelles.*"

Maria Sklodowska Curie

Al Nonno e la Nonna.

TABLE OF CONTENTS

1. Introduction ……1

1.1. Carbon cycle in subduction zones: a brief review…… 2

1.1.1. The deep Carbon cucle and the implications for the Earth geodynamics……...2

1.1.2. The role of fluids in the deep carbon cycle…….3

1.1.3. Why investigate fossil subduction zones……4

1.2. Carbon carriers in subducting oceanic lithosphere……..8

1.2.1. Carbon input from subducting carbon-bearing sediments……..9

1.2.2. Carbon input from subducting altered oceanic crust…… 10

1.3. Processes modulating carbon fluxes in subduction zones……...11

1.3.1. Devolatilization of subducting slab……...13

1.3.1.1. Decarbonation-dehydration reactions……14

1.3.1.2. Carbonate dissolution in aqueous fluids……16

1.3.2. Carbonatite melts……..……..18

1.3.3. Other possible carbon transport mechanisms……18

1.4. Carbon fluxes in subduction zone: what goes down, mostly comes up……...19

1.5. Rock carbonation: a new piece of the deep Carbon cycle? ……20

2. Geological setting…….…… 23

2.1. Geology of the Alpine belt……...24

2.2. Geodynamic and geological setting of Alpine Corsica……...27

2.2.1. Schistes Lustrés complex lithostratigraphy and metamorphism……...31

2.2.1.1. Metamorphism in the Schistes Lustrés complex……...32

2.2.1.2. The San Petrone lawsonite-eclogite unit ...……...34

2.2.1.3. Carbon and calcium metasomatism in the high-pressure units of Alpine Corsica …….……37

2.2.1.3.1. Lawsonite metasomatism in the blueschist and eclogitic unit of Alpine Corsica ……...…….38

3. Methodology and analytical techniques……..41

3.1. Scanning electron microscopy and electron microprobe……41

3.2. Optical cathodoluminescence……..41

3.3. Raman microspectroscopy……...42

3.4. Whole rock analysis……42

3.5. Laser ablation inductively coupled plasma mass spectrometer (LA-ICP-MS)……....42

3.6. Stable and radiogenic stable isotopes geochemistry……..43

3.6.1. Carbon and oxygen stable isotopes of Ca-carbonate……...43

3.6.2. Oxygen isotopes of clinopyroxene……44

3.6.3. Oxygen isotopes of antigorite……....45

3.6.4. Sr-Nd radiogenic stable isotopes……..45

3.6.5. Estimation of water/rock ratio……..46

4. Recognition of high-pressure carbonation in the lawsonite-eclogitic unit in Alpine Corsica…….……..47

4.1. Article: Carbonation by fluid rock interactions at High-Pressure conditions: implications for carbon cycling in subduction zones……..49

5. Significance and distribution of high-pressure carbonation in Alpine Corsica……..81
5.1. Article: Field and petrological study of metasomatism and high-pressure carbonation from lawsonite eclogite-facies terrains, Alpine Corsica……82
5.2. Petrographic description of selected samples from Loriani and Col di Prato outcrops……136
6. Reactive fluid flow and mass transfer during high-pressure carbonation……143
6.1. Mechanism of mass transfer……143
6.2. Mass balance calculation……145
6.2.1. Defining a geochemical reference frame……146
6.2.2. Basic equations……147
6.3. Fluid flow: historical overview……149
6.3.1. Advection-Dispersion-Reaction equations……151
6.4. Method of investigation……154
6.5. Results of mass balance……155
6.5.1. Concentration diagrams……156
6.5.2. Mass balance……159
6.6. Results of time-integrated fluid-fluxes……163
6.7. Discussion……167
6.7.1. Discussion of mass balance results……167
6.7.1.1. Major element mobilization……167
6.7.1.2. Large ion lithophile and rare earth element mobilization…….. 169
6.7.1.3. Selected transition metal elements: Cr, Ni, Co, and V……172
6.7.2. Implications on carbon fluxes in subduction zones……175
7. Oxygen, carbon, and strontium, neodymium isotopes systematic of carbonated metasomatic rocks…… 179
7.1. Oxygen, carbon and strontium, neodymium isotopic range of natural samples 180
7.2. Oxygen and carbon stable isotopes in metamorphic carbonate-bearing rocks 182
7.2.1. Oxygen and carbon stable isotopes in the HP-LT Corsican ophiolite……184
7.3. Strontium and neodymium isotopes in metamorphic carbonate-bearing rocks 185
7.4. Results…….. 185
7.4.1. Oxygen, carbon stable isotopes of carbonated metasomatic rocks and carbonate veins……..185
7.4.2. Oxygen stable isotopes of serpentinite……187
7.4.3. Sr, Nd isotopes of carbonated metasomatic rock and carbonate veins……...189
7.4.4. Mixing curve models…….. 196
7.4.4.1. Mechanical mixing……..198
7.4.4.2. Mixing models with K_d……201
7.5. Discussion……205
7.5.1. Fluid oxygen isotopes composition……205
7.5.2. Modeling oxygen isotopes profiles in the serpentinite……206
7.5.3. Possible interpretation of the meaning of O-Sr signature of the serpentinite ……..……..209
7.5.4. Significance of the isotopic signature of carbonated metasomatic rocks …...211
7.5.5. Preliminary considerations on fluid sources ……...……...213

8. Discussion……217
8.1. Recognition of the metasomatic origin of carbonates in high-pressure metamorphic units……...217
8.2. Extremely high carbon-bearing fluid fluxes: implications for carbon inventory in subduction zones ……...……...219
8.3. Chemical and physical parameters controlling carbonation reaction progress……221
8.3.1. Evaluation of rock reactivity with carbon-bearing fluids……221
8.3.2. Possible physical factors controlling reaction progress……..225
8.4. New insights on the geochemistry of deep carbon-bearing fluids……227
8.4.1. Carbon transport in high-pressure fluids……229
8.4.2. Non-volatile elements transport in high-pressure, COH fluids……...230
8.5. Fluid sources and geodynamic implications……232
9. Conclusions……235
10. Perspectives……239
10.1. Trace element data of metasomatic carbonates by LA-ICP-MS.……240
10.1.1. Sampling and analysis strategy……..241
10.1.2. Results……...242
10.1.3. Preliminary interpretation……..244
10.2. Fluid inclusions study by micro-Raman spectrometry and microthermometry ……246
10.2.1. Results ……...……...248
10.2.1.1. Petrography and composition of fluid inclusions……248
10.2.1.2. Microthermometry on fluid inclusions……250
10.2.2. Preliminary interpretation……...252
10.3. Thermodynamic modeling and thermobarometry……...254
10.4. Fieldwork in the Eclogitic Micaschists Complex (Sesia Lanzo, Western Alps) ……..256
10.4.1. Geological setting……..……..257
10.4.2. Outcrops description ……...……...258

References……261

CHAPTER 1
Introduction

Carbon is not only the chemical backbone for all organic molecules, but it is also a main constituent of the solid Earth. One peculiarity of the Earth, compared to other planets of the solar system like Venus and Mars, is that a large fraction of the carbon expelled from the mantle is returned to the deep Earth trough subduction. The carbon cycle is, as a matter of facts, balanced. Even if during the past 570 million years atmospheric carbon dioxide has oscillated due to perturbations of the ocean-atmosphere-biosphere system (Barnola et al., 1987; Berner, 1991), the carbon content of the surface reservoirs is maintained in a narrow range by a dynamic balance between volcanic and metamorphic supply, and a removal processes like weathering (e.g., Berner, 1991; Houghton, 2007). The real issue is understanding the processes responsible for net sources and sinks of carbon that, ultimately, are responsible for the long-term stabilization of temperature on Earth, a critical characteristic for planet habitability (Walker et al., 1981; Houghton et al., 2007; Coogan and Dosso, 2015). In the last decades, lots have been investigated about shallow reservoirs: atmosphere, oceans and shallow crustal environments. By contrast, little is know about the deep interior (core and mantle), which may contain more than 90% of Earth's carbon (Hazen and Shiffries, 2015). Subduction zone are particularly interesting because they are a geodynamic zone where carbon is transferred into the deep mantle and, at the same time, they represent a possible "short cut circuit" to re-inject carbon into the atmosphere through volcanic activity (DePaolo, 2015). The transfer of carbon during subduction is critical for the deep carbon cycle, but process regulating carbon fluxes in this setting are poorly constrained and important questions are still pending. For example: *what are the reservoirs of carbon in subduction zones? How*

does carbon move among these reservoirs and return to the surface? Those are fundamental questions that we need to answer to fill the gap in our understanding of the deep carbon cycle.

1.1 Carbon cycle in subduction zones: a brief review

1.1.1 The deep Carbon cycle and the implications for the Earth geodynamics

Carbon plays a role in Earth's mantle dynamics through mobilizing hydrogen from nominally anhydrous silicate minerals (Dasgupta et al., 2007; Dasgupta and Hirschmann, 2007) and by stabilizing incipient carbonated melts (e.g. Eggler, 1976; Wyllie, 1977; Dalton and Presnall, 1998; Dasgupta and Hirschamann 2006; Dasgupta et al., 2013). Thus, carbon-induced melting contributes to control the viscosity and the creep behavior of the mantle and determines whether a planet would have lasting plate tectonic cycles (e.g. the Earth) or "die" shortly (e.g., Mars and Venus; Dasgupta, 2013). While magma ocean processes controlled the deep carbon cycle during the Hadean, post magma ocean crystallization, solid state convection and plate tectonic modulated the Earth's deep carbon cycle. Since the initiation of the Wilson cycle, mantle carbon inventory is modulated by a number of processes (Fig. 1.1). The key parameters for the understanding of the role of carbon in the present-day geodynamics are: the Earth's thermal state, the efficiency of crustal carbon recycling (ingassing) through subduction and the efficiency of CO_2 release (outgassing) through partial melting in oceanic provinces. Deep carbonate subduction has being efficient at least over the Phanerozoic Eon. The question that has been address in many works (theoretical and field based) is how much carbon goes past sub arc depth and thus participates in a much longer time scale cycle involving the deep mantle and how much is directly recycled in the lithospheric mantle and then reinjected in the atmosphere through volcanism. Therefore, processes occurring in the subducting slab will determine the ultimate fate of carbon. This work will focus on rock carbonation processes occurring at HP condition during subduction.

The understanding of rock carbonation is pivotal for the evaluation of the impact of this process in modulating the residence time of carbon in subduction zones reservoirs. Actually, rock carbonation can be one of the ways to uptake carbon in the slab- and mantle-forming rocks, process that may modulate the fluctuation of CO_2 emission at volcanic arcs over geological time scales.

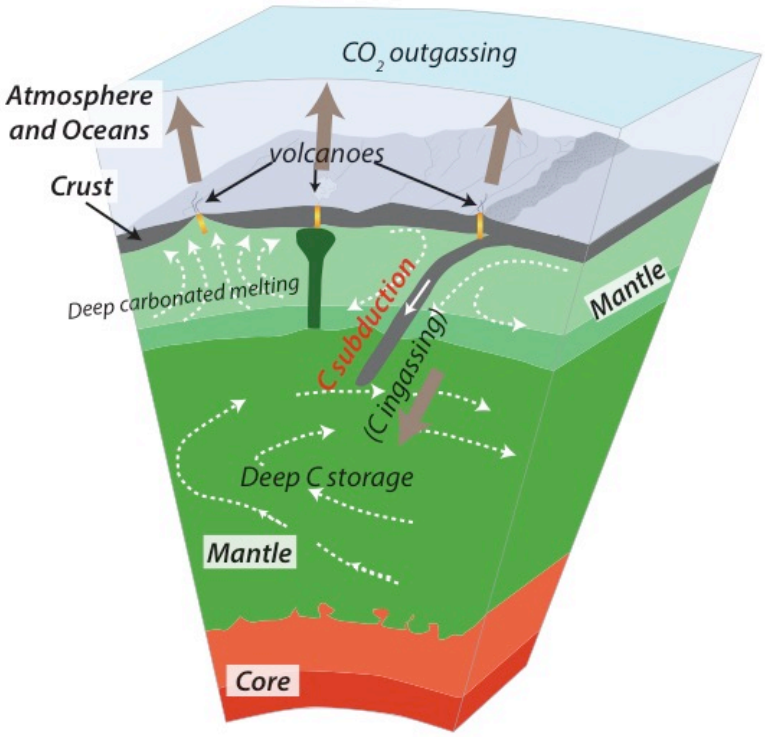

Fig. 1.1: Cartoon illustrating the range of deep-Earth processes that influence the long-term carbon cycle: magmatic outgassing (controlled by deep carbonated melting), recycling or storage through subduction (ingassing). Figure from Dasgupta (2013).

1.1.2 The role of fluids in the deep carbon cycle

The critical role of fluids in subduction zones has been addressed since the early 1970's and today it is widely accepted that fluids (aqueous fluids and hydrous melts) play a major role in recycling carbon and other volatile elements in the lithospheric mantle. Moreover, the presence of fluids controls not only mass and heat transfer, but also mineral reactions and rock rheology (e.g., Bickle and McKenzie, 1987; Gerya et al., 2002; Va Daalen et al., 1999; Vernooij et al., 2006; Ague, 2014; Goncalves et al., 2016). Altogether, these processes determine the geochemical and petrological evolution of the crust and mantle. Processes that

can release carbon from the subduction slab are decarbonation reactions (Kerrick and Connolly 1998, 2001a,b; Gorman et al., 2006; Schmidt and Poli, 2014) and dissolution in aqueous fluids (Frezzotti et al., 2011; Ague and Nicolescu, 2014), but only this later one can mobilize a significant amount of carbon at depth beneath the subduction zone arc. Also, a recent study (Poli, 2015) shows that water can strongly depresses the solidus for hydrous carbonate gabbro and limestone rocks, thus promoting the formation of hydrous carbonatitic liquids that can efficiently transfer volatile elements, calcium and silicon from the slab upward into the mantle wedge at relatively shallow depth (~120km beneath subduction zone arcs). The study of metasomatic rock is a direct way to investigate deep processes involving fluid-rock interactions. Actually, rock textures, mineral chemical zoning, isotopic modification relate to the changing effective bulk rock composition and the precipitating fluid during changing P and/or T (e.g. Tracy, 1982). In case of a closed system chemical zoning is related to the availability of reactants and the degree of reaction progress. However, in an open system, it is evidence of fluid-mediated evolution of the rock and can, indirectly, give insights on the source and nature of the fluid itself.

1.1.3 Why investigate fossil subduction zones

Subduction zone are an extremely important geodynamic settings where several phenomena take place: explosive volcanic activity, earthquakes, fast geomorphological evolution and elements recycling. The evolution of a subduction zone is related to the petrological reactions that take place in the subducting slab as well as along the slab-mantle interface (Poli and Schmidt, 2002). Superficial phenomena like volcanism and geomorphological adjustment to tectonic forces can be investigated in active subduction zones. In contrast, deeper processes responsible for volatile cycle cannot be directly studied because they occur in million years timescale. However, a record of these processes is found in fossil subduction zone, preserved

in the internal part of collisional belts (e.g. review by Ota and Kaneko, 2010). Exhumed high-pressure (HP) and ultra high-pressure (UHP)/low temperature (LT) metamorphic units are an excellent natural laboratory to directly investigate processes occurring in subduction zone at depth relevant to the subarc (70-150 km). Metamorphic overprinting during exhumation may erase the record of these processes (Ernst, 2006). Nevertheless, various mechanisms can allow the localized or even regional preservation of (U)HP/LT assemblages, for example rapid exhumation and/or absence of fluids that promote mineral reactions and equilibration with the changing P-T conditions. Recently, Yamato and Brun (2017) proposed that the switch in orientation and magnitude of tectonic stresses during the transition from compressional to extensional regime may cause a geologically-fast pressure drop, prior exhumation. Such a mechanism could explain the preservation of peak paragenesis, previously interpreted as the result of fast exhumation. Other possible mechanisms include underthrusting of lithospheric block that act as thermal blanket, preserving the (U)HP/LT assemblages from excessive heating (Chemenda et al., 1997; Malavieille et al., 1998).

The Western Alps are among the first places where the growth of HP mineral paragenesis was associated to the descent of a lithospheric plate into the mantle (Ernst, 1971) and are, by far, one of the most studied orogenic belt, considering that the first geological investigations date back to the 18th century (Dal Piaz, 2001). The recognition of coesite in the Brossasco-Isasca continental unit first (Chopin, 1984) and then in the Lago di Cignana oceanic unit (Reinecke, 1991), indicates that both continental and oceanic crust can be buried to UHP depth and then exhumed back to the surface. Subsequent research, especially with the contribution of multi-stage geochronology and thermochronology, have demonstrated that HP metamorphism occurs diachronously in different units that constitute the axial zone of the Western Alps (e.g. Duchêne et al., 1997; Rubatto et al., 1998).

The work conducted by Marco Beltrando, Lagabrielle, Manatschal outlined how several exhumed tectono-metamorphic units in the Western Alps (between the Canavese Line and the Penninic Front; e.g., Manatschal, 2004; Manatschal and Müntener, 2009; Beltrando et al., 2012, 2014; Mohn et al., 2010, 2011,2012), in the Pyrenees (e.g., Lagabrielle and Bodinier, 2008) and Alpine Corsica (Vitale Brovarone et al., 2011a; Meresse et al 2012), sample hyperextended lithosphere related to the Jurassic opening of the Alpine Tethys (Beltrando et al., 2014). These units are characterized by a lithological association of serpentinized mantle rocks, continent-derived slivers, MOR-like mafic rocks (gabbros and/or basalts) of Jurassic age and post rift sediments. This ensemble has been recognized as a fossil ocean-continent transition zone (OCT hereafter) (e.g. Manatschal, 2004). This discovery has major consequences on our vision of petrologic and tectonic processes occurring during subduction. Firstly, as pointed out by Beltrando et al. (2010; 2014) there is a link between OCT and exhumation of (U)HP metamorphic terrains. OCT are indeed in a position favorable to reach (U)HP conditions following negatively buoyant oceanic lithosphere. Moreover, hydration fronts within the oceanic lithosphere (observed in the present-day distal margins) may work as preferred detachment surface, facilitating exhumation (Lundin and Doré, 2011; Mohn et al., 2011; Beltrando et al., 2014). Secondly, this section of the oceanic lithosphere is a major carrier of volatile elements in subduction zones. Actually, a growing number of studies on present-day and fossil OCT show that exhumation of subcontinental mantle in magma-poor rifted margins is intimately related to migration of volatile rich mantle-reacted fluids that can lead to changes in mineralogy and chemistry of the mantle, crustal and sedimentary rocks (Manatschal, 1999; Manatschal et al., 2000; Engström et al., 2007; Pinto et al., 2015; Bayrakci et al., 2016). Moreover, seawater-rock interactions also affect the first km of the exposed oceanic crust from the ridge to the trench (e.g., Peacock, 2001; Ranero et al., 2003; Ranero and Sallarès, 2004). Hydrothermalism in the crust is responsible for drastic

metasomatic mass transfer and volatile addition (both H_2O and CO_2) (Alt and Teagle, 1999; Jarrard, 2003; Cannat et al., 2010). Slow and ultra-slow spreading oceans are particular favorable setting for oceanic metasomatism because much of the extension is accommodated by faulting and fluids can be channelized along lithological contacts and detachment fault, leading to extremely high fluid fluxes. Metasomatic product includes: epidotization, chloritization, rodingite and carbon uptake by carbonate precipitating in veins and silicate replacement reactions (Walker et al., 1981; Engström et al., 2007; Bach et al., 2013; Coogan et al., 2016). The study of OCT metamorphic evolution is, thus, a unique way to follow volatiles cycle from the oceanic stage until deep lithospheric mantle condition. Furthermore, hyperextended margins have a large variety of lithologies with compositions ranging from ultramafic to acid. Thus they represent a natural laboratory of a wide range of processes. However, the study of fossil OCT is not without pitfalls. Firstly, oceanic-related metasomatism strongly affects the chemistry and rock properties of the oceanic crust that will be subducted. The distinction between oceanic- and subduction-related metasomatism is quite often of difficult interpretation and demands great caution and a detailed study. Moreover, pre-Alpine rift-related structures might be erased by tectonic "shuffling" of metamorphic units during Alpine deformation events. Field study in Alpine Corsica presents remarkable advantages compared to the equivalent units in the Western Alps: (i) a coherent OCT section that undergone HP/LT metamorphism is well exposed over several kilometers; (ii) late deformation is more localized and (iii) both primary oceanic structures and HP/LT assemblages are extremely well preserved (Alpine Corsica in one between the only 10 fresh lawsonite-eclogite localities known worldwide; Tsujimori et al., 2006); (iv) a big variety of metasomatic rocks, including carbonate-bearing metasomatic rock, characterized lithological boundaries between serpentinized mantle, Mesozoic metasediments and continent-derived

slivers; (v) the preservation of HP structures and paragenesis allows to constrain metasomatism to HP conditions.

1.2 Carbon carriers in subducting oceanic lithosphere

Subducted sediments and altered oceanic crust play an important role in recycling carbon and other volatile elements into the Earth mantle, and are primary source for arc magmatism. Actually, chemical signatures imply that CO_2 in arc magmas is largely derived from carbonate of marine origin (Sano and Marty, 1995). Therefore, carbon sequestrated in marine sediments and hydrothermally altered oceanic crust is returned to the atmosphere by arc magmatism (Berner and Lasaga, 1989). Numerous contributions to the evaluation of the global budget of volatiles elements input in subduction zones derive from the studies of ODP sites and from conceptual models (e.g., Plank and Langmuir, 1998; Alt and Teagle, 1999; Jarrard, 2003; Alt et al., 2013; Staudigel, 2014). However, for both subducted sediments and oceanic crust large variation in the volatile content exist depending on the nature of the sediments, sedimentation rates, bottom water temperature, oxidation states in the atmosphere and oceans, and atmospheric CO_2 levels (e.g., Walker et al., 1981; Berner, 1991).

Carbon is recycled in subduction zones through the transport of carbonates and organic matter present in the subducted lithosphere. Recent estimations evaluate the total carbon input into subduction zones ranging from 40 to 66 Mt/yr, with two main contributions: the altered oceanic crust (22-28 Mt/yr) and the sediments (13-23 Mt/yr). Here we will present a brief overview of carbon inputs in subduction zones by presenting separately inputs from subducted sediments and inputs from altered oceanic crust.

1.2.1 Carbon input from subducting carbon-bearing sediments

Carbon in oceanic sediments was reviewed by Rea and Ruff (1996), Plank and Langmuir (1998), and Plank (2014). An average composition for subducted sediments in terms of water and carbon content is given by the GLOSS (Global Subducting Sediments) and the updated GLOSS-II (Fig. 1.X; Plank and Langmuir, 1998; Plank, 2014). For most of elements, this latter differ from the previous by less than 10%. GLOSS-II accounts for 27 different trenches, each of which is characterized by different subducting rate, thickness of the sedimantary pile and trench length. The high variability of the sedimentary pile composition is depicted in Figure 1.2. Carbonates in the sedimentary pile range from 0 to ca. 800m in thickness. This is also highlighted by the bulk rock analyses, where the CO_2 content ranges from 0 to 12 wt.%.

These works mainly focus on inorganic carbon present in carbonate minerals (note that the main carbon sink is as carbonate, also in the oceanic crust-see next section; Alt et al., 2003) and only partially account for organic carbon, which might be relevant in pelagic sediments and turbidites.

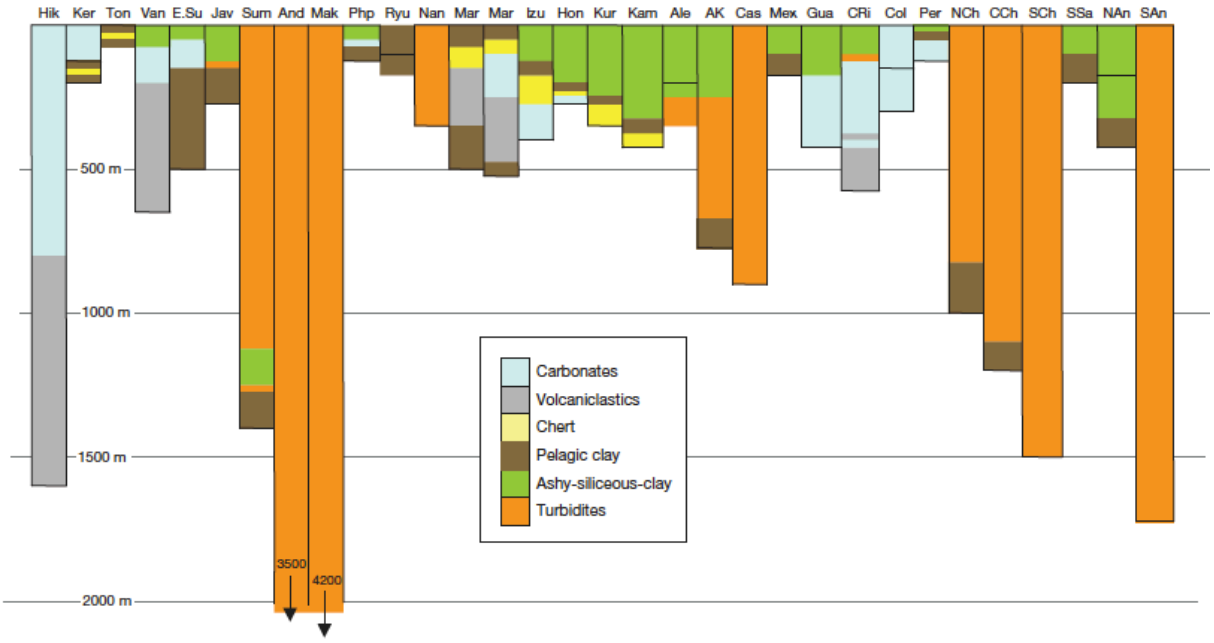

Fig. 1.2: Sedimentary sections at trenches from different present day subduction zones. Note the extremely high variability of the subducted materials. Figure from Plank (2014).

For example, hemipelagic ooze are nearly free of carbonates, but organic carbon averages around 1 wt.% (Mayer et al., 1992). Moreover, turbidites sequences can reach 2000m in thickness, thus contributing substantially in the organic carbon input into subduction zones (Fig. 1.2). The recent work of Duncan and Dasgupta (2017) questions how different forms of carbon are processed in subduction zones. The fate of graphitized carbon and diamond during subduction is poorly constrained so far, although understanding the fate of these forms of carbon in subduction zones environment is critical to understand possible mechanism of long-term sequestration of reduced carbon in the mantle and its implications for the Earth's redox state evolution.

1.2.2 Carbon input from subducting altered oceanic crust

Undegassed, fresh depleted MORB has quite low carbon and water content, of approximately 0.12 and 0.2 wt.% respectively (Fig. 1.3; Staudigel, 2014). However, ocean floor metamorphism and fluid-rock interactions results in pervasive alteration and hydration of the oceanic crust, together with the precipitation of carbonates in veins and vugs (Staudigel, 1989,1996,2014; Alt and Teagle, 1999). Notably, the alteration-related uptake of CO_2 in the oceanic crust brings the total inventory up to levels exceeding the original non-outgassed carbon content (Staudigel et al., 1989). The thickness of volatile-enrichment front can range from 800 m to a few thousand meters deep in fast spreading and slow spreading oceans, respectively. Figure 1.3 shows the CO_2 contents vs. H_2O content of the altered oceanic-crust rocks (basalts and ophicarbonates) and sedimentary cover. It can be seen that altered upper oceanic crust can uptake large quantity of carbon, up to almost 8 CO_2 wt.%. Ophicarbonates (carbonated ultramafic rocks during hydrothermal alteration) can have even higher CO_2 content (Bonatti et al., 1974). The Alpine Tethys ocean floor was mainly composed by serpentinized mantle. Carbon sink rate during low- and high-temperature alteration of the

serpentinite can be high. Alt et al. (2013) estimated for the Mesozoic serpentinite a carbon sink rate of 9.7-1.5·10^{10} mol C/yr. Compared to Cenozoic carbon sink fluxes in mafic crust (4.5-7.3·10^{11} mol C/yr; Alt and Teagle, 1999; Gillis and Coogan, 2011), the estimated carbon sink in the serpentinite amounts to 4-13% of the carbon uptake rates for mafic oceanic crust. However, in absolute terms (i.e., comparing equal volume of serpentinite vs. mafic crust), the carbon uptake by serpentinite is equal or slightly higher than that of an equal volume of mafic oceanic crust (Alt et al., 2013).

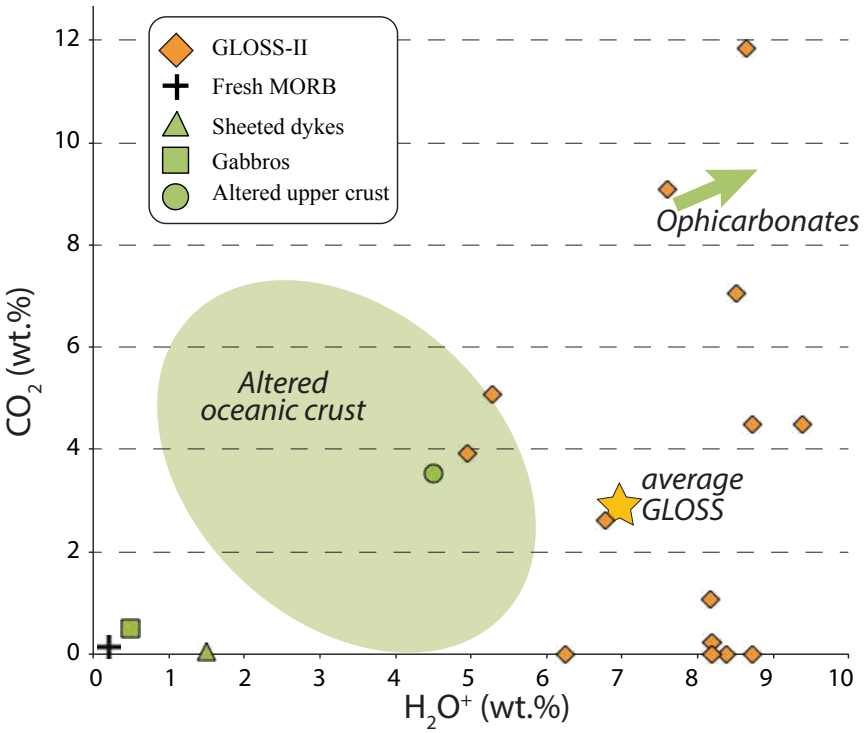

Fig. 1.3: H_2O wt.% vs. CO_2 wt.% content in subducting materials: altered oceanic crust, ophicarbonates and sediments. Figure modified after Molina and Poli (2000). Data points of GLOSS-II are from Plank (2014). Fresh MORB, sheeted dykes, gabbros, and altered upper crust are from Staudigel (2014). Shaded field representing the range composition of the altered oceanic crust is from Staudigel et al. (1996). The green arrow indicates the direction of ophicarbonates composition (Bonatti et al., 1974).

1.3 Processes modulating carbon fluxes in subduction zones

In the previous paragraph, the complexity of the subducted lithosphere has been outlined. During subduction, oceanic crust and sediments undergo continuous and discontinuous phase transformation, through P-T variation (Poli and Schmidt, 2002). The recycling in subduction

zones of carbon and volatile elements regulates crustal growth, influences arc volcanism, and refertilizes the mantle. Therefore, in order to better understand these processes, knowledge on mass and chemical fluxes associated with subduction is required. For recycling of crustal carbon, the key factor is the relative positions of metamorphic and decarbonation melting reactions of the subducted lithosphere, which in turn depend on the P-T path of the subducting slab (Dasgupta, 2013). Two main processes of carbon transfer occurring in subduction zones have been explored experimentally and theoretically: decarbonation melting reactions (i.e. carbonatite genesis; Knoche et al., 1999; Hammouda, 2003; Yaxley and Brey, 2004; Dasgupta et al. 2004, 2005; Dasgupta and Hirschmann, 2006), decarbonation reactions (Yaxley and Green, 1994; Molina and Poli, 2000; Kerrick and Connolly, 1998; 2001a,b; Gorman et al., 2006; Poli et al., 2009).

Theoretical and experimental approaches have pro and counts. Thermodynamic modeling is used to determine the direction of mineral reactions and the conditions necessary for equilibrium, with the ultimate goal of interpreting the genetic history of rocks. Petrogenetic grids are a means by which the phase relations of a geologic system can be represented as a function of properties such P, T and fluid composition. For metacarbonate rocks, petrogenetic grids are extensively used in regional metamorphism studies and for systems in which the fluid composition is not externally controlled (Connolly and Trommsdorff, 1991). In subduction settings, the location and consequences of fluid production reactions can be constrained by means of phase diagrams for relevant bulk rock composition, in conjunction with P-T path (Peacock, 1990). However, when projecting phase diagrams onto a P-T coordinate frame (i.e., petrogenetic grids), if fluids are present, univariant curves around invariant point cannot be oriented independently with respect to the direction of compositional variation in the fluid phase. Other limitations of thermodynamic modeling applied to carbonate-bearing systems are: (i) carbonate solid solution is modeled as ideal; (ii)

the thermodynamic properties of Fe^{3+} endmembers are mostly estimated, thus the redox reaction controlling carbon transfer are poorly constrained; (iii) the fluid is assumed to be an H_2O-CO_2 mixture unaffected by redox reactions, mineral dissolution in the fluid and melting processes (Poli et al., 2009).

Experimental petrology allows investigating the relationships between carbonates and fluid phases, under a large range of P-T-X-fO_2 conditions. On the other hand, the applicability of experimental studies to natural conditions is influenced by the chosen experimental strategy, for example: volatile composition and abundance, buffering technique, bulk composition, and other geological parameters like heterogeneities in rock properties (porosity, geochemical heterogeneities etc.).

The study of natural samples is complementary with theoretical and experimental works. For example, the problems concerning the complexities of fluid speciation were further demonstrated by the discoveries of HP H_2^- or CH_4-bearing fluids inclusions (Peretti et al., 1992; Fu et al., 2003; Shi et al., 2005). Furthermore, the study of natural samples from HP and UHP units brought attention on poorly investigated processes, like carbonate dissolution, that might be relevant for the petrological evolution of the subducting slab (Frezzotti et al., 2011; Ague and Nicolescu, 2014). All together, experimental, theoretical and natural studies can shed light on the processes regulating the carbon cycle in subduction zones, with large implications on our understanding of the long-term, global carbon cycle.

1.3.1 *Devolatilization of the subducting slab*

In shallower part of the slab and at relatively low temperature (<600-700°C), carbon transfer is mainly controlled by metamorphic reactions, which products are aqueous fluids that potentially can transport carbon and other elements out of the slab into the overlying mantle. In the following sections, I will briefly review the state of art about the experimental and

theoretical works investigating the relationships between carbonates-hydrous minerals and C-O-H fluids, in to outline the estimation of carbon fluxes in between subduction zone reservoirs.

1.3.1.1 Decarbonation-dehydration reactions

Different carbon reservoirs in subduction zones undergoes different histories and needs to be considered separately.

Oceanic crust. Thermodynamic modeling predicts dehydration in metabasalts and carbonate-bearing ultramafic rocks (ophicarbonates) occurring from shallow (fore arc) to deep condition (subarc) for warm and intermediate subductions, respectively. Dehydration does not occur along cold geotherms (Kerrick and Connolly, 2001EPSL). Dehydration occurring intermediate geotherms is relevant for magma genesis. Moreover, aqueous fluid infiltration may trigger decarbonation in the carbonate-bearing lithologies. If major fluid infiltration does not occur, most of the original carbon is retained to depths because decarbonation is confined to higher temperature (Kerrick and Connolly, 1998). Gorman et al. (2006) found that metabasalts are the primary source of CO_2 in the subarc, because marine metasediments undergo complete decarbonation under the forearc (Fig. 3). However, CO_2 fluxes are predicted to be very small, and most of the initial carbon is thus retained into the slab.

This scenario is reinforced by experimental works that predict that carbon can be permanently bound into carbonates and recycled into the deep mantle (Molina and Poli, 2000; Hammouda, 2003; Poli et al., 2009; Boulard et al., 2011; Merlini et al., 2013; Tumiati et al., 2013). Experiments on an altered MORB (Mid Ocean Ridge Basalt) bulk composition were performed, among others, by Poli et al. (2009). They found that hydrous phases (i.e. amphiboles, lawsonite) are stable at subarc conditions, even in the presence of carbon. Interestingly, they point out how the different degree of oceanic alteration (heterogeneous

mass gain of CO_2, Al_2O_3 and CaO) has a role in the stability of hydrous phase during subduction. Moreover, they observed, at fH_2 buffered by Hematite-Magnetite, carbonate phase fields getting wider with pressure, thus shifting the fluid toward water-rich composition in a nearly H_2O-CO_2 binary mixture. Conversely, at fH_2 buffered by Ni-NiO, carbonates are destabilized (with possible production of H_2O-CH_4 binary mixtures). Thus, they proposed that mixing of fluids generated within a subducting lithosphere, heterogeneously oxidized on the ocean floor, can enhance carbon precipitation in the form of graphite or diamond.

Collins et al. (2015) conducted a field-based study in low-grade metamorphic units and HP to UHP units in the Northern Apennines, Western Alps, and Tianshan. The aim of this work was to investigate the prograde metamorphic devolatilization. They results are in a good agreement with the thermodynamic and experimental models that predict minimal loss of CO_2 during forearc metamorphism.

Metasediments. Carbonate-bearing marine sediments are extremely rich in volatiles (Fig. 2) and are considered the major source for CO_2 released by arc volcanoes. The devolatilization history may vary depending the geothermal gradient and H_2O-rich fluid infiltration. Theoretical studies propose that along high-temperature geotherms, metasediments undergo devolatilization in the forearc region (thus before the depths at which arc magmas are generated), whereas, along low-temperature geotherms, metasediments undergo almost no devolatilization (Kerrick and Connolly, 2001a). As mentioned above, thermodynamic models, don't predict a major dehydration pulses from the metabasalts in the sub-arc region, thus precluding external fluid infiltration that could promote decarbonation. They conclude that marked devolatilization occurs either in the forearc or volatiles are retained to depth beyond the subarc. This model was further investigated by Gorman et al. (2006), considering an open system behavior (i.e. decarbonation driven by infiltration of water rich fluids). However, also

in this model the peak in CO_2 flux is in the fore arc and only a minor amount is released in the subarc, for intermediate and cool subduction (Fig. 3). Moreover, the peak in CO_2 flux corresponds with the peak of water released and, thus, it implies the formation of fluids with very low CO_2 molar fraction (X_{CO2}). Some of the field-based works in the HP units in the Western Alps seem to confirm that in case of cool subduction and limited open system behavior, a large fraction of metasediments don't undergo decarbonation in the forearc (Cook-Kollars et al., 2014; Collins et al., 2015).

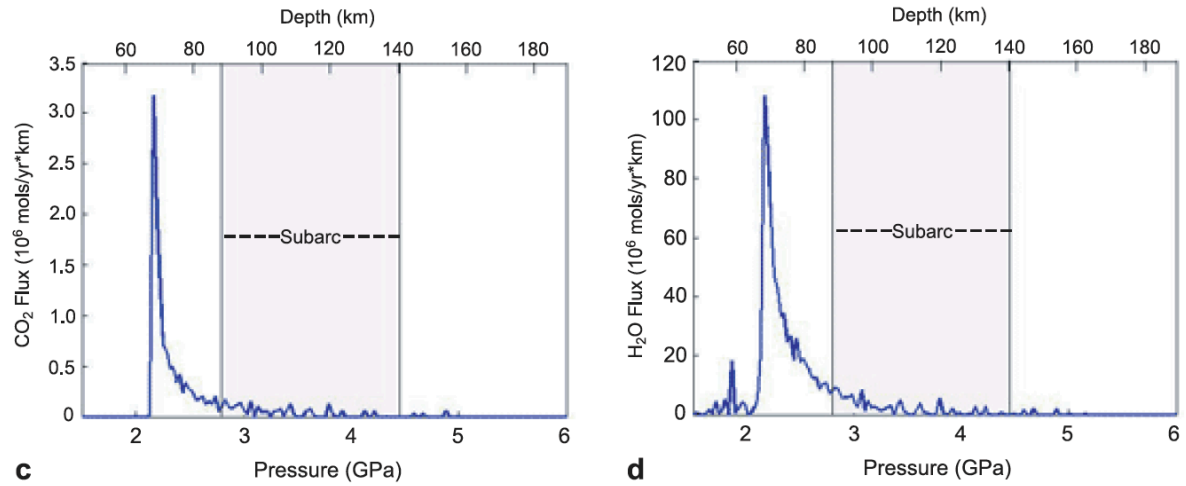

Fig 3: CO_2 and H_2O fluxes calculated with a distillation decarbonation model (open system and channelized fluid flow) for a cool subduction. The flux is obtained summing the contribution of volatiles from both metasediments and oceanic crust. The two diagrams show that the maximum devolatilization occurs in the fore arc region. The concomitance of high water released together with decarbonation is responsible for the formation of water rich fluids with X_{CO2} lower than 0.03 (Fig. from Gorman et al., 2006).

1.3.1.2 Carbonate dissolution in aqueous fluids

Thermodynamic models, experimental works and some field-based studies suggest that mineral-mineral reactions (decarbonation) occur beyond the subarc region, and CO_2 is retained in the subducting slab. This would explain the apparent carbon imbalance between subducted and expelled carbon fluxes. Kerrick and Connolly (2001a) point out that infiltration of H_2O-rich fluids is essential to promote significant decarbonation of marine metasediments. As mentioned in the previous section, the presence of fluids is critical for volatile mass transfer and mineral reactions. The discovery of bicarbonates (HCO_3^-) in fluid inclusions in

UHP rocks form oceanic unit (Frezzotti et al., 2011; Fig. 4a) and extremely high release of CO_2 from metasediments nearby active fluid conduits (up to 60-90% of the initial CO_2; Fig. 4b; Ague and Nicolescu, 2014) confirmed that, in case of fluid-mediated reactions, massive amount of CO_2 can be mobilized through carbonate dissolution in aqueous fluids (Fig. 4c).

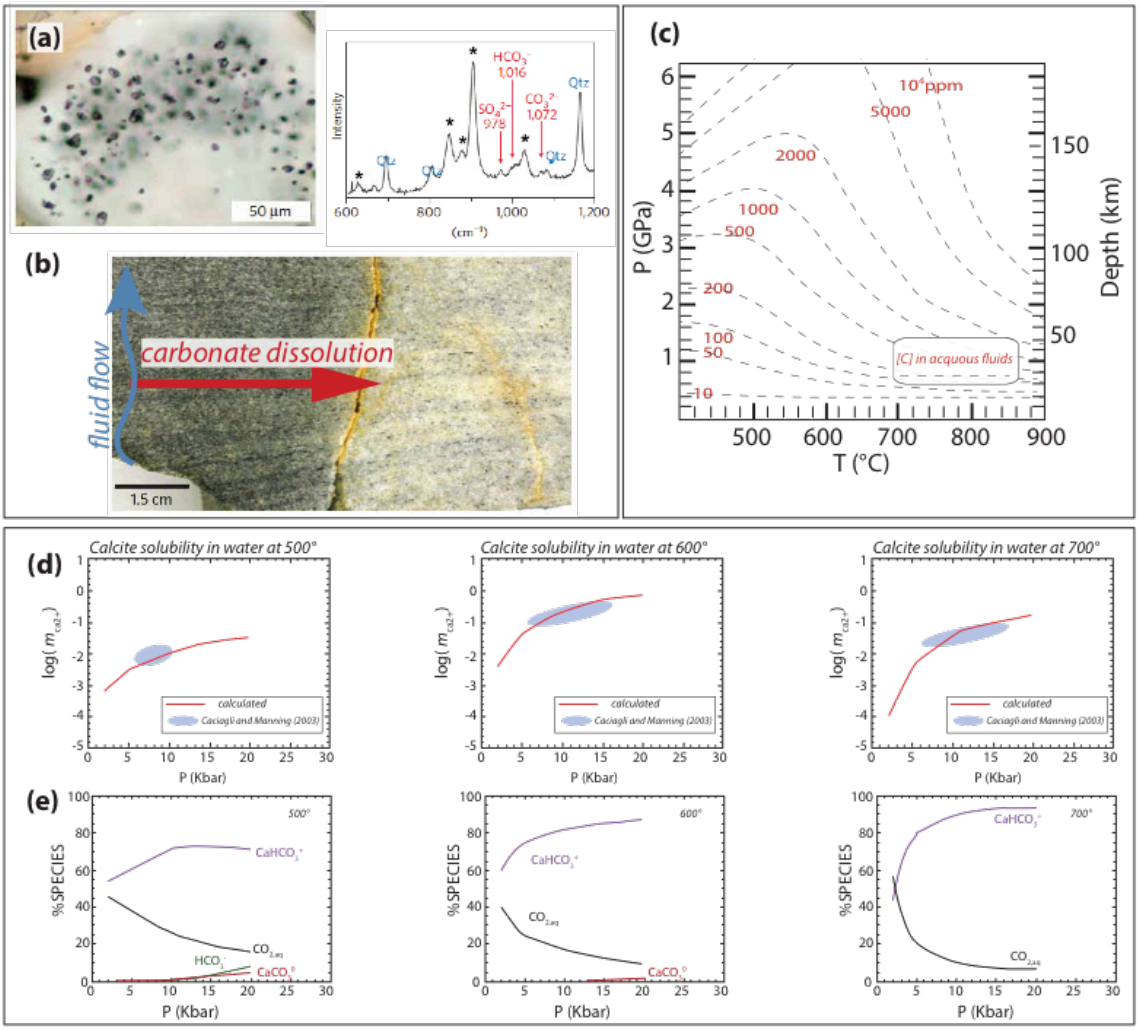

Fig. 4: Experimental, theoretical and field based studies on carbonate dissolution at HP conditions. **(a)** Photomicrograph of fluid inclusion in garnet from UHP metamorphic rocks together with Raman spectrum of the analyzed fluid showing the presence of bicarbonate ions in the metamorphic fluid (Frezzotti et al., 2011). **(b)** Rock slab of metacarbonate rock from Syros HP metamorphic unit. The metacarbonate rocks in contact with serpentinite blocks underwent decarbonation by fluid-mediated carbonate dissolution. **(c)** Contours of [C] in part per million for aqueous fluids saturated in CaCO3 as a function of P and T (Fig. from Kelemen and Manning, 2015). **d)** Theoretically calculated curves fitting the solubility of calcite from experimental studies at 500, 600 and 700°C (Facq et al., 2014; here only the area of experimental point from Caciagli and Manning (2003) is reported) and model of aqueous speciation of dissolved carbonated at 500, 600 and 700°C (**(e)**; Facq et al., 2014). This study shows that carbonate solubility increases with pressure and not only temperature. Moreover, C speciation change with P-T condition, with Ca-bicarbonate being the most abundant species.

Experimental works on carbonate dissolution (Facq et al., 2014; 2016) revealed that carbon speciation at HP condition (from 10 to 40kbars and 300 to 400°C) might be complex, with dominant HCO_3^- and $CaHCO_3^+$ (Fig. 4d,e). The role of different species in the fluid-rock interactions has yet to be completely understood. In the future, thermodynamic modeling coupled with geochemical modeling for fluid speciation, will likely shed light on this process.

1.3.2 *Carbonatite melts*

Carbonatite melt have been object of several studies because i) their importance for the understanding of metamorphic diamond formation in subduction zone environment, ii) they are extremely reactive, and iii) because they are likely to transport different types of trace elements than aqueous fluids, thus with implications for the formation of different type of sub-arc mantle metasomatism. Carbonatite are more frequently identified in mantle xenoliths (Schiano et al., 1994; Kogarko et al., 2001; Frezzotti et al., 2002), but the formation of such melts in subducted crustal rocks has also been reported in UHP-UHT metamorphic terrains (e.g. 4.3-6 GPa and 1000°C, Kokchetav massif; Korsakov and Hermann, 2006). As pointed out by Korsakov and Hermann (2006), carbonatite melts can form in the subducting slab in the sub-arc region. Poli (2015) showed by laboratory experiments that hydrous carbonatitic liquids can form in the slab even at temperatures as low as 870 to 900°C.

1.3.3 Other possible carbon transport mechanisms

Oceanic crust and metasediments that are brought into the upper mantle are much less dense than the peridotite. In particular, metasediments are 200kg/m^3 less dense than peridotite (Kelemen et al., 2003; Behn et al., 2011). This density contrast may cause the formation of metasediments diapirs that rise into the hot core of the mantle wedge and can undergo fluid-

absent partial melting. Lastly, mantle wedge corner flow could potentially drag carbonated forearc mantle into the arc magma window (Gorman et al., 2006).

1.4 Carbon fluxes in subduction zone: what goes down, mostly comes up?

After the considerable improvement of our understanding of the processes modulating the carbon residence time in different reservoirs and the transport mechanism, Kelemen and Manning (2015) realized a reevaluation of carbon fluxes in subduction zones (Fig. 5). The new evaluation gives a total carbon input in subduction zone ranging between 40-60 Mt C/yr. The total carbon fluxes from the slab into the shallow mantle results from the sum of fluxes linked to devolatilization, carbonate dissolution, carbonatitic melting and diapirism (see section 1.3), and ranges from 14 to 66 Mt C/yr. This means that, potentially, all of the subducted carbon is extracted in fluids and melts and transferred into the hanging wall of subduction zones. According to the authors, the observed carbon output from volcanoes is smaller than the subducted input, probably because the lithospheric mantle is an important reservoir. Part of this carbon may be recycled into the convecting mantle via delamination, while another component may remain within the cratonic upper mantle (Créon et al., 2016).

This also has major implications for the outgassing processes (Fig.1): if the subduction zone carbon cycle is in balance, then volcanic emissions from midocean ridges and within-plate volcanic centers would be a net flux from the mantle to the Earth's surface.

1.5 Rock carbonation: a new piece of the deep C cycle?

The discovery of carbonate formation by fluid-rock interactions during HP/LT metamorphism (Piccoli et al., 2016; Scambelluri et al., 2016) opened a number of questions about the mechanism and parameters that control rock-carbonation process at HP conditions as well as the source and composition of fluids involved.

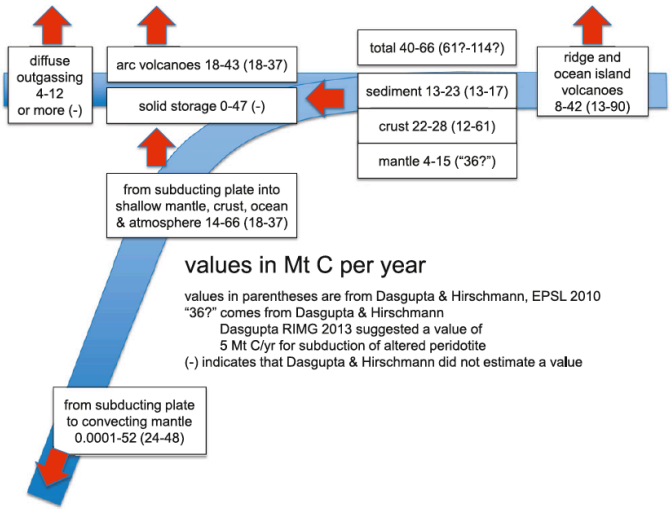

Fig. 5. Major fluxes of carbon estimated in this paper, with values from Dasgupta and Hirschmann (1) for comparison.

Fig. 5: Reevaluation of Carbon fluxes in subduction zones (Kelemen and Manning, 2015). Values in brackets are from Dasgupta and Hirschamann (2010).

The better understanding of this carbon sink process is what motivated this Ph.D. project because it might represent an important piece of the deep carbon puzzle. The carbonated metasomatic rocks object of this study were sampled in the lawsonite-eclogite unit of San Petrone (Alpine Corsica, France) and are part of a complex metasomatic system that affects lithological boundaries. Field observations, detailed petrological, geochemical and isotopic studies are the instruments used to get insights on the composition and source of the fluid responsible for rock-carbonation. In the following chapters (Chapters 4, 5), the field relationship of carbonate bearing metasomatic rocks with the surrounding rocks will described and the mineralogical composition of the study rocks will be discussed in terms chronology of mineral paragenesis and phase composition for major and trace elements. All together, these data constitute the frame for the interpretation of the mass balance and time-integrated fluid fluxes calculations (Chapter 6). This latter work was conducted at Yale University under the supervision of Jay J. Ague.

Then, we will report the stable isotopes study on oxygen, carbon, strontium and neodymium (Chaper 7). The aim of the isotopic studies is to constrain plausible fluid sources as well as

define the extension of the geochemical front, proxy for fluid-flow. Analyses of oxygen and carbon stable isotopes were performed at IPGP (Paris) in collaboration with Isabelle Martinez and Pierre Agrinier. Strontium and neodymium isotopes geochemistry was realized in the laboratory of University of Montpellier, in collaboration with Delphine Bosch.

Major results will be discussed all together in Chapter 8 and important conclusion on rock carbonation at HP will be presented at the end of this manuscript (Chapter 9).

Lastly, preliminary results on fluid inclusions study, LA-ICP-MS and thermodynamic modeling will be presented in the Chapter 10 as perspective work that deserve to be further investigated in the future. Fluid inclusions microthermometry analyses were conducted at ISTeP laboratory of University of Paris 6, in collaboration with of Anne Verlaguet, whereas LA-ICP-MS measurements were performed at the University of Montpellier, in collaboration with Olivier Alard and Olivier Bruguier.

CHAPTER 2
Geological setting

Alpine Corsica is a branch of the Alpine chain and shares with this latter structural and lithostratigraphic characteristics (Fig. 2.1). However, geodynamical complication are added by the opening of the Liguro-Provençal basin. The geodynamic context of the Western Alps is better constrained and in the following paragraph, I will briefly describe the main geological features of the Western Alps in order to outline the large-scale geodynamic setting of the study area and give the general characteristic of metamorphic ophiolites in the Alps. This brief introduction about the Western Alps is also necessary to introduce some geological unit nomenclature, give an outline of the structure of the Tethys ocean and briefly introduce the problem of the relationships between the Northern Apennine/Corsica and the Western Alps orogenic systems. Actually, these two Tethyan-type orogenic wedges are connected by the following general aspects (Molli, 2008):

- Presence of tectonic units with similar lithostratigraphic features and comparable structural evolution;
- Partially coeval age of tectonic events and deformations;
- Partially common dynamic of orogenic system(s) (pre-, syn- and post-collisional evolution);
- Superficial continuities with common and/or polycyclic (Alpine and the Apennic) evolution of tectonic units across the western Alps/Northern Apennine boundary.

Then, I will give a more detailed description of the geology of Alpine Corsica, where all the fieldwork has been conducted.

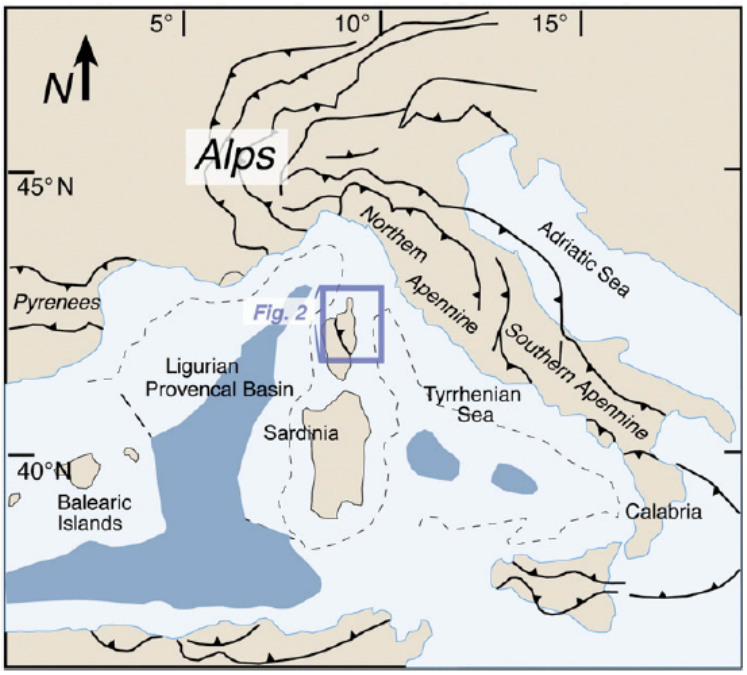

Fig. 2.1: Simplified regional setting of Alpine Corsica in the western Mediterranean area. Modified from Molli and Malavieille (2010).

2.1 Geology of the Alpine belt

The Alps mountain chain results from the collision of the European and Adriatic continental margins, after the closure of the Tethys ocean. The final closure during Eocene of the western portion of the Tethys ocean (also called Piemonte-Ligurian ocean) leaded to the formation of the western branch of the Alps, that run north-south along the border between Italy, France and Switzerland. This portion of the orogen is historically divided in two main domains: external and internal units, each of which is subdivided in units depending of the paleogeographic position. Table 2.1 gives a synthesis of the evolution of the nomenclature of alpine units with time and the relative interpretation.

The *external units* are non-metamorphic or very low grade metamorphic. All units are considered part of the European paleomargin formed by: the pre-alpine basement (Argentera, Pelvoux, Belledonne, Mont Blanc, Aiguilles Rouges, Aar and Gothard massifs) and parautochtonous Mesozoic cover.

Nomenclature of Alpine units

	JURA	EXTERNAL UNITS		INTERNAL UNITS					
				Penninic Domain				Austroalpine Units	
	Jura	**swiss molasse basin**	**Dauphinois**	**Valaisan**	**Briançonnais-Grand St. Bernard**	**Monte Rosa-Gran Paradiso-Dora Maira**	**Schistes Lustrés**	**Dent-Blanche and Sesia Lanzo**	**Ivrea zone**
Argand, 1934	Jura	swiss molasse basin	Helvetic	Lower Penninic	Middle Penninic	Upper Penninic	Mesozoic cover of penninic basement	Austroalpine	Southern Alps
Debelmas, 1974; Debelmas and Kerchove, 1980; Trumpy, 1980	Jura	swiss molasse basin	Dauphinois =Helvetique	Valaisan	Briançconnais	Piemonte zone: pre-Alpine basement and cover	Piemonte zone: ophiolitic complex and metasedimentary cover	Austroalpine	Southern Alps
Dal Piaz, 1997; de Giusti et al., 2003	Jura	swiss molasse basin	Helvetic and ultrahelvetic	External Penninic	Middle Penninic	Inner Penninic	Piemonte zone	Austroalpine	Southern Alps

Interpretation of Alpine units

One ocean model	europian continent	european paleomargin			Piemonte-Ligurian ocean	Adria paleomargin
Two oceans model	europian continent	european paleomargin	Valaisan ocean (middle Cretaceous)	briançonnais micro-continent	Piemonte-Ligurian ocean (Middle-Upper Jurassic)	Adria paleomargin

Table 2.1: Nomenclature of Alpine units and relative paleogeographic interpretation.

The *internal units* (Fig. 2.1) are composed by the Penninic domain (ascribed to the European paleomargin) and the Austroalpine units (Adriatic paleomargin) and are characterized by increasing metamorphic conditions from the west to the east. The funding of eclogite and blueschist facies imprint in the internal units led to the recognition of a fossil subduction zone (Ernst 1971; Dal Piaz et al., 1972). Actually, from Late Cretaceous to the Eocene, a number of continental and oceanic units were subducted to various depths and then exhumed to form the Austroalpine-Penninic wedge. The subduction history of the Austroalpine-Penninic wedge is recorded by a large spectrum of low-T mineral assemblages, which developed in eclogitic and locally UHP conditions (Desmons et al, 1999; Frey et al., 1999). These assemblages were overprinted by middle-high-T Barrovian metamorphism of Late-Eocene-Early Oligocene age. From the Oligocene onwards, the Austroalpine-Penninic wedge was accreted to the external Helvetic-Dauphinois unit (Coward and Dietrich, 1989) by the activation of the frontal Penninic thrust. The Canavese line separates the Austroalpine-Penninic wedge from Adria continental margin (Fig. 2.1).

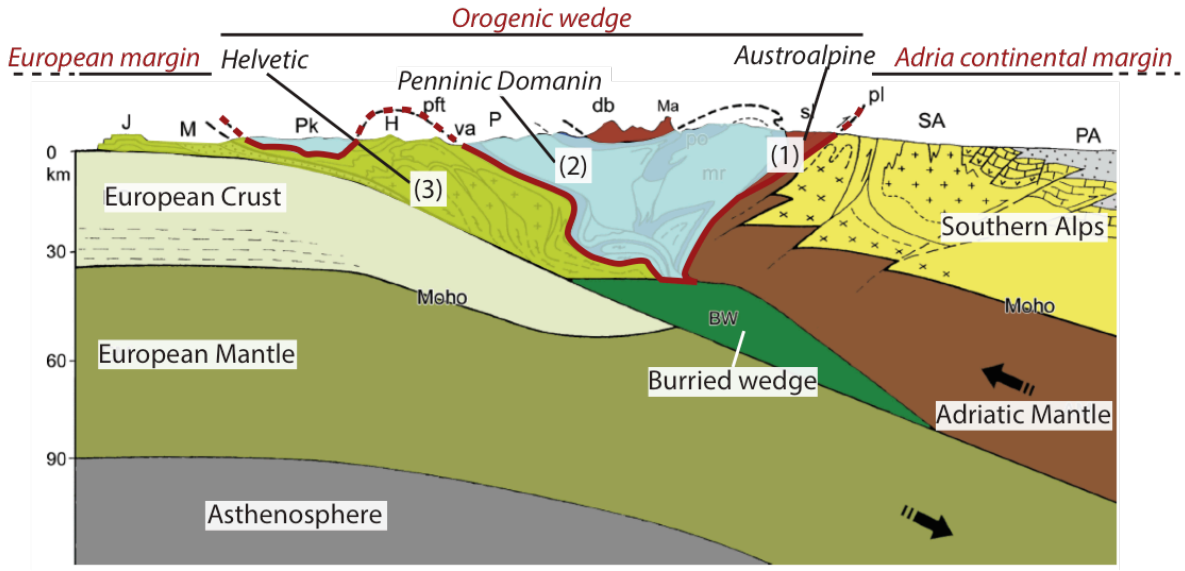

Fig. 2.1: Lithospheric section of north-western Alps. Internal units (1 and 2) thrust over the external unit (3). The Canavese line is the western portion of the Periadriatic fault system (pl). The red line underline the orogenic wedge the is border with the Periadriatic line to the east and with the Penninic front to the west

Among the internal units, the ocean-derived units are ascribed to the Piemonte zone, that is composed by ophiolitic remnants of the Jurassic Piemonte-Ligurian ocean. Several studies on the paleogeography of metamorphic units in the Alpine orogenic wedge (in both Western and Central-Eastern Alps) point to the interpretation of the tectono-metamorphic units from the Piemonte zone as portion of a magma-poor, hyper-extended lithosphere related to the Jurassic opening of the Alpine Tethys (Fig. 2.2a; e.g., Manatschal, 2004; Manatschal and Müntener, 2009; Beltrando et al., 2010,2012, 2014; Mohn et al., 2010, 2011,2012).

The eclogitic ophiolites of the Western Alps are characterized by abundant mafic cumulates and metabasalts, which total thickness never exceed 1km (Lombardo et al., 1978; Lombardo and Pognante, 1982). Commonly, pelagic sediments and mafic or ultramafic breccias stratigraphically overlie serpentinized mantle peridotite or gabbros, This lithostratigraphy is characteristic of slow-spreading oceans (Fig. 2.2b; Lagabrielle and Cannat, 1990). Eclogitic paragenesis are well preserved in the ophiolitic unit of Zermatt-Saas and in the Monviso unit, its southern homologues. Ages for subduction metamorphism constrain peak metamorphic conditions to Early-Middle Eocene (45-42 Ma; Botwell et al., 1994; Rubatto et al., 1998;

Amato et al, 1999; Mayer et al., 1999). Rb-Sr dating in the Austroalpine outliers also gives an eclogitic imprint during Eocene (49-40 Ma; Dal Piaz et al., 2001), supporting the interpretation of the continental slivers as intraoceanic extensional allochthons, stranded inside the Piemonte-Ligurian ocean.

2.2 Geodynamic and geological setting of Alpine Corsica

The island of Corsica is part of the Sardinia-Corsica micro-plate and it is occupies a central position within the western Mediterranean. Corsica and Sardinia were separated from the Iberian-European mainland by the opening of the Liguro-Provençal basin during Late Eocene (Molli, 2008). The Liguro-Provençal basin records a complex geological evolution: an early stage connected with the development of the Pyrenees orogen (Seranne, 1999; Lacombe and Jolivet, 2005), was followed, during Oligocene-Early Miocene, by Apennine-related back-arc rifting stage. During Burdigalian (19-16 Ma), the oceanic spreading provoked the 30° anticlockwise rotation of the Sardinia-Corsica micro-plate, until its present day position (Speranza et al., 2002; and reference therein).

The terrains of Corsica were also involved in the Europe-Apulia plate convergent system during the Eo-Miocene, where the closure of the slow-spreading Tethys ocean led to the formation of an orogenic belt, Alpine Corsica, now occupying the northeastern part of the island. Thus, Corsica locates at the junction between the Alps and the Apennines (Fig. 2.1; Piana and Polino, 1995; Giglia et al., 1996; Schumacher and Laubscher, 1996; Mosca et al., 2003). The geodynamic evolution of Alpine Corsica is strongly under debate because the Alps and the Apennines represent two independent orogenic segments characterized by opposite tectonic vergence, N/NW the former and E/NE the latter, roughly oriented perpendicular to their arcuate trends (Molli and Malavieille, 2010).

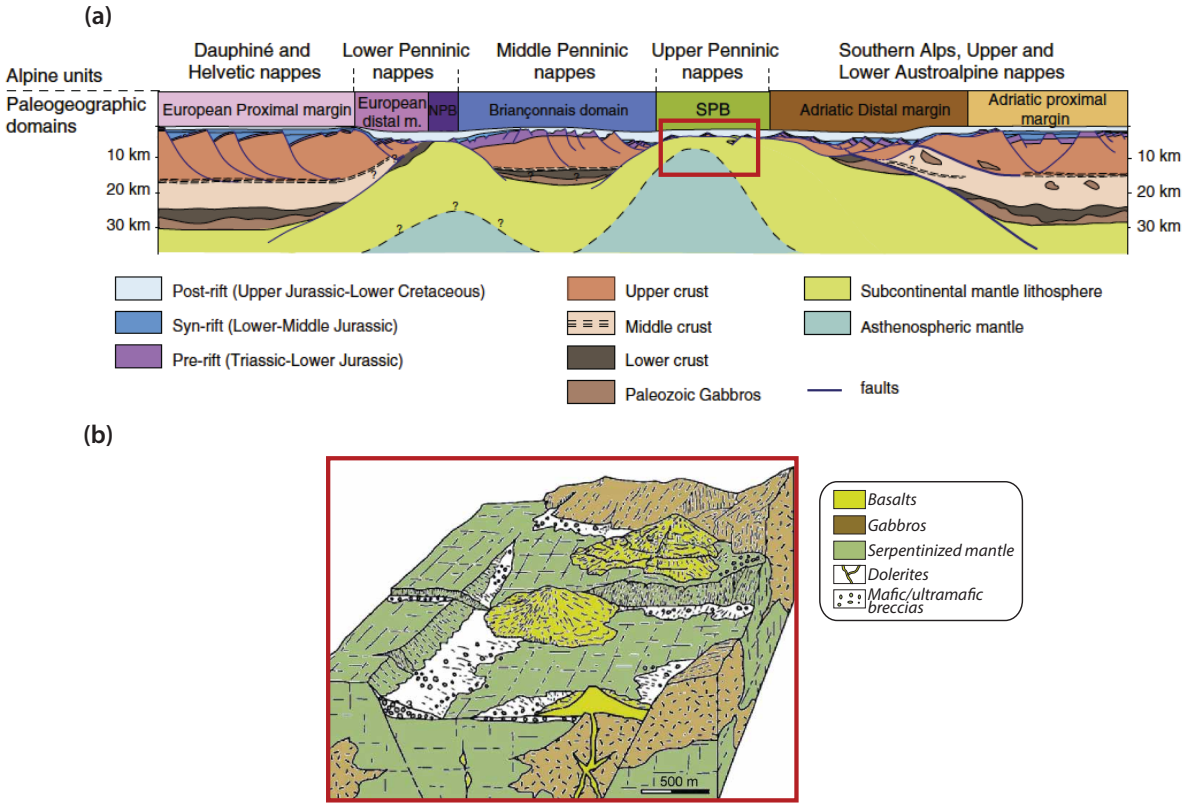

Fig. 2.2: a) Jurassic paleogeography of the Alpine Tethys as reconstructed from observations performed in the Central and Eastern Alps and Western Alps (Fig. from Beltrando et al., 2014). **b)** Schematic reconstruction of the Jurassic Alpine Tethys basement based on field observations in ophiolitic unit from the Western Alps (Queyras area). Figure from Lagabrielle and Cannat (1990).

Corsica is subdivided into two main structural domains (Table 2.2: the autochthonous Hercynian Corsica to the west, composed by undeformed series of Corsica microplate (basement rocks intruded by granites, and a sedimentary cover up to Eocene; Molli, 2008) which largely escaped Alpine subduction and orogenesis; the Alpine Corsica, in northeastern part of the island. This latter forms a metamorphic core complex superimposed on the previous Alpine compressional orogen and thrust over the western part of the island (Fig. 3 geodinamica Jolivet et al., 1991). The boundary between these two structural domains is morphologically accentuated by longitudinal valleys of the Ostriconi river and the middle reach Golo River. Figure 4a shows how, in simplified terms, Alpine Corsica consists of a stack of variably metamorphosed units (Mattauer et al., 1981; Durand-Delga, 1986; Malavieille et al., 1998; Vitale Brovarone et al., 2013). From bottom to top, they are:

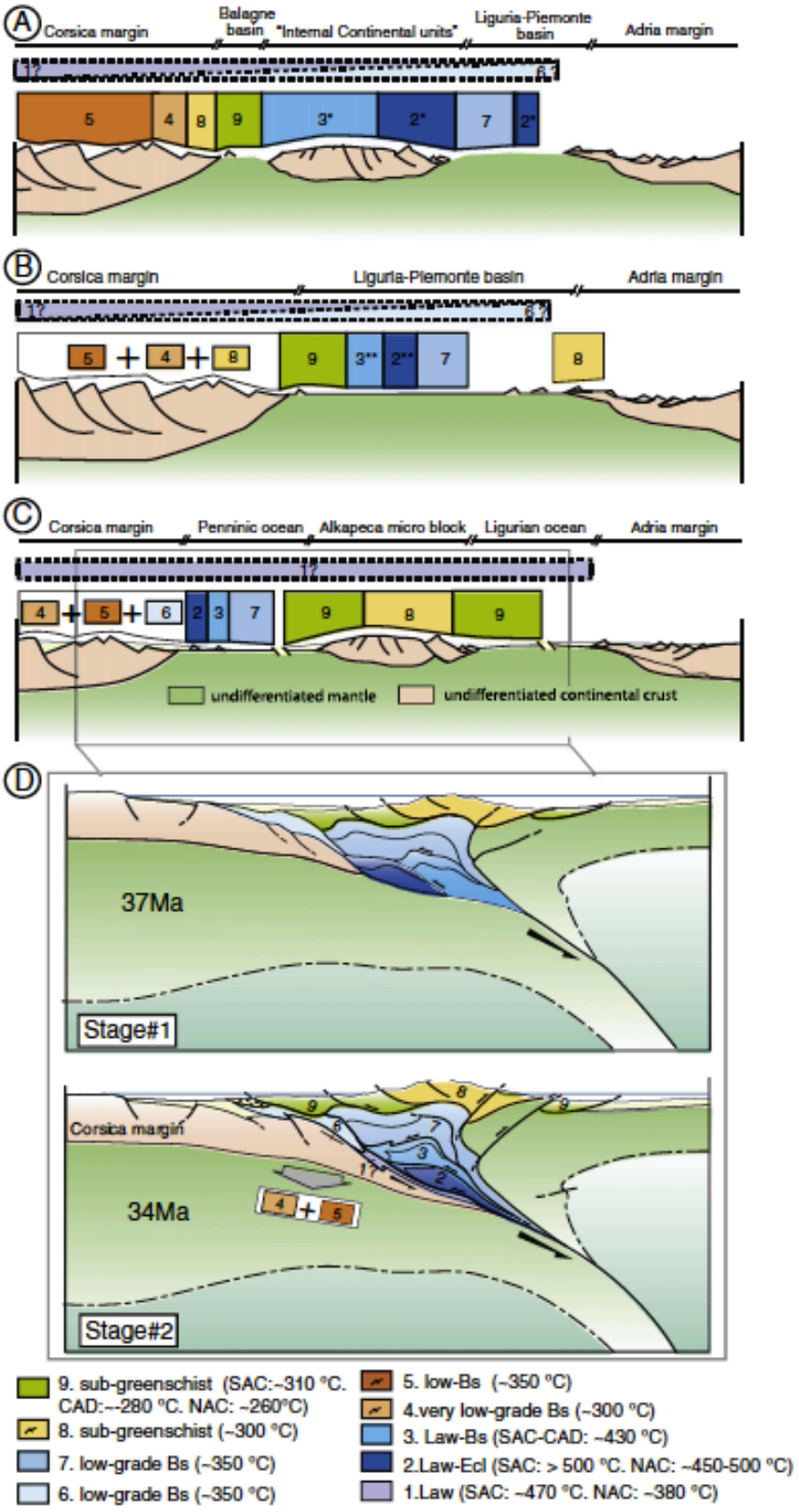

Fig. 2.3: a,b,c,) Paleogeographic reconstructions at Late Cretaceous. **d)** Possible tectonic model for Alpine Corsica considering a progressive underplating of contiguous lithospheric sections. In this interpretation, an east dipping subduction is chosen. Figure from Vitale Brovarone et al., 2013.

i. Continental units, that comprise: the External Continental units and the Internal Contiental units. These units are formed by Hercynian granitoids with minor relicts of host-rock basement and metasedimentary rocks of Permian to Eocene ages with Briançonnais affinity (see Tables 2.1 and 2.2). The Continental units underwent different metamorphic conditions and are now observable in different structural positions within the nappe stack.

ii. The Schistes Lustrés (SL) complex is formed by Piemonte-Ligurian ocean derived ophiolitic sequences (mantle ultramafics, gabbros, pillow basalts and associated Jurassic to Cretacous metasediments; e.g. Lagabrielle and Lemoine, 1997). This work focuses on metasomatic processes occurring along fluid channels in this unit. Thus, a detailed description of each lithology and relative structural relationship will be given later in this chapter.

iii. The Balagne-Nebbio-Macinaggio system (also called *Nappes Supérieures* in the French literature) is formed by low-grade metamorphism ophiolitic and continental units overthrusted in a geometrically high structural position within the nappes stack.

In Alpine Corsica compression ceased in Late Oligocene, time when it was separated by the rest of the main chain by the extension and opening of the Liguro-Provençal basin and the Tyrrhenian sea (Jolivet et al., 1991). This extensional phase is recorded in the Miocene basin sediments.

As mentioned above, the attribution of Alpine Corsica to an east-dipping (i.e., Alpine) or west-dipping (i.e., Apennine) subduction is still debated. Nevertheless, the choice between the Alpine vs. Apennine subduction model strongly influences the paleogeographic interpretation of some tectonic unit (Fig. 2.3, Vitale Brovarone et al., 2013). The paleogeographic reconstruction shown in Figure 2.3 is based on a east-dipping subduction model, which

implies a structure of the belt by means of progressive underthrusting of contiguous lithospheric sections of a subducting thinned continental margins and associated OCT. The Alpine subduction model is the most acknowledged in recent publications (e.g., Molli, 2008 and references therein; Argnani, 2009; Handy et al., 2010; Molli and Malavieille, 2010; Ravna et al., 2010), and it is consistent with the observed rejuvenation of peak metamorphic ages from the upper to the lower structural positions and with the increase of the metamorphic conditions from the highest-to the lowest-grade units.

2.2.1 Schistes Lustrés complex lithostratigraphy and metamorphism

The stack of metamorphic units that compose the SL complex is folded within a N-S antiform (e.g. Caron, 1977; Jolivet et al., 1990; Molli and Malavieille, 2010) and occupies the eastern flank of the Corsica belt (Fig. 2.4). In the literature, the SL complex is subdivided into three groups based on their lithological features and structural position, namely continental, transitional and oceanic (Lahondère, 1988; Lahondère and Caby, 1989; Lahondère et al., 1992; Lahondère, 1996; Rossi et al., 2001). Alternatively, most geological maps and tectonic schemes are built in a lithostratigraphic or tectono-metamorphic perspective. These two latter classifications are those that I will use in this work. Since they do not match uniformly throughout the belt, they will be presented separately.

Lithostratigraphy:

i. The *Castagniccia formation* (Delcey, 1974; Caron and Delcey, 1979; Caron et al., 1979). This formation is composed by a lower carbonate rich sequence and an upper carbonate poor sequence. In the southern part of Alpine Corsica, the upper part of the Castagniccia formation is observed in association with the Santo Pietro di Tenda sediments (Rossi et al., 1994a,b).

ii. The *Santo Pietro di Tenda formation* (Caron and Delcey, 1979). This formation forms a thin continuous rim bordering meta-ophiolites and slices of continental basement rocks. Continent derived debris are characteristic of this formation, which is referred to an Ocean-Continent Transition paleogeographic domain (Fig. 4c,d; e.g. Caron and Delcey, 1979; Vitale Brovarone et al., 2011a,b).

iii. The *Bagliacone-Riventosa formation*, which crop out in a restricted area and its emplacement predates the deposition of non-metamorphic Eocene sediments (Egal, 1992).

iv. The *Inzecca formation* is a typical Tethyan supra-ophiolitic sedimentary sequence consisting, from the lower to the upper term, of: metaradiolarite, marbles, impure marbles, calcschists and metapelites.

2.2.2 Metamorphism in the Schistes Lustrés complex:

In the SL complex, metamorphic zonation has been limited to diagnostic lithologies, like metamaphic rocks. We can distinguish four tectonometamorphic domains, that are, from the bottom to the top (Figs. 2.4b):

i. The lawsonite–blueschist, metasediments rich zone. *Castagniccia*-type metasediments are the most abundant lithology. However, it locally includes continent derived material such as meta-arkose and meta-conglomerate within metasedimentary sequences (*Santo Pietro di Tenda formation*), and slices of basement rocks that are ascribed to a Tethyan Ocean–Continent Transition (OCT) zone (Meresse et al., 2012; Vitale Brovarone et al., 2011a). Metamorphic conditions are estimated at 300-380°C and 1.4–1.7 GPa (Jolivet, 1998).

ii. The lawsonite–eclogite zone. This unit includes meta-ophiolite (serpentinites and metabasalts, and associated metasedimentary rocks; e.g. Lagabrielle and Lemoine,

1997) and slivers of continental basement rocks (Internal Continental units, Table 2.2). These rocks are interpreted to represent a magma-rich segment of the Tethys basin, and show lithostratigraphic characters very similar to those of the eclogite-facies units exposed in the Piemonte Zone of the Western Alps (e.g. Monviso/Rocciavré/ Zermatt–Saas area, Lagabrielle and Lemoine, 1997; Lombardo et al., 2002). Based on tectono-stratigraphic considerations, this unit has been referred to an ocean-continent transition (OCT) zone (Vitale Brovarone et al., 2011a). Metamorphic conditions are estimated at ~490–550 °C and 1.9–2.6 GPa (Ravna et al., 2010; Vitale Brovarone et al., 2011a), and the most recent radiometric estimates point to a Late Eocene metamorphic climax (~34 Ma) by means of U–Pb on zircon from paragneiss (Martin et al., 2011) and garnet Lu-Hf ages from metabasalts in the lawsonite-eclogite facies unit (Vitale Brovarone and Herwartz, 2013). The study of this work-the San Petrone unit- is within this metamorphic unit. More details will be given below and in Chapter 4.

iii. The lawsonite blueschist-facies zone. The lithologies of this unit are similar to the previous domain and P-T estimates are ca. 1GPa and 300 ±50° C (Lahondère, 1996). Notably, in Cima di Malaspina area, fresh aragonite, grossular garnet and wollastonite are documented associated with HP metasomatism (Chopin et al., 2008; Malvoisin et al., 2011; Galvez et al., 2013a,b).

iv. A low-grade blueschist meta-ophiolite-rich domain. Petrological investigations from the Golo valley yielded P=0.8 ±0.2 GPa and T<450°C (Levi et al., 2007).

Nomenclature of Corsica units									
Structural domain	**HERCYNIAN CORSICA**		**ALPINE CORSICA**						**Liguro-Provençal Basin**
Alpine equivalent	**(External units)**		**(Penninic domain)**						**(Apennines-subduction related)**
origin	**Variscan**		***Alpine orogenic wedge***						***Early to Middle Miocene***
	Hercynic basement	*Sedimentary cover up to Eocenen*	*Lower External continental units*	*Upper External Continental units*	*Tenda massif*	*Internal continental Units*	*Schistes Lustrés (SL) complex*	*Nappes Supérieures*	
Units	--	--	Annunciata-Volparone/Popolasca/Corte/Rizzo Bianco	Santa Lucia-Falconaia/Caporalino/Linguizeta	--	Centuri/Serra di Pigno/Farinole/Morteda/San Petrone/Golo/Sant'Andrea di Cotone	low-grade Inzecca/law-bluschist/law-eclogite units	Balagne/Nebbio/Rio Magno/Pineto/Maci naggio	--
structural position	--	--	below SL complex	overlay SL complex	separated from the Balagne Nappe and SL complex by shear zones	interlayered within the SL complex	thrust over the External Continetnal units	highest structural position	half-graben on the top of the Nebbio unit
Protolith	kinzigite basement; Permo-Carboniferous granitoids	Eocene auchtonous formations	Hercynian basement; Permian to Eocene sedimentary cover	Hercynian basement; Triassic to Eocene sedimentary cover; serpentinite and stratified mafic complex	amphiobole biotite granodiorites; cogenetic dacitic volano-sedimentary formations	HT paragneiss; orthogneiss; leucocratic dyke	Ligurian Tethys metaophiolites and metasedimentary cover	ophiolitic and continent derived rocks	limestones and conglomeratic deposits
Alpine metamorphism	--	--	low-grade blueschist	subgreenschist facies	blueschist-facies conditions	from low-grade blueschist to lawsonite-eclogite facies	from low-grade blueschist to lawsonite-eclogite facies	sub-greenschist	--

	Interpretation of Corsica units			
	Europian continent	distal European Continental margin	Piemonte-Ligurian ocean	Apennines subduction back-arc basin

Table 2.2: Nomenclature of Corsica unit and relative paleogeographic interpretation (Lahnodère, 1988; Lahondère and Caby, 1989; Lahonère et al., 1992; Lahondère, 1996; Lahondère et al., 1999; Rossi et al., 2001)

2.2.3 San Petrone lawsonite-eclogite unit

In Alpine Corsica, lawsonite-eclogite and lawsonite-blueschist are present as pods or lenses in retrograded epidote-blushischist or greenshist facies rocks (Péquigon et al., 1984; Miller et al., 2000; Ravna et al., 2010). In the San Petrone area, the HP rocks are especially well preserved, and retrogression is generally localized along shear zones and only locally present as static overprint. This unit, which experienced the highest-pressure conditions among all the internal Continental Units, is tectonically sandwiched between the blueschist-facies Castagniccia and the lawsonite-blueschist facies zone. The San Petrone unit is characterized by a basal body of serpentinite overlain by a laterally variable lithostratigraphy, which comprises: i) slivers of continental basement rocks; ii) metabasalts; and iii) *Inzecca formation*-like Mesozoic metasedimentary rocks. Ophicarbonates are locally found between the serpentinite and the overlying rocks. The continental basement slivers lie directly upon the serpentinite, and contain both ortho- and paragneiss. These continental basement slivers are interpreted as continental extensional allochthons emplaced on top of an ultramafic substratum during the

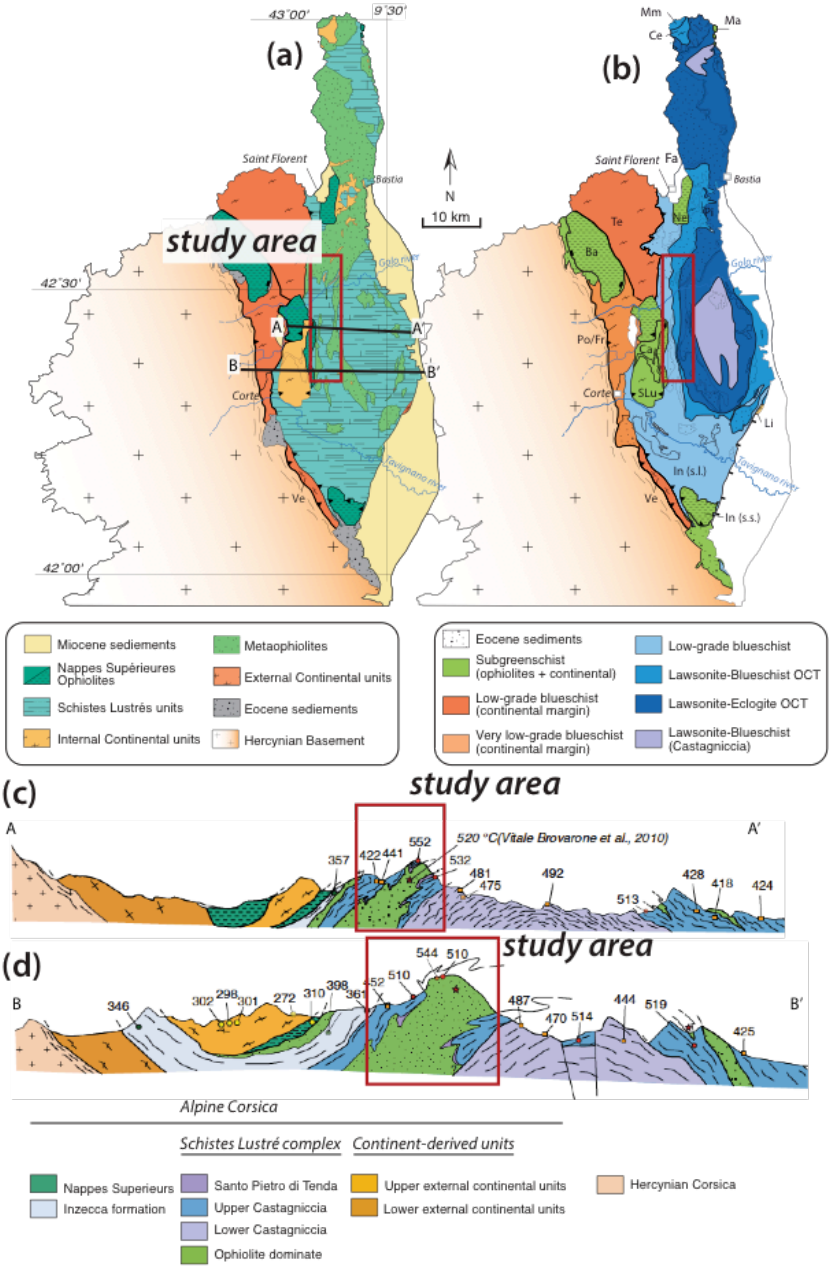

Fig. 2.4: Geology of Alpine Corsica. Simplified geological **(a)** and metamorphic **(b)** maps of Alpine Corsica. **c-d)** Geological cross sections compiled after the 1:50000 geological maps (BRGM) and original data from Vitale Brovarone et al. (2013). In both cross sections vertical distances are exaggerated with Height=2Lenght. Shaded symbols indicate the temperature estimated by Raman spectroscopy on carbonaceous material. Figures modified after Vitale Brovarone et al. (2013, 2014a) and Vitale Brovarone and Herwartz (2013).

opening of the Tethyan basin in a Jurassic OCT zone (Vitale Brovarone et al., 2011a and references therein).Mesozoic metasedimentary rocks variably overlie the serpentinite, the continental slivers, and/or the ophiolite-type rocks. The Mesozoic metasediments can be divided into early post-rift and post-rift sediments. The first group consists of metacherts

(likely radiolarian metacherts) and marbles of plausible Jurassic sedimentary age; the second group mainly includes calcschists sensu stricto (s.s.), i.e., quartz-pelitic layers (with carbonate in variable abundance) of Cretaceous sedimentary age (see Vitale Brovarone et al. 2011a for review). This composite tectonostratigraphic sequence is folded by a series of large (km in length) N-S non-cylindrical anticlines and synclines that locally overturn the overall upright tectonostratigraphy. The HP minerals mark the main regional schistosity. Because of the non-cylindrical folds, the entire lithostratigraphy is affected by local and discontinuous synformal and antiformal structures with N-S trending fold axes. The whole tectonolithostratigraphic suite of the San Petrone unit underwent consistent peak metamorphic conditions of about 500-550 °C and ~2.2-2.4 GPa (Vitale Brovarone et al., 2011a) in the Late Eocene (~34 Ma, Martin et al., 2011; Vitale Brovarone and Herwartz, 2013).

Within the San Petrone unit, we can distinguish different types of carbonate bearing rocks: calcschists, marbles, ophicarbonates and peculiar lithologies previously referred to as meta-hardgrounds (Vitale Brovarone et al., 2011a).

- Calcschists represent the metamorphosed Mesozoic sedimentary cover of Tethys Ocean. As their equivalent in the Western Alps, they are characterized by the alternation of impure marbles and more terrigenous levels.
- Marbles are widely distributed all along the Monte San Petrone unit and vary in thickness from a few tens of centimeters to several meters. The thickest portions commonly contain detrital layers with continental basement pebbles ranging in diameter from a few centimeters to a few tens of centimeters (e.g., east of PuntaVentosa, Monte Calleruccio and Aja Rossa).
- Ophicarbonates, interpreted to result from the hydrothermal alteration of exhumed mantle at the ocean floor. In the area of this study, they crop out nearby Punta Ventosa. Serpentinite clasts vary in size from a few millimeters to several meters.

- Rocks referred to as meta-hardgrounds form discontinuous lenses that only occur at the bottom of the Mesozoic metasedimentary pile, in contact with both the serpentinized basement and the continental basement sliver. They typically consist of banded silicate-rich marbles with anomalous mineralogy relative to the other surrounding carbonate-rich rocks, including garnet, clinopyroxene and lawsonite. The re-evaluation of the petrology of these rocks as metasomatic product and the understanding of the mechanism leading to their formation, are the motivations behind this work.

2.2.4 Carbon and calcium metasomatism in the high-pressure units of Alpine Corsica

In the HP units of Alpine Corsica, the overall exceptional preservation of HP paragenesis allowed the preservation of metasomatic product formed during peak metamorphism. Two main types of metasomatism have been described in Alpine Corsica so far: carbonate reduction and precipitation of abiotic graphite along a serpentinite/marble contact at the Malaspina ridge (Malvoisin et al., 2011; Galvez et al., 2013a,b) and Ca metasomatism associated with the massive crystallization of lawsonite (Vitale Brovarone et al., 2011a; Martin et al., 2011; Vitale Brovarone et al., 2014a).

In the Cap Corse, the Malaspina ridge exposes a contact between metasediments and serpentinites (Meresse et al., 2012). The contact between the serpentinite and the overlaying calcschist is characterized by a ca. 10 cm thick reaction zone, which has been subject of several studies (Chopin et al. 2008, Malvoisin et al. 2011, Galvez et al., 2013a,b). The reaction zone is composed of quartz, wollastonite, Ca-rich garnet, and carbonaceous material (Malvoisin et al., 2011; Galvez et al., 2013a,b). The results of these studies demonstrate that graphite in the reaction zone formed by abiotic nucleation and grow after carbonate reducing

reaction during HP metamorphism (Malvoisin et al., 2011; Galvez et al., 2013a,b), following the reactions:

$$CaCO_3 \text{ (calcite)} + SiO_2 \text{ (quartz)} = CaSiO_3 \text{ (wollastonite)} + C \text{ (graphite)} + 2O$$

In Malaspina ridge, carbonate reduction occurred in relatively closed system (dominant diffusion mass transfer through fluid filled porosity): the serpentinite body imposed reducing conditions and carbonate reduction was promoted by the presence of H_2 ($\pm$ CH_4) aqueous intergranular fluids. It is worth noting, that graphite is a highly refractory material, and it is plausible that it will be scarcely re-mobilized, unless of course large fluid fluxes and open system metasomatism. Thus, carbon storage by carbonate reduction might represent an important carbon sink process.

Lawsonite metasomatism in the eclogite facies San Petrone unit displays a large variety of metasomatic product. Moreover, these metasomatic rocks are successively affected by carbonation. A more detailed description will be given in the following paragraph.

2.2.4.1 Lawsonite metasomatism in the blueschist and eclogitic unit of Alpine Corsica

Metasomatic rocks in the blueschist and eclogitic (San Petrone) unit show a wide petrographic variability. In the blueschist unit lawsonite metasomatite only affect the metasediments in contact with mafic/ultramafic rocks. Metasomatic products include massive lawsonite-chlorite fels with matrix composed by chlorite, together with phengite, quartz, albite, blue-amphiboles and locally Ca-carbonate. In the eclogite unit, metasomatism affects both the metasedimentary cover and the continental basement sliver in contact with the serpentinite basement. In most of cases, deciphering a protolith is difficult, considering the high variable composition of the precursor rocks. Metasomatic products include lawsonite with dominant clinopyroxene in the matrix (Figs. 2.5a,b). Metasomatic lawsonite is always very fresh and exhibit randomly oriented black, inclusion-rich crystals. Metasomatic

clinopyroxene is also very abundant and confers a yellowish-greenish color to the rock (Fig. 2.5b). Metasomatic crystals grow on pre-existing compositional layers, resulting in a compositional layering of lawsonite-rich and lawsonite-clinopyroxene rich domains (Vitale Brovarone et al., 2014a). Clinopyroxene veins also are found in association with the lawsonite-metasomatite (Fig. 2.5c)(see Vitale Brovarone et al., 2014a for details). The process of lawsonite metasomatism corresponds to a dramatic chemical modification of the rock with strong enrichment in Ca and depletion in SiO_2, Na_2O and K_2O. The increase in the modal amount of lawsonite in the rock, in some cases from 0 vol.% to more than 75 vol.%, also corresponds to a tremendous increase in the rock's water content, up to ca. 12 wt% (Vitale Brovarone and Beyssac, 2014). The chemical patterns of lawsonite metasomatism are similar to rodingitization, as observed at the ocean floor or in the Alpine metamorphic rocks. Despite that, on the basis of inferred paragenesis, textural observations (equilibrium between lawsonite and garnet rim) and garnet composition in major and trace elements, Martin et al. (2011) clearly demonstrated that this metasomatism occurred at HP conditions during subduction. Cr and Ni mass gain after lawsonite-metasomatism gave robust indications of serpentinite-derived external fluids (Fig. 2.5d). This hypothesis was subsequently confirmed by oxygen isotopic measurements (Martin et al., 2014). On the basis of these data, all the authors have proposed metasomatism occurred in open system with highly channelized fluid flow along the lithological boundaries.

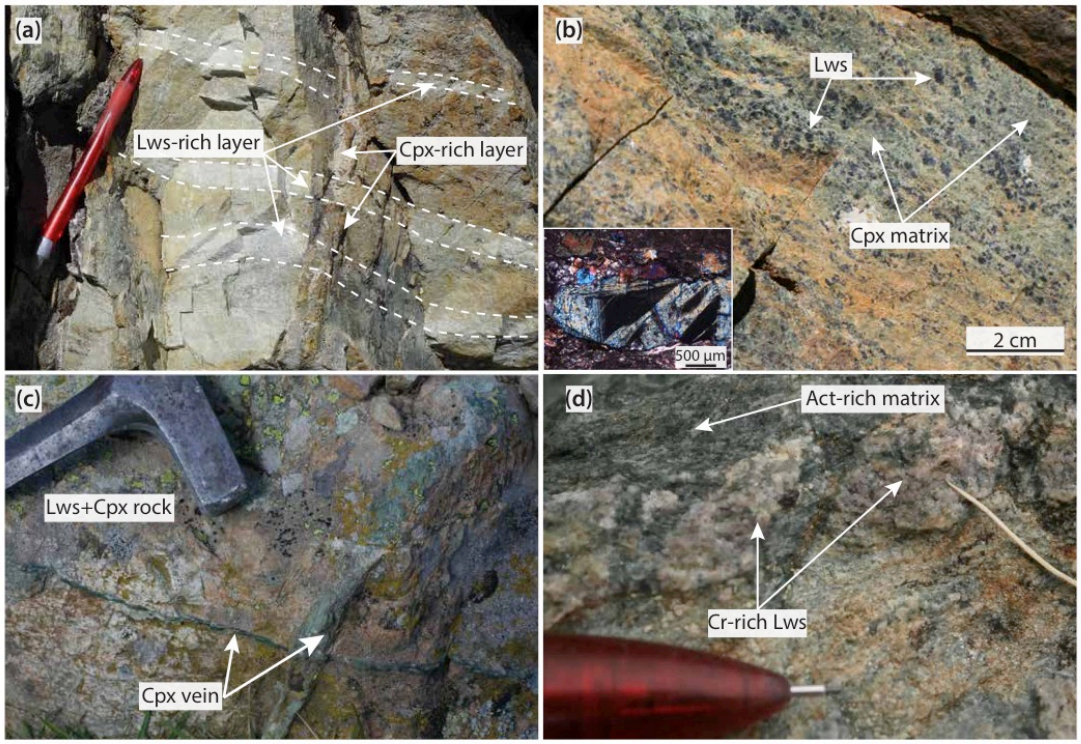

Fig. 2.5: Example of lawsonite metasomatite from the eclogite unit of San Petrone in the Aja Rossa area. a) Example of lawsonite metasomatite forming on layered continental basement rocks, while preserving the protolith fabric; b) Example of lawsonite metasomatite composed by clinopyroxene and inclusion rich lawsonite (mainly carbonaceous material, sulphides and rutile). In the box, a photomicrograph at crossed polarized light of sample 1cor12-11L is reported. In the photomicrograph, it can be recognized a fresh crystal of lawsonite with abundant carbonaceous material inclusion, in a clinopyroxene rich matrix. c) Clinopyroxene vein cutting across the lawsonite-metasomatite (courtesy of T. Duretz). d) Lawsonite metasomatite with dominant actinolite matrix. The pinkish color of lawsonite crystal is due to the high Cr content.

CHAPTER 3
Methodology and analytical techniques

3.1 Scanning electron microscopy and electron microprobe

Petrographic thin sections were carbon coated for scanning electron microscopy (SEM). Observations were performed at a working distance of 7.5 mm using a Zeiss Ultra 55 field emission gun SEM operated at 15 kV with a 60 and 120 μm aperture. Backscattered electron (BSE) mode was used to investigate chemical heterogeneities using an Angle Selective Backscattered Detector (AsB) or an Energy Selective Backscattered Detector (EsB). Energy dispersive X-ray spectrometry (EDXS) maps were acquired using an EDXS QUANTAX system equipped with a silicon drift detector XFlash 4010 (Bruker). Data were processed with the software Esprit (Bruker). Mineral analyses were performed on a Cameca electron microprobe (either SX-100 or SX Five) (Camparis, Université Paris 6). Common analytical conditions were adopted for spot analyses [15 kV, 10 nA, wavelength-dispersive spectroscopy (WDS) mode], using Fe_2O_3, $MnTiO_3$ (Mn, Ti), diopside (Mg, Si), orthoclase (Al, K), anorthite (Ca) and albite (Na) as standards. The automated Cameca ZAF procedure was used for quantification (Tables at the end of the manuscript).

3.2 Optical cathodoluminescence

Cathodoluminescence images were collected at the Department of Earth Science (University of Turin, Italy) with a microscope performed with CITL 8200 mk3 equipment. Operating conditions were 17 kV a d 400 mA. The luminescence of carbonates (e.g., Habermann et al., 1996; 1998) is suppressed by some major or trace elements (typically Fe, Sr) and activated by others (e.g., Mn, Na, Ti, Sm, Dy, Tb). The Fe/Mn ratio is more important than their absolute

concentration (e.g., Jarc and Zupancic, 2009). Crystallographic structure, reticular defects, and crystallographic orientation of minerals also influence their luminescence (e.g., Schertl et al., 2004).

3.3 Raman microspectroscopy

Raman microspectroscopy was performed using a RenishawInVIA Reflex microspectrometer (IMPMC Paris). We used a 532nm Laser Physics argon laser in normal polarization. The laser was focused on the sample by a DMLM Leica microscope with a 50x objective (numerical aperture 0.75).

3.4 Whole rock analysis

Rocks samples were crushed and then pulverized in an agate mill for trace elements whole-rock analyses (WR). Analyses of major elements on WR were performed at the "Service d'Analyse des Roches etdes Minéraux" (SARM, Nancy, France) by X-ray fluorescence (XRF). Trace elements on WR were analyzed by ICP-MS using an Agilent 7700× from the "Analyse des Elements Trace dans l'Environnement (AETE)" technical platform from Montpellier University (France). Bulk rock chemical analyses for major and trace elements for the selected samples for mass balance calculation (Chapter 6) were carried out by SGS Minerals Services using X-ray fluorescence (XRF) and inductively coupled plasma-mass spectrometer (ICP-MS) techniques (For a summary of analytical methods and uncertainties, see Ague, 1994a, 2003a) (Tables 4.2, 6.1 and 7.3.1 at the end of the manuscript).

3.5 Laser ablation inductively coupled plasma mass spectrometer (LA-ICP-MS)

In-situ trace element concentrations were analyzed using a Laser ablation inductively coupled plasma mass spectrometer (LA-ICP-MS) at Géoscience Montpellier (France). The used LA-

ICP-MS consists of an excimerGeolas 193 nm laser coupled to a ThermoFinnigan XR-element ICP-MS. The ICP-MS was operated at 1350 W and tuned daily to produce maximum sensitivity for the medium and high masses, while keeping the oxide production rate low ($^{248}Th/^{232}Th \leq 1\%$). The laser ablation was performed in a pure He atmosphere ($\approx 0.61\ min^{-1}$) with the following conditions: spot size was 26, 51, 77 and 102 μm, depending on mineral size and required spatial resolution, repetition rate and energy density were set at 7 Hz. The gas background was measured for approximately 90s before firing the laser during ablation times of 60s. For pyroxene crystals, the gas background was measured longer, approximately 105s. Data reduction was carried out using the GLITTER software (Griffin et al., 2008). Quantification of trace element concentrations by LA-ICP-MS requires an external calibration standard and the concentration of an internal standard that has been obtained by an independent method. In this study, the NIST 612 and BIR-1G glasses (reference values from Pearce *et al*., 1997) were used for the external standardization. Internal standard was Si or Ca, using the SiO_2 or CaO weight percent measured by electron microprobe.

3.6 Stable and radiogenic stable isotopes geochemistry

3.6.1 Carbon and oxygen stable isotopes of Ca-carbonate

Chips of carbonate were taken from hand-samples and crushed in an agate mortar. Raman and SEM analyses establish that the carbonate is nearly pure Ca-carbonate. The isotopic composition of calcite was measured by an AP2003 continuous flow mass spectrometer at LGIS, IPGP. Approximately 2 to 2.5 mg of sample were loaded in vials; three standards of pure calcite were also used for calibration of both concentration and isotopic composition. After flushing with ultrapure helium, orthophosphoric acid (H_3PO_4) was introduced in each tube in order to produce gaseous CO_2. After 4 hours of reaction at ambient temperature, calcite completely decomposes to release CO_2 (McCrea, 1950); gases were then transferred

into the mass spectrometer for analysis. In order to improve the precision of the measurements, each analysis was repeated four times for each vial, and each sample analysed twice. The isotopic $^{13}C/^{12}C$ and $^{18}O/^{16}O$ ratios are expressed using the conventional δ-notation relative to PDB and SMOW international standards. The precision is 0.1‰ for $\delta^{13}C$ and 0.2‰ for $\delta^{18}O$. The results are reported in Table 7.3 at the end of this manuscript. When an average value is indicated, the standard deviation (1σ) is also reported.

3.6.2 Oxygen isotopes of clinopyroxene

A polished sample of omphacite+carbonate vein hosted in diopside-lawsonite rock was first studied by SEM to identify zones representative of Stage#1 diopside and Stage#2 omphacite (Figs. 3d and S2). Aliquots of carbonate+omphacite vein were crushed (<100 μm) and single crystals of omphacite were separated by hand-picking under a binocular microscope. Diopside-rich protolith rock was sampled out of the vein selvage (ca. 2 cm from the vein) in order to avoid the isotopic contribution of the vein-related omphacite rims, as checked by SEM. Rock was crushed (<100 μm) and single crystals of diopside were separated by handpicking under a binocular microscope. Approximately 2 mg of omphacite and 2 mg of diopside were analyzed using laser fluorination at IPGP (Paris, France) along with UWG-2 garnet standard. Analytical methods are similar to those documented in Rumble et al. (1997). The oxygen isotopic ratios are reported using the international V-SMOW standard. Measurement of UWG-2 garnet standard aliquots gave 2σ external error on $\delta^{18}O$ of ±0.036‰, which is in the same range of in-run uncertainties for individual measurements (<0.03‰). Measurements were duplicated for omphacite, while for diopside the material collected was not sufficient. Fractionation factors (Hoffbauer et al., 1994) were used to infer oxygen isotopes equilibrium temperature between carbonate and clinopyroxenes (Table 4.3.1).

Estimated errors using a Monte Carlo simulation on the calculated temperatures are 30°C and 20°C for the omphacite-calcite and diopside-calcite equilibrium, respectively.

3.6.3 Oxygen isotopes of antigorite

Four samples of serpentinite were analyzed for oxygen isotopes, two samples from near the contact and two samples far from the contact (equivalent of deeper position in the mantle basement). Serpentinite samples were coarsely crushed in tungsten carbide mortar and washed in dilute HCl overnight to remove any carbonate material. After 4 hours drying at 150°C under vacuum, oxygen was extracted from silicate rocks using bromine pentafluoride at 600°C (Clayton and Mayeda, 1963) and reacted with carbon to produce O_2. The O_2 was introduced into a Finnigan Delta E mass spectrometer to determine the $^{18}O/^{16}O$ ratio. The isotopic composition of a sample is given as $\delta_{sample} = (R_{sample}/R_{standard} -1)\cdot 1000$ (in percent), where R is the $\delta^{18}O/^{16}O$ ratio and the standard is V-SMOW. Analytical errors for oxygen are less than 0.2‰ (σ)

3.6.4 Sr-Nd radiogenic stable isotopes

For isotope analyses, powdered samples were weighted to obtain approximately 100–200 ng of Sr and Nd. A 1 hour 6 N HCl leaching step at 95 °C was performed before acid digestion. After leaching, residues were rinsed three times in Milli-Q H2O. The samples were subsequently dissolved during 72 h on a hot plate with a mixture of 48% HF and 13N HNO_3 (1:1) and few drops of $HClO_2$. After evaporation to dryness, 2 ml of HNO_3 was added to the residue and kept at 95 °C for 24–48h. Three successive concentration/purification steps were necessary to separate Sr and Nd. The procedures used were modified from Pin et al. (1994). Sr isotopic ratios were measured by thermal ionization mass spectrometry using a Triton Finnigan Mat spectrometer at Labogis from Nîmes University. Nd analyses were performed

using a Nu 500 HR MC-ICP-MS at the "Service Commun national d'Analyse" from the Ecole Normale Supérieure (ENS, Lyon, France). Mass dependent fractionations were corrected using a $^{86}Sr/^{88}Sr$ ratio of 0.1194, a $^{146}Nd/^{144}Nd$ ratio of 0.7213 for Sr and Nd analyses, respectively. Standards were measured repeatedly during the course of this study and yielded average values of $^{87}Sr/^{86}Sr=0.710256 \pm 6.4\times10^{-6}$ (2σ, n=3) and $^{87}Sr/^{86}Sr=0.710260 \pm 3.9\times10^{-6}$ (2σ, n=10) for the NBS987 standard, $^{143}Nd/^{144}Nd=0.5118773 \pm 5\times10^{-6}$ (2σ, n=24) for the "Rennes" in house Nd standard (Chauvel and Blichert-Toft, 2001). All measured isotopic ration were corrected for in situ decay using a Miocene age of 34 Myr according to estimated peak metamorphic age of *Lawsonite-eclogite unit* (Vitale Brovarone and Herwartz, 2013).

3.7 Estimation of water/rock ratio

The extent of water-rock interaction in lithospheric sections is commonly characterized by water/rock (W/R) ratio and can be quantified with Sr and Nd isotope composition. Water/rock ration are based on mass balance calculations and assume final isotope equilibrium and were first applied by Taylor (1977) to stable isotope studies and by Spooner et al. (1977) for Sr isotopes. In Chapter 7, the open system equation to describe the W/R will be used (Albarède, 1996)

$$\frac{W}{R} = \left(\frac{X_r}{X_w}\right) \ln\left[\left(\frac{\varepsilon_r^i - \varepsilon_r^f}{\varepsilon_r^f - \varepsilon_w^i}\right) + 1\right] \quad (3.1)$$

In this equation, W is the mass of the fluid, R the mass of the rock being altered, ε_r^i is the initial isotopic ration of the rock, ε_r^f is the final isotopic ration of the altered rocks and is equal to that of the fluid, ε_w^i is the initial isotopic composition of the fluid. Importantly, estimated of W/R rations are based on the assumption that the fluid phase and rock are in equilibrium (Albarède et al., 1981) and that Sr and Nd concentrations are not modified during the fluid-rock interaction.

CHAPTER 4
Recognition of high-pressure carbonation in the lawsonite-eclogitic unit in Alpine Corsica

The lawsonite-eclogite unit of Monte San Petrone in Alpine Corsica has been extensively studied by previous works because here the tectono-stratigraphic characteristic of OCT were preserved from Alpine deformation and are particularly well exposed (Vitale Brovarone et al., 2011). The overall exceptional preservation of HP paragenesis is what makes Alpine Corsica an excellent natural laboratory for the study of HP fluid rock interactions (Vitale Brovarone et al., 2011a; Martin et al., 2011; Vitale Brovarone et al., 2014). Vitale Brovarone et al. (2011a) described the range of metasediments found stratigraphically overlying the serpentinite basement and the continental sliver. As mentioned in section 2.2.3, the early post-rift cover mainly consists of alternating layer of metaradiolarites and marbles (Fig. 3.a Section 5.1). In their work, they already recognized a particular lithology composed by carbonate together with silicate-rich mineral assemblage, including Na-pyroxene and garnet. This peculiar lithology is observed only where the continental sliver becomes thinner. They interpreted this kind of rock as a meta-hardground. However, this lithology is only observed within metasomatic rind developing at the expense of the continental crust or metasedimentary cover. The close structural relationship between carbonates and metasomatic system needed to be investigated. Actually, the carbon behavior during subduction metamorphism has long received a wide interest in the Earth Sciences community. Understanding processes that may involve transfer of carbon from solid to fluid, and vice-versa, is crucial for any attempt to balance the deep carbon cycle. A growing number of studies have highlighted the high

mobility of carbon by fluid-rock interactions and have overturn older paradigms to the point that some authors propose that almost all subducted carbon can actually be transferred to the lithospheric mantle. In such a model, virtually no carbon is transferred to the deep mantle (Kelemen and Manning, 2015). Rock carbonation of Ca-Mg silicate rocks during HP metamorphism may represent a new mechanism to uptake carbon in slab- and mantle-forming rocks, with major consequences on the fluxes between carbon reservoirs in subduction zones.

In this article published in *Earth and Planetary Science Letters*, we present the petrological and geochemical evidence that attest to the metasomatic origin of carbonates and we proposing that carbonation reaction can occur at HP-LT conditions in the subducting slab. In this article, we focus on the importance of reaction microstructures between silicates and carbonate that suggest silicate-replacement by carbonate. The carbonate metasomatic origin is supported by their oxygen isotopic signature that indicates that carbonates precipitated from fluids in equilibrium with mafic/ultramafic rocks. The discovery of HP carbonation process has profound consequences on the residence time of carbon in subduction zone reservoirs, as well as the isotopic signature of subducted carbonates. Lastly, considering a longer time-scale perspective, HP carbonation may ultimately influence the fluctuation of CO_2 emissions at volcanic arcs.

In this article, we use the term *"metasomatic marbles"* to indicate carbonates that formed during HP metasomatism. However, in the following chapters, the term "*carbonated metasomatic marbles"* is preferred, in to avoid misunderstanding with other terms used in the literature to describe impure marbles that undergo fluid-rock interactions, and to stress that carbonation occur during HP metamorphism. Note also that a new number is given to the figures in order to follow the numbering of the manuscript, whereas sections maintain the numbering of the published version.

4.1 Article: Carbonation by fluid-rock interactions at High-Pressure conditions: implications for carbon cycling in subduction zones

Francesca Piccoli[a,*], Alberto Vitale Brovarone[a], Olivier Beyssac[a], Isabelle Martinez[b], Jay J. Ague[c,d], Carine Chaduteau[b] [1]

Published in *Earth and Planetary Science Letters*, April 2016

Abstract

Carbonate-bearing lithologies are the main carbon carrier into subduction zones. Their evolution during metamorphism largely controls the fate of carbon, regulating its fluxes between shallow and deep reservoirs. Recent estimates predict that almost all subducted carbon is transferred into the crust and lithospheric mantle during subduction metamorphism via decarbonation and dissolution reactions at high-pressure conditions. Here we report the occurrence of eclogite-facies marbles associated with metasomatic systems in Alpine Corsica (France). The occurrence of these marbles along major fluid-conduits as well as textural, geochemical and isotopic data indicating fluid-mineral reactions are compelling evidence for the precipitation of these carbonate-rich assemblages from carbonic fluids during metamorphism. The discovery of metasomatic marbles brings new insights into the fate of carbonic fluids formed in subducting slabs. We infer that rock carbonation can occur at high-pressure conditions by either vein-injection or chemical replacement mechanisms. This indicates that carbonic fluids produced by decarbonation reactions and carbonate dissolution may not be directly transferred to the mantle wedge, but can interact with slab and mantle-

[1] [a]Insitut de Minéralogie, Physique des Matériaux et Cosmochimie (IMPMC), UPMC-CNRS Campus Jussieu, case courrier 115, 4 Place Jussieu, 75005, Paris, France. Tel. 0033 (0)1 44 27 25 60

[b]Institut de Physique du Globe de Paris, Sorbonne Paris Cité, Université Paris Diderot, UMR 7154 CNRS, 1 rue Jussieu, F-75005 Paris, France

[c]Department of Geology and Geophysics, Yale University, P.O. Box 208109, New Haven, CT 06520-8109, USA

[d]Peabody Museum of Natural History, Yale University, 170 Whitney Avenue, P.O. Box 208118, New Haven, CT, 06520-8118, USA

forming rocks. Rock-carbonation by fluid-rock interactions may have an important impact on the residence time of carbon and oxygen in subduction zones and lithospheric mantle reservoirs as well as carbonate isotopic signatures in subduction zones. Furthermore, carbonation may modulate the emission of CO_2 at volcanic arcs over geological time scales.

1. Introduction

Subduction exerts a key role in the long-term carbon cycle by regulating the fluxes of carbon between the Earth's surface and the deep Earth. The redistribution of carbon between the exogenic and endogenic reservoirs largely depends on the evolution of carbonate-bearing lithologies in subduction zones. Carbonates are present in sedimentary, mafic and ultramafic lithologies, and constitute the dominant reservoir of carbon in the subducting lithosphere (Alt and Teagle, 1999; Kelemen & Manning, 2015). There is growing evidence that carbonates can be extremely reactive during subduction metamorphism via devolatilization reactions (Cook-Kollars et al., 2014; Kerrick & Connolly, 2001), as well as carbonate dissolution via fluid-rock interactions at high-pressure conditions (Frezzotti et al., 2011; Ague and Nicolescu, 2014; Kelemen and Manning, 2015), carbonate reduction reactions (Galvez et al., 2013a; Malvoisin et al., 2012), or melting of the subducting crust (Poli, 2015). Nonetheless, key questions remain regarding the mechanisms of carbonic fluid transfer from the slab to the lithospheric mantle in the sub-arc region, their role in mantle wedge metasomatism, and their contribution to the CO_2 degassing at volcanic arcs.

To address these questions, a growing number of studies have been carried out using both experimental petrology (Molina and Poli 2000; Poli et al., 2009) and thermodynamic modeling (Kerrick and Connolly 2001; Gorman et al., 2006). All these studies agree that, considering a "closed system" (no external fluid supply), significant carbon transfer to the mantle wedge is feasible only at shallow depth in the forearc region. This transfer is made possible via devolatilization reactions that, based on experimental and thermodynamic results,

are much more limited at deeper, subarc conditions (Connolly, 2005; Poli et al., 2009). Nevertheless, the role of fluid-rock interactions appears to be critical for the stability of carbonates. Recently, field based studies (Ague and Nicolescu, 2014; Frezzotti et al., 2011) as well as theoretical and experimental works (Facq et al., 2014; Sverjensky et al., 2014) have pointed out that massive carbonate dissolution in fluids may occur at high-pressure-low temperature conditions and can generate large amounts of carbonic fluids (see Kelemen and Manning, 2015 for review). Accounting for carbonate dissolution at high-pressure conditions in comprehensive budgets overturns older paradigms on carbonate stability with respect to carbon mobility in subduction zones. The most recent budgets actually predict that carbonate dissolution allows almost all subducted carbon to be transferred to the mantle wedge (Kelemen & Manning, 2015). Owing to the very recent discovery of these processes, much remains to be learned about the fate of these carbonic fluids and their interaction with slab- and mantle-forming rocks.

Here, we report the occurrence of eclogite-facies marbles formed by fluid-rock interaction processes (metasomatism) occurring along intensely metasomatized lithological interfaces (Alpine Corsica, France). We present and discuss the occurrence, textures, mineralogy and geochemistry of these metasomatic marbles. We then propose a mechanism of carbonates formation by precipitation and mineral carbonation by carbonic fluid-rock interactions at high-pressure conditions. Finally, the implications and contribution of rock carbonation to the deep carbon fluxes and cycling are discussed.

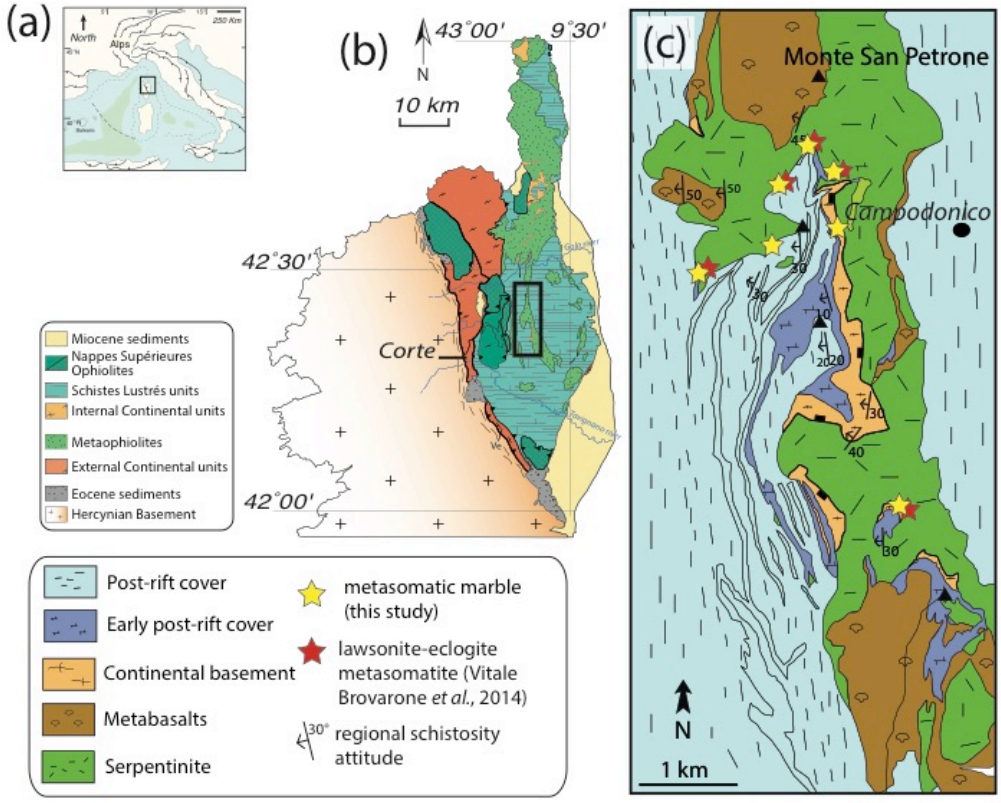

Fig. 4.1: Geological background of the study area. a) Simplified regional setting of Alpine Corsica (France) in the Western Mediterranean region. Modified after Molli and Malavieille (2011). b) Simplified tectono-stratigraphic map of Alpine Corsica. The black box indicates the position of the study area. c) Simplified geological map of the San Petrone unit. Figures modified after Vitale Brovarone et al. (2013).

2. Geological setting

Alpine Corsica (France) is a branch of the Alpine orogenic system (Jolivet et al., 1991; Molli and Malavieille, 2011) (Fig. 4.1a). The belt mainly includes remnants of subducted Mesozoic slow-spreading oceanic and passive margin lithosphere, which formed part of the Tethys Ocean basin. This rock package is classically referred to as the Schistes Lustrés Complex (Fig. 4.1b; Jolivet et al., 1990; Fournier et al., 1991; Malavieille et al., 1998; Vitale Brovarone et al., 2013). The exceptional preservation of prograde-to-peak mineral assemblages, including widespread lawsonite, makes the Schistes Lustrés of Alpine Corsica an excellent site for field investigations related to subduction. These units underwent various metamorphic overprints during the Alpine subduction ranging from subgreenschist-facies conditions of about 300°C and 0.5 GPa to lawsonite blueschist and lawsonite eclogite-facies conditions

which reached 500-550 °C and ~2.3 GPa (e.g. Fournier et al., 1991; see Vitale Brovarone et al., 2013 for review).

Carbonate-bearing rocks are widespread in the Schistes Lustrés of Alpine Corsica. The most typical carbonate-bearing lithologies are metamorphosed oceanic sediments (referred to as calcschists hereafter), ophicarbonate, and carbonated metabasalts (Miller et al., 2001; Ravna et al., 2010; Vitale Brovarone et al., 2011b). In each lithology, primary carbonates and various generations of carbonate veins are observed (Miller et al., 2001; Ravna et al., 2010; Vitale Brovarone et al., 2011b). These veins have been shown to be in most cases in isotopic equilibrium with the host rocks with little effect of external fluid infiltrations and metasomatism (Cartwright and Buick, 2000). On the other hand, evidence for high-pressure-low temperature fluid-rock interactions and metasomatism in the Schistes Lustrés of Alpine Corsica is widespread, most typically localized at lithological interfaces. In this work, we focus on processes occurring where serpentinites are in contact with metasedimentary rocks.

Here, past results on high-pressure metasomatism in Alpine Corsica are briefly summarized. In the blueschist-facies zone, reactions between serpentinites and overlying metasediments led to carbonate reduction and precipitation of wollastonite and abiotic graphite at blueschist-facies conditions (Malvoisin et al., 2012; Galvez et al., 2013a). Except for the influx of external, serpentinite-derived fluids, the reacted metasediments revealed largely conservative carbon budget (Galvez et al., 2013a). In similar lithological settings, massive precipitation of lawsonite from fluid-rock interactions at the expense of metasedimentary rocks in contact with serpentinites testifies to the reincorporation of large amounts of water in the rock at prograde blueschist-to-eclogite-facies metamorphic conditions (Martin et al., 2011; Vitale Brovarone et al., 2014; Vitale Brovarone and Beyssac, 2014;). This process is characterized by a dramatic whole-rock chemical modification leading to mafic/ultramafic, Ca-rich metasomatic products.

The carbonate-rich rocks studied herein are intimately related to the latter Ca-rich metasomatic rocks and were collected in the lawsonite eclogite-facies San Petrone unit. This unit is characterized by a basal body of serpentinite variably overlain by Jurassic pillow metabasalts, Mesozoic metasediments (e.g. calcschists, marbles, Mn-metacherts) or slivers of Hercynian continental basement rocks mainly consisting of pre-Alpine, carbonate-free, high-temperature metasediments and granitic rocks overprinted at high-pressure-low temperature conditions during the Alpine subduction (Vitale Brovarone et al., 2011b; Fig. 4.1c). Ophicarbonate rocks are locally found at the top of the serpentinite body. The San Petrone unit has been considered as a remnant of a Mesozoic hyper-extended passive margin (Vitale Brovarone et al., 2011b; Beltrando et al., 2014). Peak metamorphic conditions in this unit are estimated at ca. 490-530 °C and ~2.3 GPa by means of pseudosection modeling and thermometry based on Raman spectroscopy of carbonaceous material (Ravna et al., 2010; Vitale Brovarone et al., 2011a, 2013). The peak metamorphic age of ~34 Ma has been determined by several techniques including U-Pb zircon and Lu-Hf garnet and lawsonite geochronology (Martin et al., 2011; Vitale Brovarone and Herwartz, 2013).

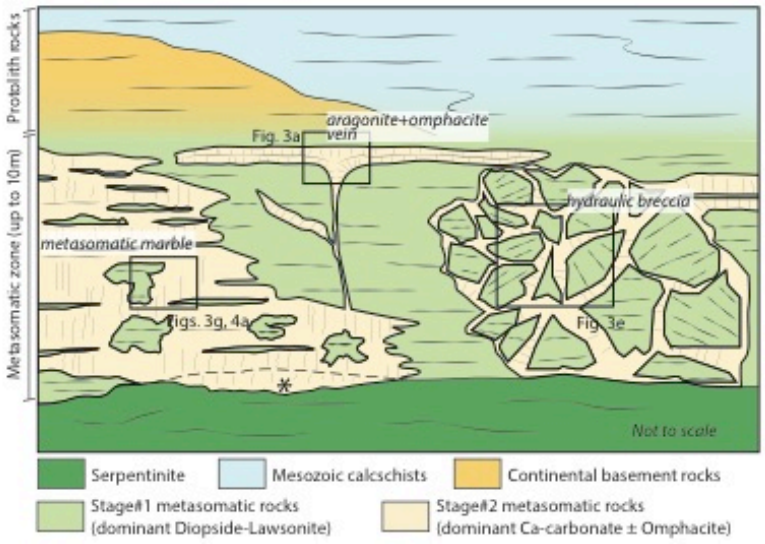

Fig. 4.2: simplified structural sketch summarizing the field relationships between the different rock types and the location of the study samples. The star refers to metasomatic marbles formed at the expense of former serpentinites.

3. Structural occurrence of metasomatic marbles

The carbonate-rich rocks which are the subject of this paper occur along a regional lithological boundary separating serpentinites from either slivers of Hercynian basement rocks (dominantly pre-Alpine high temperature metasedimentary rocks) or Mesozoic metasedimentary rocks (Figs. 4.1c and 4.2). The first few meters of rock above the serpentinites exhibit intense Alpine metasomatism that has already been described in previous studies (Martin et al., 2011; Vitale Brovarone et al., 2011b, 2014). These metasomatic rinds can be followed for several kilometers along the top of the serpentinite body and are characterized by lawsonite-rich assemblages, but diopside-rich rocks are also common. These rocks are referred to as Stage#1 diopside-lawsonite rocks (Fig. 4.2). The carbonated rocks which are the subject of this study are referred to as Stage#2 metasomatic marbles (or simply metasomatic marbles), these form discontinuous patches or lenses of variable thickness and lateral extension (from a few tens of cm to several m, Fig. 4.2), and are preferentially associated with diopside-rich rather than the lawsonite-rich metasomatic rocks. The petrological differences between Stage#2 metasomatic marbles and Mesozoic metasediments are discussed in Section 5.

The metasomatic marbles show a range of structural relationships with the surrounding diopside-lawsonite rocks, and the carbonate/host rock ratios are extremely variable. Figure 4.2 summarizes the field relationships between the different rock types, i.e. serpentinites, Stage#1 diopside-lawsonite rocks, Stage#2 metasomatic marbles, and the inferred protolith rocks (continental basement rocks or Mesozoic metasediments). The transition from diopside-lawsonite rocks to Stage#2 metasomatic marbles is marked by a gradual increase of carbonate/host rock ratio, passing from diopside-lawsonite rocks to isolated carbonate-rich veins in Stage#1 host rocks, to Stage#2 metasomatic marbles with remnants of Stage#1 rocks. Isolated veins have crack-seal texture and are mainly composed of rod-shaped Ca-carbonate ±

omphacite (Figs. 4.3a, b, d). Carbonate rods are perpendicular to the vein walls (Fig. 4.3b). Omphacite grows from the vein wall toward the center (Fig. 4.3d). Some veins exhibit interaction with the host Stage#1 rocks characterized by omphacite replacement of the precursor diopside (Al-Na gain; Ca-Mg loss) and local carbonate precipitation (Fig. 3d). The abundance of omphacite decreases from the vein wall to the host rock. Diopside far from the vein does not display any chemical zoning involving Na-Al enrichment. The isolated veins are connected to dm-thick layers (ca. 20 cm) showing similar crack-seal textures (Figs. 4.2 and 4.3a). These layers are meter-scale and are parallel to the wallrock foliation (Fig. 4.2). Outcrop-scale hydraulic breccias consisting of cm- to m-scale angular clasts of Stage#1 diopside-lawsonite rocks embedded within a carbonate vein network provide strong evidence for diffuse hydrofracturing and carbonate precipitation (Figs. 4.2, 4.3e,f). In some outcrops, serpentinites are overlain by a sequence of metasomatic marbles ranging in thickness from less than one m to ~10m (Figs. 4.2, 4.3g and 4.4a). These metasomatic marbles are hosted within the diopside-lawsonite rock and contain remnants of the host rock—ranging from a few microns to several centimeters—floating in a carbonate-dominated matrix. Remnants of diopside-lawsonite rocks in the metasomatic marbles differ from the angular clasts found in the hydraulic breccias. First, they have embayed margins and microtextures (see Section 5) suggest digestion of the silicate portions into the carbonate matrix. Second, the host rock remnants preserve their original orientation (Fig. 4.4a), whereas the clasts in the hydraulic breccias have random rotation (Figs. 4.2). Last, the diopside remnants are commonly rimmed by omphacite, the latter being in textural equilibrium with the carbonate as observed in the isolated carbonate veins.

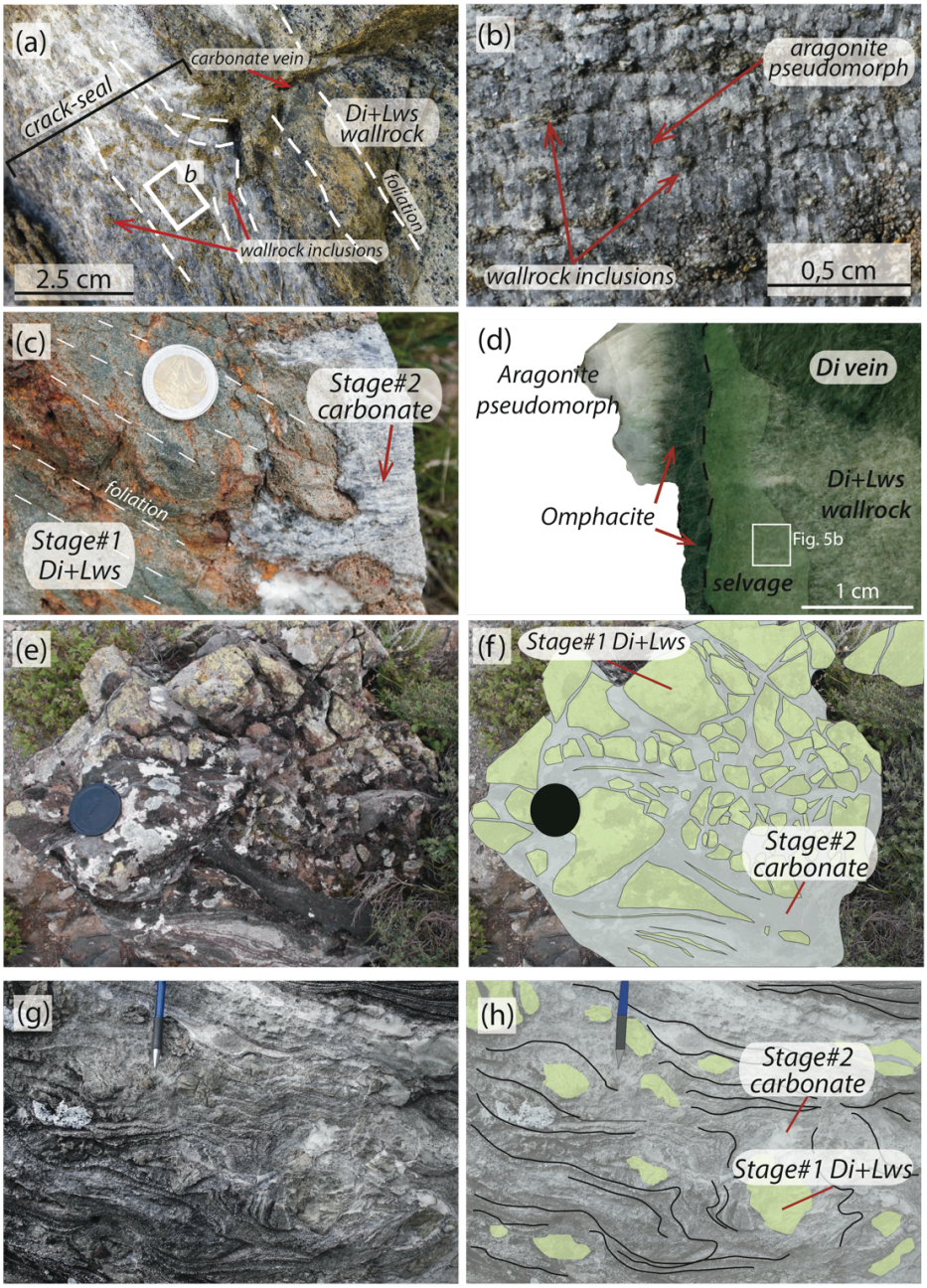

Fig. 4.3: Representative textural features of metasomatic marble in the field. a) Crack-seal texture in a metasomatic marble lens located in the metasomatic rind formed along the continental basement-serpentinite contact. Dashed lines mark the schistosity in the host rock and the orientation of the remains of the host rock in the carbonate-rich domain (see detail in b). Note that the silicate layers are deflected toward the carbonate vein. b) Detail of carbonate layers containing rod-shaped aragonite pseudomorphs alternating with vein-parallel bands of wallrock inclusions. c) Interdigitation of rod-shape carbonate with Stage#1 diopside-lawsonite rock. d) Carbonate+omphacite vein cutting across Stage#1 diopside+lawsonite rock. The black dotted line marks the vein wall and the green area overdrawn marks the selvage extension. e) and f) Photograph and related interpretative sketch of a hydraulic breccia (types defined by Jébrak 1997) consisting of angular clasts of diopside+lawsonite rock (Stage#1 metasomatism) sealed by a network of veins containing rod-shaped carbonate crystals. g and h) Outcrop with high carbonate/silicate ratio and corresponding sketch. Rounded chunks of Stage#1 diopside-lawsonite rock float in a carbonate matrix. Microtextures in the carbonate-rich domains suggest digestion and chemical replacement of Stage#1 silicates by carbonate. Di=diospide; Lws=lawsonite.

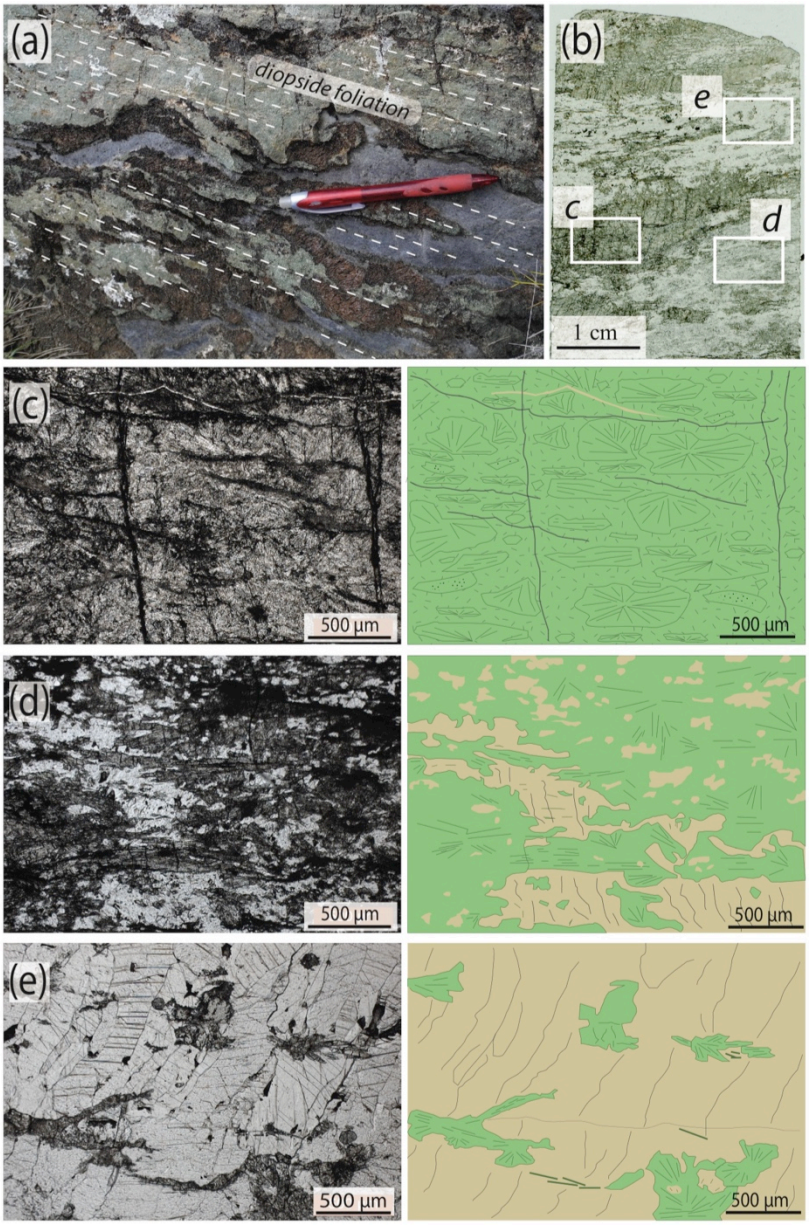

Fig. 4.4: Progressive transformation of a precursor Stage#1 carbonate-free, diopside-lawsonite rock into a Stage#2 metasomatic marble. a) Stage#2 metasomatic marble cropping out along the serpentinite-metasediment contact. The marble (grey) is interdigitated with the host Stage#1 diopside-lawsonite rock (green). The foliation of the diopsode-lawsonite rock (dashed line) can be followed in the carbonate layer. b) Thin section scan showing the interdigitation texture of silicate and carbonate layers analogous to that documented at the outcrop scale in part (a). Different degrees of carbonation are observed. White boxes indicate the location of the photomicrographs c, d and e. c) Plane polarized light photomicrograph and corresponding sketch of the preserved portion of the metasomatic diopside + lawsonite protolith; fan-shape diopside and lawsonite crystals statically crystallized. d) Plane polarized light photomicrograph and corresponding sketch of the patchy distribution of carbonate pods that characterizes a partially carbonated domain. Here, Stage#1 diopside aggregates are cut by the carbonate and some fragments are preserved as relicts in carbonate layers. e) Plane polarized light photomicrograph and corresponding sketch of a highly carbonated portion. Here the rock is transformed into a metasomatic marble; prismatic carbonate crystals are well developed. A few remnants of Stage#1 diopside are preserved; these relicts display embayed rims and atoll-like textures. In every sketch, Stage#1 diopside + lawsonite domains are represented in green, whereas rod-shaped carbonate is in light beige.

4. Methods

4.1 Scanning electron microscopy and electron microprobe

Petrographic thin sections were carbon coated for scanning electron microscopy (SEM). Observations were performed at a working distance of 7.5 mm using a Zeiss Ultra 55 field emission gun SEM operated at 15 kV with a 120 μm aperture. Backscattered electron (BSE) mode was used to investigate chemical heterogeneities using an Angle Selective Backscattered Detector (AsB) or an Energy Selective Backscattered Detector (EsB). Energy dispersive X-ray spectrometry (EDXS) maps were acquired using an EDXS QUANTAX system equipped with a silicon drift detector XFlash 4010 (Bruker). Data were processed with the software Esprit (Bruker). Mineral analyses were performed on a Cameca electron microprobe (either SX-100 or SX Five) (Camparis, Université Paris 6). Common analytical conditions were adopted for spot analyses [15 kV, 10 nA, wavelength-dispersive spectroscopy (WDS) mode], using Fe_2O_3, $MnTiO_3$ (Mn, Ti), diopside (Mg, Si), orthoclase (Al, K), anorthite (Ca) and albite (Na) as standards. The automated Cameca ZAF procedure was used for quantification (Tables 4.4, 4.5, and 4.6).

Sample	Metasomatic marble (n=4)	1σ	OF3598[a]	COE5[b]
			Stage#1 rock	
SiO2	20,44	5,65	45,30	40,6
Al2O3	4,97	2,94	15,11	25,6
Fe2O3	3,22	1,14	5,03	2,28
MnO	0,18	0,16	0,11	0,13
MgO	3,14	1,77	6,95	1,8
CaO	39,23	5,32	20,62	17,65
Na2O	0,92	0,95	0,47	0,51
K2O	0,12	0,16	0,01	0,24
TiO2	0,18	0,11	0,65	1,94
P2O5	0,09	0,04	0,11	0,41
LOI	27,05	5,12	5,57	7,94
Tot	99,54		99,94	99,10

[a]from Vitale Brovarone et al., 2014
[b]from Martin et al., 2011

Table 4.1: whole rock major element composition for metasomatic marbles (see Table 4.2 for detailes), Stage#1 diopside-lawsonite rock (OF3598) and Stage#1 rock with lawsonite>70% (COE5)

4.2 Whole rock major and trace element data

Chips of low to highly carbonated rock were removed from hand-samples. Samples were crushed in an agate mortar (grain size < 80μm) and sent for major and trace element, CO_2 and organic carbon analyses at the Service d'Analyse des Roches et Minéraux (SARM, Centre de Recherches Pétrographiques et Géochimiques, Nancy, France) by alkali fusion of rock samples ($LiBO_2$), followed by concentration measurements using an ICP-OES Icap 6500 (Thermoscientific) for major elements, and an ICP-MS X7 (Thermoscientific) for minor elements (protocol by Carignan et al., 2001). The modal proportions of silicates vs. carbonate were estimated first with optical microscopy and then checked using whole rock and mineral composition. In two cases, samples 1COR12-20d and COR13-29c, two different chips were taken: one representative of the metasomatic marble, where silicates are present as clasts, and another one representative of a Stage#1 diopside+lawsonite rock, where carbonate is a minor constituent. When an average value is indicated, the standard deviation (1σ) is also reported (Tables 4.1 and 4.3.1).

4.3 Carbon mass balance calculation

In/out carbon fluxes in the subducting slab (during high-pressure metamorphism) are estimated from the grams of CO_2 per 100g of rock released by decarbonation reaction and carbonate dissolution vs. the grams of CO_2 per 100g of rock bound by rock carbonation process (Section 8.3). The CO_2 bound in the rocks of this study was back calculated from whole rock analyses removing the measured organic carbon content to the measured CO_2 (red bar in Fig. 4.8a, see also Table 4.2). Values for CO_2 released per 100g of rock after carbonate dissolution (Ague and Nicolescu, 2014) and decarbonation of calcschists (Cook-Kollars et al., 2014) are taken from the literature. For the data on carbonate dissolution (Ague and Nicolescu, 2014), we took the average of the estimated CO_2 loss in samples from Syros

(35.1g) and Tinos (22.2g), thus resulting in 28.65 g of CO_2 lost during carbonate dissolution (blue bar in Fig. 4.8a). For samples affected by decarbonation, we took the calcschist modeled by Cook-Kollars et al. (2014). This rock initially contains 40 wt.% carbonate (i.e. the initial CO_2 content is 17.6g per 100 of rock) and it loses 50% of its initial CO_2, thus 8.8g per 100g of rock (green bar in Fig. 4.8a). Cook-Kollars et al. (2014) highlighted that natural samples from Schist Lustrés and Cignana suite show a lower extent of decarbonation. They conclude that decarbonation reactions during metamorphism may cause the loss of 10 to 20% of the initial CO_2. We took the intermediate value of 15%. Thus, considering the same initial CO_2 content of 17.6g per 100 g of precursor rock, the CO_2 lost is 2.64g per 100g of rock (orange bar in Fig. 4.8a).

4.4 Stable isotope data

4.4.1 Carbon and Oxygen isotopes of calcite

Chips of carbonate were taken from hand-samples and crushed in an agate mortar. Raman and SEM analyses establish that the carbonate is nearly pure Ca-carbonate. The isotopic composition of calcite was measured by an AP2003 continuous flow mass spectrometer at LGIS, IPGP. Approximately 2 to 2.5 mg of sample were loaded in vials; three standards of pure calcite were also used for calibration of both concentration and isotopic composition. After flushing with ultrapure helium, orthophosphoric acid (H_3PO_4) was introduced in each tube in order to produce gaseous CO_2. After 4 hours of reaction at ambient temperature, calcite completely decomposes to release CO_2 (McCrea, 1950); gases were then transferred into the mass spectrometer for analysis. In order to improve the precision of the measurements, each analysis was repeated four times for each vial, and each sample analysed twice. The isotopic $^{13}C/^{12}C$ and $^{18}O/^{16}O$ ratios are expressed using the conventional δ-notation relative to PDB and SMOW international standards. The precision is 0.1‰ for $\delta^{13}C$ and 0.2‰

for $\delta^{18}O$. The results are reported in Table 4.3. When an average value is indicated, the standard deviation (1σ) is also reported.

4.4.2 Oxygen isotopes of clinopyroxene

A polished sample of omphacite+carbonate vein hosted in diopside-lawsonite rock was first studied by SEM to identify zones representative of Stage#1 diopside and Stage#2 omphacite (Figs. 4.3d and S2). Aliquots of carbonate+omphacite vein were crushed (<100 μm) and single crystals of omphacite were separated by handpicking under a binocular microscope. Diopside-rich protolith rock was sampled out of the vein selvage (ca. 2 cm from the vein) in order to avoid the isotopic contribution of the vein-related omphacite rims, as checked by SEM. Rock was crushed (<100 μm) and single crystals of diopside were separated by handpicking under a binocular microscope. Approximately 2 mg of omphacite and 2 mg of diopside were analyzed using laser fluorination at IPGP (Paris, France) along with UWG-2 garnet standard. Analytical methods are similar to those documented in Rumble et al. (1997). The oxygen isotopic ratios are reported using the international V-SMOW standard. Measurement of UWG-2 garnet standard aliquots gave 2σ external error on $\delta^{18}O$ of ±0.036‰, which is in the same range of in-run uncertainties for individual measurements (<0.03‰). Measurements were duplicated for omphacite, while for diopside the material collected was not sufficient. Fractionation factors (Hoffbauer et al., 1994) were used to infer oxygen isotopes equilibrium temperature between carbonate and clinopyroxenes (Table 4.3.1). Estimated errors using a Monte Carlo simulation on the calculated temperatures are 30°C and 20°C for the omphacite-calcite and diopside-calcite equilibrium, respectively.

5. Petrography of selected metasomatic marbles

Metasomatic marbles have characteristic features that make them different from any other carbonate-bearing rocks of the Schistes Lustrés (i.e. Mesozoic impure marbles, calcschists and ophicarbonates), although they may display mineralogical and chemical variations from one to another outcrop. As an example, the matrix carbonate in these rocks systematically displays a rod-shaped habit with rods oriented at high angles to the regional schistosity or to the margin of Stage#1 clasts in hydraulic breccias (Fig. 4.3b). In all but one metasomatic marble, the carbonate is a Ca-carbonate phase. Matrix carbonate is calcite, whereas aragonite was found as inclusions in garnet and apatite (see Fig. S1). Dolomite was detected in only one sample by Raman spectroscopy and it was in very small proportions compared to Ca-carbonate (dolomite content below X-ray diffraction detection limit). No ankerite was observed in these rocks, whereas it is common in calcschists and ophicarbonates of the Schistes Lustrés. As Ca-carbonate is the dominant carbonate phase, we will use hereafter the term "carbonate" to indicate compositionally pure Ca-carbonate (i.e. calcite after aragonite).

In thin section, metasomatic marbles display a characteristic structure defined by carbonate-rich and diopside-lawsonite-rich domains, the latter occurring as either continuous layers or isolated patches (Figs. 4.4b, d, e). A compositional layering is defined by the alternation of carbonate aggregates with diopside (±lawsonite) aggregates. Calcite rods are mm-sized; diopside and lawsonite grain size ranges from μm to mm. The mineral assemblage most commonly consists of carbonate, diopside and lawsonite, with modal proportions varying from sample to sample (Fig. 4.4). Garnet is also present in several samples. It is found as euhedral, μm to mm-sized crystals in textural equilibrium with carbonate. Its composition ranges from grossular to almandine-spessartine solid solution (Table 4.5). Phengite, epidote, quartz and pumpellyite (Table 4.6) are also present. Common accessory phases are titanite, apatite and graphite. Although such assemblages are described in calcschists in the Western

Alps (see e.g. Cook-Kollars et al., 2014), they have never been documented in Alpine Corsica to our knowledge. Moreover, the textural and mineralogical features of these silicates indicate that they resulted from intense metasomatism during their high-pressure evolution, as described below.

For simplicity, two dominant mineralogical assemblages representative of Stage#1 and Stage#2 rocks are distinguished, i.e. diopside + lawsonite and carbonate + omphacite, respectively. As mentioned above, additional phases may be present from one sample to another. The chronological relations between the two mineralogical assemblages may be deciphered from the outcrop-scale down to the micro-scale. Diopside ($Quadrilateral_{96.5}$ $Aegirine_{3.5}$; classification after Morimoto, 1989; see Tab. S1) formation at high-pressure conditions during subduction is demonstrated by: (i) the occurrence of diopside veins cross-cutting lawsonite-bearing fabrics (Fig. 3d) and (ii) the fact that the diopside veins are in turn cut by carbonate+omphacite veins, indicating near peak P-T metamorphic conditions. In the carbonate-bearing domains, diopside in contact with

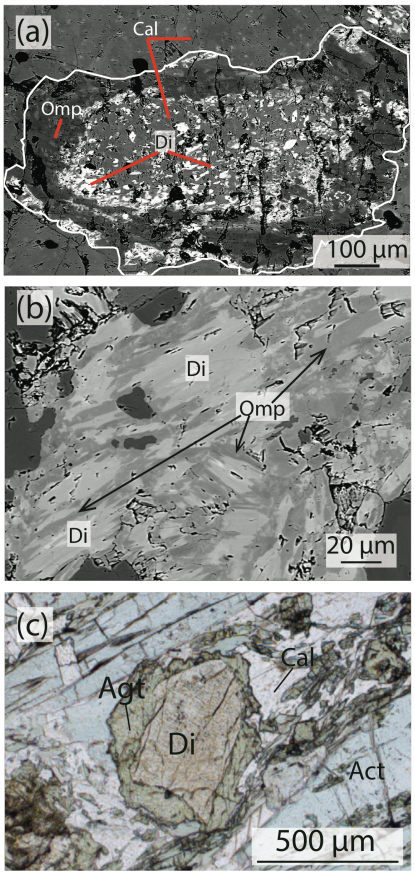

Fig. 4.5: Backscattered electron (BSE) images obtained by SEM depicting micro scale textural relationships resulting from fluid-rock interaction. a) BSE image of atoll-like Stage#1 diopside suggesting a digestion of a silicate clast by carbonate; the Stage#1 diopsidic core is dissolved in favor of carbonate while a Stage#2 Na-Al rich rim (omphacite) crystallized in textural equilibrium with the carbonate. Small fragments of diopside are preserved as inclusions in carbonate crystals (red lines). b) BSE image of wallrock selvage shown in Figure 3d. Diopside is overgrown by omphacite rim. Omphacite rims have the same composition as the vein infill omphacite crystals (Table 4.4). c) Plane polarized light photomicrograph of diopside with aegirine-augite rim in sample COR13-21d. Cal=calcite, Omp=omphacite, Di=diopside; Agt=aegirine-augite, Act=actinolite.

carbonate shows either embayed grain boundaries or newly-formed compositional coronas of omphacite (Figs. 4.5a; $Jadeite_{39.5}$ $Quadrilateral_{44.5}$ $Aegirine_{16}$; see Tab. S1). Tiny (c.a. 10-20 μm), second generation idioblastic lawsonite crystals were locally found in the carbonate. In the vein selvage, omphacite rims on diopside (Fig. 4.5b) have the same composition as omphacite growing together with carbonate in the vein. In metasomatic marbles, atoll-like textures show relict diopside cores being replaced by carbonate and rimmed by omphacite (Fig. 4.5a), the latter being in textural equilibrium with the carbonate matrix. The abundance of omphacite varies from one sample to another. All transitional stages from carbonate-free diopside-lawsonite rocks to carbonate-rich rocks are depicted in Figure 4.4.

Only one sample (COR13-21d) displays a different mineralogy, composed of (in order of volume abundance): calcite, actinolite, chlorite and clinopyroxene. This sample was collected within a sequence of typical metasomatic marbles, and shares with them similar characteristic features such as rod-shaped carbonate and Na-rich clinopyroxene coronas (aegirine-augite, Na-Fe^{3+} rich clinopyroxene, see Fig. 4.5c) on relict diopside. Geochemical data for this sample are given in Section 6.

6. Whole rock chemical compositions

Samples of metasomatic marbles were analyzed for their major and trace element bulk composition (Table 4.2). Reference samples of Mesozoic calcschist and ophicarbonate unaffected by metasomatism (i.e. far from the studied lithological boundaries and showing no mineralogical or textural evidence for fluid-rock interactions), were also analyzed (Table 4.2). Table 4.1 reports the average major element composition of metasomatic marble as well as the compositions of a Stage#1 diopside-lawsonite rock (sample OF3598 in Vitale Brovarone et al., 2014) and a Stage#1 rock with higher lawsonite content (lawsonite mode c.a. 75%; sample COE5, Martin et al., 2011). The variability of both Stage#1 rocks and Stage#2

metasomatic marbles hampers quantitative mass balance calculation. Here, only concentrations of the most representative oxides CaO, MgO, SiO_2 and CO_2 are presented. Metasomatic marbles have variable compositions based on the carbonate-silicate modal proportions (Tables 4.1, 4.2). The average composition is: CaO 39 wt.% (±5%, 1σ); CO_2 27 wt.% (±6%, 1σ); SiO_2 20 wt.% (±6%, 1σ) and MgO 3 wt.% (±2%, 1σ). The silicate mode in sample COR13-21d is higher, thus resulting in a slightly different bulk rock composition (CaO 22%; CO_2 12%; SiO_2 37%). Even accounting for the lower carbonate content, sample Cor13-21d has an Mg-richer composition (MgO 11 wt.%) compared to metasomatic marbles. Comparing the average composition of metasomatic marbles with Stage#1 diopside-lawsonite rock (Table 4.1), the following features can be outlined. Despite the variability of the protolith (with more or less abundant lawsonite), CaO is always enriched (CaO in metasomatic marbles is about double that in Stage#1 rocks). MgO variations are more difficult to evaluate, as they depend not only on the silicate content of metasomatic marbles, but also on the initial diopside modal proportion of Stage#1 rock (cf. samples OF3598 and COE5, Table 4.1).

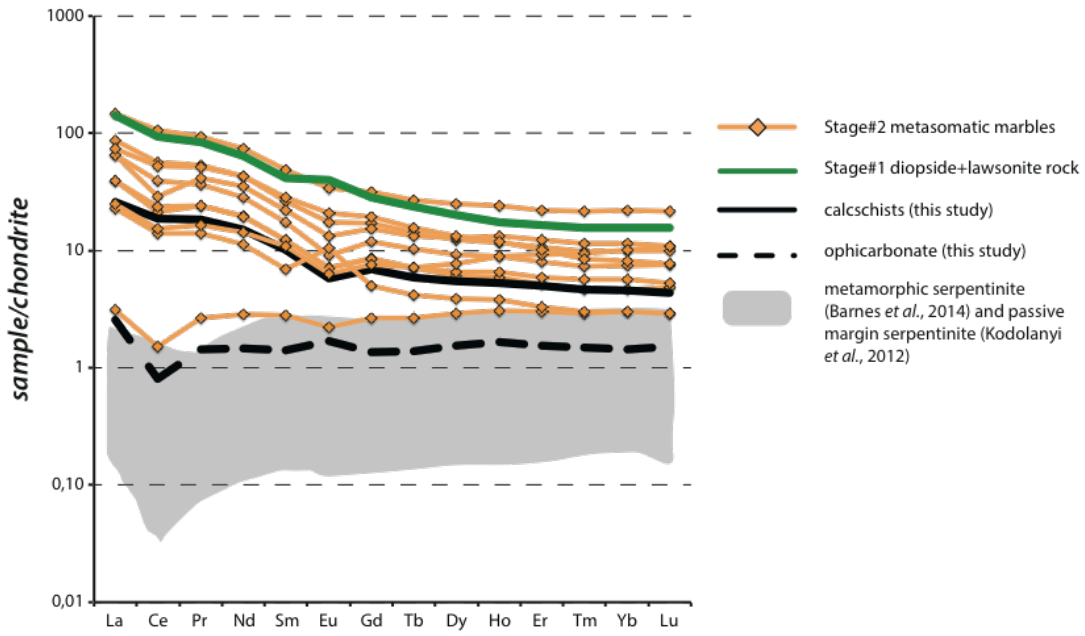

Fig. 4.6: Whole-rock chondrite normalized REE patterns (CI values from Sun and McDonough, 1989) for metasomatic marbles (orange lines, see Fig. S3 for details), reference calcschist and ophicarbonate (solid and dashed black lines, respectively), and Stage#1 diopside + lawsonite metasomatic rock (solid green line). The shaded field represents the range of passive margin serpentinite whole-rock compositions (either actual or metamorphic equivalent of Tethyan ocean floor; data from Barnes et al., 2014; Kodolányi et al., 2012).

The reference calcschist (sample COR13-32) fits the range of compositions of Alpine calcschists (Busigny et al. 2003, Galvez et al., 2013b). The reference ophicarbonate sample (sample COR13-30a), has a Mg-rich composition (13 wt.% vs. 3 wt.% in metasomatic marbles), similar to sample COR13-21d.

Whole-rock Rare-Earth Element (REE) analyses of most analyzed samples have positive slopes ($La_N/Lu_N>1$) comparable to the reference calcschist and the host diopside-lawsonite rock formed at the expense of carbonate free, continental basement metasedimentary rocks (Fig. 4.6; Martin et al., 2011; Vitale Brovarone et al., 2014). Only sample COR13-21d differs significantly. It has a rather flat REE pattern, except for a slight negative Ce anomaly (Fig. 4.6). This pattern matches reasonably well with the ophicarbonate standard and passive margin serpentinites (Barnes et al., 2014; Deschamps et al., 2013; Kodolányi et al., 2011). This sample also has a significantly higher Ni and Cr content than the other analyzed samples (1022 and 2114 ppm respectively, Table 4.2). These patterns suggest an ultramafic signature for this sample.

7. Carbon and oxygen stable isotope analysis of Ca-carbonate and clinopyroxene

C and O isotopic compositions of calcite from metasomatic marbles (including veins) were analyzes, as well as the O isotopic compositions of Stage#1 diopside and Stage#2 omphacite. For reference, calcite from calcschist and ophicarbonate was also analyzed. Analyses of carbon and oxygen isotopes of calcite are reported in Table 4.3. For all samples (reference calcschists and ophicarbonate as well as metasomatic marbles) calcite $\delta^{13}C$ values vary little and average 1.1‰ (±1.2, 1σ) (Fig. 4.7a), consistent with marine sedimentary carbonate rocks (Plank and Langmuir, 1998). The average calcite $\delta^{18}O$ value of metasomatic marbles is 14.3‰ (±3.2, 1σ) (Fig. 4.7a). The two reference calcschists (from ca. 8 to 50 m from the serpentinite, across strike) have an average $\delta^{18}O$ of 21.5‰ (±1.5, 1σ).

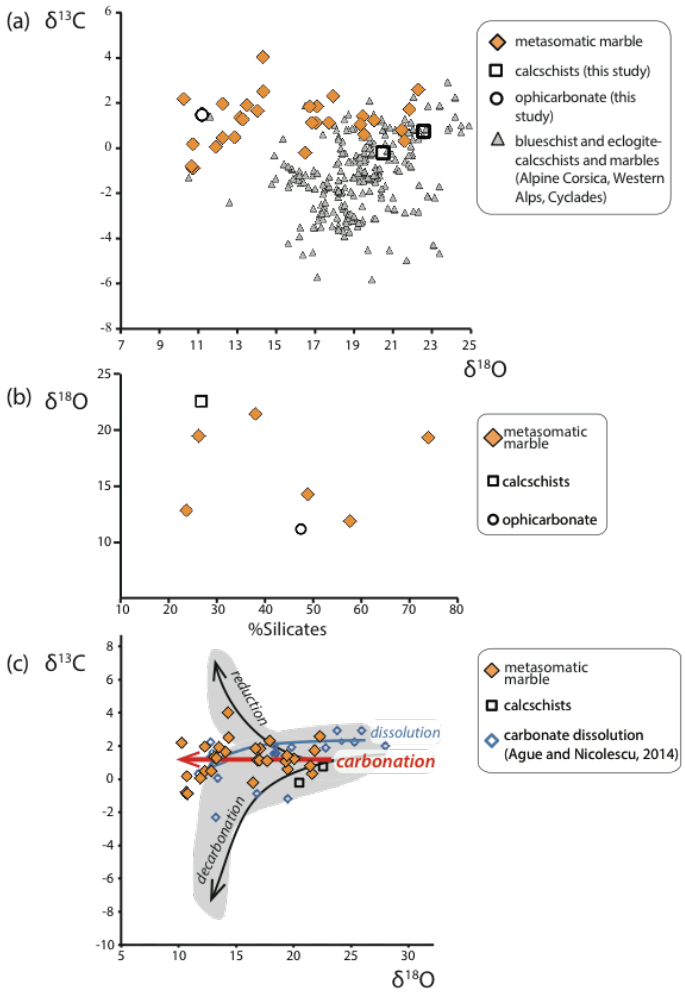

Fig. 4.7: Carbon and Oxygen stable isotopic analyses of calcite. a) Calcite $\delta^{13}C$ vs. $\delta^{18}O$ plot of metasomatic marbles (this study), blueschist and eclogite-facies marbles and calcite veins from other studies (Ague and Nicolescu, 2014; Cartwright and Buick, 2000; Cook-Kollars et al., 2014; Galvez et al., 2013b). Only data for non-metasomatic calcschists in Ague and Nicolescu (2014) and Galvez et al. (2013b) are reported. b) The rock silicate mineral content vs. calcite $\delta^{18}O$ values. The dispersion of data illustrates the lack of correlation between the light O isotopic signature and the silicate content. Analyses of reference calcschists and ophicarbonate are also reported. We plotted data for samples that were also analyzed for their bulk rock composition (samples COR13-32; COR13-30a; COR13-21b; COR13-21d; COR13-27e; COR13-17c; COR13-22c; COR13-28c; Table 4.3). c) Metasomatic marble and reference calcschists $\delta^{18}O$ vs. $\delta^{13}C$ plot. Shaded areas correspond to geochemical trend of carbonate affected by devolatilization (Bowman et al., 2009; Gerdes et al., 1995, 1999), and carbonate reduction (Galvez et al., 2013b). Isotopic composition of carbonates affected by carbonate dissolution is also reported (blue diamonds, Ague and Nicolescu, 2014).

The ophicarbonate analyzed in this study has $\delta^{18}O$ of 11‰. Carbonate in veins cutting across carbonate-free, diopside-rich rocks has very low $\delta^{18}O$ 10.6‰ (±0.2, 1σ), independent of vein distance from the serpentinite. Carbonate in samples collected from outcrops with higher carbonate/silicate ratios (e.g. carbonate mode 70%) display more dispersed values that vary from ~12 to ~18‰. In these rocks, samples collected a few centimeters from the serpentinite

body have an average value of ~14‰ (9 samples), whereas the two samples collected far from the serpentinite (i.e. more than 3m) and within the analyzed interaction zone (cf. Figs. 4.6 and S3 and Table 4.3 for sample location and respective REE patterns and isotope composition) have a heavier signature of ~18‰. A simple correlation cannot be established between the distance from the serpentinite and the $\delta^{18}O$ values within the reaction zone. Indeed, Stage#2 omphacite-carbonate veins far from the serpentinite body (up to 8 m from the contact) have low $\delta^{18}O$ values similar to metasomatic marble sampled a few cm from the serpentinite body (e.g. samples 2COR14-4i and 1COR14-11a; Table 4.3). However, taken as a whole, metasomatic marbles, overlying the serpentinite body, have lower $\delta^{18}O$ compared to the reference calcschists. Indeed, calcschists that lack the petrographic characteristics of intense fluid-rock interaction present in metasomatic marbles always have heavier values (ca. 21‰, see samples COR13-32 and 1COR12-11Q, Table 4.3), even if they crop out at less than 1m from the metasomatic zones.

Reconnaissance oxygen isotope measurements on silicate minerals were performed in order to test for isotopic equilibrium between the two clinopyroxene generations (Stage#1 diopside and Stage#2 omphacite) and the vein infill carbonate. The analyzed sample is composed of the host Stage#1 diopside-rich rock cut across by a Stage#2 calcite-omphacite vein (Figs. 4.3d and S2). Diopside has $\delta^{18}O$ values of ~6‰. Vein infill omphacite has heavier $\delta^{18}O$ of ~7‰. Fractionation factors available from literature data ($\Delta_{calcite\text{-}clinopyroxene}$ from Hoffbauer et al., 1994, Table 4.3.1), give equilibrium temperature of 494°C (±30°) for the omphacite-carbonate assemblage and 426°C (±20°) for diopside-carbonate using the same database. These differing temperatures are consistent with textural disequilibrium between the mineral pairs (carbonate-diopside and diopside-omphacite). The omphacite-calcite thermometer yields temperatures closer to the estimated peak T conditions of the metamorphic unit (490-530°C,

see Section 2). This observation suggests isotopic equilibrium for the omphacite+carbonate paragenesis and confirms the microtextural observations (see Section 5).

Equilibrium was likely reached by fluid-mediated reactions. However, this interpretation must be taken with caution because only one sample was analyzed. The composition of an aqueous fluid in equilibrium with these minerals was also calculated at 500 °C (i.e. near peak conditions). The $\delta^{18}O$ of a fluid in equilibrium with the measured Ca-carbonate is 10.1‰ ($\Delta_{cal\text{-}H2O}$=0.62, Zheng et al. 1994). For the analyzed omphacite composition, the water $\delta^{18}O$ obtained is 8.4‰ ($\Delta_{di\text{-}H2O}$=-1.95, $\Delta_{ae\text{-}H2O}$=-0.07 and $\Delta_{jd\text{-}H2O}$=-0.14, Zheng et al., 1993). Although the fractionation factors for lawsonite are not available, the diopside-water equilibrium, can be used as a proxy for fluid in equilibrium with the Stage#1 assemblage implying that the fluid $\delta^{18}O$=8‰. The mismatch between calcite-water and omphacite-water oxygen composition equilibrium is quite small as well as for water in equilibrium with diopside. It is worth noting that the estimated fluid composition is similar for both metasomatic stages.

8. DISCUSSION

8.1 Fluid-mediated carbonation at high-pressure conditions

Detecting metasomatism in metasedimentary rocks is often challenging owing to the variability of protolith compositions (Bebout and Burton, 1989; Ague, 2003). The occurrence of carbonate in metasedimentary rock is common, and in most cases likely reflects the primary composition of the subducted rocks. However, the direct spatial association of Stage#2 metasomatic marbles along major fluid conduits characterized by intense metasomatism (Martin et al., 2011; Vitale Brovarone et al., 2014) suggests that the evolution of these rocks was mediated by the interaction with external fluids (e.g. Ague, 2003).

Rod-shaped calcite crystals in marbles from eclogite-facies terrains have been described in Syros (Greece) and the Sivrihisar belt (Turkey) (Brady et al., 2004; Seaton et al., 2009), and have been interpreted as topotactic pseudomorphs of calcite after aragonite. Both studies regard carbonate as a primary constituent of the rock and do not consider fluid-mediated precipitation. In the study case, we consider this hypothesis unlikely based on several lines of evidence. Textures like crack-seal and networked carbonate veins cutting across carbonate-free metasomatic rocks suggest high pore fluid pressure and hydrofracturing (e.g. Bebout and Barton, 1989). This evidence clearly points to the percolation of carbonic fluids along lithological boundaries, and their precipitation of carbonate. As reported in Sections 2 and 5, field relations and microstructural features (Fig. 4.4) suggest carbonation of the Ca-Mg-rich silicate rocks. The lateral (along schistosity) transition from carbonate-free diopside-lawsonite rocks and metasomatic marbles is evidence for chemical interaction occurring between a carbonic fluid and the host-rock assemblage. Progressive replacement of diopside-rich rocks by carbonate is demonstrated at the microscale by the corroded texture of precursor minerals (embayed and atoll-like diopside, Figs. 4.4d, e and 4.5a) and producing coronas in contact with carbonates (e.g. omphacite rims on diopside, Figs. 4.5a,b). The carbonate isotopic composition presented in this work (Section 7) further supports the hypothesis of fluid-mediated carbonate precipitation. All metasomatic marbles are composed of Ca-carbonate (calcite after aragonite). This appears unlikely in the case of metamorphic recrystallization of rocks containing significant whole rock Mg (Table 4.2). These observations suggest that carbonate precipitation occurred via two concurrent processes of fluid-rock interaction: crack-sealing (carbonation by volume increase, Section 3) and mineral replacement (Section 5). Note that carbonation of mafic rocks during high-pressure metamorphism was also suggested by Boundy et al. (2002) for eclogite-facies rocks from the Lindås Nappe (Caledonides, Western Norway) and by Kleine et al. (2014) for blueschist-facies rocks from Syros. Both

authors proposed carbonation of mafic eclogites along a shear zone affected by fluid circulation. Similarly, Nishiyama (1990) proposed metamorphic carbonation during exhumation of blueschist-facies metabasic rocks in association with serpentinites in the Nishisonogi metamorphic complex (Japan).

Based on these observations, the metasomatic history of the Corsican eclogite-facies marbles can be subdivided into two stages, both occurring at high-pressure conditions during subduction.

Stage#1: calcic metasomatism of protolith metasedimentary rocks or continental basement transforms metasediments in contact with serpentinites to Ca-Mg rocks dominantly composed of diopside and lawsonite during prograde metamorphism (cf. Martin et al., 2011; Vitale Brovarone et al., 2014).

Stage#2: carbon-bearing fluid reacts with the pre-existing diopside-lawsonite rock and associated serpentinites leading to the precipitation of carbonate-dominated assemblages as either crack-filling material, or by replacing silicate minerals. The metamorphic conditions for this stage are constrained to high-pressure conditions by the assemblage aragonite + omphacite + lawsonite + garnet that characterize several of the analyzed samples ($P > 1.5$ GPa at 450-500 °C), and supported by the estimated O isotope Ca-carbonate-omphacite equilibrium T of ca. 500 °C.

8.2 Stable isotopes: marker of rock carbonation and fluid source?

Stable isotope geochemistry has provided important information for the study of high-pressure metasomatic processes involving carbonates (Valley 1986; Wang & Rumble 1999; Ague and Nicolescu, 2014; Galvez et al., 2013a,b). The trends of decreasing $\delta^{13}C$ and $\delta^{18}O$ isotopic composition of the metamorphic carbonates may be attributed to: (i) inheritance of protolith isotopic signatures (Wang and Rumble, 1999), (ii) carbonate-silicate isotopic

exchange; (iii) devolatilization reactions driven by increasing temperatures (Wang and Rumble, 1999), or (iv) interaction with COH fluids (Ague and Nicolescu, 2014; Galvez et al., 2013a,b).

	$\delta^{18}O$‰	1σ
omphacite*	7,25	-
diopside	6,02	-
calcite**	10,71	0,06
		equilibrium T(°C)
Δcc-omp	3,47	494
Δcc-di	4,70	426
*analyses made in duplicate		
**analyses made in quadruplicate		

Table 4.3.1: Stable oxygen isotopes analyses of clinopyroxenes, average value of calcite filling vein and calculated equilibrium temperatures.

In this study, hypothesis (i) can be ruled out by comparison of the isotopic signature of metasomatic marbles with calcschists far from the metasomatic zones. The reference calcschists have $\delta^{13}C$ values of ca. 0‰ and $\delta^{18}O$ of ca. 21‰ similar to those of calcschists and carbonate veins (for similar metamorphic conditions) in Alpine Corsica (Cartwright and Buick, 2000; Miller et al., 2001), Western Alps (Cartwright and Barnicoat, 1999; Cook-Kollars et al., 2014), and Cyclades (Ague and Nicolescu, 2014) (Fig. 4.7a). The metasomatic marble $\delta^{13}C$ values are shifted toward heavier values, although still overlapping the compositional range of seawater carbonates, whereas $\delta^{18}O$ values display a much greater dispersion towards lower values (Fig. 4.7a).

Partial silicate-carbonate oxygen isotope exchange (hypothesis ii) is an alternative way to explain low $\delta^{18}O$ (with almost no change in $\delta^{13}C$). We discard this scenario for two reasons. 1) At temperatures of 500°C, isotopic exchange by diffusion between two solid phases is expected to be very slow and thus restricted to grain margins. 2) Even if interface-coupled dissolution precipitation allowed faster isotopic exchange (Putnis and John, 2010), the $\delta^{18}O$ achieved in the carbonate after such equilibration should be correlated with the silicate content (the lowest $\delta^{18}O$ being observed for the highest silicate content; Wang and Rumble

1999; Cook-Kollars et al. 2014). Figure 4.7b shows that no correlation exists between the $\delta^{18}O$ of carbonate and the silicate content in the rock.

As a test for the third hypothesis, the metasomatic marbles are compared with carbonates that have experienced devolatilization reactions. Carbonates in skarns formed by contact metamorphism are characterized by a strong decrease of $\delta^{13}C$ coupled with a smaller $\delta^{18}O$ decrease during decarbonation (e.g. Valley 1986). The trend observed in Corsican metasomatic marbles of $\delta^{18}O$ decreasing with $\delta^{13}C$ remaining constant is actually different from a devolatilization trend (Fig. 4.7c).

Considering the compelling evidences for fluid-rock interactions and metasomatism, interactions between rocks and COH fluids (hypothesis iv) is considered the most likely hypothesis. Galvez et al. (2013b) reported carbonate reduction to graphite in contact with serpentinites in the high-pressure units of Alpine Corsica. In this study, carbonates display a peculiar variation showing a decreasing $\delta^{18}O$ coupled with increasing $\delta^{13}C$. Residual carbonate in samples affected by carbonate dissolution driven by serpentinite-derived fluids described by Ague and Nicolescu (2014) show a drop in oxygen isotopic signature compared to the protolith (6 to 10‰ lower values). However, changes in $\delta^{13}C$ are very small, with only a 1.5‰ decrease. Both carbonate precipitation and dissolution seem to be characterized by a large decrease in $\delta^{18}O$ and little to no change in $\delta^{13}C$ (Fig. 4.7c; cf. Section 8.3 for additional discussion). The $\delta^{13}C$ values of metasomatic marbles are similar to those typical of carbonates in marine sediments (e.g. Hoefs, 2013) and subducted oceanic suites ($\delta^{13}C$ close to 0‰; e.g. Miller et al., 2001), thus indicating that carbon in the fluids derives from marine carbonates, likely from the overlying carbonate-bearing metasedimentary rocks. The low $\delta^{18}O$ values rather point to fluids equilibrated with silicates in mafic or ultramafic rocks, possibly including Stage#1 metasomatic rocks (Miller et al., 2001; Martin et al., 2014; Vitale Brovarone et al., 2014; Angiboust et al., 2014). The large serpentinite body in contact with

the rocks of this study would represent a plausible source for aqueous fluid with a light oxygen signature. Despite the lack of evidence for serpentinite dehydration (e.g. metamorphic olivine) in the samples from Alpine Corsica, a growing number of studies (Faccenda 2014; Wilson et al., 2014) have proposed that fluids generated at depth can move up along the plate interface and interact with shallower slab-forming rocks. Ague and Nicolescu (2014) proposed that fluid equilibrated with mafic and ultramafic rocks can drive stoichiometric carbonate dissolution, resulting in aqueous fluid enriched in carbon with $\delta^{13}C$ around 0‰. However, if fluids were diluted, the contribution of oxygen from dissolved carbonates to the oxygen isotopic signature of the fluid is expected to be very low. The preservation of lawsonite requires very low X_{CO2} fluid concentrations ($X_{CO2}<0.005$; e.g. Nitsh, 1972), demonstrating that the carbon-bearing fluid was dominantly aqueous. Altogether, these considerations point to metasomatic marbles formation by interaction with aqueous fluids bringing isotopic signatures of both dissolved carbonates and mafic/ultramafic reservoirs.

8.3 Rock carbonation during subduction: implications for the deep carbon cycle

The behavior of carbonate, more specifically Ca-carbonate, during subduction has long been a matter of debate. Few experimental studies of Ca-carbonate solubility in H_2O have been conducted at P-T conditions appropriate for subduction metamorphism (Walther and Long, 1986; Fein and Walther, 1989; Newton and Manning, 2002; Caciagli and Manning, 2003; Manning et al., 2013; Facq et al., 2014). Caciagli and Manning (2003) showed that calcite solubility increases with P and T at high-pressure conditions. Ca-carbonate dissolution at high-pressure conditions has been demonstrated to be very efficient in natural environments ($P > \sim2$ GPa, Frezzotti et al., 2011; Ague and Nicolescu, 2014), and it is now considered as a major process for the mobilization of carbon in subduction zones (Kelemen & Manning, 2015). Carbonic fluids produced by carbonate dissolution are thus a potential source of

carbon for carbonate precipitation in subduction zones. Figure 4.8a shows a rough carbon fluxes mass balance (see Section 4.3 for method of carbon fluxes calculation) considering carbon bound by rock carbonation in metasomatic marbles vs. the amount of carbon dioxide released by dissolution and devolatilization reactions estimated in previous field-based studies in analog geological settings (Ague and Nicolescu, 2014; Cook-Kollars et al., 2014). The amount of CO_2 released by decarbonation (green and orange bars) is small compared to that released by dissolution (blue bar). Consequently, processes related to carbonate solubility mobilize carbon in greater quantities than simple decarbonation reactions (Ague and Nicolescu, 2014). A possible explanation for this result is that devolatilization reactions are controlled and limited by the presence of silicate phases with which the carbonate minerals can react, regardless of the fluid fluxes. The red bar in the diagram indicates the inferred amount of CO_2 transferred from the fluid to the rock by rock carbonation, considering an initial carbon content of 0 g per 100g of precursor rock. The amount of carbon bound per 100g of rock is directly comparable with that released by carbonate dissolution. This observation suggests that a large amount of dissolved carbon can be re-bound into the solid phase by rock carbonation, and that carbonate dissolution and rock carbonation at high-pressure conditions are both crucial processes controlling carbon fluxes during subduction. Slab-parallel ascent of fluids may represent a suitable configuration to enhance the efficiency of rock-carbonation reactions, if favorable conditions occur (Lazar et al., 2014; Kelemen and Manning, 2015; Sverjensky et al., 2014). Figure 4.8b shows the Ca-carbonate solubility in aqueous fluid as a function of P and T (after Kelemen & Manning 2015) along with the predicted P-T path for cold subduction (after Syracuse et al., 2010). Deep metamorphic fluids ascending parallel to the downgoing slab would cut across the solubility curves during their ascent.

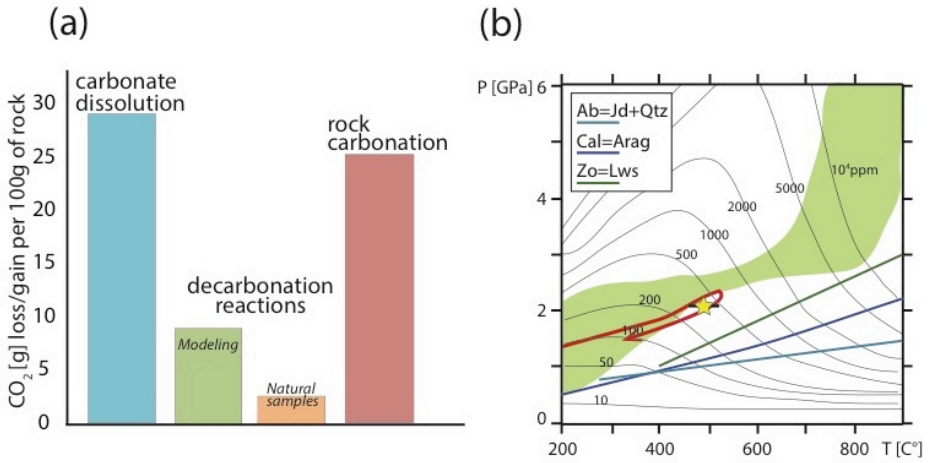

Fig. 4.8: Carbon fluxes during subduction metamorphism. a) Bar diagram reporting the estimation of grams of CO_2 release per 100 g of precursor rock during carbonate dissolution (Ague and Nicolescu 2014, blue bar) and decarbonation reactions (Cook-Kollars et al., 2014, calculation by Perple_X software and natural sample estimation, green and orange bars respectively) and grams of CO_2 bound per 100 g of precursor rock via carbonate precipitation (red bar, this study). b) Contours of [C] in parts per million for aqueous fluid saturated in $CaCO_3$ as a function of P and T. The red arrow indicates the P-T path of Alpine Corsica (Vitale Brovarone et al., 2011a). The star corresponds to the $\Delta_{cal\text{-}omp}$ equilibrium temperature. The green field represents the predicted P-T path for active subduction (D80 model, Syracuse et al., 2010). Figure adapted from Kelemen & Manning (2015).

Although prediction of fluid slab-parallel ascent by numerical modeling is still limited (e.g. Faccenda, 2014; Wilson et al., 2014), natural samples from high-pressure (this study) and ultrahigh-pressure exhumed metamorphic terrains may preserve records of the interactions of deep-fluids with the slab-forming rocks. In this study, it is shown how major lithological interfaces (e.g. crust-metasediments) may represent ideal settings for fluid channelization. In addition, the data presented here also show that Ca-Mg-rich rocks (diopside-rich) and ultramafic rocks are reactive lithologies for rock carbonation at high-pressure conditions.

Interaction between slab-derived fluids and mantle-wedge rocks also represents a possible lithological configuration for rock carbonation. High amounts of carbonic fluids resulting from slab carbonate dissolution are expected to percolate through the mantle wedge, where ultramafic rocks may represent a suitable reactant (Kelemen and Manning 2015). Based on the current knowledge of processes occurring along the plate interface (e.g. Syracuse et al., 2010), carbonation of the hydrated mantle wedge overlying subducting slabs seems unlikely in the case of vertical upward migration (rising T), whereas it is more plausible along the

slab-mantle interface (decreasing T). Exhumation of cold serpentinite diapirs in forearc settings may also be a possible environment for rock carbonation (Fryer, 1992). Future studies on rocks ascribed to the mantle wedge are needed to test this hypothesis.

9. Conclusions

The petrological and geochemical results of this study indicate that the Corsican eclogite-facies marbles found along major fluid conduits have a metasomatic origin and were formed at high-pressure conditions during subduction.

These rocks formed by carbonation of Ca-Mg silicate rocks by percolating carbonic fluids (Fig. 4.9). This implies that carbonic fluids formed during prograde carbonate dissolution may not be directly and fully transferred to the mantle wedge, but can also flow along slab interfaces (i.e. crust-metasediments) and reprecipitate carbonates under favorable conditions in both slab- and mantle-forming rocks. Carbonates precipitating from these fluids then display a characteristic geochemical and isotopic signature. Therefore, carbonation of Ca-Mg silicate rocks at high-pressure-low temperature conditions can be an efficient process to lock carbon in the rock, as is well documented at shallow and seafloor conditions (Guyot et al., 2011; Matter and Kelemen, 2009). The widespread occurrence of these rocks in the units of Alpine Corsica is likely a consequence of the overall exceptional preservation of pristine high-pressure-low temperature assemblages in this belt. This suggests that analogous rocks

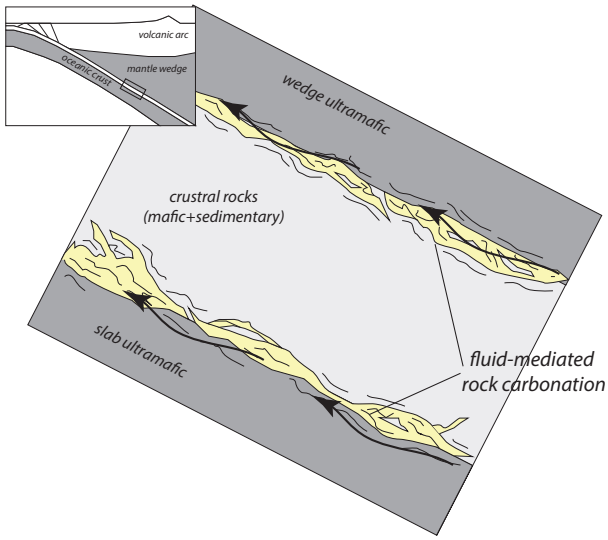

Fig. 4.9: Schematic illustration showing the percolation of COH fluids parallel to the subducting slab. The decreasing T and consequent decrease in carbonate solubility along this ascent path together with the interaction with slab or mantle rock is a suitable context for carbonate precipitation via vein injection and mineral carbonation.

and processes may have occurred in more retrogressed high-pressure belts, such as the Western Alps, the Cyclades and Turkey, and may be happening today in present-day subduction zones as well.

Whether or not high-pressure rock carbonation permanently binds carbon in the rock cannot be easily established at present. For example, high-pressure carbonated rocks can experience successive carbonate dissolution in deeper parts of subduction zones. Nonetheless, carbonation of slab- and mantle-forming rocks (Fig. 4.9) likely modulates the residence time of carbon in different reservoirs, and can modify the oxygen and carbon isotopic signature of carbonates in subduction zones. Considering a longer time-scale perspective (e.g. time elapsed from subduction initiation to continental collision), carbonation at high-pressure conditions may ultimately influence the fluctuation of CO_2 emissions at volcanic arcs during the life of a subduction zone, and thereby the fluctuation of atmospheric CO_2 over geological time scales (e.g. Berner & Kothavala, 2001).

Acknowledgment: The research leading to these results has received funding from the Deep Carbon Observatory, the University Pierre et Marie Curie (Paris 6) and Sorbonne Universités. Imène Esteve and Sébastien Charron are thanked for their technical support in the SEM platform. Benoit Baptiste is thanked for his technical support in the XRD platform. Scanning Electron Microscope (SEM) facility of the Institut de Mineralogie, Physique des Materiaux et Cosmochimie is supported by Région Ile de France grant SESAME 2006 N_ I-07-593/R, INSU-CNRS, INP-CNRS, University Pierre et Marie Curie – Paris 6, and by the French National Research Agency (ANR) grant no. ANR-07-BLAN-0124-01. Michel Fialin and Nicolas Rividi (CAMPARIS service) are thanked for their technical support during EMPA measurement.

CHAPTER 5
Significance and distribution of high-pressure carbonation in Alpine Corsica

High-pressure rock carbonation has been described in two localities so far: Alpine Corsica (Piccoli et al., 2016) and Ligurian Voltri Massif (Scambelluri et al., 2016). The two units share similar peak metamorphic conditions and type of rocks forming the HP unit, namely: serpentinite, metagabbros, metabasalts and metasedimentary rocks. However, the geological interpretation of the HP Corsican units differs significantly from the Voltri Massif. Actually, this later is interpreted as a tectonic mélange resulting from the evolution along the plate interface of tectonically coupled units of different provenance (slab and mantle wedge)(Federico et al., 2007; Scambelluri and Tonarini, 2012; Malatesta et al., 2012). Other possible setting potentially favorable for rock carbonation are the mantle wedge, the forearc mantle, and the shallow mantle thermal boundary layer beneath arcs and back arcs. All these geological loci might represent hidden carbon reservoirs in subduction zones.

In order to better evaluate the significance of HP carbonation and globally quantify the importance of this process, the distribution of carbonated metasomatic rocks need to be elucidate. In this article submitted to Lithos, we provide a detailed structural, microstructural and geochemical overview of carbonated metasomatic rocks from Alpine Corsica. Our tectonostratigraphic reconstruction revealed that a wide range of lithologies (from mafic to metasediemtnary and metafelsic) was affected by carbonate metasomatism during HP metamorphism. One of the most salient point that come from this study is that fluids responsible for rock carbonation have a characteristic signature that points to a multi source nature with contribution of both ultramafic and metasedimentary reservoirs. This finding has

profound implications for models of fluid flow and mass transfer in the subducting slab. Lastly, our data suggest that carbonation happened at oxidized condition (ΔFQM = 3 at 520°C and 2.3GPa). Considering that carbonation can affect also more reduced lithologies (i.e., the serpentinite), the question arises about the role of redox conditions for rock carbonation.

5.1 Article: Field and petrological study of metasomatism and high-pressure carbonation from lawsonite eclogite-facies terrains, Alpine Corsica

Francesca Piccoli[a,*], Alberto Vitale Brovarone[a], Jay J. Ague[b,c1]

UNDER REVIEW at Lithos (date of submission 14/07/2017)

Abstract

We describe the field and petrological features of carbonated metasomatic rocks discovered in the lawsonite-eclogite unit of Alpine Corsica (France). The study rocks are found along major, inherited lithospheric lithological boundaries of the subducted oceanic-to-transitional plate. The pervasive metasomatism often completely overprints the protolith rocks through the interplay of silicate carbonation and veining processes. In this work, we present a tectonostratigraphic reconstruction of the metasomatized lithological contacts based on field observations and a detailed petrological study. We show that a large variety of rocks ranging from metasedimentary to metamafic/ultramafic and metafelsic can react with carbon-bearing fluids at high-pressure conditions and form carbonated assemblages. The microstructural and mineralogical data strongly suggest that the metasomatism was mediated by the infiltration of

[1] [a]Insitut de Minéralogie, Physique des Matériaux et Cosmochimie (IMPMC), UMR7590, CNRS-UPMC-MNHN-IRD, Campus Jussieu, case courrier 115, 4 Place Jussieu, 75005, Paris, France.
[b]Department of Geology and Geophysics, Yale University, P.O. Box 208109, New Haven, CT 06520-8109, USA
[c]Peabody Museum of Natural History, Yale University, 170 Whitney Avenue, P.O. Box 208118, New Haven, CT, 06520-8118, USA

external fluids of mixed origin, including both ultramafic and metasedimentary sources. Our results support the following three-step evolution: (i) Serpentinite dehydration releases aqueous fluids at depth of ca. 100km; (ii) These fluids channelize along major lithological interfaces at the base of the subducted metasedimentary pile. Aqueous fluid-rock interactions along fluid conduits dissolve carbonates under high carbonate solubility conditions and generate fluids enriched in Ca and carbon as well as alkalis, notably Na; (iii) Decompression and cooling of these fluids at depths of ca. 70km led to carbon saturation in the fluid, carbonate precipitation and carbonation of pre-existing silicate-rich lithologies. This study highlights the importance of carbonate-bearing fluids decompressing along down-T paths, such as along slab-parallel lithological boundaries, for the sequestration of carbon in subduction zones, and suggests that similar processes may also happen in collisional settings.

1. Introduction

The petrological evolution of subducting rocks exerts a major control on global geochemical cycling at active margins, including arc magma generation, the formation of new continental crust, and transport of crustal material and volatiles into the deep mantle (Bell and Rossman, 1992; Schmidt and Poli, 1998; Hermann et al., 2006; Spandler and Pirard, 2013). Fluids produced by prograde devolatilization processes are critical for metamorphic reactions and phase equilibria in the down-going slab, and have been called upon in both petrological and geochemical models to facilitate large-scale bulk rock changes (metasomatism) and mass transfer in the subducted crust and overlaying mantle wedge (Bebout and Barton, 1989; Selverstone et al., 1992; Hermann et al., 2006; Zack and John, 2007; Marschall and Schumacher, 2012; Vitale Brovarone and Beyssac, 2014). Metasomatic rocks equilibrated in fluid-mediated systems and exhumed in mountain belts can be used to investigate the processes of fluid-rock interactions and mass transfer taking place at depth during subduction

and their pressure-temperature (P-T) conditions.

Field-based studies in high-pressure (HP) units demonstrate that carbon can be extremely mobile during subduction metamorphism through decarbonation reactions and carbonate dissolution (Frezzotti et al., 2011; Ague and Nicolescu 2014). The resulting carbon-bearing fluids may migrate to the mantle wedge along up-T gradients, favoring mantle metasomatism and the genesis of arc magmas (Frezzotti et al., 2011; Ague and Nicolescu, 2014; Poli, 2015). Alternatively, recent studies on the exhumed eclogite-facies units of Alpine Corsica and the Western Alps report that carbon-bearing fluids migrating within the slab can be extremely reactive with mafic and ultramafic rocks and lead to HP rock carbonation, with large-scale implications on the global carbon cycle (Piccoli et al., 2016; Scambelluri et al., 2016). However, the identification of carbonates of metasomatic origin (precipitated from fluids during metamorphism) from metamorphosed carbonates initially present in the rocks may be challenging owing to the absence of diagnostic mineral assemblages, and to the effect of metamorphic overprinting and deformation.

In this perspective, a detailed field, microstructural, and petrological characterization of carbonate metasomatism and the resulting carbonated metasomatic rocks is needed to facilitate their recognition in more retrogressed HP belts, and to better assess the impact of this process on the carbon inventory in subduction zone reservoirs. In this contribution, we present structural, petrological and geochemical data for several occurrences of carbonated metasomatic rocks in the lawsonite eclogite-facies terrains of Alpine Corsica, France. The aim of this work is twofold. Firstly to provide an exhaustive picture of the nature and diversity of these carbonated metasomatic products and their protolith rocks. Secondly, to discuss the fluid sources and the P-T-X-fO_2 conditions at which HP carbonation occurred in the selected case study so as to elucidate general petrological and geochemical features characterizing carbonate metasomatic processes at HP conditions in subduction zones. A

conceptual model of large-scale reactive fluid flow is proposed at the end of the manuscript based on the collected field, petrological and geochemical data.

2. Geological setting

2.1 Geology of Alpine Corsica and San Petrone unit

Alpine Corsica occupies the northeasterner part of the island of Corsica, France, and is a segment of the Alpine orogenic system (Jolivet et al., 1991; Molli and Malavieille, 2011; Fig. 5.1a). The belt is subdivided into three domains (see Vitale Brovarone et al., 2013 for review): 1) the continent-derived units; 2) the Schistes Lustrés complex; and 3) the uppermost thrust sheets (*Nappes Supérieures*) (Fig. 5.1b).

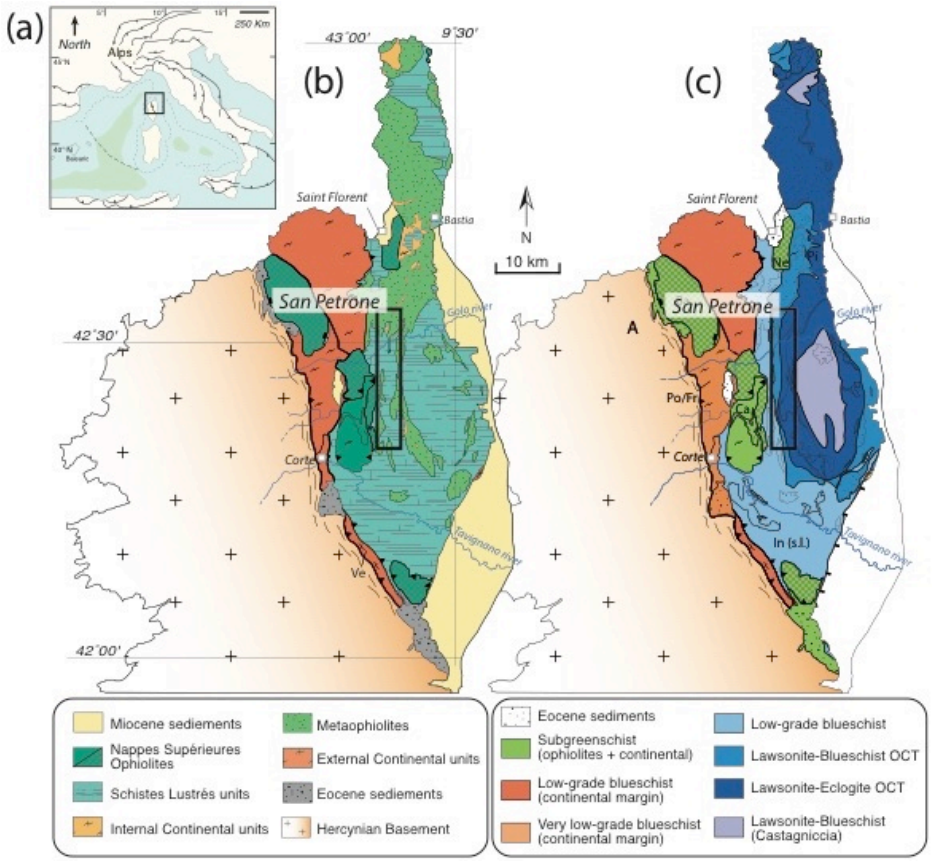

Fig. 5.1: Geological setting of the study area. **a)** Simplified regional setting of Alpine Corsica (France) in the Western Mediterranean region. Modified after Molli and Malavieille (2011). **b-c)** Simplified tectono-stratigraphic and metamorphism maps of Alpine Corsica. The black box indicates the location of the San Petrone unit, belonging to the lawsonite-eclogite terrains. Modified after Vitale Brovarone et al. (2014a).

Altogether, these units were thrust over the western and southern part of the island, which largely escaped the Alpine subduction and orogenesis. The Schistes Lustrés complex consists of remnants of subducted Mesozoic slow-spreading oceanic and passive margin lithosphere of the Tethys Ocean, and shows lithostratigraphic features analogous to those of the eclogite-facies units exposed in the Piemonte Zone of the Western Alps (e.g. Queyras/Combin/Monviso/Rocciavré/ Zermatt–Saas area; Lagabrielle and Lemoine, 1997; Lombardo et al., 2002; Vitale Brovarone et al., 2014a). The Schistes Lustrés complex forms a N-S antiformal stack with metamorphic grade increasing from the top to the bottom, with the exception of the lowermost structural unit (Castagniccia unit, Fig. 5.1c). The peak metamorphic grade varies from subgreenschist-facies conditions of about 300°C and 0.4GPa to lawsonite blueschist- and lawsonite eclogite-facies conditions of 500-550°C and ~2.3GPa (e.g. Fournier et al., 1991; Ravna et al., 2010; Vitale Brovarone et al., 2013).

In this study, we focus on the San Petrone unit, which belongs to the lawsonite eclogite-facies terrains (Vitale Brovarone et al., 2011a) (Fig. 5.2a). The San Petrone unit is interpreted to represent a coherent segment of subducted oceanic-to-transitional lithosphere and consists of a basal body of serpentinite (altered lithospheric mantle) overlain by a laterally variable lithostratigraphy comprising: i) slivers of continental basement rocks; ii) pillow metabasalts; and iii) Mesozoic metasedimentary rocks (Fig. 5.2b). Ophicarbonates are locally found between the serpentinite and the overlying rocks. Metagabbros are rare in this unit and occur as small pods within the serpentinite. The continental basement slivers lie directly upon the serpentinite (Fig. 5.2a,b), and contain both ortho- and carbonate-free para-gneiss. These continental basement slivers are interpreted as continental extensional allochthons emplaced on top of an exhumed mantle substratum during the opening of the Tethyan basin in a Jurassic hyper-extended margin or ocean-continent transition (OCT) zone (Vitale Brovarone *et al.*, 2011a; Beltrando et al., 2014). Mesozoic metasedimentary rocks variably overlie the

serpentinite, the continental slivers, and/or the ophiolite-type rocks (Fig. 5.2a,b). The base of the Mesozoic metasedimentary suite is referred to the original basal unconformity of marine sediments in the Tethys basin (Vitale Brovarone et al., 2011a; Beltrando et al., 2014). The Mesozoic metasediments can be divided into early post-rift and post-rift metasediments. The first group consists of metacherts (likely radiolarian metacherts) and marbles of inferred Jurassic sedimentary age; the second group mainly includes calcschists sensu stricto, i.e., quartz-pelitic layers alternating with carbonate-rich layers of Cretaceous sedimentary age (Vitale Brovarone et al. 2011a). This composite tectonostratigraphic sequence is folded by a series of large (km in length) N-S non-cylindrical anticlines and synclines that locally overturn the overall upright tectonostratigraphy (Fig. 5.2b). Because of the non-cylindrical folds, the entire lithostratigraphy is affected by local and discontinuous synformal and antiformal structures with N-S trending fold axes (Fig. 5.2b,c,d). The HP minerals mark the main regional schistosity. The whole tectonolithostratigraphic suite of the San Petrone unit underwent consistent peak metamorphic conditions of about 500-550°C and ~2.2-2.4GPa (Vitale Brovarone et al., 2011a) in the Late Eocene by both U-Pb zircon and Lu-Hf garnet/lawsonite geochronology (~34Ma, Martin et al. 2011; Vitale Brovarone and Herwartz, 2013).

2.2 Fluid-rock interaction and metasomatism in the San Petrone unit

Previous studies have documented rock affected by strong fluid-rock interactions and metasomatism in this unit, and mainly affecting the continental basement slivers and the base of the Mesozoic metasedimentary sequence (inherited basal unconformity) overlying the serpentinite (Vitale Brovarone et al., 2011,2014b; Martin et al., 2011; Vitale Brovarone and Beyssac, 2014; Piccoli et al., 2016) (Fig. 5.2b-e). The metasomatic products mainly include a first stage characterized by lawsonite-diopside rich rocks (Stage#1 metasomatic rocks)

(Martin et al., 2011; Vitale Brovarone et al., 2014b) and a second stage characterized by carbonate metasomatism and the formation of carbonated metasomatic rocks and carbonate (± omphacite) veins (Stage#2 metasomatic rocks; Piccoli et al., 2016). The first stage is constrained to prograde-to-peak metamorphic conditions by petrological and geochemical data and U-Pb zircon geochronology (Martin et al., 2011), whereas the second stage took place under peak-to-early retrograde conditions based on microstructural and petrological observations (Piccoli et al., 2016). Of particular interest for this study are the carbonated metasomatic rocks and carbonate-bearing metasomatic products of Stage#2 metasomatism, for which we report herein a new field, including several new localities and structural occurrences, and petrological data.

3. Tectonostratigraphic occurrence of carbonated metasomatic rocks

Carbonated metasomatic rocks in the San Petrone unit occur along three main types of regional lithological interfaces (Fig. 5.2a), which are described in the following together with their most notable structural and lithological features. The reconstruction of the pre-metasomatism metasedimentary sequences was done by integrating field and petrological observations from our survey and previous studies (Vitale Brovarone et al., 2011a, Martin et al., 2011). Figure 5.3 summarizes the main field lithostratigraphic observations by means of interpretative tectonostratigraphic logs and representative field images.

3.1 Serpentinite-Mesozoic metasediments

This regional lithological interface can be observed almost continuously over about 13 km (Fig. 5.2a). The best examples of metasomatism along this type of lithological interface are exposed in the localities of Col del Prato, Punta Favalta and Loriani (Figs. 5.2a,c and 5.4a,b,c). The main lithological features of this interface are summarized in the reconstructed

tectonostratigraphic logs of Figure 5.3a. In these zones, the serpentinite below the contact is massive to foliated. Only the very top centimeters of the serpentinite exhibit a marked schistosity parallel to the contact with the overlaying rocks and are more weathered. At the regional scale, relicts of the Mesozoic metasedimentary rocks not affected by metasomatism and overlying the serpentinite commonly consist of quartz-rich, carbonate-free layers alternating with impure marbles (Fig. 5.3a1,a2), followed upward by calcschists sensu stricto (quartz-pelitic layers with more or less abundant carbonate layers).

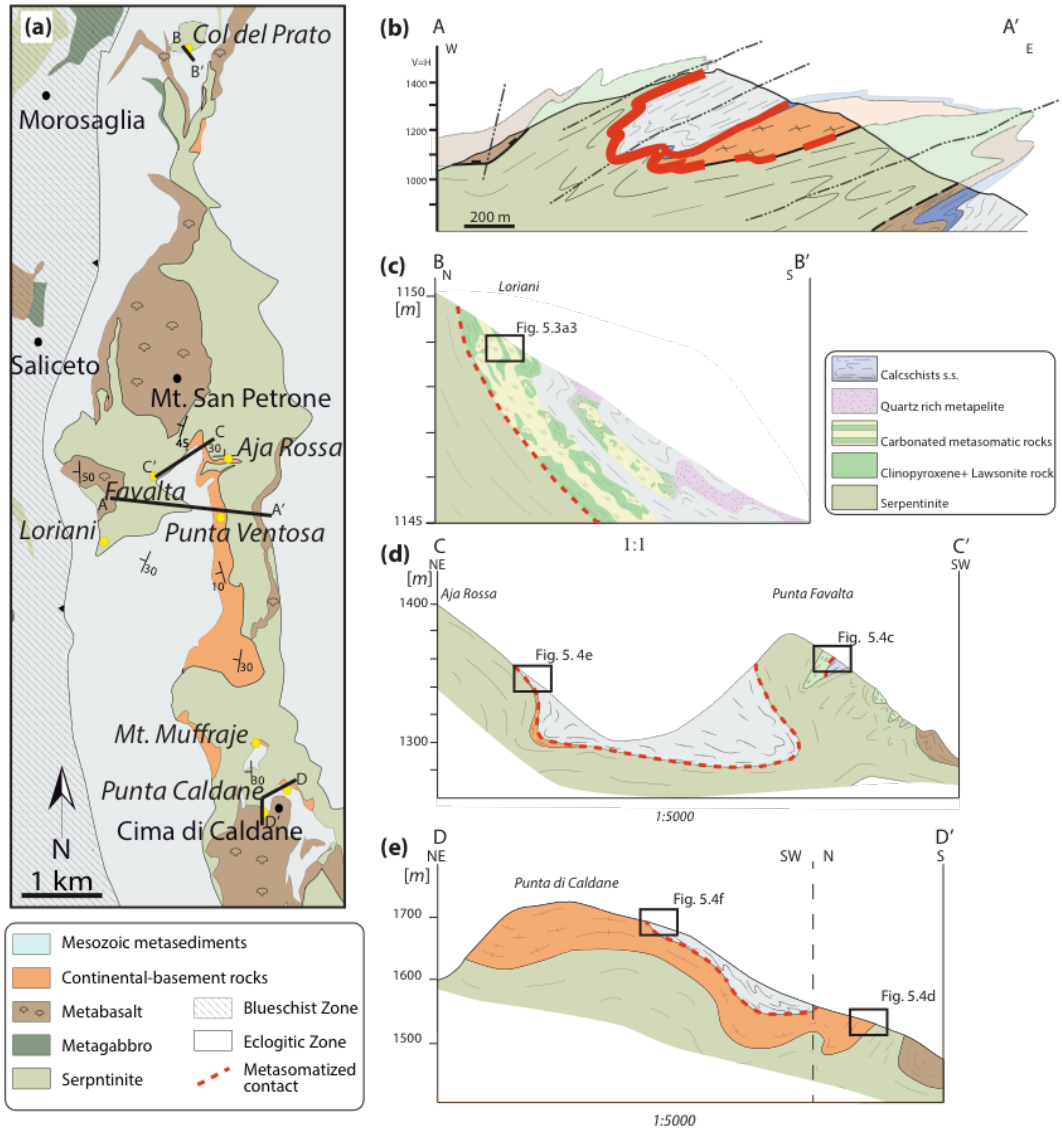

Fig. 5.2: a) Simplified geological map of the San Petrone unit. Modified after Vitale Brovarone et al. (2014a). Outcrops location is indicated by yellow dots. Black solid lines indicate the direction of geological cross sections. **b,c,d,e)** Geological cross sections. Dashed red line indicates metasomatized lithological boundaries.

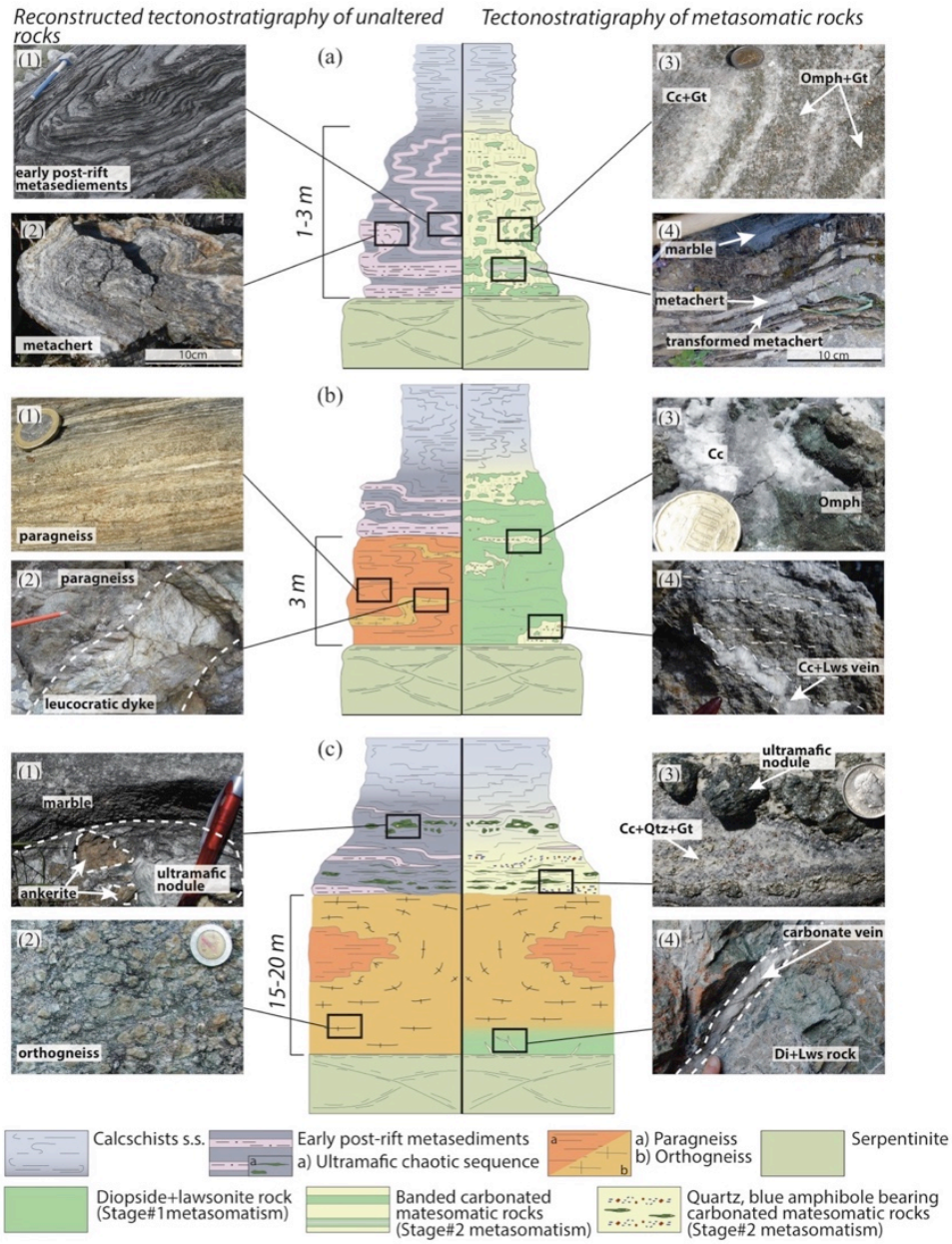

Fig. 5.3: Interpretative logs of the metasomatized lithological contacts and relatively outcrop images. In each log, the left side represents the pristine tectonostratigraphic sequence, whereas the right side is the metasomatic equivalent as it looks like in the field. **a)** Serpentinite-early post rift metasediments contact and metasomatic equivalent. a1) Unaltered early post-rift metasediments sequence composed by alternating quartz-rich and carbonate rich layers. a2) Preserved quartz-blue amphibole bearing metachert. a3) Banded carbonated metasomatic rock from Col del Prato area. a4) Preserved metachert level in carbonated metasomatic rock. Note that preserved metachert is pinkish colored while the border is green indicated a partial rock transformation. **b)** Serpentinite-thin continental crust sliver contact. Note that in the metasomatic equivalent marbles, veins and crack-seals occur. b1) Pre-Alpine paragneiss. b2) Leucocratic dyke intruding a paragneiss (Photo from Vitale Brovarone et al., 2011a). b3) Omphacite + carbonate vein. b4) Fresh cut of a banded carbonated metasomatic rock cut across by a carbonate + lawsonite vein (Mt Muffraje area). **c)** Serpentinite-thick continental crust sliver contact. c1) Ultramafic nodule with ankerite in marble level (Punta Ventosa area). c2) Orthogneiss. c3) Detail of a quartz, blue amphibole bearing carbonated metasomatic rock with metasomatized ultramafic nodules (Punta Caldane area). c4) Detail of the metasomatic rind at the base of an orthogneiss sliver in contact with the serpentinite (west of Punta di Caldane): the lowermost part of the metasomatic rind displays pervasive carbonate veins, discordant to the rock foliation. Mineral abbreviations from Kretz (1983).

The quartz-rich layers, commonly metacherts (Fig. 5.3a2), are continuous and range in thickness from a few cm to about 1m, and are especially common at the base of the sedimentary sequence (first 3m above the contact). Metacherts commonly contain Mn-rich minerals suggesting transformations of Mn-bearing radiolarian metacherts typical of the lowermost portion of the Tethyan Mesozoic sedimentary cover sequences preserved in this unit (Vitale Brovarone et al., 2011a and references therein). The metasedimentary rocks are affected by polyphase deformation leading to non-cylindrical and disharmonic folding and a marked composite schistosity (Fig. 5.3a1) that locally resulted in boudinage of the quartz-rich layers.

The contact between the serpentinite and the metasediments is commonly affected by a strongly asymmetric metasomatic overprint, with the lower part of the metasedimentary pile (1-3m) overlying the serpentinite marked by metasomatism products, i.e. diospide-lawsonite-rich rocks and carbonated metasomatic rocks (Figs. 5.3a3, 5.3a4, 5.4b) (Martin et al 2011; Vitale Brovarone et al., 2014b; Piccoli et al., 2016), and no marked evidence for metasomatism in the serpentinite. The two metasomatic end-members (diopside-lawsonite and carbonated metasomatic rocks) overprinting the Mesozoic metasediments are observed at various scales with two main modes of occurrence. In some cases the two rock types form a layered structure that mimics the structure of former metasedimentary sequences formerly composed of folded impure marbles and metachert layers (Fig. 5.3a). Some outcrops show partial replacement of the protolith metasedimentary rocks by the metasomatic assemblages. The most remarkable example was observed in the Loriani outcrop (Figs. 5.2a, 5.4a), where a progressive transformation of former metachert layer into diopside-lawsonite-rich rocks can be clearly seen on the outcrop (Fig. 5.3a4). The diopside-lawsonite domains are then replaced by carbonate. This process leads to heterogeneous consumption and segmentation of the silicate-rich layers of the initial metasedimentary sequence (Fig. 5.4b). The latter process is

commonly mediated through processes of fracturing and brecciation of the silicate-rich domains and formation of carbonate crack-seals, along with chemical replacement of silicates by carbonate (Piccoli et al., 2016). Field and microstructural observations define chronological constraints for the metasomatic events, including carbonation, post-dating the main regional-scale folding event.

In the Punta Favalta area, a ca. 8m thick sequence of variably metasomatized and intensely deformed rocks is found atop the regional serpentinite. Here, the serpentinite basement is intensely folded and capped by ophicarbonates. A small lens of metasediments is sandwiched in a tight, recumbent syncline. The outcrop is located in the overturned limb of the fold (Fig. 5.2d). The rocks overlying the serpentinite are intensely metasomatized and affected by strong deformation along a main shear zone. This metasomatic and tectonic complexity makes the nature of the protolith rocks difficult to establish. Figure 5.4c shows the shear zone between less deformed lawsonite-rich rocks and highly strained carbonated metasomatic rocks.

3.2 Serpentinite-continental basement rocks

Metasomatism and HP carbonation also occurred at the expense of initially carbonate-free, pre-Alpine continental basement rocks resting on top of the serpentinite (Figs. 5.2b, 5.3b,c). The extent of carbonation most commonly inversely correlates with the thickness of the continental basement slivers, such that no carbonate-bearing rocks were found at the base of the thickest (>20m) portions of the continental basement slivers. The most notable examples of metasomatism in this structural setting are found in the area between Punta di Caldane, Monte Muffraje and Aja Rossa (Fig. 5.2a,d). In the southern part of the study area (Punta di Caldane), where a 15-20m thick (minimum thickness) sliver of continental basement rock crops out discontinuously and forms patches of variable thickness. In the vicinity of Punta di

Caldane, this body mainly consists of orthogneiss (± discontinuous paragneiss lenses; Figs. 5.2e, 5.3c2, 5.4d) overlying the serpentinite. The uppermost tens of cm of the serpentinite nearby the contact show a marked schistosity parallel to the contact and no alteration halos have been observed. Above the contact, the first 2m of rock consist of Stage#1 metasomatic diopside-lawsonite rock formed at the expense of the orthogneiss, as indicated by the primary structure of the orthogneiss preserved in the metasomatic rind. In the lowermost part of the metasomatic rind, several carbonate veins cut across the metasomatized orthogneiss (Fig. 5.3c4). The veins reach about 2cm in thickness and have sharp contacts, with no alteration selvage observable in the field. No evidence for carbonation by replacement of former silicates was observed here.

The same contact is exposed in the Monte Muffraje area. Here, a 2 to 3m-thick patch of metasomatic rocks cap the serpentinite, and are followed upwards by unaltered Mesozoic calcschists. The contact between the metasomatic rind and the serpentinite is parallel to the regional schistosity and dips gently to the west. As for the previous cases, the serpentinite doesn't show marked evidence for strong fluid-rock interactions. In the field, the distinction between metasomatized pre-Alpine and Mesozoic rocks cannot be easily done owing to the outcrop conditions and the pervasive metasomatism. However, petrographic analysis (see Section 5) indicates that the metasomatic rocks above the serpentinite formed at the expense of both pre-Alpine continental basement rocks (lower part of the metasomatic rind) and Mesozoic origin (upper part)(Fig. 5.3b). The metasomatic rind consists of both Stage#1 and Stage#2 metasomatic rocks. Stage#1 rocks dominantly consist of diopside and lawsonite, and occur as dismembered, partially corroded patches embedded in a Stage#2 carbonate-rich matrix (Fig. 5.3b4). Stage#1 domains preserve a weak foliation inherited from the protolith and overgrown by the quasi-static precipitation of diopside + lawsonite. The orientation of the foliation in the patches of Stage#1 rocks is consistent at the outcrop scale (i.e. no clast

rotation) and indicates that carbonate precipitation occurs statically. In the Stage#2 rocks, carbonate (calcite after aragonite, see Section 5) in most cases forms rods oriented at high-angles to the regional schistosity. Carbonate and carbonate + lawsonite veins, often with crack-seal texture, are widespread and locally discordant to the regional foliation (Fig. 5.3b4). Like in the previous case, in the Aja Rossa area, a few meters of continental basement rocks are extremely metasomatized (Fig. 4e). The metasomatic rind in this outcrop extends over the continental material and also affect the overlying Mesozoic metasediments for a total thickness of ca. 8m.

3.3 Continental crust-Mesozoic metasediments

Metasomatic rocks and HP carbonation was also observed along the top of the pre-Alpine continental basement rocks in contact with Mesozoic metasedimentary rocks. The two most notable examples crop out in the area of Punta di Caldane and to the East of Punta Ventosa (Fig. 5.2a,e). In the vicinity of Punta di Caldane, Mesozoic metasedimentary rocks cap a 15-20m thick sliver of continental basement rocks, which in turn overlie the basal serpentinite (section *3.2*). In the first 5m above the contact with the orthogneiss, metasomatism and deformation of the metasedimentary sequence lead to the formation of a chaotic ensemble made of deformed clasts/blocks of mafic/ultramafic composition –ranging from a few cm to ca. 50cm in diameter– dispersed in a carbonate-rich matrix (Fig. 5.3c1; 5.4f). Some clasts are intensely strained and form discontinuous layers mainly consisting of green amphibole + chlorite. Ankerite nodules are observed within the ultramafic clasts (Fig. 5.3c1). Carbonated rocks with mafic/ultramafic nodules and layers are overlain by quartz-rich rocks. In the upper part, ca. 5m above the contact with the continental sliver, the metasedimentary sequence becomes more homogeneous and dominated by calcschists.

In the region of Punta Ventosa (Fig. 5.2a), deformed carbonated metasomatic rocks with abundant nodules of mafic/ultramafic composition are in contact with the pre-Alpine basement (equivalent to Fig. 5.3c1). Ankerite nodules and Ca-carbonate crack-seals associated within green amphibole-chlorite lenses are also observed. These rocks are followed upward by impure marble layers with abundant deep green clinopyroxene, blue amphibole, garnet, and minor quartz (Fig. 5.3c3). This kind of carbonated rock never occurs in the metasedimentary sequence far from major lithological interfaces, where only monotonous rocks such as calcschists are found.

The heterogeneity of the chaotic sequence in these two areas makes the identification of individual metasomatic events more challenging than the previous cases and, therefore, the reconstruction of a pre-metasomatism tectonostratigraphy. No unaltered protolith rocks with comparable structural features were found, with the exception of a small body of brecciated serpentinites ~150 m from the Punta Ventosa outcrop. This suggest that the mafic/ultramafic clasts, rich in typical metasomatic assemblages such as chloritite, actinolitite, may represent transformation of former serpentinite clasts embedded in the metasedimentary pile, as commonly described in active slow-spreading oceans and their metamorphic equivalents .

4. Methods

4.1 Scanning electron microscopy and electron microprobe

Petrographic thin sections were carbon coated for scanning electron microscopy (SEM). Observations were performed at a working distance of 7.5 mm using a Zeiss Ultra 55 field emission gun SEM operated at 15 kV with a 120μm aperture. Backscattered electron (BSE) mode was used to investigate chemical heterogeneities using an Angle Selective Backscattered Detector (AsB) or an Energy Selective Backscattered Detector (EsB).

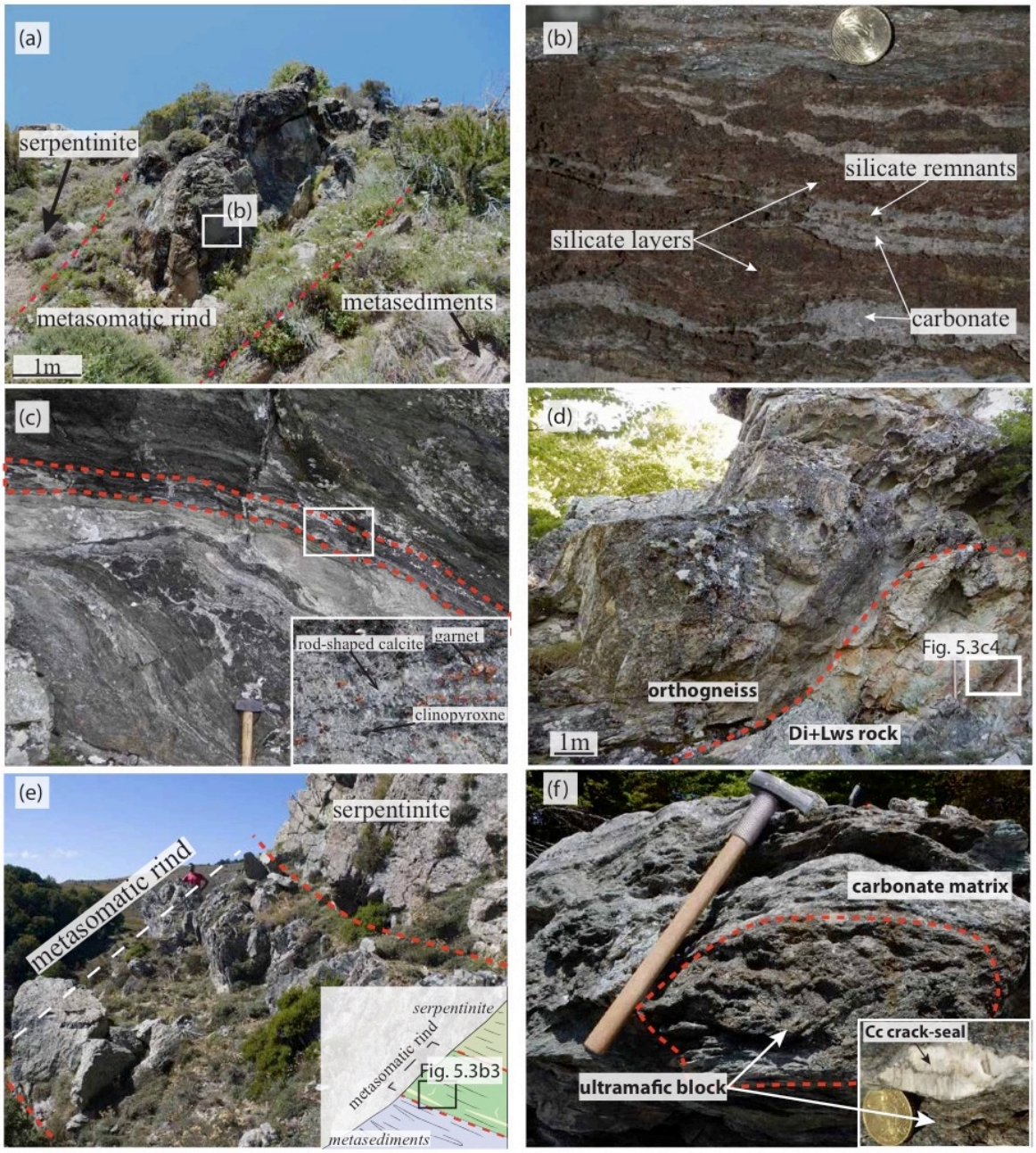

Fig. 5.4: Outcrop of carbonated metasomatic rocks along different lithological contacts. **a)** Loriani outcrop. Here the metasomatic rind width ranges between 1m and 2.5m. **b)** Detail of Loriani outcrop showing the heterogeneous carbonation of the silicate rock. **c)** Shear zone in the metasomatized contact in Punta Favalta area. The dashed red lines indicate the carbonated metasomatic rock level, the detail of which is reported in the white box. **d)** Metasomatic rind on the orthogneiss in contact with serpentinite nearby Punta Caldane. **e)** Aja Rossa outcrop and simplified geological cross section (modified after Vitale Brovarone et al., 2014b). **f)** Outcrop in Punta Caldane area: mafic block embedded in carbonate matrix. A detail of a carbonate crack-seal opening within the mafic block is reported in the white box.

Energy dispersive X-ray spectrometry (EDXS) maps were acquired using an EDXS QUANTAX system equipped with a silicon drift detector XFlash 4010 (Bruker). Data were processed with the software Esprit (Bruker). Mineral analyses were performed on a Cameca electron microprobe (either SX-100 or SX Five) (Camparis, Université Paris 6). Common analytical conditions were adopted for spot analyses (15 kV, 10nA, wavelength-dispersive spectroscopy [WDS] mode), using Fe_2O_3, $MnTiO_3$ (Mn, Ti), diopside (Mg, Si), orthoclase (Al, K), anorthite (Ca) and albite (Na) as standards. The automated Cameca ZAF procedure was used for quantification.

4.2 Petrogenetic grid calculations

Petrogenetic grids were calculated using the software Perple_X (version 6.7) and the internally consistent thermodynamic database of Holland and Powell (1998, revised 2004). The grids were calculated in the Na_2O-Al_2O_3-CaO-FeO-Fe_2O_3-SiO_2 system. Ferric iron was included in the system as it is a fundamental component in the rocks. However, in order to avoid the use of multiple solid solutions for which the incorporation of ferric iron is still uncertain, MgO was neglected. This choice does not affect the modeling of carbonate phases in our case because in the selected sample the only carbonate is Ca-carbonate. To account for the absence of Mg in the system, the activity of Mg-bearing minerals was modified, with the exception of amphibole (see below). The activity of almandine (as proxy for garnet) and aegirine (as proxy for clinopyroxene) was calculated using the software AX (Holland and Powell, 1998) using the measured microprobe analyses (see Sections 6 and 7, Table 5.3). Comparative AX calculations at 1.5 to 2.3GPa and 380 to 520°C show that the almandine activity does not vary significantly, and was fixed at 0.25. The modified mineral activities have only a slight effect on the topology of the modeled reactions, with a slight decrease for both P (ca. 0.1GPa) and X_{CO2} (ca. 0.005) compared to pure end-members. Epidote activity

was set to unity because epidote is nearly pure (Table 5.3). Considering the complexity of amphibole solid solution and the risk to use inappropriate values for amphibole activity, riebeckite was used as a proxy for amphibole, and its activity was not modified. These calculations were done by considering previous estimates of the prograde P-T path and geothermal gradient of the Alpine Corsica lawsonite eclogite-facies unit (Vitale Brovarone et al., 2011b).

Locality	Interface	Protolith	Stage#1	Stage#2	Late stages
Loriani	Serpentinite/ Mesozoic metasediments	Metachert, Calcschists	Di, Lws	Cc, Agt, (±Gt)	Pmp, Ep, Ab
Col de Prato	Serpentinite/ Mesozoic metasediments	Metachert, Calcschists	Di, (Lws?)	Cc, Omph, Gt	Ab, Phg
Punta Favalta	Serpentinite/ Mesozoic metasediments	Metachert (?)	Ep, Rieb, Qtz, Hem, Deer	Cc, Agt, Gt, Qtz, Hem, Deer	--
Aja Rossa	Serpentinite / pre-Alpine HT continental rocks / Mesozoic metasediments	Paragneiss (?), Calcschists (?), Metachert (?)	Di, Lws	Cc / Cc+Omph	Phg
Muffraje	Serpentinite/ pre-Alpine HT continental rocks / Mesozoic metasediments	Paragneiss, Orthogneiss, Metachert (?)	Di, Law, ±Gt	Cc, Omph, Gt, (Lws?), (Qtz)	Phg
Punta Caldane	Pre-Alpine HT continental rocks / Mesozoic metasediments	(?)	Di, Law/Act, Chl	Cc, Agt, Gt, Qtz	Gln, Phg
Punta Ventosa	Pre-Alpine HT continental rocks / Mesozoic metasediments	Metachert (?)	Act, Chl, (Lws?)	Cc, Omph-Agt, Gt, Qtz	Phg

Table 5.1: Summary table reporting mineral paragenesis of the study rocks

5. Petrography

Here we present an overview of the characteristic microstructures of the main rock types studied, including the protolith rocks and their metasomatic equivalents from the three types of tectonostratigraphic settings described in the previous section. Table 5.1 reports most characteristic mineral paragenesis for the main metasomatic stages, and for each outcrop. Mineral modal volumes for the studied thin sections are reported in Table 5.2, whereas mineral chemistry is described in the next section and representative analyses reported in Table 5.3. Carbonates are always compositionally pure $CaCO_3$, unless otherwise specified. In the matrix calcite replaces aragonite, whereas fresh aragonite is locally preserved as inclusions in garnet and hematite.

5.1 Unaltered protolith rocks

5.1.1 Mesozoic metasediments (samples cor13-32, 1cor12-11q, cor16-42d, 1cor12-20c, 1cor14-5)

Relicts of Mesozoic metasediments unaffected or least affected by metasomatism range from metachert (sample cor16-42d) to quartz-carbonate rich rocks (samples 1cor12-20c and1cor14-5, Figs. 5.3a1, 5.3a2). In thin section, the first variety displays disjunctive schistosity (Passchier and Trouw, 2005) marked by phengite rich layers and oriented blue amphibole alternating with coarse-grained granoblastic quartz domains (Figs. 5.5a, 5.6a). Small euhedral garnet grew in the amphibole-phengite domains (Fig. 5.6a). The second rock type is characterized by alternating mm-thick layers of carbonate and quartz (Figs. 5.5b, 5.6b). Euhedral garnet is found in the silicate-rich domains (Fig. 5.6b). Iron-rich carbonate and opaque minerals form clumps wrapped by phengite, blue amphibole, and epidote (Fig. 5.5b). Mn-rich epidote is also locally present (1cor14-5c, Table 5.2). Calcschists sensu stricto (samples cor13-32 and 1cor12-11q) have a marked schistosity defined by phengite flakes embedded in a carbonate + quartz granoblastic matrix. In these samples, accessories phases are chlorite, epidote, opaque minerals, and carbonaceous material, the latter being concentrated in the phengite-bearing domains. Pseudomorphs after lawsonite may be present and consist mainly of white mica, chlorite, and opaque minerals.

5.1.2 Pre-Alpine gneiss

Pre-Alpine rocks forming the continental basement slices are polymetamorphic micaschists and metamafic paragneiss intruded by Permian granitoids (now orthogneiss, Fig. 5.3b1, 5.3b2, 5.3c2) (Vitale Brovarone et al., 2011a and references therein; Martin et al., 2011).

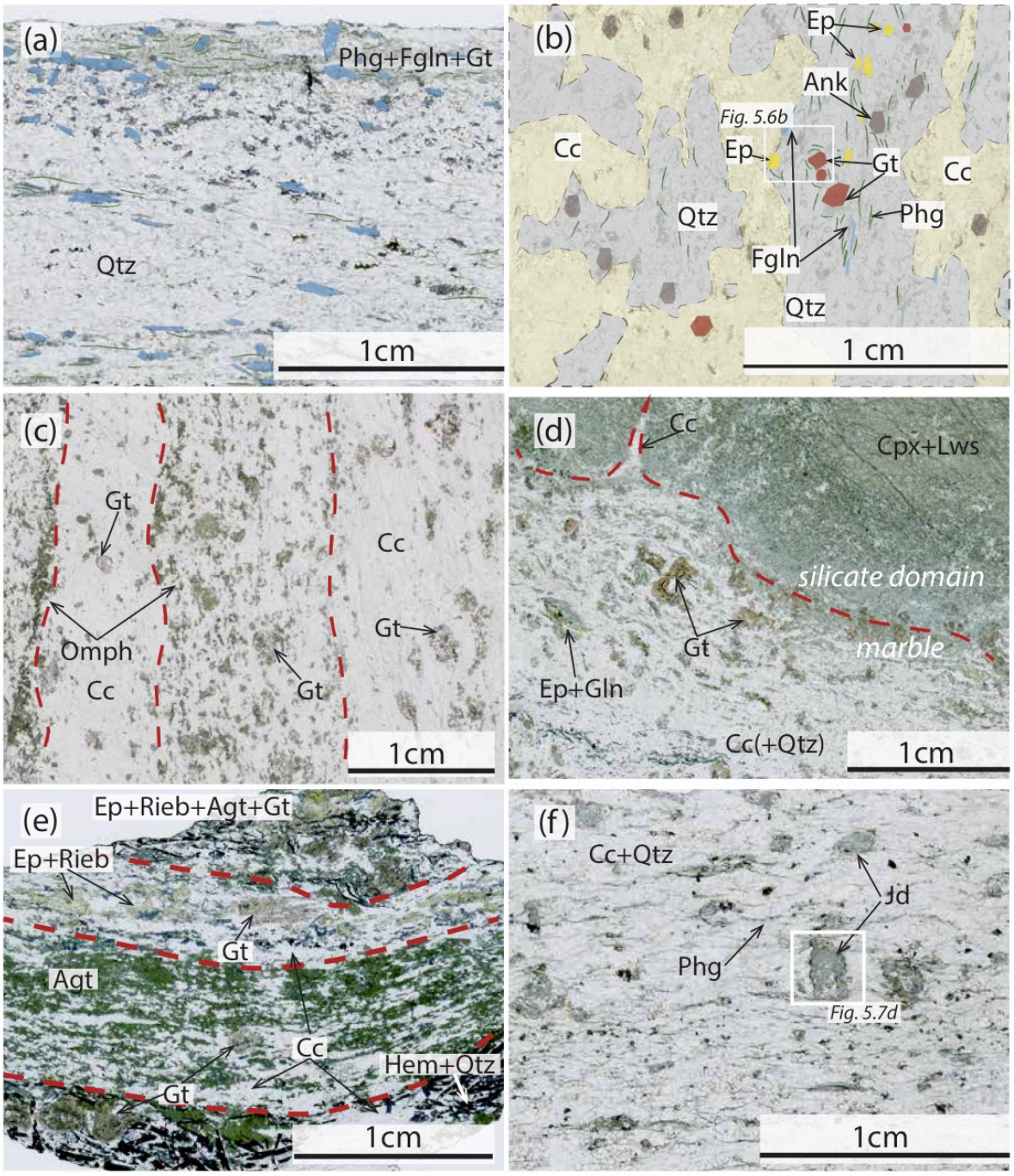

Fig 5.5: Thin section scans. **a)** Non-metasomatized metachert from Loriani outcrop (sample cor16-42d). Phengite and blue amphibole levels are highlighted with colors. **b)** Quartz-carbonate rich metasediment from Col del Prato area (sample 1cor12-20c). Minerals are shaded with colors. Carbonate and quartz domains are shaded in yellow and grey respectively. Epidote, blue amphibole, garnet and ankerite are shaded in yellow, blue, red, and brown, respectively. **c)** Banded carbonated metasomatic rock from Col del Prato. The scan shows the occurrence of silicate rich levels composed by omphacite, garnet and carbonate (bands delimited by dashed red lines). Note that large garnet porphyroblasts are present in both carbonate and silicate rich domain (sample 1cor12-20d). **d)** Banded carbonated metasomatic rock from Aja Rossa area. Note that carbonate cracks open in the diopside + lawsonite domain (delimited by the dashed red line). **e)** Banded carbonated metasomatic rock from the shear zone in Punta Favalta area (sample 1cor14-6a). The dashed red line marks the compositional banding. **f)** Jadeite-bearing carbonated metasomatic rock from Mt Muffraje area (sample 1cor14-10g). Jadeite crystals are partially replaced by carbonate and phengite and embedded in a matrix composed by carbonate + quartz + phengite.

The paragneiss may contain inherited HT garnet as a main distinctive feature (Martin et al., 2011), whereas the orthogneiss commonly contain jadeite porphyroblasts.

The identification of a pre-Alpine protolith in extremely metasomatized rocks was done based on field relationships, e.g. transitional mineralogical variations statically overprinting pre-Alpine basement rocks, or by the identification of the above diagnostic minerals as relict phases.

5.2 Carbonated metasomatic rocks

5.2.1 Serpentinite-Mesozoic metasediments contacts (samples 1cor12-20d; cor13-28a,c; 1cor14-12b; 1cor14-2b,c).

Stage#2 carbonated metasomatic rocks (Piccoli et al. 2016) generally display a mm to cm-scale banded structure of alternating white carbonate-rich and pale-to-deep green silicate-rich layers (Figs. 5.3a3; 5.5c). The former dominantly contains Ca-carbonate, together with garnet and green-pleochroic clinopyroxene; the latter are partially to totally inherited from the precursor Stage#1 metasomatic rock (Table 5.1), and contain diopside and lawsonite, together with a variable amount of garnet, green amphibole, quartz, epidote (with allanitic core), pumpellyite and phengite representing both syn-Stage#2 and late phases. Whenever present, phengite and amphibole preferred orientation marks the regional foliation. The boundaries between the two types of compositional layers range from sharp to embayed in response to different degrees of interaction between the carbonates and the silicates (Piccoli et al., 2016). Crystal size ranges from μm to mm. Carbonaceous materials is locally found in both compositional domains. Carbonate is found as both *calcite* and fresh *aragonite*, the latter preserved as inclusions in garnet (Piccoli et al., 2016). Ca-carbonate most commonly forms pseudo-hexagonal rods oriented at high angle to the main rock fabric. *Clinopyroxene* is a common phase in both the carbonate-rich and silicate-rich portions of the rock, and is

commonly present in multiple generations resulting from the successive stages of metasomatism (Stage#1 and Stage#2, see also next section for compositional features). In samples 1cor12-20d and 1cor14-12b, clinopyroxene crystals form either stubby neoblasts or fibrous aggregates (Fig. 5.6c), both sub-mm in size, and with pale- to deep-green pleochroism. Fibrous aggregates have embayed rims when in contact with the carbonate matrix. In sample 1cor12-20d, clinopyroxene crystals display a marked optical zoning between core and rim. The core, inherited from Stage#1 metasomatism, is pale green and commonly exhibits extensive corrosion and replacement by Ca-carbonate (Figs. 5.6c, 5.7a), whereas the rim- the stable clinopyroxene of Stage#2 metasomatism- is green pleochroic (omphacite) and is in textural equilibrium with the matrix carbonate (Fig. 5.6c). *Garnet* has different habits, from euhedral to poikilitic and skeletal, and shows strong and variable compositional zonation even by optical microscopy (Figs. 5.6d,e). Poikilitic garnet contains dominant aragonite/calcite, clinopyroxene, epidote, carbonaceous material, chlorite, and quartz inclusions. In sample 1cor12-20d and cor13-28c, large garnet crystals may show optical zoning with pink core and colorless rim. In other samples, garnet may display sigmoidal or concentric zoning (Figs. 5.6d,e) with colorless core and pink rim. BSE imaging revealed that the garnet compositional zoning can be complex, as it is shown in Figures 5.7e-h. In Figure 5.7e-f, poikilitic garnet with quartz and carbonate inclusions clearly shows a compositional zoning that varies as a function of the nature of the included mineralogy: garnet around carbonate inclusions is dark grey and has lower Mn content, whereas garnet around quartz inclusions is light grey because of higher Mn content. Figure 5.7g-h show similar zoning in skeletal garnet: when garnet is in contact with Stage#2 clinopyroxene it has lower Mn and higher Ca and Fe. Bright garnet is preserved far from the inclusions (Fig. 5.7g).

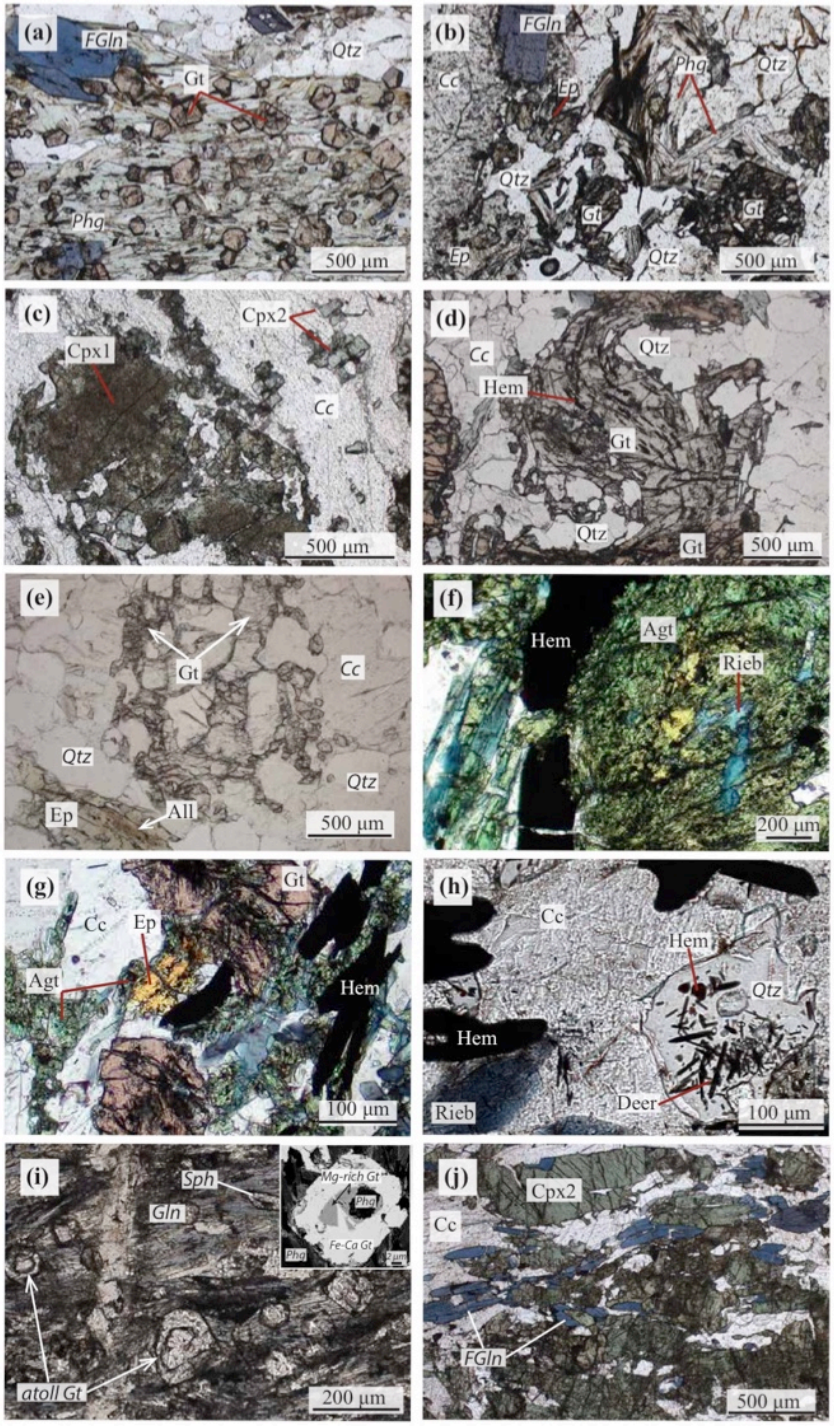

Fig. 5.6: Thin section photomicrographs depicting the microstructural characteristics of both unaltered and metasomatic rock. **a)** Garnet + phengite level in metachert (sample cor16-42d). **b)** Quartz-carbonate-rich metasediment (sample 1cor12-20c). **c)** Microstructural relationship between two clinopyroxene generations and carbonate (sample 1cor12-20d). Note that Cpx2 forms euhedral crystals in textural equilibrium with carbonate. **d)** Snowball garnet with sigmoidal-shape zoning (sample 1cor14-2). **e)** Garnet with sieve texture and optical concentric zoning (sample 1cor14-2). Note the textural equilibrium between epidote and quartz. **f)** Blue amphibole being replaced by aegirinc clinopyroxene in the deerite-bearing sample (sample 1cor14-6a). **g)** Epidote being rimmed and replaced by clinopyroxene (sample 1cor14-6a). Hematite is found as large prismatic crystals. **h)** Quartz grain with hematite and deerite inclusions (sample 1cor14-6a). **i)** Atoll-like garnet in sample 1cor14-10d together with BSE image showing chemical zoning. The dark zone is Mg rich and is a remnant of pre-Alpine HT metamorphism. (Martin et al., 2011) **j)** Clinopyroxene and ferroglaucophane in metasomatic marble overlying the continental crust (sample cor13-21b).

Lawsonite is found as either large (100-500 μm, Lws1), locally inclusion-rich prophyroclasts (with inclusions of mainly quartz, titanite, rutile and carbonaceaous material) or smaller (<50 μm in size), inclusion-free euhedral crystals (Lws2). In some samples, clinopyroxene is not present and the dominant silicate phase is green amphibole. Pumpellyite locally replaces Lws1, either rimming or totally replacing the lawsonite porphyroclasts, and is interpreted as a late stage retrograde phase (sample cor13-28c, Table 5.1). All together, the microstructural relationships suggest that the Stage#1 paragenesis clinopyroxene1 (Cpx1) + lawsonite1 (Lws1) is replaced by the Stage#2 paragenesis composed by carbonate + clinopyroxene2 (Cpx2) ± garnet ± lawsonite2 (Lws2) ± blue amphibole.

Metasomatic rocks from the Punta Favalta outcrop (sample 1cor14-6a) display some remarkable features compared to other samples in the same structural positon. The rock is characterized by a banded structure with domains of quartz + blue amphibole + hematite + deerite, and domains of carbonate + clinopyroxene + garnet + hematite + deerite with relicts of blue amphibole and epidote (Fig. 5.5e). In the quartz-rich domains, *blue amphibole* is found as large (500μm long), deep blue pleochroic, crystals oriented parallel to the rock foliation. Conversely, in clinopyroxene rich-layers, blue amphibole is only locally found as a relict phase being replaced by clinopyroxene (Fig. 5.6f). *Epidote* is found as large prismatic crystals with yellow pleochroism, oriented parallel to the rock foliation. Locally it is pseudomorphycally replaced by garnet or rimmed by clinopyroxene (Fig. 5.6g). In the clinopyroxene-rich domains, *clinopyroxene* occurs as prismatic to acicular crystals with deep green pleochroism, oriented parallel to the rock foliation. *Garnet* is found as large (mm in size) crystals, inclusions-rich with dominant clinopyroxene, carbonate, hematite, blue amphibole and epidote inclusions. *Ca-carbonate* forms equigranular, polygonal aggregates. Locally, elongated carbonate crystals are oriented at high angle to the rock foliation. Fresh aragonite was found as inclusion in hematite. *Hematite* occurs as large (500μm long) crystals

in all compositional domains and as tiny acicular crystals as inclusions in garnet, quartz, and carbonate (Figs. 5.6f, g). Furthermore, *deerite* is quite abundant and occurs as inclusions in both quartz (together with hematite) and calcite (Fig. 5.6h). It is worth noting that the assemblage quartz + deerite + hematite has been widely reported in quartzite and metacherts from many localities of Alpine Corsica (Vernié et al., 1986). The microstructural relationships in clinopyroxene-rich layers suggest that epidote and blue amphibole are destabilized to form the peak paragenenesis composed by aragonite + clinopyroxene + garnet + hematite + quartz + deerite (Figs. 5.6f, h).

5.2.2 Serpentinite-continental crust (samples cor13-22a,c,d; 1cor14-10d,g)

Samples of Stage#1 and Stage#2 metasomatic rocks were collected in the Monte Muffraje area (Fig. 5.2a). Carbonated metasomatic rocks forming at the expense of Stage#1 rocks display mm-banded fabric defined by the alternation of carbonate-rich and silicate-rich domains, the latter ones forming either continuous layers or isolated patches with thicknesses ranging from 50μm to 5mm (Fig. 4 in Piccoli et al. 2016). Silicate layers are mainly composed by Stage#1 clinopyroxene, ± lawsonite (Lws1), and ± quartz. Grain size ranges from μm to mm. *Carbonate* (calcite after aragonite) displays prismatic habit, with elongation axes oriented at a high angle to the main rock fabric, and it grew either with crack-seal texture or as pods within silicate-rich domains resulting in corrosion-like textures. Two *clinopyroxene* generations can be recognized by their different color in plane-polarized light and on the basis of microstructural evidence. The first generation of clinopyroxene (Cpx1), characteristic of Stage#1 metasomatism, comprises acicular crystals forming mm- fan-shape aggregates. Cpx1 aggregates typically display embayed margins filled by carbonate. Remnants of single clinopyroxene fibers occur within the carbonate crystals (Fig. 5.7b). The crystallographic orientation of these remnants relative to the larger aggregates indicates that

they formerly belonged to a single crystal. A second generation of clinopyroxene (Cpx2), characteristic of Stage#2 metasomatism, crystallized around Cpx1 (Fig. 5.7b) and is also present as isolated crystals in the carbonate domains. *Lawsonite* (Lws1) in metasomatic carbonated metasomatic rocks is found as large, inclusion-rich crystals (with dominant quartz, titanite, and rutile inclusions), whereas lawsonite in veins is inclusion free (Lws2, see also Section 5.2.4-3). *Garnet* is present in both carbonate and silicate rich domains with euhedral to sub-euhedral habit. Poikiloblastic garnet includes dominant quartz, titanite, carbonate (calcite/aragonite) and lawsonite. Garnet also forms veins and pods together with carbonate. When present, *quartz* is granoblastic and forms lens-shaped domains or it rims clinopyroxene aggregates together with garnet. Quartz can be either coeval with respect to carbonate and garnet (suggested by quartz rimming clinopyroxene together with garnet) or related to the retrograde evolution. Phengite is found as a late product crystallizing in fractures parallel to the rock foliation, thus suggesting that it is interpreted as late stage. Altogether, the microstructural relations suggest that a first paragenesis Cpx1 + Lws1 is replaced by a second paragenesis: aragonite + Cpx2 + garnet ± quartz. The metasomatic overprint in this outcrop is pervasive, and the definition of a protolith rock is not obvious. Nevertheless, two samples preserve features suggesting that this metasomatic rind formed at the expense of continental basement rocks. Sample (1cor14-10d) collected within the metasomatic rind appears unaffected by the typical patterns of Stage#1 or Stage#2 metasomatism, and is composed by blue amphibole, phengite, lawsonite and garnet. In this sample, garnet preserves a Mg-Fe core typical of the pre-Alpine HT paragneiss forming the continental basement slices (Martin et al., 2011), and overgrown by higher Ca-Fe component representative of the Alpine metamorphism (Fig. 5.6i; Table 5.3). Sample 1cor14-10g likely escaped Stage#1 metasomatism, but displays large evidence of Stage#2 carbonate metasomatism.

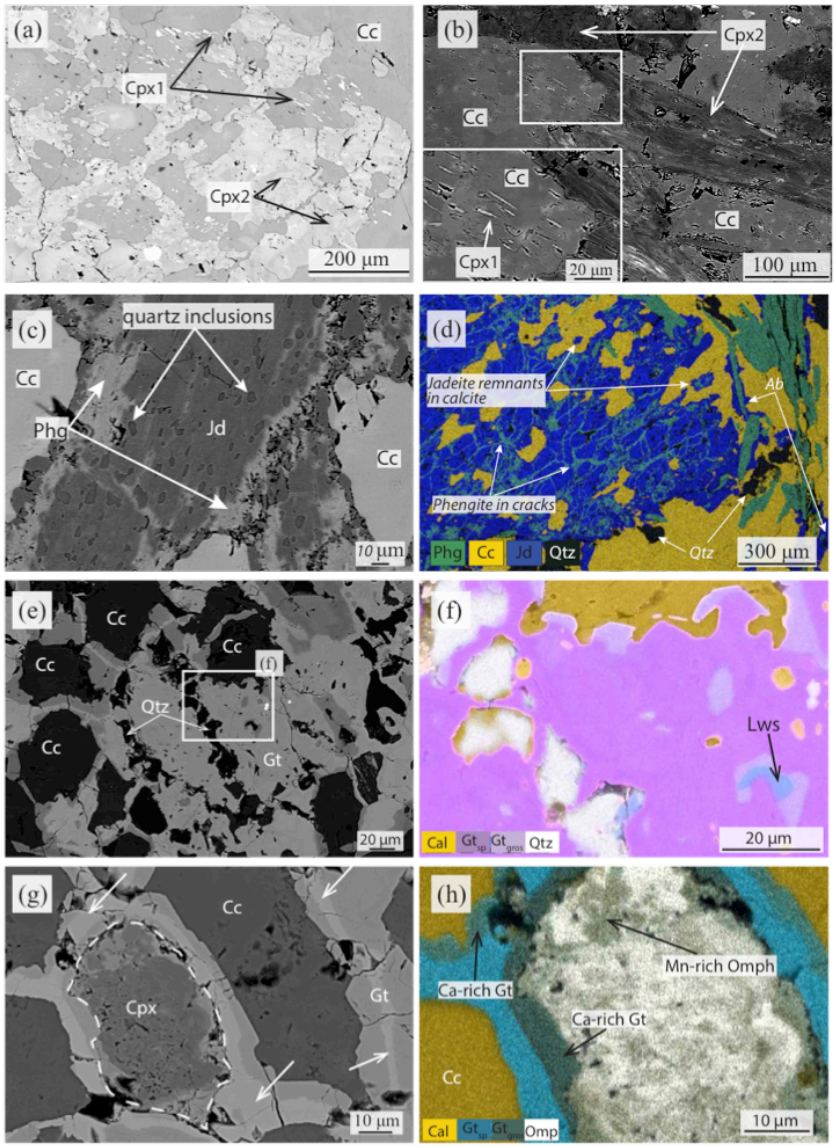

Fig. 5.7: Backscattered electron (BSE) images and EDX maps obtained by SEM depicting microstructural evidences of bulk composition changes during metasomatic events. **a)** BSE image of a skeletric clinopyroxene in sample 1cor12-20d. The image well shows the oriented remnants of Cpx1 preserved in calcite crystals, thus suggesting dissolution of Cpx1 and precipitation of carbonate + Cpx2. **b)** Fibrous clinopyroxene aggregate with embayed rims (sample cor13-22c). The small, aligned fragments preserved in carbonate crystal have Cpx1 composition. The microstructure suggests dissolution of Cpx1 and precipitation of carbonate + Cpx2. **c)** BSE image showing a detail of a jadeite clast with quartz inclusions, being replaced by carbonate and late stage phengite. **d)** EDX map of jadeite clast replaced by carbonate and phengite (sample 1cor14-10g). Some remnants of jadeite are preserved in the carbonate matrix. **e)** BSE image of complex chemical zonation in garnet (sample 1cor14-12b). Note that garnet around carbonate inclusion is dark grey, whereas it is bright gray when far from carbonate inclusions, or around quartz inclusions. The transition between chemical zones is sharp. **f)** EDX maps of garnet around quartz and carbonate inclusions. Chemical zoning is linked to different content in Mn and Ca. Garnet zones free of carbonate inclusions always have higher Mn content, whereas garnet around carbonate has higher Ca content. The former is interpreted as out of equilibrium composition, whereas Ca rich garnet crystallizes during the metasomatic stage. **g)** BSE image clinopyroxene and carbonate inclusion in garnet. Arrows indicate the high Mn content in garnet far from calcite inclusions. The preservation of the pre-metamorphism garnet shows the crystal failed in achieving the equilibrium with the matrix. **h)** EDX maps of clinopyroxene in garnet showing garnet compositional changes associated with mineral inclusions. Garnet in contact with clinopyroxene is Ca rich. Moreover, clinopyroxene has high Mn content suggesting that Mn is exchanged between garnet and clinopyroxene.

The rock has a prophyroclastic fabric defined by jadeite porphyroclasts wrapped by a foliated matrix mainly consisting of Ca-carbonate, phengite, and quartz (Fig. 5.5f). The jadeite clasts range from 100 to 500 μm in size. Some portions of the jadeite crystals contain tiny ameboidal quartz inclusions (Fig. 5.7c). This kind of microstructure is commonly described in jadeite-bearing rocks formed by metamorphic conversion of former albite following the prograde reaction albite = jadeite + quartz (Compagnoni et al., 2012), and also occurs in the jadeite-bearing orthgneiss of the studied unit. The jadeite clasts are partially replaced by Ca-carbonate and late phengite, crystallizing along fractures (Fig. 5.7c,d), following the same microstructural patterns of carbonation observed for diopside in Stage#1 rocks (Fig. 5a in Piccoli et al., 2016). Ca-carbonate is the main constituent of the matrix, found as coarse-grained granoblasts. Granoblastic quartz forms lens-shaped domains. Late albite rims the margins of jadeite clast and jadeite remnants in the carbonate matrix together with phengite. The presence of jadeite-bearing orthogneiss in the same area (west of Punta Caldane; Vitale Brovarone et al., 2011a) and the recognition of former pre-Alpine paragneiss in the metasomatic rind (this study), make us propose that this sample originally was a granitic or leucocratic igneous rock, belonging to a slice of pre-Alpine continental basement, and successively carbonated during the HP fluid-rock evolution (see Section 8). These observations suggest that in the Monte Muffraje area, the lower part of the metasomatic rind develops at the expense of a slice of pre-Alpine continental basement. This continental slice is probably the lateral termination of the thicker continental sliver that crops out southern, in the area of Punta di Caldane.

5.2.3 Continental crust-Mesozoic metasediments (samples cor13-21b,c,d; cor13-27a,c,e)

The first few meters of the metasediments overlying the continental crust consist of a chaotic sequence of carbonated rocks with more or less stretched nodules of mafic/ultramafic composition, part of which showing clear evidence for HP carbonate-metasomatism (Fig. 5.3c1). Samples of mafic/ultramafic nodules embedded in a carbonate-rich layer display a continuous foliation marked by *chlorite* and *green amphibole*, while carbonate is interstitial. When present, *clinopyroxene* forms either small stubby neoblasts with deep green pleochroism or, more rarely, larger porphyroblasts with sharp optical zoning comprising brownish cores and deep green pleochroic rims (Fig. 5c in Piccoli et al., 2016). In the latter case, the two compositional zones have a sharp boundary. Green pleochroic clinopyroxene is also present as inclusion in amphibole crystals together with calcite. Therefore, two generations of clinopyroxene are distinguished: Cpx1 porphyroblast cores and Cpx2 rimming Cpx1 or forming smaller neoblasts. Based on the microstructural relationships, only Cpx2 is considered in equilibrium with the paragenesis green amphibole + chlorite + carbonate. *Blue amphibole*, *garnet* and *phengite* may also be present in some samples. Fresh *lawsonite* is absent.

Carbonate-quartz-rich rocks are also present within the chaotic carbonated mafic/ultramafic sequence. These rocks display mm-banded fabric of alternating carbonate-rich and silicate-rich domains (quartz, clinopyroxenes and blue amphibole, Fig. 5.3c3). A continuous schistosity (Passchier and Trouw, 2005) is marked by phengite, clinopyroxene, blue amphibole, and epidote preferred orientation. Grain size ranges from μm to mm. *Clinopyroxene* is found in sub-euhedral prismatic crystals, with deep green pleochroism. No optical zoning is observed in the clinopyroxene (Fig. 5.6j). *Garnet* is present in mm-sized crystals, colorless in thin section. Some samples display weakly zoned, inclusion-rich garnet

(with pink core and colorless rim) with dominant quartz, calcite/aragonite, phengite, and zircon inclusions. More retrogressed samples display idioblastic crystals of *blue amphibole* (mm in size), with a lavender-blue pleochroism. *Phengite* wraps around garnet porphyroblasts. *Epidote* is present in prismatic, colorless crystals, except for local brown allanitic cores. *Lawsonite* pseudomorphs may also be present. *Tourmaline* is an accessory mineral. Considering the more homogeneous mineralogy and the microstructural evidence, we propose that only one equilibrium paragenesis is present: carbonate + garnet + phengite ± clinopyroxene ± blue amphibole.

5.2.4 Vein material

Several types of veins are found in association with the carbonated metasomatic systems studied herein. In all vein types, the carbonate phase is always compositionally pure Ca-carbonate with a rod-shaped habit orientated at a high angle to the vein wall. The veins crack–seal texture suggests that the mechanism that the veining event is linked to fluid-overpressure and hydrofracturing (Ramsay, 1980). This is consistent with the observation of hydraulic breccias within the metasomatic rind and suggests brittle deformation during the fluid-rock interactions at HP conditions (Piccoli et al., 2016).

Carbonate veins (OF3597, cor13-17c, cor13-27c). This kind of vein is characterized by elongated carbonate crystals and small clasts of the wallrock inclusions (amphibole, chlorite, sphene, rutile, tourmaline and pyrite) aligned parallel to the vein wall (Fig. 5.8a), features typical of crack-seal (Ramsay, 1980). This kind of vein is not associated with a selvage in the wallrock. Clinopyroxene in the wallrock inclusions or in the wallrock itself lacks of an omphacite-rich rim. Carbonate-crack seals opening in mafic nodules (see section 5.2.3).

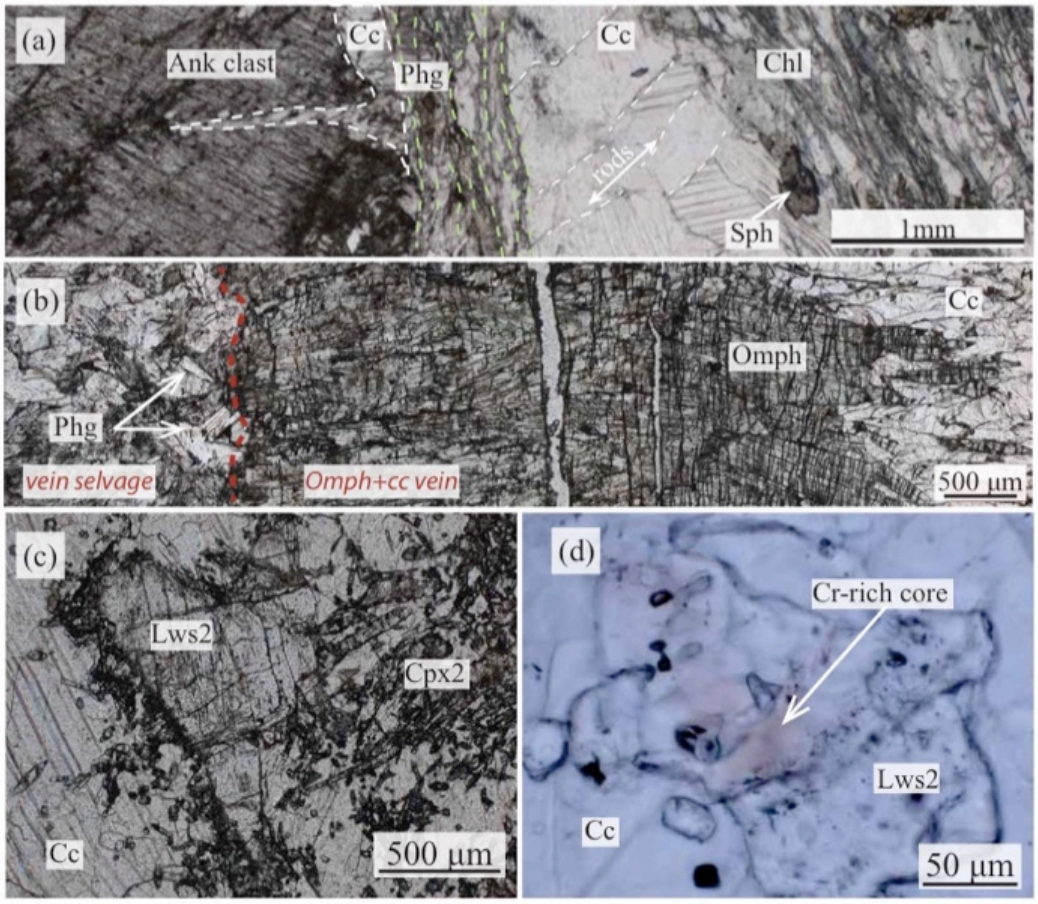

Fig. 5.8: Photomicrographs of vein materials. **a)** Carbonate crack-seal in mafic clast (sample cor13-27c). Vein carbonate is prismatic (rods are highlighted by dashed white lines) and oriented at high angle to the rock foliation, marked by chlorite preferred orientation. Ankerite porphyroclast is wrapped around by phengite (marked with dotted green lines). **b)** Omphacite + carbonate vein and vein selvage (sample 2cor14-3b). Omphacite crystals seed on the wallrock and are outgrown by calcite. Note the occurrence of well-crystallized phengite crystals in the vein selvage. **c)** Lawsonite + carbonate vein (sample 1cor14-RM). Small prismatic clinopyroxene crystals crystallize around lawsonite. **d)** Detail of lawsonite in a lawsonite + carbonate vein showing the optical zoning in lawsonite given by high Cr content.

This kind of vein was observed within the metasomatic rind along the serpentinite-Mesozoic metasediments contact and along the continental crust-metasediments contact.

Carbonate + omphacite veins (sample 2cor14-3b). Elongate blocky veins with smaller omphacite crystals seeded on the wallrock and outgrown by larger elongate calcite crystals (Figs. 5.3b3 and 5.8b). The observation of the growth competition indicates that crystals grew into a fluid-filled crack, with a crack-seal mechanism (Oliver and Bons, 2001 and referenced therein). This kind of vein displays a selvage, where the wallrock is enriched in phengite and

diopside displays omphacite rims. Phengite modal volume drastically decreases out of the selvage (Fig. 5.8b). Microstructures do not allow to establish if phengite is or not coeval to the carbonate precipitation in the vein. This kind of vein is found within the metasomatic halo along serpentinite-Mesozoic metasediments contacts.

Carbonate + *Lawsonite* ± *diopside* (samples cor13-29c and 1cor14-RM). As in the previous case, calcite crystals are elongated and parallel to the vein wall (Fig. 5.3b4). *Lawsonite* is present as poikilitic prophyroblasts together with quartz, graphite, and rare sphene and calcite inclusions, or as small (μm in size) inclusion-free crystals (Fig. 5.8c). Lawsonite is optically zoned with pinkish zones that correspond to high Cr content (Table 5.3; Fig. 5.8d). When present, clinopyroxene occurs in small (<100 μm) prismatic crystals, overgrowing lawsonite crystals (Fig. 5.8c). This kind of vein has been observed within the metasomatic rind along the serpentinite-Mesozoic metasediments and the serpentinite-continental crust contacts.

6. Mineral chemistry

Clinopyroxene. The compositional evolution of clinopyroxene displays common patterns in samples from different tectonostratigraphic position. Figure 5.9a shows jadeite-aegirine-QUAD ternary diagrams for clinopyroxenes in Stage#1 rocks (unaffected by Stage#2, sample 1cor12-11P) and Stage#2 the carbonated metasomatic rocks from the three types of tectonostratigraphic contacts (classification after Morimoto, 1989). In general, Stage#1 clinopyroxene compositions (in both Stage#1 rock unaffected by carbonate-metasomatism and relict Cpx1 in Stage#2 rocks) plot in the QUAD field and are diopside (CaO ~24 wt.%, MgO ~12 wt.%, FeO ~8 wt.%). Most Stage#2 zoned clinopyroxene crystals (Cpx2) from samples overlying serpentinites shows Na-Al enrichment with respect to the core (Cpx1), and have omphacitic composition. However, some samples have Na-Fe^{3+} enrichment in the rim,

and plot in the aegirine-augite field. Clinopyroxene in carbonate veins is omphacite, whereas in carbonate + lawsonite veins it is diopside. Clinopyroxene in carbonated metasomatic rocks formed at the expense of metasediments has high Mn content (up to ~2-3 wt.%, Table 5.3). Mn may be present in the core as well as in the newly crystallized omphacite (Fig. 5.7a and h, respectively). Chromium in clinopyroxene occurs in significant amounts only in two samples: cor13-21d and 1cor14-6a. In sample cor13-21d, Cpx1 has higher Cr content (~1 wt.%, Table 5.3) rather than in the rim, Cpx2 (~0.6%). The plausible ultramafic origin of this sample has been discussed in Piccoli et al. (2016) based on bulk-rock trace element analysis. In sample 1cor14-6a, clinopyroxene is zoned and Cr rich domains have Cr_2O_3 up to ~1 wt.%.

Garnet. Figure 5.9b reports the garnet composition for the carbonated metasomatic rocks in a grossular-almandine-spessartine ternary diagram; the pyrope content is always very low (X_{Mg} ranging from ~0 to 0.03). Garnet in samples along the serpentinite/metasediment contact is zoned. In some cases, (Fig. 5.9b) the rim corresponds to a sharp enrichment in the spessartine component (with X_{Sps} rising from ~21 to ~43%, X_{Alm} decreasing from ~53 to ~34%, and X_{Grs} remaining stable, see also sample 1cor12-20d in Table 5.3). Figure 5.9b also shows a electron microprobe map of garnet from sample 1cor12-20d: together with the increase in MnO, garnet rim also displays an oscillatory zoning in Cr_2O_3 (Cr_2O_3 up to ~0.15 wt.%). In this same sample, smaller, euhedral crystals have a more homogeneous composition (X_{Alm} ~25%, X_{Sps} ~36%, X_{Grs} ~39%). As discussed in the previous section, garnet in sample 1cor14-12b displays complex compositional zonation. Mn rich garnet preserved around quartz inclusions has an average composition of X_{Alm} ~20%, X_{Sps} ~60%, X_{Grs} ~20%, whereas Ca-richer garnet around calcite or clinopyroxene has average composition of X_{Alm} ~20%, X_{Sps} ~20%, X_{Grs} ~60%. Matrix garnet in carbonated metasomatic rocks formed at the expense of continental basement rocks (sample cor13-22a and cor13-22c) has a Fe-Mn rich composition (X_{Alm}

~20%, X_{Sps} ~49%, X_{Grs} ~31%), while anhedral crystals or garnet in veins is grossular rich (X_{Alm} ~2.5%, X_{Sps} ~1%, X_{Grs} ~96.5%). Garnet in samples overlying continental basement (cor13-21b and cor13-27e) are unzoned with X_{Sps} varying from one sample to another (Fig. 5.9b and Table 5.3).

Phengite. Potassium-rich white micas are phengites (Table 5.3), with Si content ranging between 3.5 and 3.6 atoms per formula unit (a.p.f.u.). All phengites have K around 1 a.p.f.u and quite homogenous Fe^{2+} and Mg content (~0.1 and ~0.5 a.p.f.u., respectively), with the exception of sample 1cor14-10g that has lower Fe-Mg content. Figure 5.9c shows phengite composition plotted on the Si vs. (Fe^{2+} + Mg) (a.p.f.u.) diagram. Only phengite in samples cor13-21b and 1cor14-10g approach the ideal Tschermak substitution, whereas the other samples plot above the ideal substitution line. The high Mg-Fe contents might results from a partial substitution of Al with Fe^{3+}, quite common in HP terranes (Miyashiro and Shido, 1984). In sample cor13-22c, phengite crystals in the matrix display a decrease in celadonite content, compared to phengite replacing clinopyroxene, suggesting a requilibration of the first one at lower P condition.

Amphibole. Carbonated metasomatic rocks formed at the top of continental basement contain abundant sodic amphibole with composition ranging from glaucophane to ferroglaucophane. Green amphibole in the chaotic mafic sequence is a calcic with tremolite composition (sample cor13-21d). Sodic amphibole formed in samples overlying serpentinite has composition ranging from riebeckite to Mg-riebeckite, whereas green amphibole is actinolite (Fig. 5.10, classification after Leake, 1997).

Epidote. Epidote composition is given using the ternary classification from Franz and Liebescher (2004). As Mn-bearing compositions are common, the ternary diagram was constructed with clinozoisite, epidote and piemontite endmembers. In sample 1cor12-20d, epidote has high Mn and Fe content (X_{Cz} ~0, X_{Ep} ~0.5 and X_{Pie} ~0.5; Table 5.3), but in some sample very high Mn epidote (X_{Pie} ~0.7) and piemontite (X_{Pie} ~1) are found (samples cor13-28c and 1cor14-5). In sample cor13-27e, epidote is Fe rich but Mn poor (X_{Cz} ~0.6, X_{Ep} ~0.4). Generally, epidote overgrowing lawsonite is related to retrograde evolution and has high clinozoisite content (X_{Cz} ranging from ~0.7 to ~0.9). In sample 1cor14-6a, epidote has high Cr_2O_3 content, up to ~2wt.%.

Lawsonite. Lawsonite in carbonated metasomatic rocks is close to pure composition. In some carbonate + lawsonite veins, it is Ti-rich (TiO_2 up to ~1 wt.%, Table 5.3) and/or Cr-rich (Cr_2O_3 up to ~3.25 wt.%, sample cor13-29, Table 5.3).

Carbonate. Carbonate is always compositionally pure calcium carbonate, with the only exception of iron-rich carbonate nodules found in carbonated ultramafic lithologies together with actinolite-chlorite-rich assemblages.

Deerite. Deerite is present only in sample 1cor14-6a. It is not pure and has considerable MnO (~2.4 wt.%), MgO (~2 wt.%), and TiO_2 (~0.8 wt.%), together with minor Cr_2O_3 (~0.5 wt.%) and Al_2O_3 (~0.2 wt.%).

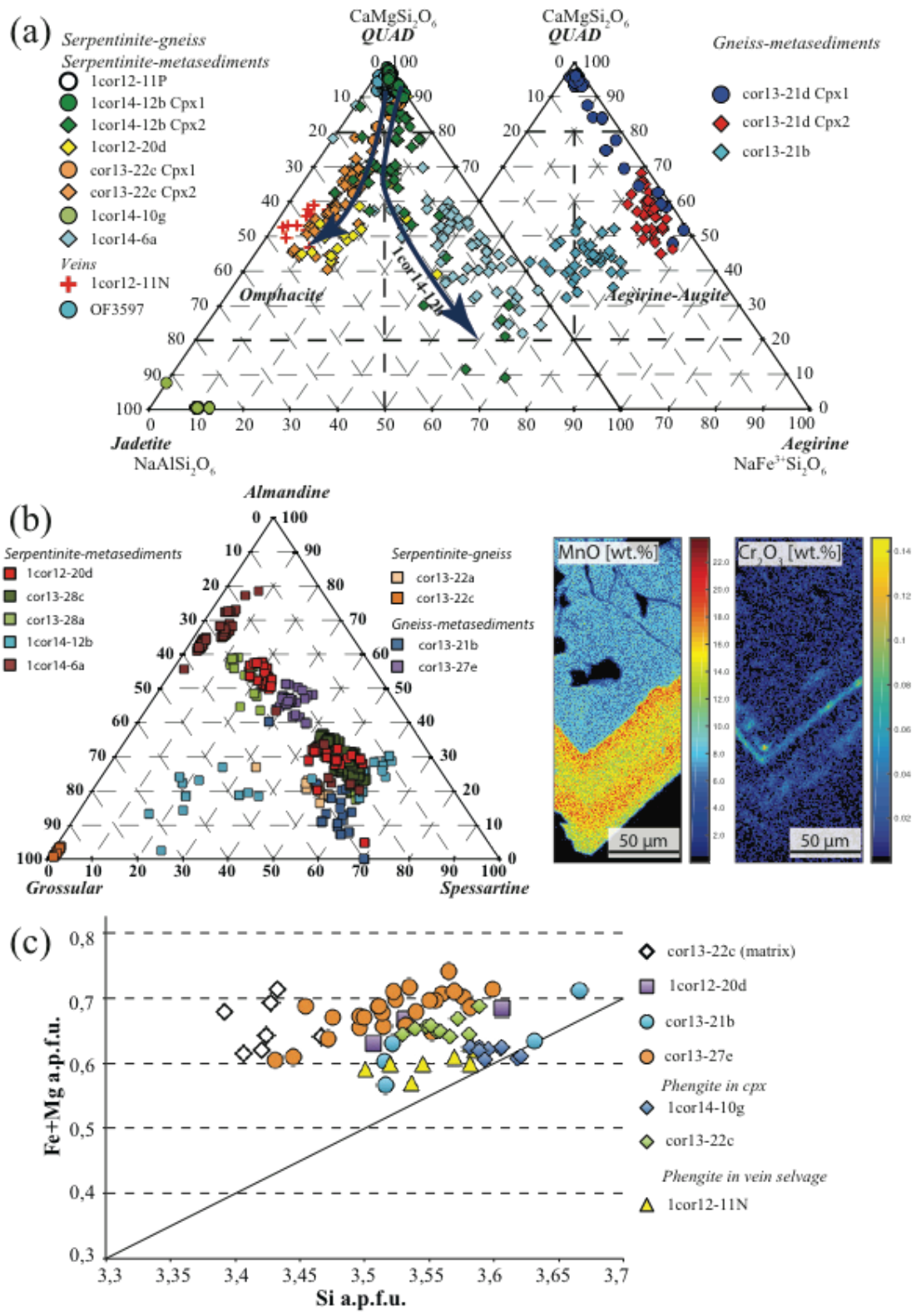

Fig. 5.9: Mineral chemistry. **a)** Ternary diagram for clinopyroxene compositions. For the each sample, Cpx1 and Cpx2 are reported with the same color, but different symbols (circle and diamond respectively). **b)** Ternary diagram for garnet compositions and electron microprobe map of garnet zoning. Optical zoning corresponds to Mn rich annulus in the rim. The microprobe maps highlight the occurrence of Mn zoning together with Cr oscillatory zoning in the rim (maps treatment with XMapTools software, Lanari et al., 2014). **c)** Phengite composition plotted on the Si vs. (Fe+Mg) diagram. The solid line represents the ideal celadonitic substitution. Si is given as atoms per formula units (a.p.f.u.) on the basis of 11 oxygens.

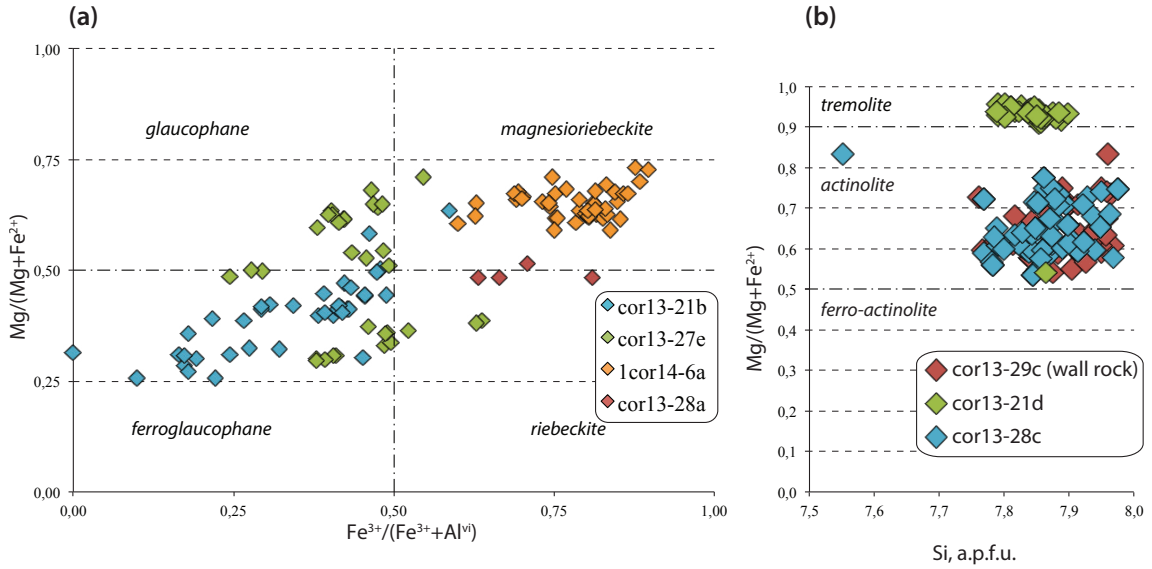

Fig. 5.10: Mineral chemistry. **a)** Classification diagram for sodic amphiboles; **b)** Classification diagram for calcic amphiboles. Classification after Leake (1997).

7. Petrogenetic grid calculation and P-T modeling

Owing to the compositional heterogeneities (mineral zoning, partial reequilibration) and the presence of multiple meta-stable parageneses in the studied carbonated metasomatic rocks, a pseudosection modeling approach based on bulk-rock compositions may not be appropriate for local phase relations (e.g., Stüwe, 1997; Guevara & Caddick, 2016). We therefore considered single or coupled reactions to solve local equilibria and better constrain P-T-fO_2 conditions of rock carbonation. Most of the samples contain mineral assemblages (e.g. diopside, Ca-carbonate, lawsonite) that may be stable over a large range of P-T conditions, and that provide little information for other parameters such as fO_2. Sample 1cor14-6a has a more suitable mineral assemblage from this perspective because it contains a more complex mineral assemblage, including fO_2-sensitive minerals such as hematite and deerite, and because mineral reactions can be deducted by microstructures. Reactions involving Fe-bearing, fO_2-sensitive minerals are also particularly useful for constraining T because they generally have very steep slopes on a P-T diagram. Moreover, in this sample, microstructures attest to carbonation via the replacement of epidote and amphibole by clinopyroxene, garnet and Ca-carbonate (see section 5.2.1), and therefore help constrain the X_{CO2} of the system. We

modeled the fO_2 buffer reactions *(1) hematite = magnetite* and *(2) deerite = quartz + hematite* in the FeO- Fe_2O_3-SiO_2 system. Reaction *(3) quartz + acmite + almandine + aragonite + hematite = epidote + riebeckite* was modeled in the Na_2O-Al_2O_3-CaO-FeO-Fe_2O_3-SiO_2 system.

Figure 5.11 shows the results of several calculations including P-T-f_{O2} grids for reactions *(1)* and *(2),* as well as P-T-X_{CO2} grids for reaction *(3)* (summarized in Fig. 5.11a). Moreover, we calculated P-X_{CO2} and T-X_{CO2} grids for reaction *(3)*, as well as a P/T-X_{CO2} grids calculated along a prograde, linear geothermal gradient for the lawsonite eclogite unit of Alpine Corsica (see section 4.2) as a function of X_{CO2} (Fig. 5.11b). By doing this, we assume that the mineral assemblage recorded the equilibrium with the fluid at specific P-T conditions along the prograde P-T path. The microstructural relationships described for sample 1cor14-6a suggest the co-stability of the assemblage deerite + quartz + hematite (Fig. 5.6g). The absence of magnetite gives a lower limit on the f_{O2} of the rock of $\log10^{-18}$ (ΔFQM = 3) at peak metamorphic conditions (2.3GPa and 520°C). Oxidized conditions are also indicated by the high Fe^{3+}content of clinopyroxene. Moreover, the widespread occurrence of hematite and deerite in carbonate domains and carbonate inclusions in hematite attest to the co-stability of carbonate with the f_{O2} sensitive minerals. Reaction *(3)* has a positive slope on a P-T diagram (Fig. 5.11a). The carbonated assemblage quartz + aragonite + almandine + acmite + hematite is stable on the high-T side of the curve, whereas riebeckite and epidote are stable on the high-P side. Figure 11b shows the P/T-X_{CO2} grid for the modeled reaction *(3)*. The reaction strongly depends on the fluid X_{CO2} and has a negative slope on this diagram; X_{CO2} decreases with increasing P-T conditions. The carbonated assemblage of the reaction is stable on the high-X_{CO2} side of the reaction. With increasing P-T conditions, if the fluid composition is internally buffered, it will evolve along the equilibrium toward very low X_{CO2} (brown arrow in Fig. 5.11b). However, in the case of an internally-buffered system, the amount of moles

produced by the reaction would be very small and cannot account for the observed carbonate modes in thin section (Table 5.2).

Three possible scenarios can be called upon to account for the observed large extent of reaction progress: (i) reaction occurred at a consolute point; (ii) reaction occurred at an invariant point; (iii) the system was buffered by the infiltration of an external fluid (externally buffered in Fig. 5.11b). The topology of the reaction shown in Figure 5.11a makes us exclude the first two cases because there is no consolute point, and because of the absence of zoisite in the sample (thus the system is not at the invariant point). By contrast, fluid infiltration would be a reasonable explanation considering that even a tiny deviation from the equilibrium can boost the reaction progress. This mechanism has been described in one-dimensional numerical models by Ague and Rye (1999) for advection-hydrodynamic dispersion-reaction.

Figure 5.11a shows the Corsica P-T trajectory together with P-T contours for a specific oxygen fugacity (reactions *(1)* and *(2)*) and fluid composition (X_{CO2} reaction *(3)*). Reaction *(3)* take place at specific P depending on the fluid X_{CO2}. Although high fO_2 should favor epidote stability (Poli and Schmidt, 2004), high CO_2 proportions in the fluid should counterbalance this effect (Poli et al., 2009). Figure 5.11a shows that increasing X_{CO2} depresses the epidote pressure stability. Thus, depending on fluid CO_2 content, the range of P at which the reaction occurred varies from a minimum of ca. 1.8 GPa up to peak metamorphic conditions and ca. 2.3GPa, with minimum fO_2 value of 10^{-20} (Δ FQM = 2) and maximum 10^{-18} (Δ FQM = 3). Reaction *(2)* occurs at higher P compared to the Corsica P-T path, consistent with the observation of the assemblage deerite + quartz + hematite in thin section.

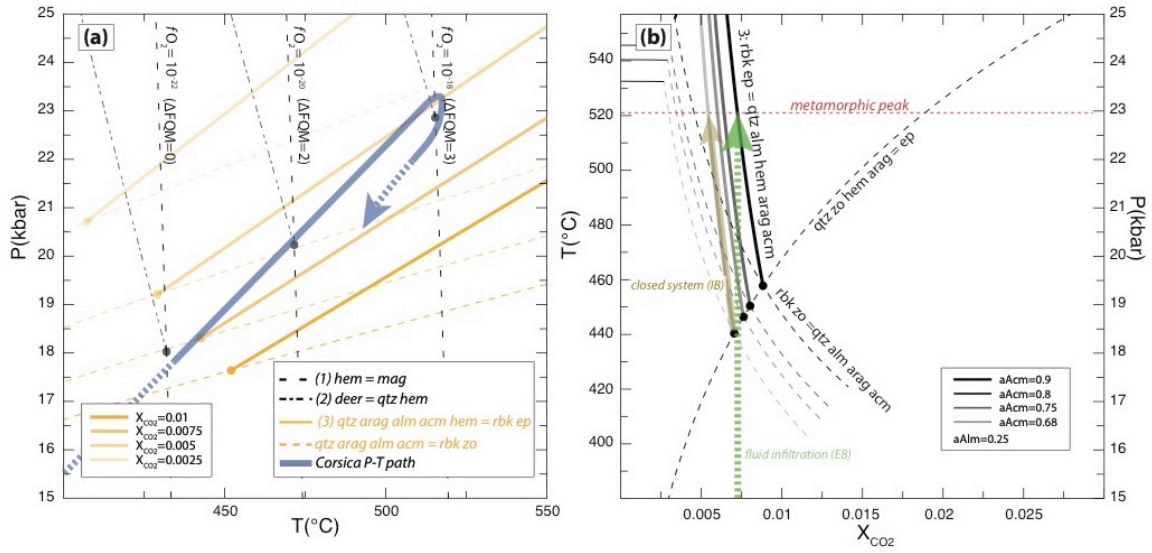

Fig. 5.11: **a)** P-T grid showing the Corsican P-T path together with the hematite-magnetite buffer for different fO_2 conditions and the carbonation reaction calculated for different fluid mole fraction of CO_2 (X_{CO2}). Reactions are written with the high temperature assemblage on the right of the = sign. **b)** PT-X_{CO2} grid for carbonation/decarbonation reactions. The different shades of grey represent reactions calculated for different acmite activity, each of them valid at one P-T point (here we report reactions at the following P-T points: 1.5GPa and 380°C, 1.8GPa and 430°C, 2GPa and 467°C, and 2.3GPa and 520°C). Acmite activity decreases with increasing P-T conditions. The arrows indicate the evolution of fluid composition in two opposite cases: internally buffered (IB, brown arrow) or, with externally buffered fluid composition (EB, green arrow). Reactions are written with the high temperature assemblage on the right of the = sign.

8. Discussion

Lithological boundaries, together with fracture sets or permeable layers, are structural features that facilitate fluid channelization (e.g. Oliver, 1996; Oliver and Bons, 2001; Zack and John, 2007; Ague, 2014; Bebout and Penniston-Dorland, 2016). The studied carbonated metasomatic rocks indicate that extensive fluid-rock interactions occurred along the main lithological boundaries of a subducted section of oceanic/transitional lithosphere that underwent lawsonite eclogite-facies conditions. Moreover, the multiple metasomatic products (Stage#1 and Stage#2) suggest that these interfaces acted as major fluid conduits for a protracted period of time, from prograde to peak and probably early exhumation stage.

Field, microstructural and geochemical data (Piccoli et al., 2016; this study) strongly indicate that carbonate minerals (mainly Ca-carbonate) were involved in these protracted fluid-mediated processes, including a strong reactivity between the silicate minerals in the rock and

the carbon-bearing fluids. The high lithological variability of the metasomatized suites provides a good means to assess: (i) the reactivity of different rock types to deep carbon-bearing fluids and rock carbonation; (ii) the fluid composition; and (iii) the fluid sources. In the following, we will firstly discuss the petrological and geochemical data to obtain a better understanding of the nature of the protolith rock. We will then discuss the P-T-fO_2 conditions of rock carbonation during HP metamorphism in the studied samples. Lastly, we will focus on the recognition of different mineral paragenesis and changes in mineral composition as proxies for fluid composition and sources to propose a model for fluid migration.

8.1 Protolith rocks

Deformation, metamorphism, and intense metasomatism in some cases make the identification of protolith rocks challenging, especially when the metasomatic rinds affected a laterally and vertically variable column of rocks including siliceous metasedimentary, mafic, ultramafic, and also felsic lithologies. The identification of mineral or compositional markers characteristic of specific protolith rocks is therefore fundamental to assess the petrological and geochemical evolution of these systems. This is particularly relevant in the case of metasomatized metasedimentary rocks, for which the distinction between carbonates that were already present in the rock before subduction and those formed by metasomatic processes in the subduction zone may be extremely challenging. The following sections discuss the main pieces of evidence allowing the identification of different protolith rocks affected by metasomatism and carbonation at HP conditions, with particular attention to carbonate-free protolith rocks.

8.1.1 Evidence for extreme transformation of Mn-metacherts

Mineral composition and microstructures may disclose important information on a rock's metamorphic evolution. For example, chemical zoning is a common feature in garnet that develops in response to changing P-T-X conditions (Kohn, 2014). Intracrystalline diffusion may be slow enough to preserve growth zoning (Ague and Carlson, 2013) and thus, prevent garnet from achieving chemical equilibrium with the matrix. The diffusion rate of garnet major components (Ca, Mg, Fe, and Mn) is relatively slow over a wide spectrum of subduction zone conditions. Garnet geochemical zoning is therefore particularly useful to recognize protolith rocks even in area where pervasive metasomatism erased all macroscopic evidences, as already done in the metasomatic rocks of Corsica (Martin et al., 2011, 2014).

In the field, incomplete metasomatic transformation and preservation of partially replaced Mn-metacherts is only locally found (Fig. 5.3a4) and characterized by the progressive overgrowth of primary Mn-rich garnet by metasomatic Ca-rich garnet. The latter generation is found as growth rims around Mn-rich cores, or as patchy compositional zones controlled by local equilibria between the primary and the metasomatic phases (see Fig. 5.7f,g,h). The local occurrence of annuli of high Mn near the rim may result from garnet resorption (Kohn and Spear, 2000). Alternatively, external fluid infiltration may add Mn to the system, or enhance the breakdown of Mn-rich phases such as epidote (Piemontite or Mn-rich epidote is very common in Alpine metacherts, e.g. sample 1cor14-5c; Young and Rivers, 2001) and the internal redistribution of Mn. The observed epidote breakdown reaction by external fluid infiltration in sample 1cor14-6a, and the presence of Mn-rich epidote (MnO up to ~22 wt.%) in some of the carbonated metasomatic rock samples (e.g. sample 1cor12-20d; cor13-28c) support the hypothesis of fluid infiltration. Moreover, in some cases the Mn enrichment in the garnet rim matches with Cr-oscillatory zoning. Cr zoning cannot be explained by the breakdown of an internal source (i.e., no Cr-bearing phase) and requires the infiltration of an

external fluid, likely derived from mafic/ultramafic rocks, which can mobilize Mn in the system. All together, these features indicate that Mn-rich garnet can be used as a marker for extremely metasomatized metacherts by both preservation of relict Mn-rich garnet core, or by fluid-mediated redistribution of Mn in the rock and growth of Mn-rich garnet rims.

An additional marker of carbonated metacherts may be the presence of Fe-rich, deerite-bearing assemblages, which are frequently described in metamorphosed metacherts from Alpine Corsica (Vernié et al., 1986) as well as other blueschist- (Franciscan, Alps, Turkey, the Aegean, and New Caledonia; Muir Wood, 1979) and eclogite-facies terrains (Tianshan, Zhang et al., 2017), otherwise rare in carbonate-bearing rocks. Generally, the formation of deerite has been considered to be restricted to Al poor, Fe-Mn rich metasediments like metachert (Vernié et al., 1986). The presence of Mn-rich garnet and the preservation of local quartz-deerite microdomains in some strongly carbonated rocks (e.g. sample 1cor14-6a; Fig. 6h) therefore support the hypothesis of intense fluid-mediated carbonation of Mn-Fe-rich metacherts.

8.1.2 Evidence for extreme transformation of mafic and felsic pre-Alpine basement

Two pieces of evidence allow identifying the pre-Alpine continental basement rocks as a protolith for some extremely metasomatized rocks. Martin et al. (2011, 2014) showed the preservation of pre-Alpine, Mg-Fe-rich HT garnet in Stage#1 metasomatic rocks is a marker of replacement of former mafic paragneiss. In our carbonated metasomatic rocks, no evidence for the preservation of pre-Alpine HT garnet was found. Nevertheless, this garnet relict was found in a lens of mafic schists within the metasomatic rind of Mt Muffraje, which escaped both Stage#1 and Stage#2 metasomatism (1cor14-10d, Fig. 5.6i). Secondly, from the same outcrop, extremely carbonated rocks (sample 1cor14-10g) contain relicts of jadeite porphyroclasts that likely formed by prograde transformation of large albite crystals, as

observed in orthogneiss unaffected by metasomatism in the San Petrone continental basement slices. This observation suggests that the continental crust slice in this area also contained jadeite-bearing orthogneiss. Alternatively, the presence of albitic feldspar later converted to jadeite in carbonate bearing rocks may be explained by an arkosic detrital component in the original sediment. Silicoclastic metasediments are found throughout the HP units of Alpine Corsica, known as the San Pietro di Tenda metasedimentary formation, where the presence of arkosic layers within basaltic effusions have been reported (e.g., Caron and Delcey, 1979; Caron et al., 1981; Péquignot et al., 1984; Lahondère, 1996). However, even if the origin of the rock remains unclear (metagranite or arkose), the microstructures show jadeite being replaced by carbonate (Fig. 5.7d), thus supporting the high reactivity, at HP conditions, between carbonate and clinopyroxene characteristic of metafelsic lithologies.

The above pieces of evidence indicate that in this area, HP fluid-mediated carbonation affected both mafic paragneiss and felsic orthogneiss belonging to a continental basement slice. Noticeably, the jadeite-bearing sample suggests that carbonation also occurred without a precursor Stage#1 diopside-lawsontie meytasomatic stage, and represents the first evidence for carbonation of felsic rocks during HP-LT metasomatism. This feature suggests that HP carbonation by infiltration of carbon-bearing aqueous fluids may be an important process for deep carbon sequestration in continental subduction and collisional settings.

8.1.3 Evidence for metasomatism and carbonation of ultramafic rocks

The serpentinitic basement of the San Petrone unit does not show significant metasomatic overprint, suggesting that either this lithology was not reactive or it was not infiltrated by fluids. In Punta Ventosa and Punta Caldane areas, chaotic sequences of ultramafic material embedded in carbonate matrix overlie the continental crust sliver and show evidence for HP metasomatism. These rocks were proven to have an ultramafic origin based on their

mineralogical assemblage (i.e. chlorite, actinolite, and minor clinopyroxene and ankerite) and based on whole rock signature (Piccoli et al., 2016). These rocks might represent the metasomatic transformation of metasedimentary breccia containing serpentinite clasts transformed into carbonate + chlorite + actinolite assemblages by infiltration of carbon-bearing fluids during Stage#2 metasomatism. Moreover, carbonate mobilization and precipitation is proved by the large abundance of carbonate veins and crack-seals in the ultramafic layers (Figs. 5.4f, 5.8a). Therefore, these rocks represent the evidence that when fluid infiltration occurs at HP conditions, ultramafic rocks are extremely reactive with carbon-bearing fluids.

8.2 Strong asymmetry of the metasomatic front

Rocks adjacent to major lithospheric lithological boundaries in the lawsonite-eclogite unit undergo a long history of metamorphic fluid-rock interactions during subduction metamorphism, that lead to at least to well distinguishable metasomatic events: Stage#1 and Stage#2. Metasomatic rinds can be followed over several km and they always appear to be strongly asymmetric. The Mesozoic metasedimentary rocks localize the metasomatism and carbonation when in contact with either the serpentinite or continental basement gneiss, whereas the gneissic rocks get preferentially metasomatized when in contact with the serpentinite. Nevertheless, carbonation of all the above rock types was found within the unit. For example, the transformation of ultramafic material embedded in metasomatized metasedimentary rocks indicates that also serpentinites are suitable to experience HP carbonation (Section 8.1.3), and confirms observations in other HP systems (Scambelluri et al. 2016). Moreover, the observed carbonation of both mafic and felsic material of continental origin above serpentinites indicates that these lithologies were suitable for HP carbonation under specific circumstances (Section 8.1.2). These features suggest that the

asymmetry of the metasomatic rinds along single lithological contacts was most likely due to permeability rather than lithological factors. The existence of permeability contrasts between two adjacent lithologies has the effect of diverting the fluid flow toward higher permeability region, leading to asymmetrical distribution of reaction progress (Ague, 2007). In our specific case studies, it is reasonable to believe that the serpentinite was less permeable than the overlying metasedimentary or gneissic rocks. Likewise, the metasedimentary rocks were probable more permeable than the slices of gneissic continental basement, consistently with other studies on metamorphic fluid fluxes (i.e. Rye et al., 1976; Chamberlain and Conrad, 1991; Yardley and Lloyd, 1995; Skelton et al., 1995). The superposition of multiple metasomatic events (Stage#1, Stage#2) may have further enhanced this pre-existing permeability contrast. These considerations make us propose the existence of a gradient in the fluid fluxes, driven by permeability contrast, responsible for the formation of strongly asymmetric metasomatic rinds (Fig. 5.12c,d). These permeability contrasts also probably controlled the channelization at the scale of the unit, with high fluid fluxes focused along major lithological boundaries. Extremely channelized fluid flow is also consistent with the lack of pervasive isotopic homogenization at the scale of the Corsican metaophiolite (Miller et al., 2001). Furthermore, our data indicate that strong fluid percolation and metasomatism were mainly localized at the base of the original basal unconformity of the subducted metasedimentary pile, and only affected the thinnest portions of the continental basement slices where the permeability was likely higher compared to thick gneissic bodies.

8.3 P-T-fO2 condition for high-pressure carbonation

Carbon mobility in metamorphic fluids has long been a topic of interest and rock carbonation by the infiltration of carbon-bearing fluids has been reported in different geological settings for both subduction zones (e.g., Nishiyama, 1990) and regional metamorphism (e.g., Skelton

et al., 1997). In both cases, rock carbonation occurs in greenschist facies conditions. Carbonation of HP-LT mineral assemblages like glaucophane, clinopyroxene and olivine has been reported, in different tectonic settings and occurring in different lithologies (Kleine et al., 2014, Piccoli et al. 2016, Scambelluri et al. 2016). Kleine and co-workers describe glaucophane carbonation along a shear zone juxtaposing garnet-mica quartzite with metabasite. Moreover, they report that carbonate replacing HP minerals is usually pure calcite, whereas late-stage carbonate veins have dolomitic composition. They observed carbonation being more extensive closer to shear zones acting as conduits for CO_2 bearing fluids. In the Ligurian Voltri Massif, Scambelluri et al. (2016) reported the presence of carbonated-ultramafic rocks which origin is ascribed to fluid-rock interactions during HP metamorphism. The authors report carbonate + olivine veins and carbonation affecting metamorphic olivine and diopside together with the precipitation of metasomatic dolomite. They estimate that the carbonation occurred at P ranging between 2 and 2.5GPa and T between 500 and 600°C. In our case study, the P-T conditions for metasomatism and carbonation are deduced by the stability of typical HP phases such as omphacite and aragonite and their isotopic equilibrium T (494°C ± 30°C, Piccoli et al., 2016) and modeled carbonation of epidote + amphibole assemblages (1.8 - 2.3GPa, Fig. 5.11a). These values are in good agreement with the Voltri Massif case (Scambelluri et al., 2016). Moreover, the modeled reactions indicate that rock carbonation occurred at oxidizing condition (i.e. in the hematite stability field; ΔFQM = 3 at 520°C and 2.3GPa) through the infiltration of external fluids. This observation is consistent with theoretical and experimental works that predict increasing carbonate stability with increasing P-T condition in a HM-buffered system (Molina and Poli, 2000; Poli et al., 2009). Serpentinites are otherwise known to be more reduced systems, and predicted to become progressively more reduced and to produce oxidizing fluids during prograde antigorite breakdown (Debret et al., 2014; 2017 in press).

However, the interaction of these deep oxidized fluids with serpentinites at lower P-T conditions may create suitable conditions for carbonation of serpentinites.

8.4 Fluid sources

Evidence of reactive fluid flow are, for example, multiple veining events with associated wallrock selvages and mineral chemical zoning. Moreover, the geochemical characteristics of this fluid-induced alteration might be used to infer fluid composition and sources. The data permit us to identify a series of characteristic geochemical patterns of HP carbonation in Alpine Corsica, such as changes in mineral compositions. In this section we discuss the main identified fluid tracers, namely Ca, C, Na (±K), and Cr, as well as the available C and O stable isotope signatures of these rocks. In the next section, we will combine the inferred fluid sources to propose a model for the origin and evolution of these fluids and their migration pathways.

The most striking characteristic of the Corsica carbonated metasomatic rocks is the very high whole rock Ca and C gain. Ca enrichment in silicates is characteristic of Stage#1 metasomatism, for which fluid sources such as mafic, ultramafic and sedimentary rocks was proposed (Martin et al., 2011; Vitale Brovarone et al., 2014b). Although such Ca enrichment in silicates is also locally observed during Stage#2, most Ca gain of the latter stage appears to happen through carbonate precipitation and silicate replacement, thus implying a combined supply of Ca and C. This feature cannot be exclusively explained by the infiltration of fluids derived from mafic/ultramafic reservoirs, and suggests the contribution of carbonate-bearing metasediments as plausible source for the Ca-C component of the infiltrating fluid. Processes of Ca-carbonate dissolution in aqueous fluids are expected to release fluids with 1:1 molar $Ca:CO_2$ ratios (Ague and Nicolescu, 2014) that would easily explain the reprecipitation of Ca-carbonate rich assemblages (Piccoli et al., 2016). Frezzotti et al. (2011) show that during

oceanic subduction at UHP conditions, the subducting rocks are infiltrated by carbon-bearing fluid enriched in Ca-Mg-Mn-Fe components after carbonate dissolution. Moreover, they report the occurrence of Mg-bearing carbonates and diamond as solid inclusions, thus showing that trapped fluids can reach carbon saturation at UHP conditions and precipitation of carbonates other than Ca-carbonate.

Na (±K) is also characteristic of Stage#2 metasomatic fluids. The Ca-precipitation is in most cases accompanied by the formation of Na-rich clinopyroxene (Cpx2) compared to the precursor Ca-Mg-rich clinopyroxene (Cpx1), such as omphacite (Na-Al) or aegirine (Na-Fe^{3+}) depending on the nature of the protolith lithology. Considering the very low Na content in Stage#1 metasomatic rocks because of mass loss (-80%, Vitale Brovarone et al., 2014b), this suggests that Na was added again to the systems during carbonate metasomatism by the infiltrating fluid, as also suggested by the presence of carbonate-omphacite veins (Fig. 5.3b3). Moreover, omphacite (± phengite) forms in Stage#2 carbonate veins, thus providing a robust constrain on the circulation of Na-(±K)-C-Ca-bearing fluids. Na mass gain during HP metasomatism is widely reported in different geological settings (Beinlich et al., 2010; Spandler and Hermann, 2006; Galvez et al., 2013; Ague and Nicolescu, 2014; Taetz et al., 2016). Water-rich alkalis- and carbon-bearing fluids are documented by fluid inclusion studies in eclogite-facies oceanic suites. Philippot and Selverstone (1991) reported the occurrence of aqueous brines enriched in CO_3^-, Ca, Na, K, Ca, Fe, Si and Al species in fluid inclusions hosted in omphacite from eclogitic veins (Monviso, Western Alps). Selverstone et al. (1992) report fluid variability in 2 GPa banded eclogite from a sequence of ophiolitic rock and shelf sediments in the Tauren Window (Austria). Their model shows the existence of different saturated saline brines, carbonic fluids, or immiscible pairs of both in different layers of the banded eclogite. In both studies, calcite is a common daughter mineral in the fluid inclusions.

Chromium oscillatory zoning in Stage#2 minerals such as garnet and lawsonite provides additional information on the origin of the infiltrating fluid. Cr-bearing minerals in veins (samples cor13-29c, 1cor14-RM) are a robust proof of the presence of this element in the circulating fluids at HP conditions. High Cr contents and oscillatory zoning in eclogite-facies fluid-mediated rocks such as veins has been reported in several settings including Stage#1 metasomatic rocks from the studied unit, and generally interpreted as tracer of serpentinite-derived fluids (e.g. Tsujimori et al., 2006; Spandler et al., 2011; Tsujimori & Ernst, 2014; Angiboust et al., 2014; Vitale Brovarone et al., 2014JMG). Experimental studies consider Cr as fluid immobile (Kosigo et al., 1997; Green and Adam, 2003). Nevertheless, in case of advective flow and high fluid fluxes (in the order of 10^6 m^3_{fluid}/m^2_{rock}) even elements generally considered immobile like Ti can be mobilized (Ague, 2014). Other possibilities are local mobility by diffusion (Rubatto and Hermann, 2003) or scavenging. Considering the very low Cr content in the host rock, the occurrence of Cr-rich lawsonite in veins, and Cr oscillatory zoning is garnet, we consider this hypothesis unlikely.

The participation of ultramafic rocks to the signature of the HP fluids responsible for carbonation is therefore the most plausible one for the origin of Cr enrichment. Such a hypothesis also agrees with the oxygen stable isotopes of these rocks, indicating a light $\delta^{18}O$ (~10‰ vs. SMOW) reservoir such as serpentinites for the dominant aqueous component of the infiltrating fluid (Piccoli et al., 2016). Subducted serpentinites are a well-established source of aqueous fluids (e.g., Ulmer and Trommsdorff, 1995; Rupke et al., 2004). Scambelluri et al. (1997) after the observation of high salinity fluid inclusions in eclogitized hydrous peridotite (Erro-Tobbio peridotite, Western Alps). Such a fluid can account for the observed Na enrichment, but it cannot alone account for the observed Ca and C gain. Alternatively, possible sources of Na and Ca are metasediments and altered metamafic crust like metabasalts. Water-rich fluids released from lawsonite breakdown in altered metabasalts

would have light $\delta^{18}O$ signature and would spawn carbonate devolatilization and/or dissolution in the oceanic crust and/or in the metasedimentary pile. The carbon stable isotope signature of the Corsican carbonated metasomatic rocks is consistent with recycling of subducted marine carbonate (Piccoli et al., 2016), but does not allow discriminating between metasedimentary or metamafic origin. Altogether, the here reported data point to multiple fluid sources including ultramafic, mafic and metasedimentary lithologies.

8.5 *Fluid evolution migration pathways*

The aqueous nature of the infiltrating fluid (see section 7), together with the dominant low O isotopic signature of the reacted rocks points to ultramafic/mafic rocks (serpentinite and metabasites) as the main source of fluid. However, major dehydration reactions in hydrated ultramafic systems are not predicted at the P-T conditions of the San Petrone unit (~500°C and 2GPa), with the exception of the partial antigorite breakdown in the presence of brucite (Ulmer and Trommsdorff, 1995; Kerrick and Connolly, 2001; Gorman et al., 2006). More significant dehydration reactions in these systems are expected to take place at higher metamorphic conditions, in the range of 700°C and 3GPa (Fig. 5.12).

Several authors have already proposed that deep fluids generated at these depths can migrate along the plate boundary and cause metasomatism at lower P conditions (e.g., Bebout and Barton, 1993; Herms et al., 2012; Angiboust et al., 2014). This petrographic study points out that only a complex geochemical evolution of the fluid by reactive flow can account for the observed geochemical features. We propose that at least some of the fluids released by serpentinite dehydration (and/or lawsonite breakdown) at depths of ca. 100km can migrate parallel to the slab (Fig. 5.12a). Such a conceptual model is also supported by thermo-mechanical, numerical models (Faccenda et al. 2014; Wilson et al., 2014). In our case, fluid release would happen ~30-40km deeper than the estimated conditions for metasomatism and

carbonation in the study unit (Fig. 5.12a,b). Compared to analogue models in mélange-type plate interfaces (Bebout and Barton, 1989; Bebout and Barton, 1993; Bebout and Penniston-Dorland, 2016), our study points to two important conclusions. Firstly, the structural localization of metasomatism along the basal unconformity of the subducted metasedimentary pile suggests an important role exerted by major inherited lithospheric lithological discontinuities for the channelization and upward migration of these deep fluids. This does not contradict the possible equivalent role played by the plate interface, but suggests that major fluid migration pathways can be channelized at different levels within the subducting slab. Secondly, the proposed multiple fluid sources permit proposing an updated model for the evolution of deep fluids along these major fluid pathways by reactive fluid-flow. Figure 5.12 summarizes the main stages of fluid release and fluid-rock interactions bearing on the origin of HP carbonation in the units of Alpine Corsica. Lawsonite and antigorite breakdown releases large amounts of aqueous fluids with light $\delta^{18}O$ signatures ("1" in Fig. 5.12a) and characteristic mantle tracers such as Cr. These fluids move upwards within the subducted mantle lithosphere and are then channelized along the basal unconformity of the metasedimentary pile (*"2"* Fig. 5.12a,c). The channelized fluid migration, parallel to the slab and along a down-T, down-P geothermal gradient as well as along lithological contrasts gives the necessary chemical potential for reactive fluid flow. At the P-T condition of antigorite dehydration (ca. 650°-700° and 3GPa), water-rich fluid that infiltrates metasediments can dissolve carbonates owing to the high carbonate solubility at those conditions (*"2"* in Fig. 5.12b,c). Alkalis, notably Na, may also be plausibly leached from the pelitic component of metasediments. Successively, these carbon-bearing fluids ascending parallel to the slab encounter lower P-T conditions (ca. 2GPa and 500°C) and become oversaturated in carbon, leading to and carbonate precipitates and intense carbonation (*"3"* in Fig. 5.12a,d).

This conceptual model, supported by the reported carbonation processes in green-schist (Nishiyama, 1990; Skelton et al., 1997), blue schist (Kleine et al., 2014) and eclogite facies terrains (Piccoli et al., 2016; Scambelluri et al., 2016; this study), may have significant implications on the carbon cycle in subduction zones because it implies that rock carbonation processes may be efficient over a very wide range of P-T conditions. The model is built on observations from an Alpine-type slab characterized by slow-spreading and transitional lithosphere. Its applicability to the global range of subducting slabs will require additional work and the consideration of the specific nature of single subducting plates and the associated metasedimentary suites. Furthermore, the reactivity of metafelsic lithologies, i.e. orthogneiss, to carbon-bearing fluids opens new perspectives for the evaluation of carbonation processes happening during continental subduction in collisional settings.

9. Conclusions

This work provides a structural, microstructural and geochemical overview of carbonate metasomatism in lawsonite-eclogite facies rocks from Alpine Corsica. Reactive fluid flow along major lithospheric lithological interfaces is evidenced by pervasive metasomatism and carbonation accompanied by multiple veining events. Our tectonostratigraphic reconstruction of carbonated metasomatic rocks facilitates inferences regarding the nature of the protolith rock. Carbonate metasomatism is characterized by field evidence for fluid overpressure, like hydraulic breccias and crack-seal veining, and by reaction rinds between disparate lithologies. In most of the cases, the resulting structural and microstructural relationships give corrosion-like textures, notably with heterogeneous consumption and segmentation of silicate-rich domains. Fluid-rock interactions are recorded by microtextures (e.g. atoll-like minerals or embayed crystal rims), mineral zoning, and isotopic changes. Garnet, when present, is an extremely useful tracer of the P-T-X evolution during HP carbonation. We infer

a fluid composition consistent with previous fluid inclusion studies in similar HP settings, but also pointing to a final fluid composition resulting from successive equilibration during reactive fluid flow. We propose that deeper fluids produced by major dehydration reactions can percolate through slab interfaces and chemically evolve by reactive flow (Fig. 5.12). The interaction of these evolved fluids with rocks occurs at ca. 2GPa and 500°C. The modeled conditions of oxygen fugacity in some of the studied samples indicate that carbonation can take place under oxidized conditions (ΔFQM = 3).

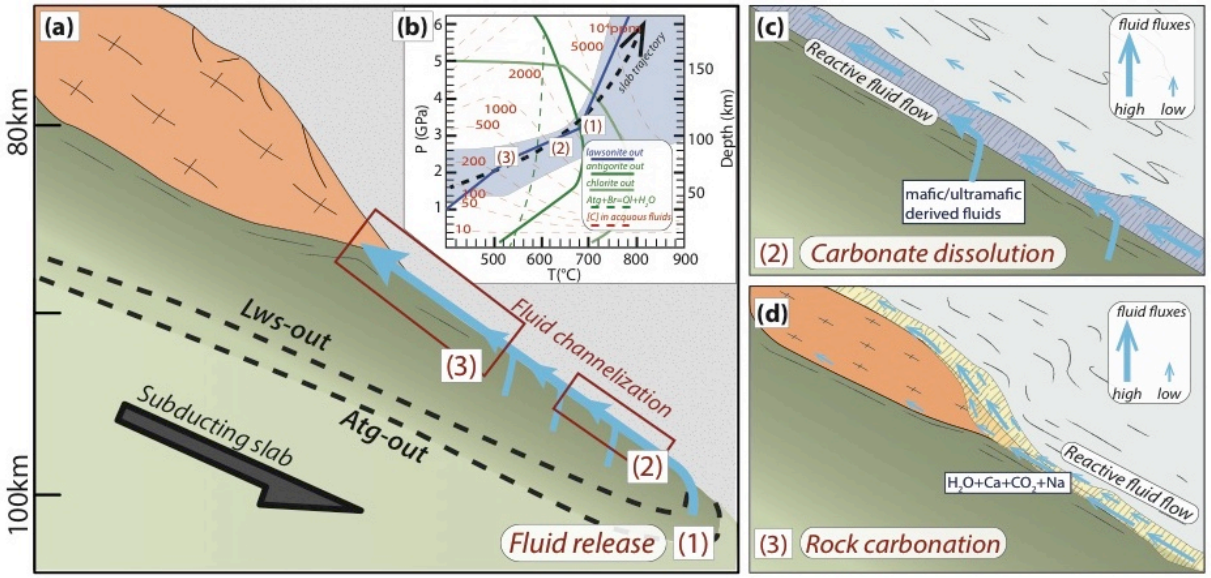

Fig. 5.12: a) Conceptual model of the genesis, migration and evolution of the metamorphic fluids responsible for HP rock carbonation. Fluids are released by lawsonite and antigorite breakdown at depth of ca. 100km (1). Then fluids migrate upward and are channelize along the major slab interfaces like lithospheric lithological boundaries (2; Fig.5.12c). At this stage, aqueous fluids interact with carbonate-bearing rock at condition of carbonate high solubility (Fig. 5.12b), thus leading to carbonate dissolution and fluid enrichment in Ca-C and alkali (Fig. 5.12c). These fluids equilibrated at depth, will become oversaturated in carbonates during decompression and will precipitate carbonates through veining and silicate minerals replacement (3, Fig. 5.12d). **b)** P-T diagram reporting the predicted P-T path for active subduction (D80 model, Syracuse et al., 2010) together with the main fluid-releasing reactions for basalt+H_2O (lawsonite breakdown) and peridotite+H_2O systems (antigorite+brucite, antigorite and chlorite breakdown)(Poli and Schmidt, 2002). Dashed red lines indicate the carbon contours in parts per million for aqueous fluid saturated in $CaCO_3$ (Kelemen and Manning, 2015). The dashed black arrow indicates the trajectory for a cold subduction. This diagram shows how a fluid, equilibrated with carbonates at depth, will become oversaturated in carbonates when decompressing. **c)** Schematic representation of reactive fluid flow of serpentinite derived fluids in metasediments. When water-rich fluids flush carbonate rich metasediments, carbonates are dissolved and fluids become enriched in elements like Ca, C and alkali. d) Schematic representation of a successive interaction of fluids with mafic/ultramafic rock of the oceanic crust and acid rock of the subducted continental crust. At this stage, fluids are geochemically evolved and have both serpentinite and metasediments signature. Rock carbonation occurs during this stage.

Nevertheless, HP carbonation in more reduced lithologies, such as serpentinites, has been shown to take place at similar metamorphic conditions. This suggests that HP carbonation can occur under a rather large range of oxygen fugacity. Local variations in the metasomatic products may be explained by the protolith composition. Lastly, we demonstrate that rock carbonation can also be efficient in rocks with felsic compositions like orthogneiss (Fig. 5.12d). Therefore, subducted continental crust should be considered as a possible carbon reservoir during continental collision. Carbonation of metafelsic rocks might be particularly relevant for orogenic CO_2 cycling in continental subduction and active collisional settings like the Himalaya. Future studies of fluid-rock interactions during continental collision are needed to elucidate the hitherto poorly understood role of subduction zone carbon reservoirs in the long-term global carbon cycle.

Acknowledgements:
The research leading to these results has received funding from the Deep Carbon Observatory, the University Pierre et Marie Curie (Paris 6, Sorbonne Universités) and INSU grant AO2017-999403. Imène Esteve is thanked for her technical support in the SEM platform. Scanning Electron Microscope (SEM) facility of the Institut de Mineralogie, Physique des Materiaux et Cosmochimie is supported by Région Ile de France grant SESAME 2006 N_ I-07-593/R, INSU-CNRS, INP-CNRS, University Pierre et Marie Curie – Paris 6, and by the French National Research Agency (ANR) grant no. ANR-07-BLAN-0124-01. Michel Fialin and Nicolas Rividi (CAMPARIS service) are thanked for their technical support during electron microprobe measurement.

5.2 Petrographic description of selected samples from Loriani and Col di Prato outcrops

Samples collected during the fieldwork in summer 2016 in Col di Prato and Loriani present some differences from samples already characterized from the same localities. Here I will report a brief description of mineral assemblages (Table 5.4) and microstructures observed of some selected samples. These samples are used for mass balance estimations and, are also analyzed for their Sr-Nd isotopic composition (Chapter 6 and 7, respectively).

Col del Prato

Several samples were collected along a profile perpendicular to the lithological boundary between the serpentinite and metasediments. The first half meter of the unaltered metasedimentary pile is characterized by quartz-rich metasediments (sample cor13-63a), followed by calcschists s.s. (sample cor16-63b). Sample of unaltered metasediments (cor16-63a) is comparable to samples described in Section 5.1 (sample 1cor12-20c). It is composed by alternating lens-shaped domains of granoblastic quartz and carbonate (Fig. 5.13a). Phengite, epidote, with minor chlorite and blue amphibole mark a spaced schistosity (Fig. 5.13a,b). Garnet occurs in euhedral and skeletal crystals, most frequently in quartz-rich domains. Opaques minerals and plausible remnants of iron-rich carbonated are also observed. Sample cor16-63d is the metasomatic sample closest to the serpentinite (ca. 50cm-1m from the contact). Near the contact, pervasive albitization overprint Stage#1 and Stage#2 metasomatism. Albite is found as large (mm in size) phenocrystals crystallizing statically and overgrowing the rock foliation (Fig. 5.13c). Microstructures attest that albite post-date the carbonation event metasomatic stage (Fig. 5.13d). Sample cor16-63d underwent complete decarbonation (carbonate dissolution?) and carbonate is only preserved as inclusion in clinopyroxene domain (Fig. 5.13d). Accessory minerals are apatite and sphene. Sample cor16-63f and cor16-63g were samples at ca. 2m from the contact. The first sample

represents a portion of the rock richer in silicates, whereas the second one is representative of the carbonate rich portion (see also Fig. 3a3 in Section 5.1). Clinopyroxene are strongly zoned and display characteristic atoll-like structures (Fig. 5.13e,f). A first generation of clinopyroxene (Cpx1) is destabilized and replaced by carbonate, and a second generation (Cpx2) crystallized around (Fig. 5.13e,f,g). Cpx1 and Cpx2 are distinguishable with the petrographic microscope by different pleochroism and birefringence (Fig. 5.13f), and EDX mapping with SEM reveals that Cpx1 has a Fe-Na rich composition (aegirine), whereas Cpx2 is more Na-Ca-Al rich (omphacite). BSE image shows that the contact between Cpx1 and Cpx2 is characterized by high porosity suggesting dissolution/precipitation (Fig. 5.13g). Euhedral, inclusion-free garnet and garnet with sieve texture are present and texturally in equilibrium with carbonate and Cpx2 (Fig. 5.13h). The geochemical front extends for ca. 3m, after that unaltered metasedimentary sequence is found.

Loriani

Sampling along a conceptual profile has been done in the Loriani outcrop. As described in Section 5.1, in this area the metasomatic rind reaches 2-3m in thickness and has an anastomosed shape. We therefore sampled rocks representative of silicate-rich (carbonate free) domains, carbonated metasomatic rocks and unaltered metasediments. Sample Lor16-1 is silicate-rich clast in the hydraulic breccia (Fig. 5.3e in Section 5.1). The rock is foliated with alternating levels of pumpellyite and clinopyroxene (Fig. 5.14a). The breccia clast is cut across by a first generation of veins composed by epidote, and a second generation of albite (± epidote) veins (Fig. 5.14b). Pervasive, late stage, small carbonate veins are also observed. In the same outcrop, subsequent deformation lead to boudinage of silicate rocks in the carbonate matrix (Fig. 5.15a,b).

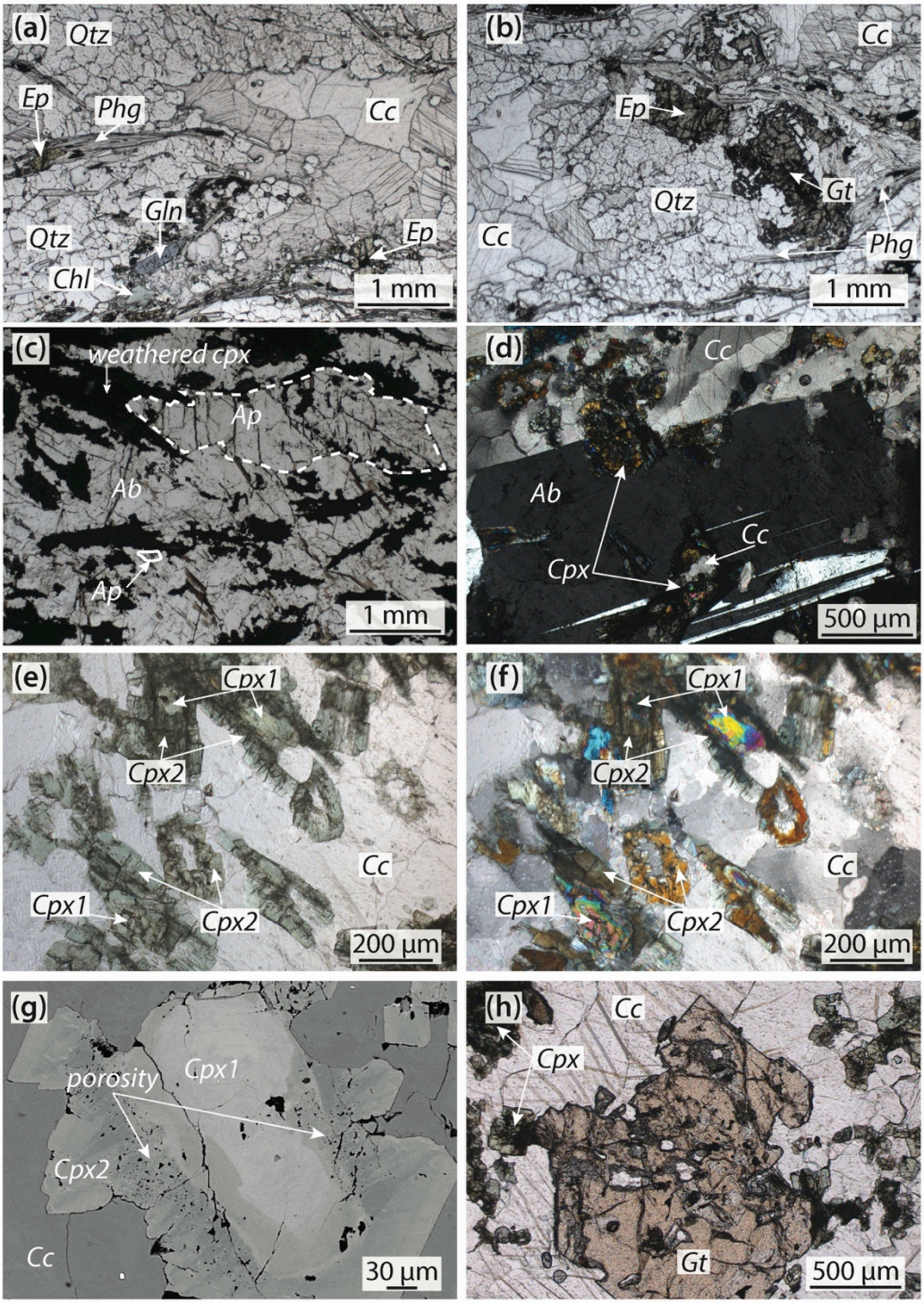

Fig. 5.13: Petrographic photomicrographs and BSE image of samples from Col del Prato outcrop. a-b) Photomicrographs at plane polarized light of unaltered rock (sample cor16-63a). c) Photomicrograph at plane polarized light of sample cor16-63d, which underwent complete decarbonation and it's composed by albite and clinopyroxene. d) Microstructural detail showing albite overgrowing clinopyroxene, which contain carbonate inclusion (sample cor13-63f), thus attesting to the chronological relationships between the phases with albite related to a late stage. e-f) Photomicrographs at plane polarized light (e) and crossed polarized light (f) of clinopyroxenes and carbonate in sample cor16-63f. Some crystals are atoll-like, whereas when the core (Cpx1) is not replaced, it displays a strong optical zoning. g) BSE image of clinopyroxene in sample cor16-63f showing the high porosity at the contact between Cpx1 and Cpx2. h) Euhedral garnet in sample cor16-63f with soma clinopyroxene and carbonate inclusions. Mineral abbreviations from Kretz (1983).

In thin section, carbonate crystals are dynamically recrystallized and prismatic crystals are preserved only in less strained domain. Therefore, it is proposed that deformation occurs after metasomatic carbonation. Late stage deformation could also be responsible for the more extensive retrocession that promotes pumpellyite and epidote crystallization. In thin section, clinopyroxene forms very fine-grained aggregates (crystals range from 10 to 20μm; Fig. 5.14a) and it is unzoned (Fig. 5.14d). In clinopyroxene domains, or near the interface between the clinopyroxene and pumpellyite domains, euhedral garnet is commonly found (Fig. 5.14e). Garnet is unzoned and fractured (Fig. 5.14f). Fractures are filled with carbonates and more rarely with albite. Zircons are common in both samples (Lor16-1 and cor16-4a; Fig. 5.14g,h) together with sphene. Large zircon crystals (50μm) are fractured (Fig. 5.14g), suggesting a detrital origin.

Sample 1cor14-11a and 1cor14-11d

These samples were collected at Loriani, along the same contact of the samples described above. Sample 1cor14-11a was adjacent to the serpentinite, whereas sample 1cor14-11d was ca. 3 m from the contact. Also in this section of the outcrop, deformation post-date the carbonation event (Fig. 5.16a,b). In the less deformed domain, characteristic microstructures describe for rock carbonation are observed. For example, Cpx2 overgrows Cpx1 (Cpx1 is Ca-Mg-rich, whereas Cpx2 is Na-Al rich), and euhedral garnet is found in carbonate-rich domain (Fig. 5.16c,d). Both samples display a mineral assemblage comparable to that sample 1cor14-12b (carbonate + Cpx1 + Cpx2 + garnet, ± chlorite, ± pupellyite). In sample 1cor14-11a, clinopyroxene is found as small, stubby crystals, forming aggregates. These aggregates often display corroded textures and are replaced by carbonate and garnet. Moreover, chlorite-rich (±pumpellyite) layer is also present. SEM observations of sample 1cor14-11a attest to the high Cr and Ni content in chlorite. A possible explanation is mechanical mixing with the

serpentinite. Garnet is present in both samples, but in 1cor14-11a it has a sieve textures and growth around clinopyroxene crystals grains, whereas in sample 1cor14-11b it is present as euhedral crystals (Fig. 5.4d).

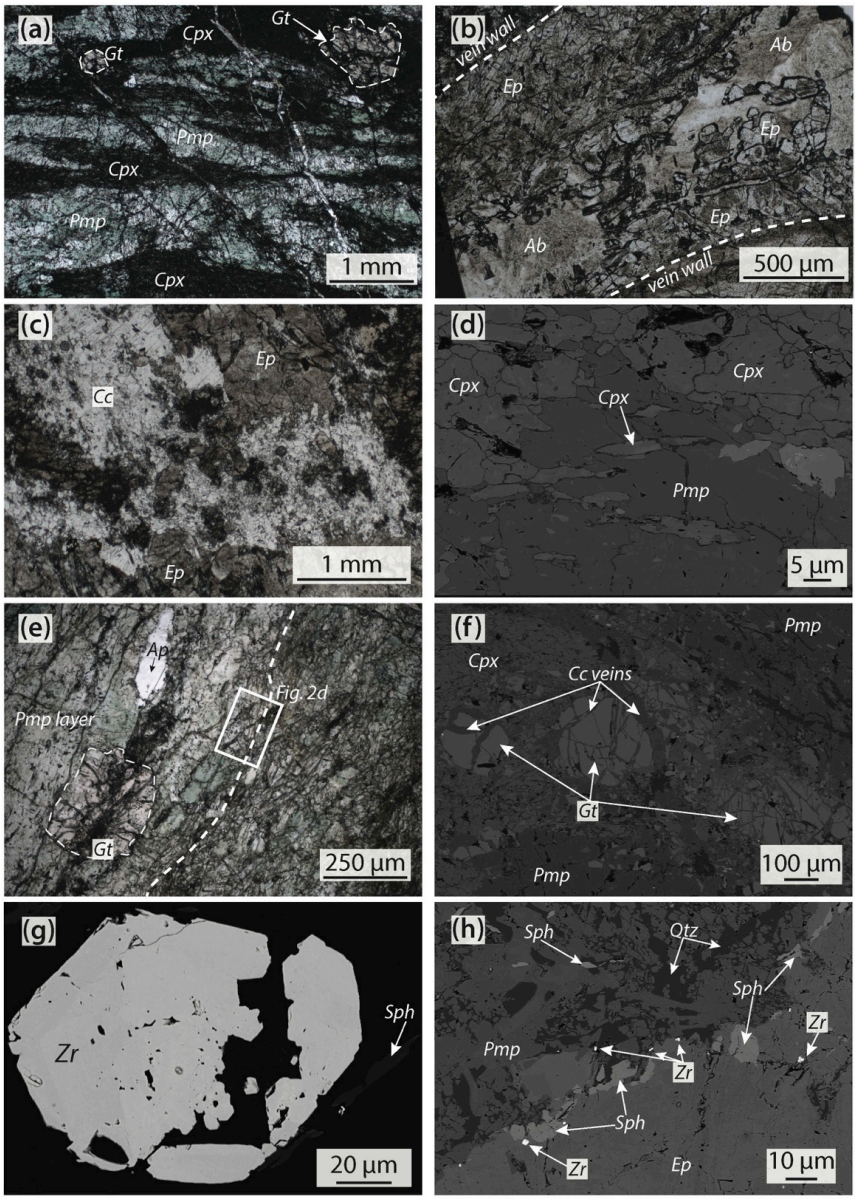

Fig. 5.14: Photomicrographs and BSE images of samples from Loriani outcrop. **a)** Photomicrograph at plane polarized light of sample Lor16-1. The image shows that garnet is present in clinopyroxene level. **b)** Photomicrograph at plane polarized light of sample Lor16-1 showing an albite + epidote vein. **c)** Photomicrograph at plane polarized light of sample cor16-4a showing the microstructural relationship between epidote and carbonate. **d)** BSE image of clinopyroxene and pumpellyite from sample Lor16-1. **e)** Photomicrograph at plane polarized light of sample Lor16-1 showing the contact between clinopyroxene and pumpellyite domains with large garnet crystal and apatite. **f)** BSE image of fractured garnets in clinopyroxene domain with fractures filled by carbonate (sample Lor16-1). **g)** BSE image of fractured zircon from sample Lor16-1. **h)** BSE image of contact between epidote and pumpellyite domains in sample cor16-4a. Along the contact zircons and sphene are abundant. Moreover, quartz crystallizes as interstitial material in the pumpellyite domain.

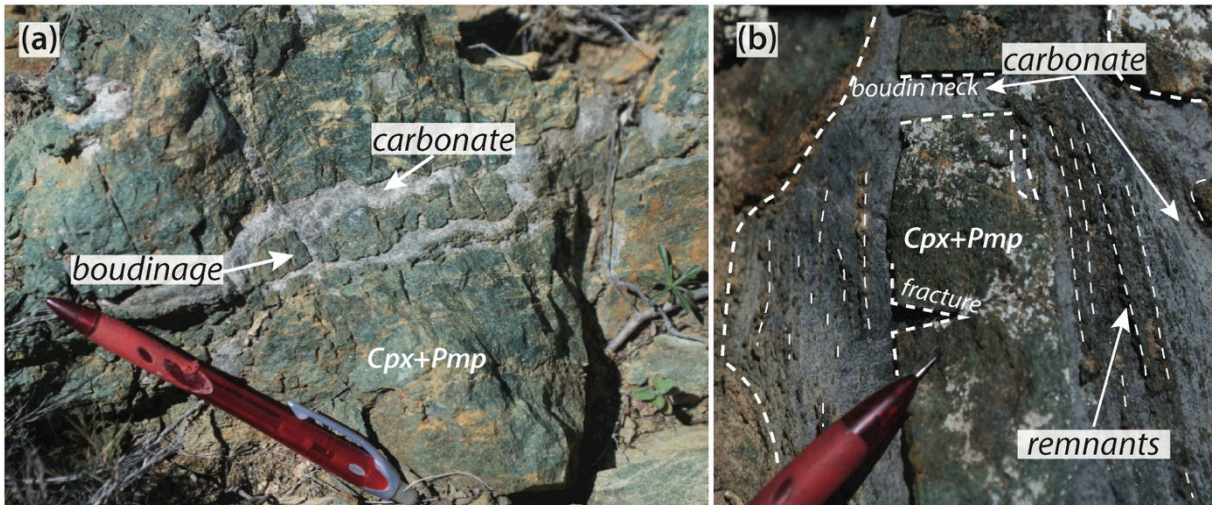

Fig. 5.15 a-b) Pictures of outcrop in Loriani. Deformation affects the carbonated metasomatic rocks provoking the boudinage of more competent silicate rich rocks.

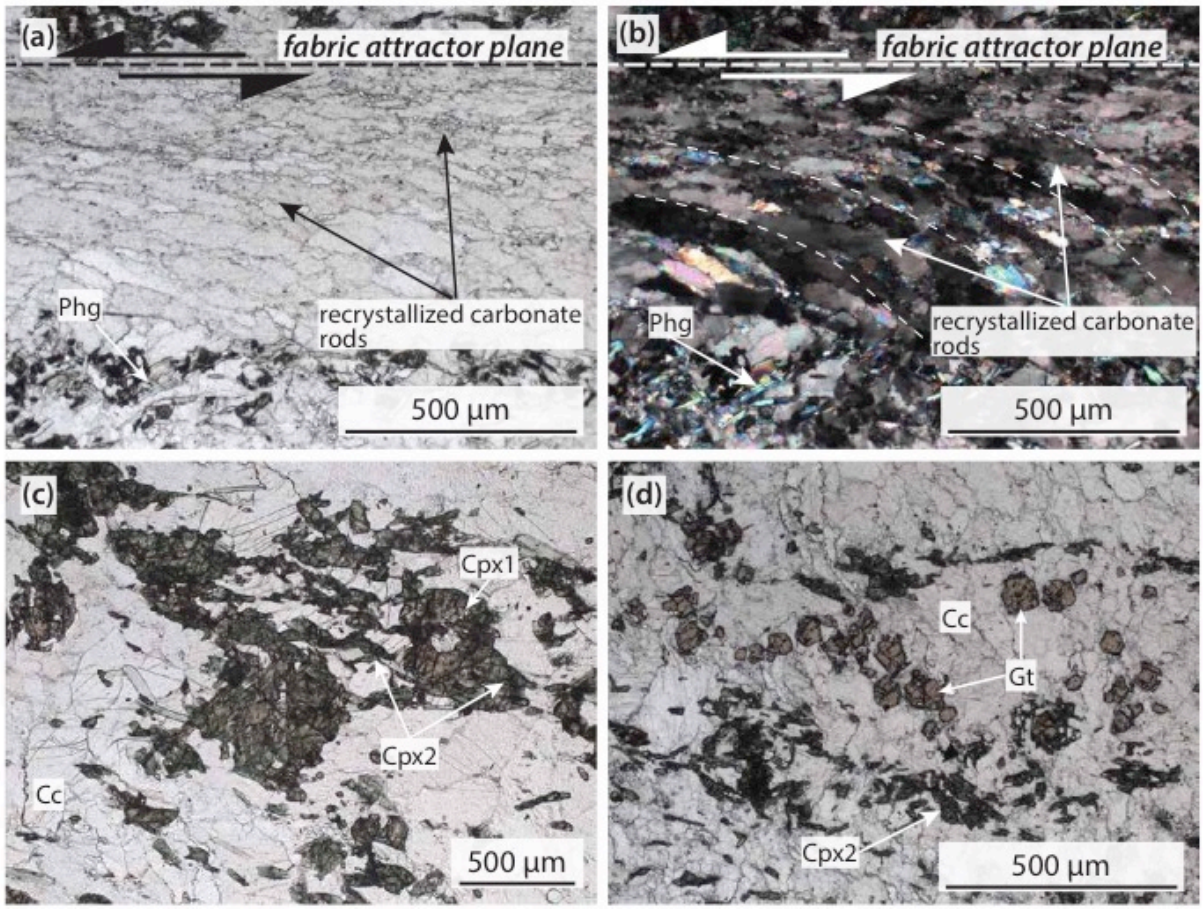

Fig. 5.16: Photomicrographs of sample 1cor14-11b. **a-b)** Plane polarized and cross polarized photomicrographs displaying deformation in a carbonate domain. The shear plane is materialized by the deflection of carbonate prism. Moreover, carbonate crystals are dynamically recrystallized. **c)** Plane polarized photomicrograph showing the two generations of clinopyroxene. **d)** Plane polarized photomicrograph showing euhedral garnet in a carbonate-rich domain.

Table 5.4: mineral occurrences in analyzed thin sections. Mineral modal volumes precentages are estimated by optical microscopy with the support of the chart for modal volume percentacge (Terry and Chilinger, 1955).

	Minerals	***Cc***	***Qtz***	***Cpx***	***Gt***	***Ab***	***Ep***	***Pmp***	***Phg***	***Chl***	***Accessories***
	Sample										
Unaltered rock	cor13-63a	25%	40%		5%		10%		10%		Gln, Chl
Col di Prato	cor16-63d			50%		50%					Sph, Cc, Ap
	cor16-63f	55%		30%	5%	10%					
	cor16-63g	75%		15%	5%	5%					
Loriani	Lor16-1			40%	5%			50%			Cc, Ap, Zr, Sph
	cor16-4a	5%					40%	55%			Ap, Zr, Sph
	cor16-4b	50%					10%	40%			Zr?
	1cor14-11a	40%		30%	<5%			20%		10%	
	1cor14-11b	50%		30%	5%			10%	5%		

CHAPTER 6
Reactive fluid flow and mass transfer during high-pressure carbonation

In this chapter will focus on mass balance and time-integrated fluid-fluxes characterizing carbonate metasomatism. Firstly, a general overview on how mass transfer can occur and the basic equation used for the mass balance calculation of will be given. Then, the focus will be on the role of fluid flow as mean of mass transfer: an historical overview will be presented in to outline the differences between water/rock ratio and time-integrated fluid fluxes. Then, the focus will be on the equations that describe fluid transport process and fluid-rock interaction. After this generic introduction, mass balance results and time-integrated fluid fluxes calculation will be presented.

6.1 Mechanisms of mass transfer

Metamorphic fluid exert a major control on heat and mass transfer in the crust and mantle, as well as on rock rheology and reaction kinetics (e.g., Fyfe et al., 1978). Mass transfer via fluid flow thus determines the distribution of elements and isotopes at a variety of scales. Fluid-rock interaction and metasomatism can deeply modify rock bulk chemistry and stabilize or destabilize minerals.

Mass transport and reaction can occur within grains and/or around grains through fluid-filled pore spaces and cracks. At low to moderate grade, however, intracrystalline diffusion is commonly assumed to be slow enough to be neglected (Ague, 2014). Nevertheless, mass transport to and from crystals by coupled dissolution and precipitation may influence the

chemical and isotopic compositions of crystals and migrating fluids (e.g., Putnis, 2002; Putnis and John, 2010).

In fluid-filled pore space, mass transfer can occur trough diffusion, advection or a combination of the two. Both mechanisms can operate during metamorphism, even simultaneously. However, their rates are very different, and they act on a very different scale in time and space (Ague, 2014).

Diffusion occurs when a chemical potential gradient produces a net transfer of atoms down the gradient, and diffusion through a fluid is described by Fick's first law. In a rock, however, diffusion rate will be considerably slower because of low interconnected porosity and also by the geometry of the interconnected porosity that is convolute and tortuous. Consequently, the diffusion flux must be reduced for the tortuosity factor (τ), that ranges from 0 to 1 (Bear, 1988).

Advection occurs when fluids migrate along grain boundaries or fractures and the way they move can be pervasive or channelized. The first one is define as fluid migration around individual grains through an interconnected porosity (*pervasive* or *porous media flow*). The second one (*channelized* or *focused flow*) implies preferential fluid motion along high permeability conduits, i.e. permeable layers, lithological contacts, fractures (Ferry, 1994; Ague, 2014). The first study on grain boundaries in metamorphic rocks with transmission electron microscopy revealed tubular pores at grain corners and isolated pores on grain faces (White and White, 1981). However, conditions favorable to pervasive fluid flow are unlikely to develop during metamorphism. Actually, experimental works show that an interconnected network of completely wetted grain boundaries should not exist in metamorphic rocks (dihedral angle, θ, close to zero has never been measured for any combination of mineral, fluid, and P-T conditions. Ferry, 1994). In contrast, microcracks were proved to form a pervasive interconnected network since their presence influences rock properties like

electrical resistivity (Brace et al., 1965; Brace and Orange, 1968) and permeability (Brace et al., 1968). This is also supported by the common observation of swarms of fluid inclusion in planar arrays (Roedder, 1984). During metamorphism, the main crack-forming mechanism is likely hydrofracturing (Ferry, 1994). Processes that can raise pore fluid pressure are, for example, devolatilization reaction (products, i.e. fluid+mineral, have greater volume than reactants)(e.g., serpentinite dehydration, Raleigh and Paterson, 1965), deformation (Vrolijk, 1987), faster pore fluid expansion than the rock matrix during increasing metamorphic conditions, and replacement processes (Jamtveit et al., 2009). How fast fluids can move along the network (transport rate) is determined by the geometry of the channel network, the viscosity of the fluid, and the P-T causing the flow (Philpotts and Ague, 2009).

In advection regime, another process call mechanical dispersion can be very important. Even if it is the result of advection, its effects are similar to those of diffusion and it is treated mathematically like this latter. In one dimension flow, we can write:

$$D_{MD,L} = \alpha_L |v_x| \tag{6.1}$$

where $D_{MD,L}$ is the corresponding coefficient of mechanical dispersion, α_L the coefficient of dispersivity in the direction of the flow (longitudinal dispersivity), and $|v_x|$ the absolute value of the pore velocity. The combined effect of diffusion and mechanical dispersion ($D_{MD,L}+D\cdot\tau$) is referred to as hydrodynamic dispersion ($D_{HD}=D_{MD,L}+D\cdot\tau$).

6.2 Mass balance calculation

Element mobility during subduction metamorphic fluid flow has been demonstrated by the examination of metamorphic veins and their associated alteration selvages (e.g. Beinlich et al., 2010; Gao et al., 2007; Spandler et al., 2003, 2008; van der Straaten et al., 2012; Vitale Brovarone et al., 2014 JMG), and supported by physical-chemical principles (e.g. Hofmann et al., 1974) and isotopic studies (e.g. Rye et al., 1976). The fluid infiltration histories of fossil

metamorphic flow systems are recorded when the fluid reacts with rock, otherwise, there were would be no evidence of the flow (Ague, 2014). Therefore, the goal is to quantify the changes in the masses of fluid species due to internal chemical reactions to have access to fluid flow estimations.

Reaction occurs when fluid that is out of equilibrium with a rock mass infiltrates and drives reactions. The rates of chemical reactions link the timescales of mineralogical and fluid composition changes to those of mass (and heat) transfer. When studying metamorphic rocks, however, the fluid phase in not longer present, except for fluid inclusions in minerals. Nevertheless, rocks can preserve chemical and isotopic alteration. The physical boundary between the reacted and unreacted regions in the rock is known as *reaction front* or *geochemical front*. When the geochemical front is identified in the field, the analysis of reacted and not reacted rocks can give insight on mass transfer mechanism during fluid-rock interaction and allow mass balance calculations. One of the advantages of mass-balance calculations is that erroneous interpretations of mass changes resulting from *residual dilution* (because overall mass gain) or *residual enrichment* (because of overall mass loss) can be avoided, because calculations are always based on an immobile reference element whose mass should remain unchanged during metasomatic processes.

In this section I will briefly describe the definition of a geochemical frame and the mathematical formalism used to assess the mass balance on carbonated metasomatic rocks.

6.2.1 Defining a geochemical reference frame

The identification of relatively immobile elements during chemical alteration is the first step to define the geochemical reference frame needed to assess absolute mass and volume changes. Great care must be exercised in reference frame selection because even elements generally considered immobile as Zr, Ti, Th and HFSE, may be mobilized under certain

pressure and temperature and fluid composition conditions (e.g. Zeitler et al., 1990; Brocker and Enders 2001; Rubatto and Hermann, 2003; Gao et al., 2007). A difficult part is to define a correct geochemical reference frame in terms of an immobile reference element, but also in terms of the least altered reference precursor rock. The element considered as an immobile reference should not be concentrated in minerals which grew in response to metasomatism, nor should it have large concentration uncertainties.

6.2.2 Basic equations

Mass balance methods are used to quantify metasomatism (e.g. Gresensa, 1967; Grant, 1986; Ague, 1994a; Baumgarnter and Olsen 1995; Ague and van Haren, 1996) and follows from the first principle of thermodynamics. The equations used here to quantify mass and volume changes follow Ague (1994a), Ague and van Haren (1996), Phillipotts and Ague (2009) and references cited therein. The gain and loss of elements during metasomatism will result in changes in rock mass. The overall or total rock mass change ($T_{mass,i}$) calculated using a reference species *i* is given by:

$$T_{mass,i} = \frac{c_i^0}{c_i'} - 1 \tag{6.2}$$

$T_{mass,i}$ is a fraction; the percentage mass change can be found by multiplying it by 100. The superscripts 0 and ' indicate the precursor and altered rocks respectively. If rock mass has been lost, the concentration of *i* will be greater in the altered rock than in the precursor rock (residual enrichment of *i*). Conversely, if rock mass has been gained, the concentration of *i* will be less in the altered rock than in the precursor rock (residual dilution of *i*).

The mass change of a mobile species *j* estimated using species *i* as a reference is:

$$\tau_i^j = \left(\frac{c_i^0}{c_i'}\right)\left(\frac{c_j'}{c_j^0}\right) - 1 \tag{6.3}$$

where c_j indicated the concentration of *j* and τ_i^j is the fractional mass change for *j*.

The overall rock volume strain (ε_i) using a reference species *i* is given:

$$\varepsilon_i = \left(\frac{c_i^0}{c_i'}\right)\left(\frac{\rho^0}{\rho'}\right) - 1 \tag{6.4}$$

where ρ^0 and ρ^j are the precursor and metasomatic rock density respectively. Here, I modeled rock densities using the software Perple_X (version 6.7) and internally consistent thermodynamic database of Holland and Powell (1998, revised 2004).

As a spatial profile is unavailable, a statistical analysis of compositional data has been used. The approach for assessing an average τ_i^j value is based on the geometric (logarithmic) mean concentration ratios (Ague, 1994a). Taking logarithms of equation (5.2):

$$\ln(\tau_i^j + 1) = \ln\left(\frac{c_i^0}{c_j^0}\right) + \ln\left(\frac{c_j'}{c_i'}\right) \tag{6.5}$$

Then, the mean precursor log ration (ML^0) is given by:

$$ML^0 = \frac{1}{N^0}\sum_{n=1}^{N^0} \ln\left(\frac{c_{i,n}^0}{c_{j,n}^0}\right) \tag{6.6}$$

Whereas the mean altered rock log ratio (ML') is:

$$ML' = \frac{1}{N'}\sum_{n=1}^{N'} \ln\left(\frac{c_{j,n}'}{c_{i,n}'}\right) \tag{6.7}$$

In which *n* denotes a particular sample and N^0 and N' are the total numbers of precursors and altered rock samples, respectively. The average mass change value and the associated 2σ uncertainty range are computed from:

$$\hat{\tau}_i^j = \exp(ML^0 + ML' \pm 2\sigma) - 1 \tag{6.8}$$

where $\hat{\tau}_i^j$ denotes the mean mass change value and σ is the standard error. The standard error is estimated by summing the standard error on ML^0 and ML' in quadrature:

$$\sigma = [(\sigma_{ML^0})^2 + (\sigma_{ML'})^2]^{1/2} \tag{6.9}$$

where the standard errors are simply the sample standard deviations on ML^0 and ML' divided by $\sqrt{N^0}$ and $\sqrt{N'}$, respectively.

6.3 Fluid flow: historical overview

The first recognition of the role of metamorphic fluids for heat and mass transfer in the crust date back to the second half of the 19th century, where in the probably first American geology textbook, Dana recognized that "loss of water or other vaporizable ingredients" from rocks was an essential effect of metamorphism (Dana, 1863). Over the last decades, recognition of the importance of fluid flow in the process of metamorphism was the core an enormous amount of petrological studies to understand the mineralogical evolution of metamorphic rocks. Actually, one of the most important turning point in metamorphic petrology was the quantitative demonstration of how mineral equilibria depend on the composition of the fluid as well as on P and T (Greenwood, 1961, 1962, 1967). However, Greenwood (1967) also proposed that equilibria involving hydrates and carbonates likewise could buffer the composition of the coexisting CO_2-H_2O fluid, thus the amount of reaction should be negligible unless a large quantity of fluid is present. However, several field observations reveals significant reaction progress (e.g., Hewitt, 1973; Moore and Kerrick, 1976; Rice, 1977a,b), observation that looked in contradiction to theoretical predictions. The solution to this dilemma emerged with the recognition of the role of fluid flow and fluid composition in controlling the mineralogical evolution of metamorphic rocks (Ferry, 1986; Ague and Rye, 1999). From that moment, lots of effort has been put in evaluating fluid composition and fluxes during metamorphism. Sheppard et al. (1969) demonstrated that measuring the shift in isotopic composition, and knowing or estimating the fluid composition, the amount of fluid involved could be computed from mass balance as water/rock ratio. Later works (e.g., Ferry 1978, 1986) demonstrated that also measuring the progress of metamorphic dehydration-

decarbonation reactions, the mass balance can lead to calculation of water/rock ratio. Since the first works in the 80's demonstrating that mutually consistent conclusions about metamorphic fluid flow could be obtained from both petrologic and stable isotopic data on the same sample (e.g., Ramble et al., 1982; Ferry, 1986), mineralogical, chemical, and isotopic data became routinely used to identify the conduits of fluid flow in metamorphic terrains, to quantify the fluid flow and to constrain the direction of flow relative to P-T gradients, lithological contacts and structural features.

The measurement of water/rock ratio was fundamental to strengthen arguments for the occurrence of fluid-flow, but it doesn't give information on the amount of fluid involved. This is because fluid/rock ratio refers to static, zero-dimensional "box" models, with no relation with the dynamic process of flow (Fig. 5.1a; Baumgartner and Ferry, 1991). The first efforts to overcome the shortcoming of fluid/rock ratio conceptually involved connecting a series of boxes together to form a kind of flow path and applying the fluid/rock ratio calculation sequentially to each box (e.g., Spooner et al., 1977). Fluid fluxes may be coupled analytically to the rate of chemical reaction in a porous media by the continuity equation, a statement of mass balance (De Groot and Mazur, 1969). Because rocks record the time-integrated effects of fluid flow, this equation must be integrated with respect to time. The result quantitatively links the fluid amount as a time-integrated flux ($q_{TI}\,[m^3_{fluid}\,m^{-2}_{rock}]$) to the amount of reaction expressed as reaction progress for the duration of flow. The time-integrated fluid fluxes are defined as the total amount of fluid flow that passes across an area of interest during a given time interval (Ferry and Gerdes, 1998)(Fig. 6.1b).

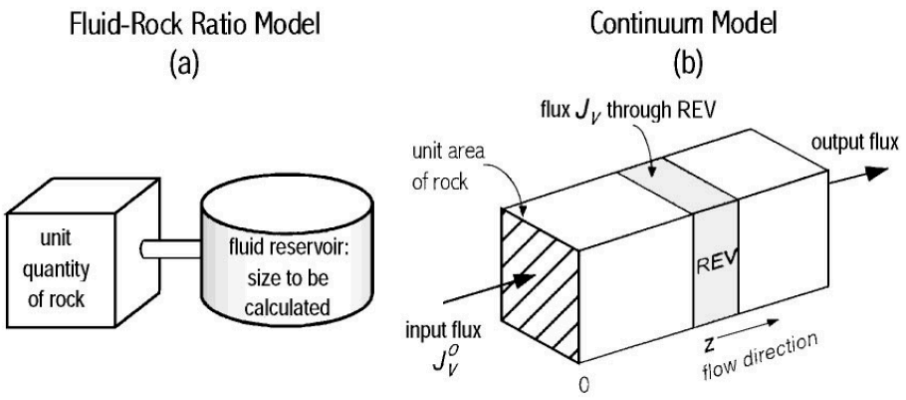

Fig. 6.1 from Ferry and Gerdes, 1998: conceptual models for fluid-rock interaction. (a) Fluid-rock ratio model; (b) Continuum model for fluid flow linked to fluid-rock reaction.

6.3.1 Advection-Dispersion-Reaction equations

Regional scale advection is the main promoter of mass transfer with also important implications on rock deformation, and rate of metamorphism (e.g., Jamtveit et al., 1990; Jamtveit and Austrheim, 2010). Fluids flow through rocks and react with it. Interestingly, the amount of reaction is in some way proportional to the amount of flow. In many case, isotopic, mineralogical and chemical evidence for reactive fluid flow can be inverted to constrain time-integrated fluid fluxes (q_{TI}) and the direction of the flow relative to T gradients. The estimation of fluid fluxes requires quantitative expressions that relate fluid transport process and fluid-rock reactions. The solution to the required partial differential equations describing mass conservation for a fully saturated porous media, are known (Carslaw and Jaeger, 1959 p. 388; Ogata and Banks, 1961).

One of the possible approaches is to use concentration profiles resulting from advection and hydrodynamic dispersion (Philpotts and Ague, 2009). The variation in concentration of a species of interest (*s*) can be modeled with the following equation:

$$c_s^{x,t} = c_s^0 + (c_s^B - c_s^0) \times \frac{1}{2}\left(erfc\left[\frac{x - v_x t}{2\sqrt{(D_{HD} t)}}\right] + \exp\left[\frac{v_x}{D_{HD}}\right] erfc\left[\frac{x + v_x t}{2\sqrt{(D_{HD} t)}}\right]\right) \quad (6.10)$$

where $c_s^{x,t}$ is the concentration of *s* at position *x* and time *t*, and *erfc* is the complimentary error function erfc(y)=1-erf(y). In order to solve partial differential equation, boundary

conditions must be specified. In this case, the boundary conditions are: c_s^0 (initial concentration of *s*) and c_s^B fluid constant composition at x=0. Notes that this equation is for *steady state* with respect to a fluid composition (i.e., the fluid composition doesn't change with time even though the solid does). An additional term that accounts for fluid compositional change during reaction must be also incorporated. To do so, the relationship between the concentration of species *s* in the fluid and the solid is given by the equilibrium fluid/solid partition coefficient by volume, K_v ($[mol\ m^3_{fluid} \cdot mol^{-1}\ m^{-3}_{rock}]$. With some rearrangement, the new equation will have the same form of Eq. (6.10), by substituting v_x for $K_v v_x \phi$ (where ϕ is the porosity) and D_{HD} for $K_v D_{HD} \phi$.

We will use the Eq. (6.10), with the K_v term, in to model the oxygen isotopic front in the serpentinite (see section 7.5.2). In contrast, this equation was not applied for the carbonated metasomatic rocks because carbonate metasomatism implies changes in the mineral composition and modal volumes during reaction progress, thus it would required an equation with partition coefficient changing in time, whereas in Eq. (6.10) K_v is fixed to a unique value.

Data from concentration profiles can be inverted to obtain time-integrated fluid fluxes. As mentioned before, the effective velocity of geochemical front migration is reduced by the factor $K_v \varphi$. Thus, the average distance of the solute front (*d*) migration during reactive fluid flow is:

$$d = k_v v_x \phi t \tag{6.11}$$

It can be demonstrated that $v_x \phi t$ is equal to the time-integrated fluid fluxes (q_{TI}). Therefore, for advecting transport, constant porosity and fluid velocity, the distance of the geochemical front migration is directly related to q_{TI} (Bickle, 1992):

$$q_{TI} = \frac{d}{k_v} \tag{6.12}$$

Alternatively, in case of advection-dominated systems with small porosity (ϕ<~0.01), the time integrated fluid fluxes is approximated by (Ague, 1998):

$$q_{TI} = L_{GF} \frac{m_i}{(C_i^{eq} - C_{i,x=o}^{Input})} \tag{6.13}$$

where L_{GF} is the distance of geochemical front propagation, m_i is the number of moles of i produced or consumed per unit volume rock ($[mol\ m^{-3}]$), C_i^{eq} is the fluid composition that would be in equilibrium with the mineral assemblage, $C_{i,x=o}^{Input}$ is the initial fluid composition. C_i^{eq} is a difficult parameter to set without direct measurement. However, setting C_i^{eq} to zero (i.e., the fluid has completely reacted and the element transferred to the rock) represents a conservative choice that will give a minimum value of q_{TI}.

For simple H_2O-CO_2 fluid, Baumgartner and Ferry (1991) presented a method for quantification of the time-integrated fluid fluxes along a P-T gradient. It can be demonstrated that q_{TI} is:

$$q_{TI} = \frac{\overline{V}(m_s - X_s[m_{CO2} + m_{H2O}])}{\left(\left(\frac{\partial c_s}{\partial T}\right)\frac{\partial T}{\partial x'} + \left(\frac{\partial c_s}{\partial P}\right)\frac{\partial P}{\partial x'}\right)} \tag{6.14}$$

Where $\overline{V}$ is the molar volume of the fluid, s is either CO_2 or H_2O, m_s is the total mole of species s produced or consumed, $\frac{\partial c_s}{\partial T}$ and $\frac{\partial c_s}{\partial P}$ is the concentration gradient along T and P gradient, in the direction of the flow, x' denotes the direction of the flow. A series of assumptions are made in the expression (Baumgartner and Ferry, 1991):

(1) Fluid advection is dominant over diffusion and dispersion for mass transfer.

(2) The reaction progress is caused by fluid flow along the P and T gradients. If P and T did not change along the flow path, there would be no reaction progress by this mechanism.

(3) The infiltrated fluid is locally buffered by the mineral-fluid equilibria.

(4) The fluid flow is confined to an individual lithologic unit.

This equation estimates the time-integrated fluid flux at any specific P-T points where the fluid in the system reaches local equilibrium with the mineral assemblage. It requires the measured progress of mixed volatile reactions in rocks, the equilibrium fluid composition and its P and T derivatives, and the P and T gradients. Actually, the chemical potential for reaction can come from either lithological contrast and/or changes in P-T conditions along the fluid flow path. As pointed out by Bebout and Barton (1993), mass transfer because of fluid infiltration across boundaries between sedimentary, mafic, and ultramafic lithologies can be very important. Mass transfer along gradients in P and T can be critical for driving reactions among minerals and C-O-H fluids (Baumgartner and Ferry, 1991), and can lead to changes comparable to the effects predicted from flow between contrasting lithologies, but with some important implications (Bebout and Barton, 1993). In fact, the nature of metasomatic changes is sensitive to the fluid flow path. This means that coupling the study of metasomatism in terms of geochemical and isotopic characteristics together with experimental data on mineral solubilities it is possible to reconstruct the direction of the flow. However, at the time, specific geological examples and good experimental data on solubilities were lacking. Today, new experimental data on mineral solubility and speciation at high P-T conditions are available. Here, we will use the data on carbonate and carbon solubility (Facq et al., 2014; Kelemen and Manning, 2015) coupled with the mass balance results for the calculation of time-integrated fluid fluxes.

6.4 Method of investigation

Samples were collected from two localities where Mesozoic metasediments are juxtaposed to serpentinite: Loriani and Col di Prato (Chapter 5). Samples were categorized as (i) protolith rocks, with no major evidence for fluid-rock interactions (calcschists and metacherts), (ii) Stage#1 host rock (precursor, carbonate free metasomatic rock) and (iii) carbonated

metasomatic rock. Rock samples were prepared for chemical analysis by isolating the portion of interest using a rock saw. The cut surfaces were thoroughly abraded with silicon carbide paper to remove any contamination due to sawing. Samples were then ultrasonically cleaned in distilled, deionized water. Five protoliths, three precursors and seven carbonated metasomatic rock samples were selected based on freshness and geological relationships. Moreover, samples cor13-17c (carbonate crack-seal) and relative host rock (sample OF3598) from Aja Rossa outcrop, will be also described.

Averaging and statistical analysis of compositional variation is not without pitfalls (Aitchison, 1986; Ague, 1994a; Ague and Van Haren, 1996). Importantly, limited number of samples is subject to large uncertainties and may yield meaningless results and interpretations. In Chapter 5, the varieties of metasomatic products has been presented and discussed. Considering the large variability of pre-metasomatism rocks (i.e., metachert, calcschists, para- and orthogneiss) and also the large variability of Stage#1 rocks (Vitale Brovarone et al., 2014), a careful strategy of sampling has been adopted. The two outcrops of Loriani and Col di Prato were selected because: i) field and petrographic observations attest to the relatively uniformity of the protolith rock, i.e. Mesozoic calcshists; ii) Stage#1 rocks are relatively homogeneous; iii) clear field relationship between Stage#1 and Stage#2 are observable at the scale of the outcrop, thus every altered rock is directly compared to its precursors.

6.5 Results of mass balance

Carbonation mainly affects Stage#1 rocks, this latter will be used as "precursor" rock for the mass balance calculation into constrain mass changes between Stage#1 and Stage#2 metasomatic events.

6.5.1 Concentration diagrams

A convenient graphical technique for evaluating relative mass changes is to plot altered/precursor concentration ratios on the *y*-axis for elements of interest on the *x*-axis (CR diagrams in Fig. 6.2). This graphical approach allows identifying the relatively "inert" elements in order to define a geochemical reference frame. Moreover, it can be a useful graphical technique to compare the same type of rocks and evaluate natural variability. Figure 5.2 reports the CR diagrams for the two Stage#1 metasomatic rocks sampled at Loriani and the other two from Col di Prato. In Col di Prato, the concentration ratio between the two sampled "precursor" rocks shows that they have very different composition, with sample cor16-63d being enriched in light rare earth elements (LREE). This difference can be relied to an initial heterogeneity of the rocks (i.e., prior any metasomatism) or to late stage metasomatism, linked to the pervasive albitization (Chapter 5, section 5.2). The big uncertainties on the precursor rocks hamper any attempt of mass balance calculation. Hereafter, we will focus on the samples from Loriani. The two Stage#1 metasomatic rocks from Loriani have similar composition except for Sr, which concentration is ca. 8 times higher in sample cor16-4a rather than in sample Lor16-1. It is worth noting that both samples have the same initial content of CaO and volatiles (Loss on ignition-LOI). This observation implies that results of CaO and LOI gain during carbonate metasomatism are not biased by initial heterogeneities (see below). This is also important because these two elements will be used for the calculation of time-integrated fluid fluxes (see section 6.6). Figure 6.2 reports the CR diagrams for carbonated metasomatic rocks from Loriani outcrop and for the carbonate crack-seal in Aja Rossa area, for comparison. A general trend of higher mobilization of major elements and most incompatible trace elements (e.g. Sr, Rb, Ba) can be recognized in both cases. Samples from Loriani (Fig. 6.3a) display a large variability. The low number of samples is responsible for the large error bars. Despite these uncertainties, Zr behaves as "inert", thus it will be used as geochemical reference frame for both, Loriani and Aja Rossa samples.

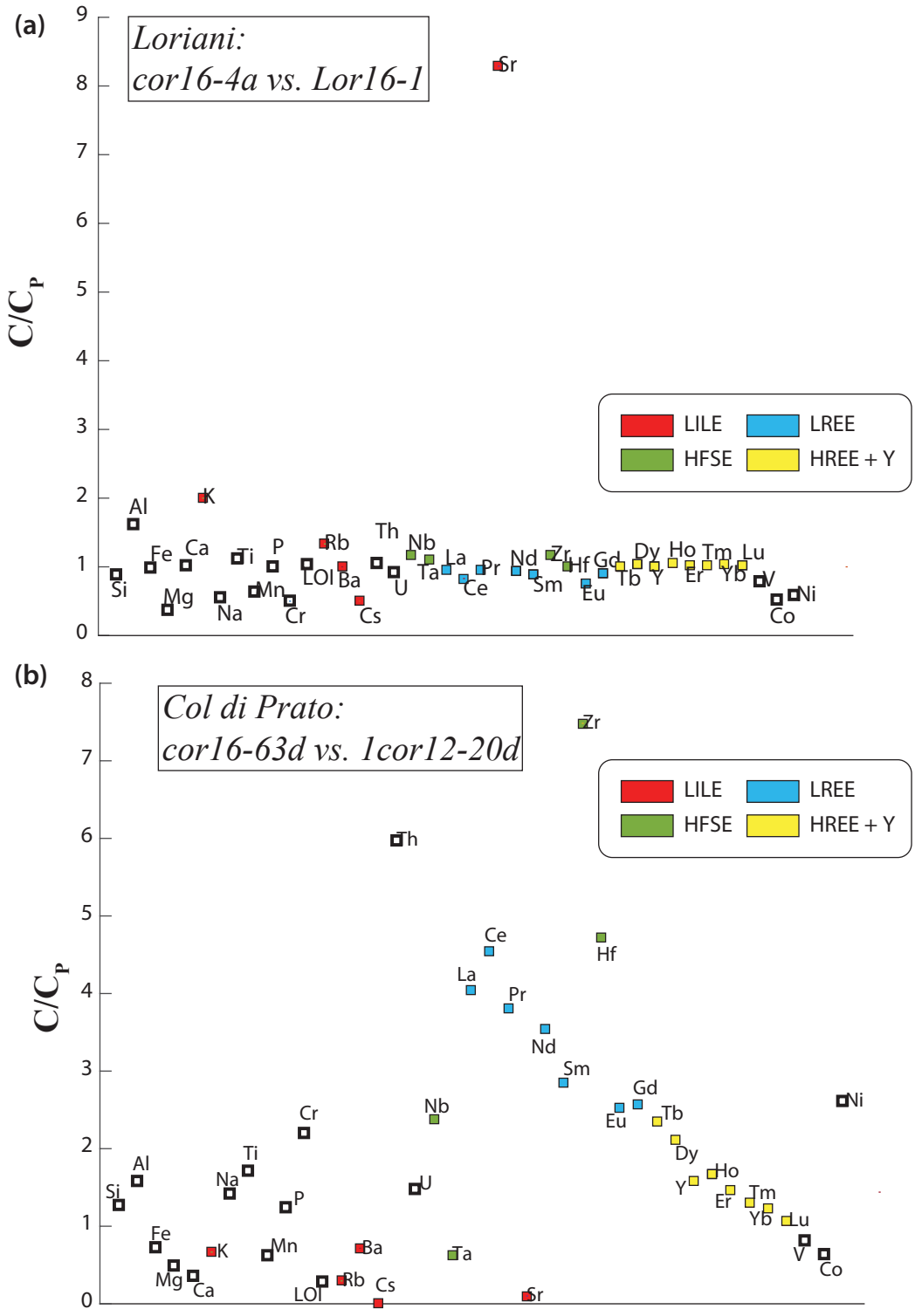

Fig. 6.2: Concentration diagram (CR) for samples of carbonate-free metasomatic rocks. **a)** CR diagram for the Stage#1 metasomatic rocks in Loriani. **b)** CR diagram for the Stage#1 metasomatic rocks in Col di Prato.

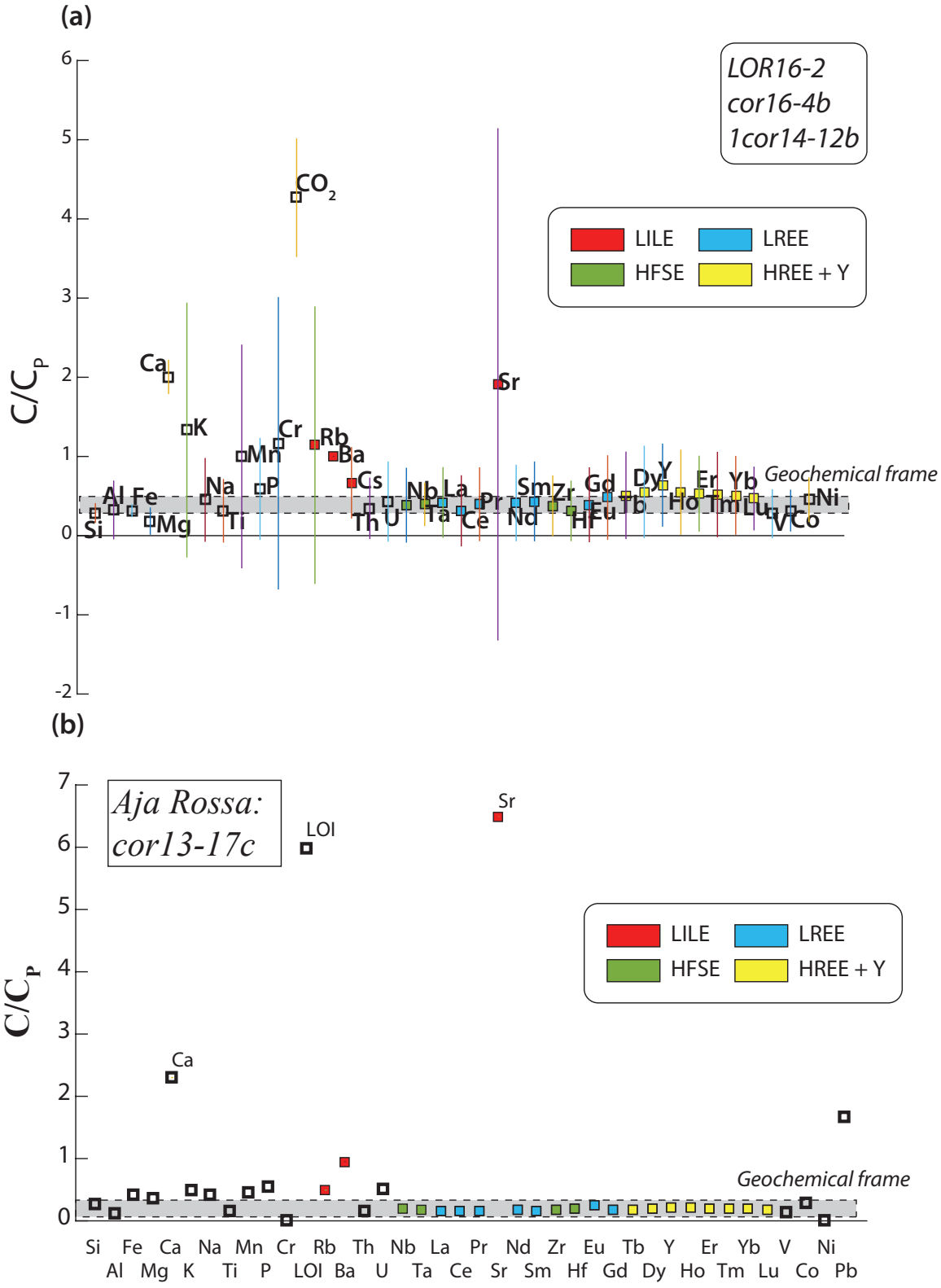

Fig. 6.3: Concentration diagram (CR) for samples of carbonated metasomatic rocks relative to carbonate-free metasomatic rocks. a) Lor16-2, cor16-4b and1cor14-12b relative to Lor16-1 and cor13-4a. b) Sample cor3-17c relative to OF3598 (bulk rock composition of OF3598 is from Vitale Brovarone et al., 2014).

5.5.2 Mass balance

Samples Lor16-1 and Lor16-2

Sample Lor16-1 and Lor16-2 are a Stage#1 and Stage#2 rocks, respectively. The first one is representative of the carbonate-free clast in the hydraulic breccia, whereas the second is representative of the carbonate-rich matrix sealing the breccia (Fig. 6.5a,b). Figure 6.5c reports the percentage mass change diagram for selected major and trace elements between these two samples. It is important to point out that all the following mass change diagrams are not chondrite-normalized, but rather depictions of elemental absolute mass change in percentage. Stage#2 rock display a strong enrichment in CaO and LOI of ca. 930 and 2200%. Analyses are reported as weight percent (Table 6.1). Considering that the main volatile bearing phase is carbonate, the LOI gain has been considered as CO_2 gain. Converting from wt.% to moles, the CaO:CO_2 gain is stoichiometric, 1:1. Other elements displaying significant enrichment are Na, Mn, Cr, Sr, and Ba (155%, 560%, 630%, 2860%, 385%). Moreover, also Ni and Y are slightly enriched (100% and 85% respectively). Enrichment in K and Cs are probably related to late stage mica crystallization.

Samples 1cor14-12b

This sample is composed by carbonated metasomatic rocks cut across by omphacite + carbonate veins (Fig. 6.6a, Fig. 4a in Chapter 5). In thin section, it doesn't show evidence of retrogression and displays carbonate + Mn-rich omphacite (Cpx2) + garnet paragenesis (with relict of diopside, Cpx1; see the petrographic description in Chapter 5). Whole rock composition of sample 1cor14-12b has been compared to "precursor" rocks Lor16-1 and cor16-4a (Fig. 6.7a). The trend in mass changes is comparable with that described for sample Lor16-1.

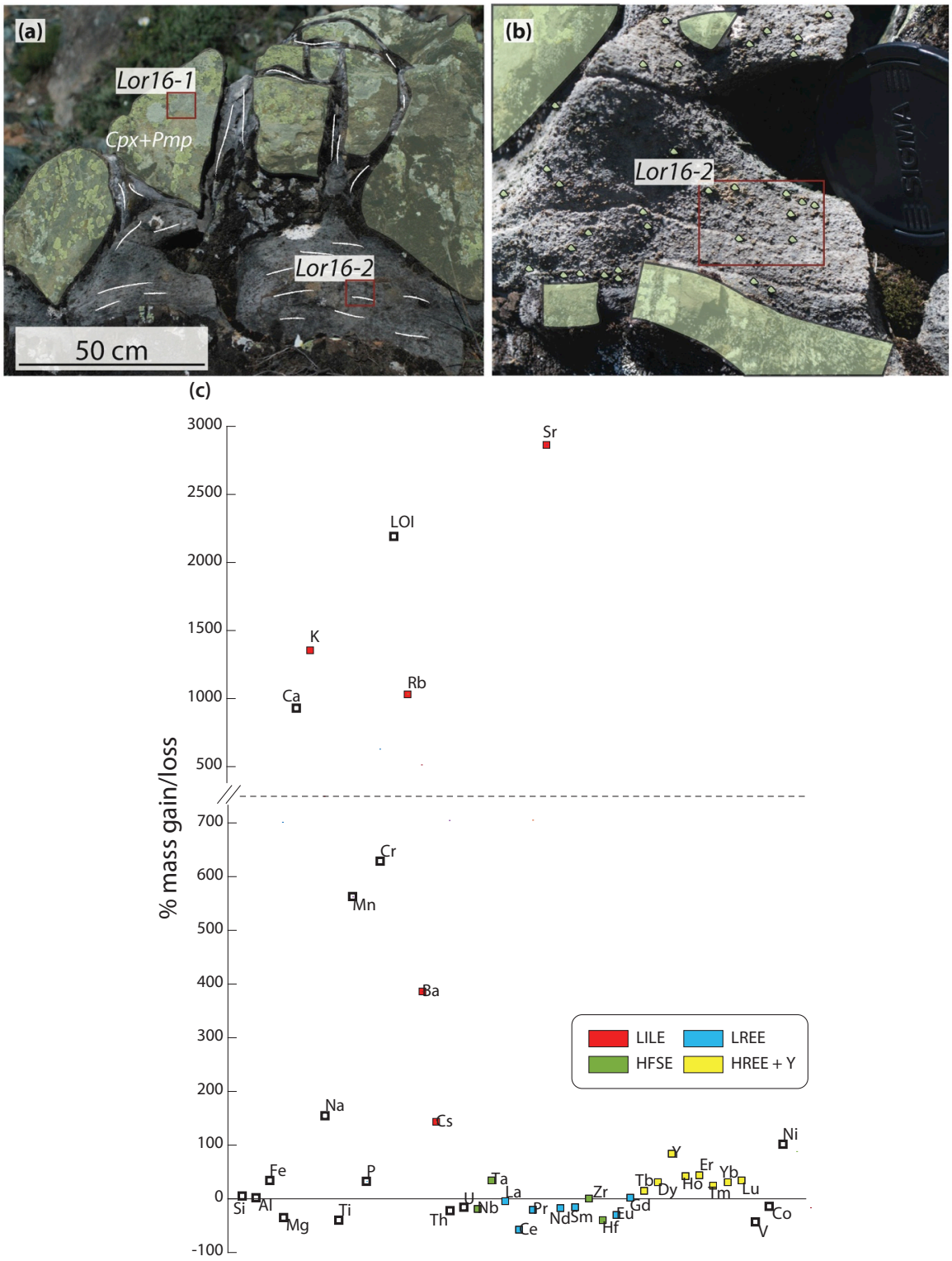

Fig. 6.4: Pictures of the analyzed samples as they look like in the field and calculated elements mass change. Major elements are oxides (from Si to LOI), whereas trace elements are in part per million. **a)** Carbonate free clast are shaded in green, the foliation in the carbonated portion is highlighted with white lines. **b)** Green dots are used to indicate the presence of abundant remnant of metasomatic carbonate free rock in the carbonate domain. **c)** Percentage mass change diagram for the evaluation of compositional changes (mass gain are positive, losses negative). Here, sample Lor16-2 is compared to sample Lor16-1.

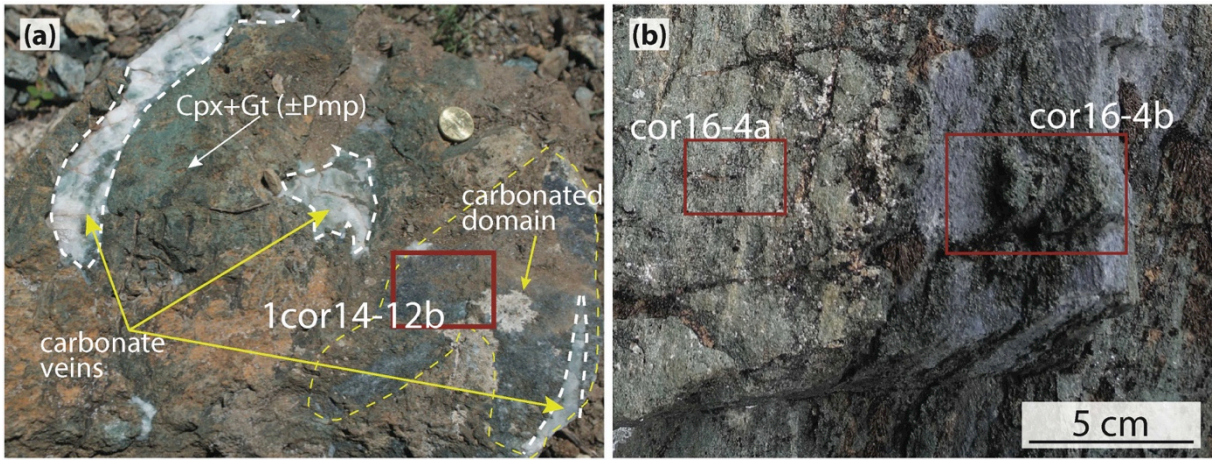

Fig. 6.5: Pictures of the analyzed samples as they look like in the field. **a)** Block of carbonated metasomatic rock cut across by carbonate + omphacite veins. **b)** Transition from carbonated to non-carbonated metasomatic rocks.

Sample cor16-4a, cor16-4b

These samples represent a possible former hydraulic breccia, successively deformed by boudinage (Fig. 6.6b). CaO and LOI mass gain is observed in sample cor16-4b, with an enrichment of ca. 260% and 630%, respectively. P, Sr, Ba, and Y are enriched (75%, 170%, 80%, 70%), but with an order of magnitude lower than sample Lor16-2. In this sample, Cr and Ni do not show any mass change, whereas major elements Si, Al, Mg, Fe, Na and Mn are loss (-30%, -24%, -40%, -30%, -40%, -20%) (Fig. 6.7b).

Sample cor13-17c

A carbonate crack-seal sample (cor13-17c) has been compared to the host rock (sample OF3598; Vitale Brovarone et al., 2014) (Fig. 6.8a,b). Mass gain is mainly due to mass gain in CaO, LOI and Sr (1180%, 320%; 3500%). Moreover, the sample displays a strong mass gain in Pb. The possible fractionation of Pb during carbonate precipitation is also suggested by the high Pb content in other carbonated metasomatic rocks (sample cor13-22c, Table 6.1. Mass balance not shown here). These observations are consistent with the trace element distribution in eclogitic metamarl (Spandler and Pirard, 2013).

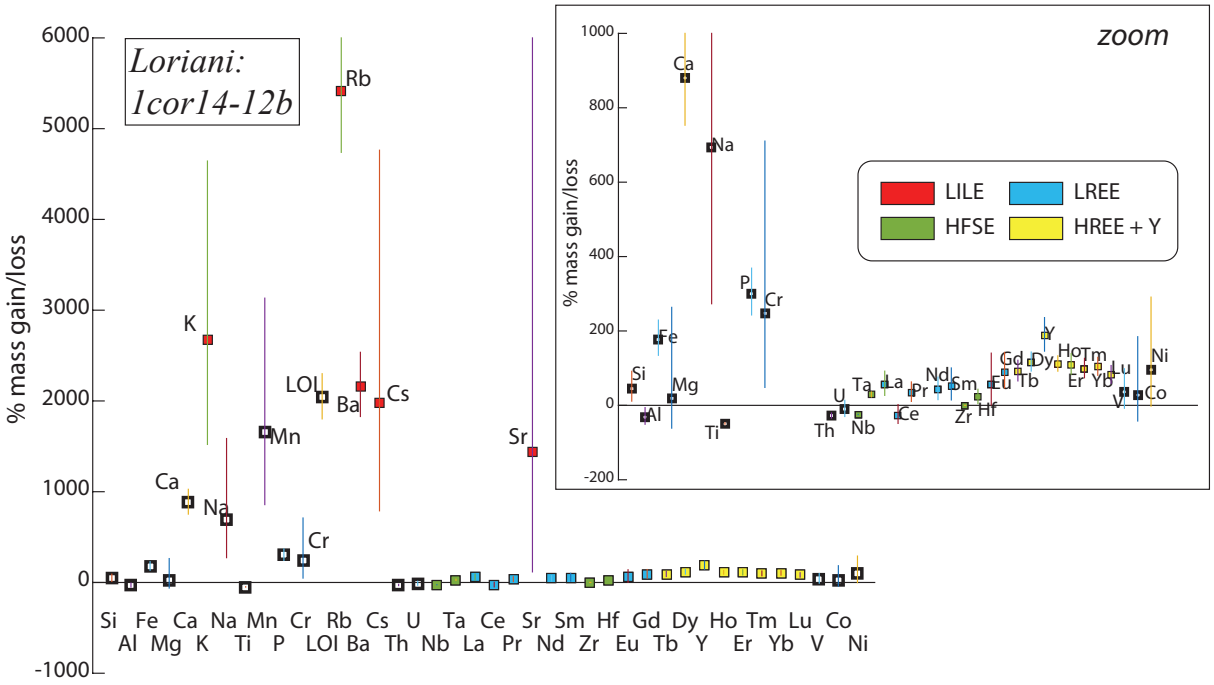

Fig. 6.6: Percentage elements mass change diagram (mass gain are positive, losses negative) between sample 1cor14-12b and precursors samples Lor16-1 and cor16-4a. Major elements (from Si to LOI) are oxides, whereas trace elements are in part per million.

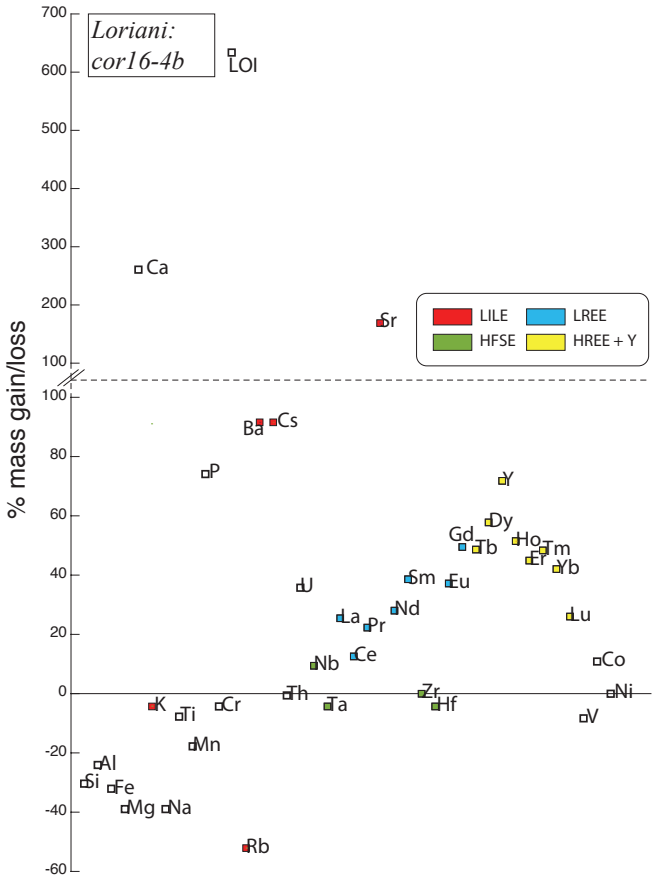

Fig. 6.7: Percentage elements mass change diagram (mass gain are positive, losses negative) between sample cor16-4b and precursors sample cor16-4a. Major elements (from Si to LOI) are oxides, whereas trace elements are in part per million.

Figure 6.8b also shows a mass gain in major elements: Si, Mg, Fe, Na, and Mn. However, this enrichment might be linked to the highest modal proportion of clinopyroxene in the fractured portion of the host rock compared to the average modal abundance of lawsonite and clinopyroxene in the Stage#1 metasomatic rock in this outcrop. Actually, clinopyroxene-rich domains seems to be more affected by carbonation and veining compared to lawsonite-rich ones.

6.6 Results of time-integrated fluid fluxes

Origin, magnitude and transport mechanism of metamorphic fluids are matter of controversy and estimated time-integrated fluid fluxes ranges from near zero to more than 10^3 m^3/m^2. The variation in estimates of time-integrated fluid fluxes may reflect the different methods used to measure paleo fluid flow. In the literature, two main approaches have been used: 1) measurement of advective displacements of compositional heterogeneities within the rocks (e.g., Bickle and Baker, 1990); 2) reaction progress of mineral assemblages (e.g., Baumgartner and Ferry, 1991). Since a unique reaction for rock carbonation with a precise stoichiometry has not been determined, the approach used in this work is the first one.

In section 6.3.1, two different equations for the estimation of time-integrated fluid fluxes for advection transport mechanism were presented. For equation *(5.13)*, we used results of mass balance for CaO and CO_2 mass gain (m_i) and fluid composition at 2 GPa and 500 °C from literature (Facq et al., 2014; Kelemen and Manning, 2015; for CaO and CO_2 respectively; Table 6.2). For equation *(6.14)* concentration gradient were calculated from data from the literature (Facq et al., 2014; Kelemen and Manning, 2015; Table 6.2). A critical point in equation *(6.14)* is the choice of the geothermal gradient, especially temperature.

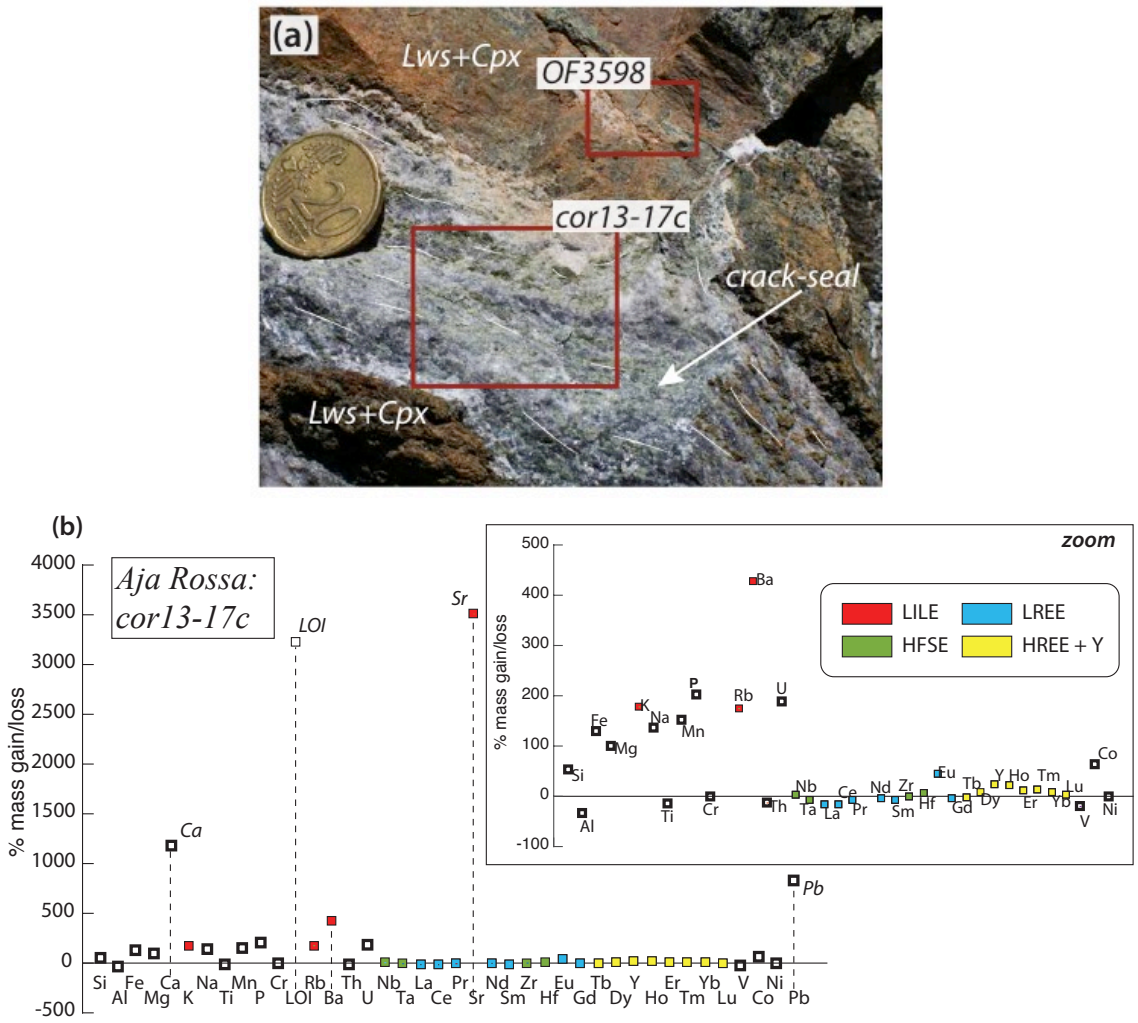

Fig. 6.8: a) Picture of carbonate crack-seal opening in a lawsonite + clinopyroxene rock in Aja Rossa outcrop (see also Fig. 3a,b in Piccoli et al., 2016). **b)** Percentage mass change diagram for sample cor13-17c vs. precursor rock OF3598. Major elements (from Si to LOI) are oxides, whereas trace elements are in part per million.

Actually, the P term in equation *(14)* is very small because is multiplied for the X_{CO2} pressure concentration gradient (dX_{CO2}/dP is in the range of 10^{-13}; Table 6.2). Here, we chose to use a lithostatic pressure. However, considering that the pressure term is so small to be negligible, errors in pressure gradients will not affect the results. Conversely, the choice of temperature gradient has a strong impact on the results. Most of the works on the variation of cold spring water chemistry on the overriding slab (e.g., Mottl et al. 2004) point to a dominant vertically upward fluid pathways. This interpretation is also supported by geodynamic simulations (e.g., Gerya and Yuen, 2003; Arcay et al., 2005; Gerya, 2011). The inverted thermal gradient on the

slab surface varies from 40 °C/km to 120 °C/km in the geodynamic models, depending on the slab dip, convergence rate, slab-mantle coupling, and the mantle flow model (e.g., Peacock, 1996, 2003; van Keken *et al.*, 2002; Abers *et al*., 2006; Syracuse et al. 2010). Here, 60 °C/km gradient (perpendicular to the slab surface; van Keken *et al.*, 2002) was used for our order-of-magnitude estimates. Assuming the slab dip is 45°, the T gradient along fluid flows is 42°C/km (Table 6.2). In addition to the vertical component of fluid flow, recent two-phase flow modeling shows that when compaction is induced, the local devolatilization reactions drive slab-parallel flow within low-permeability layers (Faccenda et al., 2014; Wilson et al. 2014). The slab-parallel flow would lead to a shallower T gradient and thus larger time-integrated flux, so the fluxes derived here should be viewed as conservative estimates. The choice of a upward fluid pathway might seem in contradiction with the model proposed in Chapter 5, for a slab parallel fluid flow. However, as it is shown in Figure 5.12a fluid flow is fed from the lower units (i.e., the serpentinite), thus with vertical upward pathway. For the point of interest near the slab surface where the calculation is applied to, the inferred local slab-parallel flow satisfies condition *(4)* for the applicability of equation *(*6*.14)* (i.e. fluid confined to a unique lithological unit). Results of time-integrated fluid fluxes using equations *(*6*.13)* and *(*6*.14)* are reported in Figure 6.8. Sample Lor16-2 and 1cor14-12b has been grouped together, thus the reported values in Table 6.2 are the geometric mean of the two.

Concentration gradients	*Kelemen & Manning (2015):* carbon concentrations for aqueous fluid saturated in $CaCO_3$						*Facq et al. (2014)*: Ca concentration in fluids in equilibrium with aragonite				
	T/P	CO wt.%	mol/100g	mol/m³	X_{CO2}		T/P	mol/kg	mol/m3		gradient
	550° (2 GPa)	0,06	0,005	58,50	0,00089		500°	0,032	37,44	dC_{Ca}/dT	0,3627
	500° (2 GPa)	0,04	0,0033	39,00	0,00059		400°	0,001	1,17		
	2 GPa (500°)	0,04	0,0033	39,00	0,00059		2 GPa	0,032	37,44	dC_{Ca}/dP	$4{,}095\,10^{-8}$
	1.8 GPa (500°)	0,03	0,0025	29,25	0,00044		1.8 GPa	0,025	29,25		

Fluid molar volume [m³/mol]‡	*V*	0,00001516	*Ca and CO_2 mass change [mol m⁻³]*	**CO_2**	**Lor16-2/ 1cor14-12b**	**cor16-4b**	**CaO**	**Lor16-2/ 1cor14-12b**	**cor16-4b**
Gradients	dX_{CO2}/dT	$5{,}9\,10^{-6}$		*[LOI] wt% precursor**	7,6	7,91	*[CaO] wt% precursor**	23	23
	dX_{CO2}/dP	$7{,}4\,10^{-13}$		*% mass gain***	2304%	633%	*% mass gain***	942%	261%
	dT/dx [K m⁻¹]	-0,042		*CO_2 gain [wt.%]*	175	50	*CaO gain [wt%]*	--	--
	dP/dx [Pa m⁻¹]	-28000		*mol/100 g rock*	4	1	*mol/100 g rock*	3,9	1,1
				mol/m³	121777	34822	*mol/m³*	118352	32802

‡ calculated with Perple_X
*from whole rock analysis
**from mass balance calculation

Table 6.2: Parameters for the calculation of time-integrated fluid fluxes with eqautions (6.13) and (6.14).

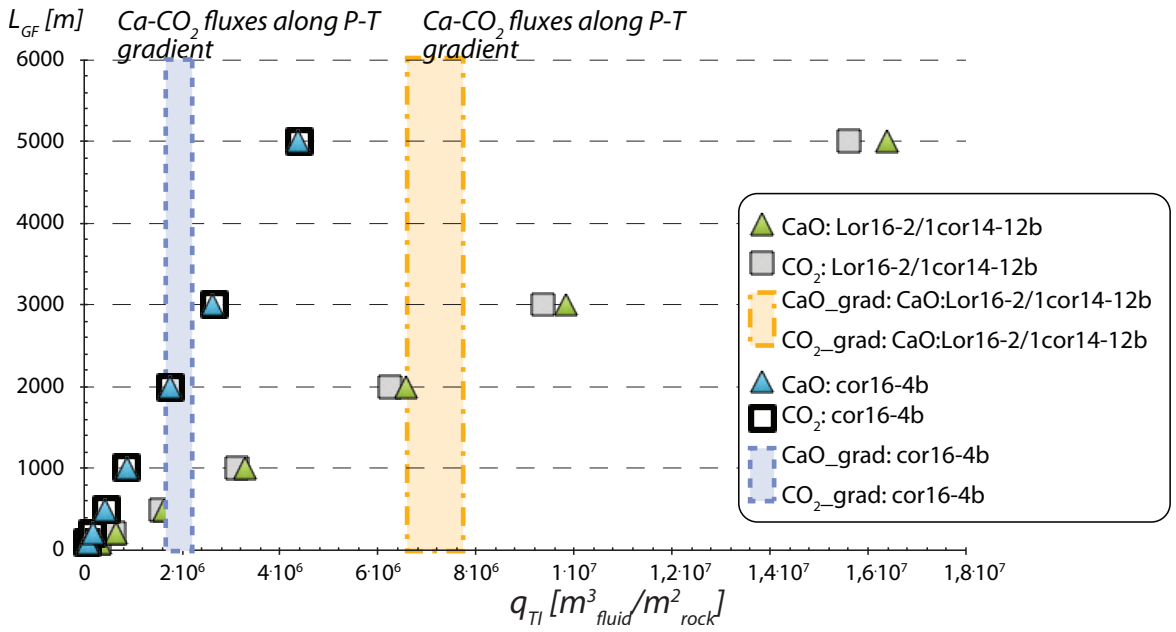

Fig. 6.9: Time-integrated fluid fluxes (q_{TI}) vs. distance of the geochemical front (L_{GF}). Time-integrated fluid fluxes calculated along a P-T gradient are also plotted.

Sample cor16-4b, since it has a different trend with loss of major element, has been considered separately. One of the first things that comes out from Figure 6.8 is that, independently from the method, q_{TI} calculated for Ca and CO_2 are consistent. Moreover, q_{TI} calculated with equation (6.14) even if it does not have any relation with the length of geochemical front (L_{GF}) it falls in the linear trend of values estimated with equation (6.13). All together, the data obtained point to q_{TI} of the order of 10^6 m^3_{fluid}/m^2_{rock} and an extension of L_{GF} of 1-3 km, that is in good agreement with the field observations (Fig. 5.2). This value indicates that fluid flow occurred in open system (>10^4 m^3/m^2; channelized flow) (Ague, 2014) and fluxes were much higher than the time-integrated fluid flux proposed at the top of an oceanic slab for a vertical flow ($3 \cdot 10^2$ m^3/m^2 ; Zack and John, 2007).

	ρ [kg m^{-3}]	[Zr ppm]	T_i	ε_i
Samples				
Lor16-1	3359	144	--	--
cor16-4a		158	--	--
Lor16-2		24,7	483%	
cor16-4b		83,4	89%	108%
1cor14-12b*	3090‡	29,1	395%	443%
1cor14-12b**			443%	
OF3598	3220	122,9	--	--
1cor13-17c	3041	22,12	456%	488%

‡density modeled with Perple_X software
* relative to Lor16-1
**relative to cor16-4a

Table 6.3: Evaluation of total mass change (T_i) and total volume change (ε_i).

6.7 *Discussion*

6.7.1 Discussion on mass balance results

Field and microstructural evidence indicates that carbonation variably affect sialic metasomatic rocks. The results reported here show how the interaction of rocks with fluids circulating during HP metamorphism, may result in significant element redistribution (John et al., 2008; Spandler and Pirard, 2013). The study of the carbonated metasomatic rocks offers a window on the composition of these fluids and their capability to mobilize and redistribute elements. Moreover, the inferred total mass and volume change potentially has implications on rock rheology. Table 6.3 shows that all samples undergo significant mass gain of ca. 450% and consequent volume strain of the same order of magnitude (ca. 460%). Only one sample display less dramatic mass gain (89%, sample cor16-4b) because CaO-CO_2 gain goes with a loss of major elements.

6.7.1.1 Major element mobilization

The metasomatic parageneses described in Chapter 5 and the here reported mass balance calculation allow drawing some generalities on element mobility during HP carbonation.

Carbonated metasomatic rocks display extensive mobilization of alkaline and alkaline earth metals major elements, such as Ca, Na, together with Mn and P. Except for samples displaying late stage micas, K mass gain is not observed. The enrichment in these elements cannot be related to carbonate precipitation alone. For example, Na, Mn enrichment is more likely linked to omphacite crystallization (Cpx2), whereas P enrichment can be related to apatite crystallization. This latter observation can be relevant for the trace element budget (see next section).

The metasomatic rocks in this unit underwent a long history of fluid-rock interaction. However, both Stage#1 and Stage#2 metasomatism take place during HP metamorphism, at conditions where fluids are supposed to be aqueous and very diluted. It is thus interesting to try to outline the overall element mobility during both stages. With this attempt, in Figures 6.9 and 6.10 are reported the wedge diagrams for the evaluation of compositional changes for major and trace elements. In order to get a broader view on the general trends, sample cor13-32 (calcschist), cor13-22c (carbonated metasomatic rock from Mt Muffraje) and sample cor13-17c and OF3598 from Aja Rossa are also plotted (see also Table 6.1). Comparing Stage#1 rocks with metasediments, we observe similar trend to those described in Vitale Brovarone et al. (2014) for lawsonite metasoamtism: Si, P loss, and Al, Mg, Ti gain. An exception exists for Fe that during Stage#1 metasomatism does not undergo any mass change, whereas in Vitale Brovarone et al. (2014) it was reported a 25% mass loss. Carbonated metasomatic rocks are diluted compared to Stage#1 precursor in Si, Al, (± Mg) and Ti (Fig. 5.9, residual dilution= decrease due to overall rock mass gain). Conversely, Fe, Na mass gain is observed (note the difference with residual enrichment, where the increase in concentration due to overall rock mass loss). Considering the little number of samples, a unique trend for Mn and P cannot be established. Sample Lor16-2 is enriched in Mn, but display no P mass gain, whereas the opposite situation is found in sample cor16-4b. Sample 1cor14-12b displays

Mn and P mass gain. It is worth noting that the mobility of Mn in this sample has been discussed also in Chapter 5, where we reported the enrichment in Mn in the second generation of clinopyroxene (Cpx2). However, based only on petrographic observations, an internal source of Mn can not be excluded (breakdown of Mn bearing phase like epidote). Considering these new data, an external input of Mn is now the favored explanation.

Ague (2017, submitted) reports that subduction zone rocks do not display correlations in Na-Ca mass changes because these elements are distributed across multiple phases. In Alpine Corsica, during lawsonite metasomatism, rocks undergo Na mass loss and Ca mass gain (Vitale Brovarone et al., 2014). However, we show here that carbonated metasomatic rocks display a mass gain in both elements, together with CO_2 mass gain. Moreover, it is interesting to note that the crystallization of Cpx2 (Na-rich) is not accompanied by Si mass gain. This might be interpreted as a recycling of Si from Cpx1 dissolution to crystallize Cpx2. However, Mg loss is expected in case of Cpx1 dissolution since no Mg-bearing phase was observed (no Mg-carbonate, nor amphibole or chlorite). Considering the high variability in Mg content of Stage#1 rocks, we prefer a conservative interpretation of the data and propose that Mg is likely diluted.

5.7.1.2 Large ion lithophile and rare earth element mobilization

Trace alkaline, alkaline earth and REE elements during carbonate metasomatism display different trending, depending on the mineralogical control on element redistribution and partitioning between fluid and rock.

During Stage#1 lawsonite metasomatism, major and trace alkali elements (Na, K, Rb, Cs) and alkali earth (Ba) were removed (-100% mass), mainly because the destabilization of phengite (Vitale Brovarone et al., 2014). Such a trend is quite common in may subduction zone metasomatism studies (e.g., Beinlich et al. 2010). Large ion lithophile elements (LILE) like

Sr, Pb were strongly enriched, whereas U behaved as inert. Light rare earth elements (LREE) were more enriched than MREE and HREE, consistently with the crystallization of lawsonite. High field strength elements (HFSE), notably Ta, Nb, Ti, Zr and Y, are also enriched because of crystallization of key accessory phases, i.e. sphene and zircon. In Chapter 5, we reported the large abundance of these accessory minerals in the Stage#1 rocks sampled in Loriani. Mass balance show that for Stage#2 metasomatism, the lower concentration of HFSE elements is due to dilution because overall mass gain. Conversely, Stage#2 metasomatism is characterized by enrichment in LILE (Sr, Ba, Pb, ± U; Fig. 5.10a,b,c,d), but no significant variation in REE mass occurred, except for MREE and Y (HFSE) mass gain. The mobilization of REE is, in general, strongly function of the growth or breakdown of REE-bearing phases, notably apatite, monazite, allanite/epidote and lawsonite (Hermann and Rubatto, 2009; Ague, 2017). Carbonate precipitation can explain the LILE enrichment, whereas HREE enrichment can be related to garnet growth. In Loriani, however, pumpellyite is very abundant and HREE (Martin et al., 2011; see also Chapter 9) and Y gain might be also related to a late stage. Nevertheless, the observed mass gain in HREE in sample 1cor14-12b (Fig. 6.7a) that has no pumpellyite allows proposing that this mass gain can occur during carbonate metasomatism. If the P mass gain actually corresponds to apatite crystallization, enrichment in LREE and MREE would be expected. One possible explanation is that late stage lawsonite substitution by pumpellyite could cause a mass loss of LREE and MREE. Therefore, the "integrated-signal" would give in an overall apparent mass conservation of REE, that actually results from a first gain (during carbonation) and then loss (late stage). Possible lawsonite destabilization is also suggested by Eu mass loss (sample Lor16-2, Fig. 6.5c). Alternatively, it might be related to sampling bias. Actually, carbonation seems to preferentially affect clinopyroxene domains, thus the carbonated portion of the rock would

have an initial lower concentration of LREE and MREE compared to the average composition of the bulk precursor rock (relatively enriched in lawsonite and L- and MREE).

Mass gain of Sr and Ba is not in the same proportion. Moreover, Ba enrichment is not directly related to K and/or Cs enrichment, so it can't be uniquely related to the crystallization of late stage potassic micas (e.g. sample cor16-4b in Fig. 6.6d; Spandler and Pirard, 2013). Sr mass gain is present in every sample and the final composition fall in the range of metasediments or even higher. Ba mass gain is lower compared to that of Sr and the final composition fall below the range of metasediments (for 3 samples over 5) and in the range of metasediments (for 2 samples over 5). The reason behind the decoupling of these two elements may be related to different partition coefficients and/or initial composition of the infiltrating fluid. It is interesting to compare these results with the experimental work of Johnson and Plank (1999) and with that of Tsay et al. (2017). Johnson and Plank (1999) explored the element mobility during dehydration and melting of metasediments. Below the solidus, at the experimental condition of 650 and 700°C and 2 GPa, Rb, Sr, Ba and Pb were found to be the most mobile elements, whereas Be, Nb, Ta, HREE and Th were those with the lowest abundance in the fluid phase. Tsay et al. (2017) experimentally investigated the mobility of major and trace elements in aqueous fluids in equilibrium with allanite-bearing eclogite (garnet + clinopyroxene assemblage with minor amphibole, quartz and accessory rutile) at temperature ranging from 590 to 800° and pressure from 2.4 to 2.6 GPa. One remarkable observation is the T effect on trace element partitioning between fluids and solid residue. In particular, they measured an increase of the concentration Sr and Ba by a factor of 16.7 (± 8.3) and 2.4 (± 1.4) from 590 to 700°, and by a factor of 2.5 (± 0.6) and 2.4 (± 0.8) from 700 to 800°. This resulted in significant change in the fluid Sr/Ba ratio from 0.4 to 2.5 due to the jump in Sr solubility above the 600°C. They also observed a relative increase in LREE with respect to MREE and HREE at high temperature (700-800°). However, they also pointed out

that the concentration of these elements is strongly related to the stability of rutile, zircon, and allanite/epidote. Lastly, LILE enrichment, especially Sr and Pb, seems to be a characteristic of HP Ca-metasomatism: it was also reported for lawsonite-metasomatism (Vitale Brovarone et al., 2014) and in eclogitic vein alteration selvage from Tianshan (Beinlich et al., 2010).

5.7.1.3 Selected transition metal elements: Cr, Ni, Co and V

In Figure 6.10e,f,g,h, mafic/ultramafic fluid source tracer elements are reported. Cr and Ni enrichment is due to mass gain, whereas Co and V are simply diluted (some samples display a slight V mass loss, but considering the low statistic we prefer a conservative interpretation as residual dilution). Moreover, in the Figure 6.10 the metasediments composition and relative wedge is also reported. It is interesting to note that when element mobilization occurs, rock composition moves toward the range of metasediments element concentrations. Nevertheless, the enrichment in Cr and Ni only by metasediments contribution is unlikely. The analyzed serpentinite, consistently with the average composition of ultramafic rocks, is enriched in those elements, thus a serpentinite-derived fluid could be the cause for the observed mass gain in Cr and Ni.

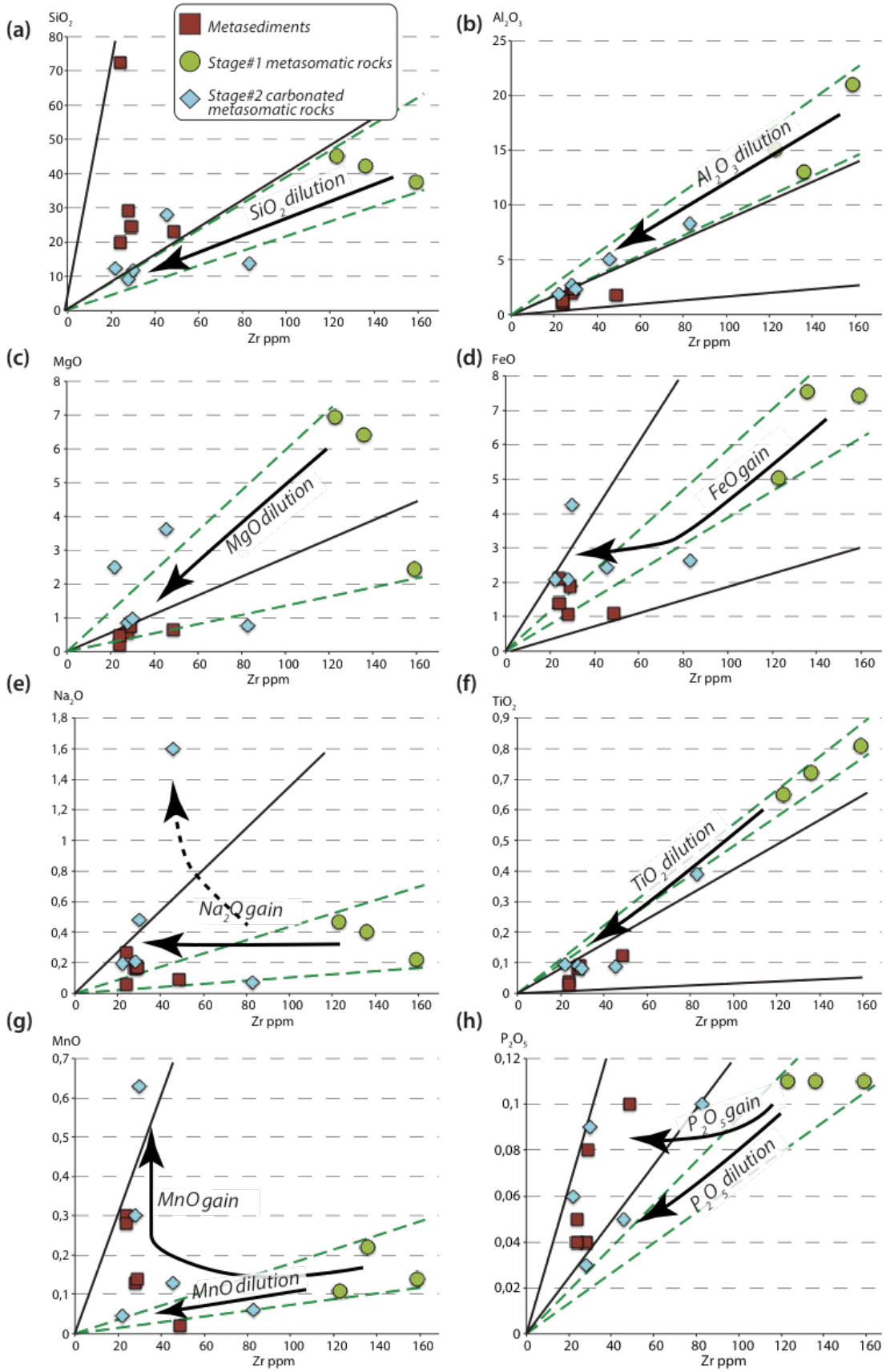

Fig. 6.10: Wedge diagrams for evaluation of composition changes between metasediments, Stage#1 rocks and Stage#2, carbonated metasomatic rocks.

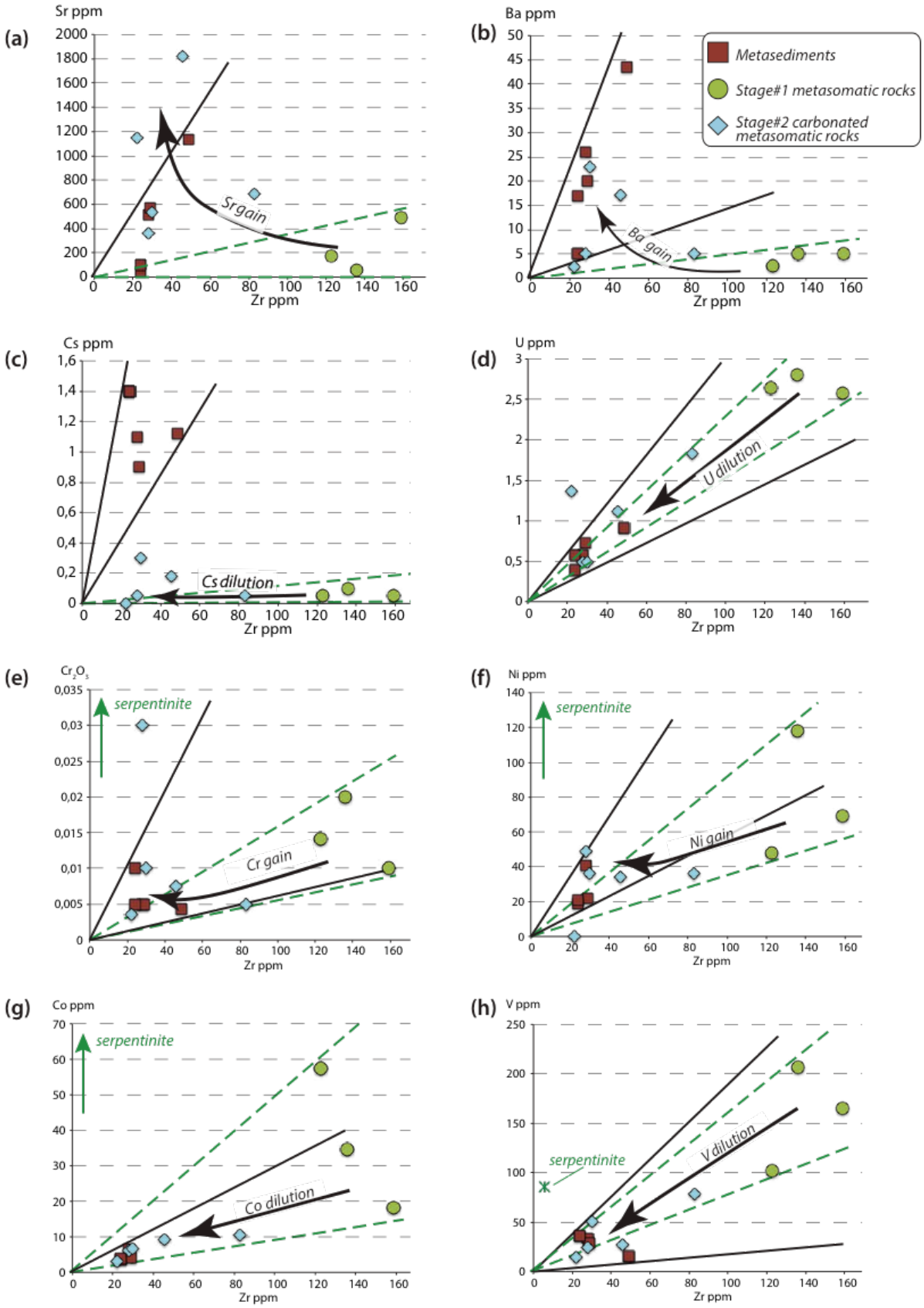

Fig. 6.11: Wedge diagrams for evaluation of composition changes between metasediments, Stage#1 rocks and Stage#2, carbonated metasomatic rocks.

6.7.2 Implications on carbon fluxes in subduction zones

Recent estimations of carbon input in subduction zones yield 39-66 Mt C/yr (Kelemen and Manning, 2015). Kelemen and Manning (2015) compilation reports that carbonate dissolution by aqueous fluids combined with metamorphic decarbonation, is responsible for a total flux of 14 to 69 Mt C/yr from the slab to the overlying arc lithospheric mantle. This large uncertainty is also due to the few constrains on the amount of fluids that percolate and react with the slab-forming rocks. Studies on HP metamorphic terrains with focus on the estimation of time-integrated fluid fluxes show the amount of fluid flow, reaction rate and element redistribution are deeply connected (e.g., Zack and John, 2007; Ague, 2014). Most exhumed subducted material, however, show only very limited evidence for fluid flow and, consequently, few works report high fluid fluxes within the subducting slab. For example, Zack and John (2007) found that only in veining systems near the top of the slab, time-integrated fluid fluxes reach 10^3 m^3/m^2. Moreover, extremely channelize fluid flow (i.e., in veins) also means that the majority of rock body will likely escape interactions with fluids. In this study, we gave evidence for extremely high fluid fluxes, in the range of 10^6 m^3/m^2, that, at peak metamorphic conditions, correspond to CO_2 flux of ca. 300 t/m^2. Notably, these estimations are not based on veining system, but on bulk rock mass changes in metasomatic rinds that have considerable width, from 3 to 8m. Moreover, we report mass gain of alkaline and alkaline earth elements (Ca, Na), LILE (Sr, Pb, Ba, ± U), together with elements that are more concentrated in ultramafic rocks like Cr and Ni. This fluid geochemical pattern matches quite well with the chemistry of fluids of mafic/ultramafic origin that interact with subducted metasediments (Breeding et al., 2004; Beinlich et al., 2010; Ague and Nicolescu, 2014). The peak pressure conditions (2.2-2.3 GPa) roughly correspond to the forearc depth of the fluid flux pulse from the subducting slab (Gorman et al. 2006). Gorman et al. (2006) estimated, for cold subduction, a peak of CO_2 flux in the forearc at ca. 70km depth. In Figure 1.3 it is shown

that the CO_2 flux peak actually corresponds also to H_2O flux peak, this latter mainly linked to lawsonite breakdown reaction (Gorman et al., 2006). In their model, the fore arc CO_2 flux is of $11.9 \cdot 10^6$ mols·km^{-1}yr^{-1}. Considering that the length extension of the Honshu arc is roughly 800km, the flux is 0.015 mols·m^{-2}yr^{-1}. We can transform the results of q_{TI} by multiplying the flux for the estimated CO_2 wt.% (0.05 wt.%, Kelemen and Manning, 2015) and for the CO_2 molar volume at 520°C and 2.3 GPa (13.3 mol·m^{-3}) in to obtain a CO_2 flux in terms of mols·m^{-2}. The resultant time-integrated CO_2 flux is $16.7 \cdot 10^6$ mols·m^{-2}. In order to compare our estimation with that of Gorman et al. (2006) we should also estimate: i) the duration of the interaction; ii) the length of the subducted slab involved. Those are difficult parameter to constrain because they require knowing the subduction rate, the dimension of the subducted slab and the extension of the exhumed portion.

As a first order approximation, knowing that the eclogitic peak is dated at 34Myr and the blueschist at 37Myr (Vitale Brovarone and Herwartz, 2013) there is a minimum duration for the HP fluid-rock interaction of 3Myr. Moreover, the Nappes Supérieures emplaced between 37 and 40My (biostratigraphic constrains). We can take a representative period of 5Myr for HP fluid-rock interaction, and obtain a CO_2 flux of 1.5 mols·m^{-2}yr^{-1}, which is two orders of magnitude higher than the values modeled by Gorman et al. (2006). Nevertheless, this value is extremely speculative and should be taken with great caution, not only because of the uncertainties on the above reported parameters, but also because the different "boundary" conditions. Actually, Gorman et al. (2006) use a model for the subducting oceanic lithosphere that is very different from the reconstructed tectonostratigraphy of Alpine Corsica. By consequence, the initial volatile content of both metasedimentary pile and altered oceanic crust will be very different. Moreover, also the location on a P-T diagram of the major dehydration reactions will be different. For example, previous study and our field observations attest to the lack of lawsonite breakdown at peak metamorphic conditions

(Vitale Brovarone et al., 2014a; Vitale Brovarone and Beyssac, 2014), whereas in the model reported in Gorman et al. (2006) the main water source, for comparable P-T conditions, was the lawsonite breakdown reaction. This means that, for the Alpine Corsica case, the water-rich fluid source must come from deeper portion of the slab.

CHAPTER 7
Oxygen, carbon and strontium, neodymium isotopes systematics of carbonated metasomatic rocks

The understanding of HP and UHP metamorphism ground on the investigation of physical and chemical processes at convergent margins, by mean of mineralogy, metamorphic petrology, experimental petrology, geochronology, structural geology, and geodynamic modeling (Rumble, 1998). Stable and radiogenic isotope geochemistry has also proven to be an important tool in HP and UHP metamorphism investigations (e.g., Yui et al., 1995; Rumble et al., 1998; Wang and Rumble, 1999). Actually, stable and radiogenic isotopes have been used not only to get absolute date, but also as a tracer of petrogenetic processes. In fact, fluid infiltration during metamorphism play a role in promoting equilibration of isotopic system used as geochronometers (Glodny et al., 2003; Schneider et al., 2007; 2008). Moreover, radiogenic isotope signature (e.g., Be-Hf-Nd-Sr-Pb) has been used to constrain nature and source of deep fluids/melts (e.g., Tera et al., 1986; Cannaò et al., 2015; Fernandez et al., 2016).

Stable isotopes have been largely used to get insights on protoliths, geothermometry, fluid-rock interactions, and fluid sources. For example, Rumble and Yui (1998) demonstrated that the isotopic composition heterogeneities of inherited pre-subduction garnet can be preserved even in rocks transformed at coesite-bearing facies conditions. Actually, even during metamorphism, full isotopic homogenization may not be achieved in rocks that remain devoid of fluids (Glodny et al., 2003, 2008), given that without fluids, isotopic resetting is kinetically locked or restricted to sluggish intermineral diffusion. The finding of preservation of isotopic

signature through metamorphism had major geodynamic implications because it proved that rocks that were at Earth's surface can actually be brought down in subduction zones. Moreover, the observed preservation of the protolith rock isotopic signature over large distances proved that the study UHP rocks were subducted and exhumed as coherent unit.

7.1 Oxygen, carbon and strontium, neodymium isotopic range of natural samples

The average composition of the oceanic lithosphere is well defined, but chemical and isotopic compositional heterogeneities may exist (e.g., Rampone and Hofmann, 2012). Moreover, the oceanic crust undergoes a complex history of seafloor weathering and various degree of hydrothermalism. For example, low temperature alteration in the upper section of the oceanic crust produces high $\delta^{18}O$ values (>5.7‰), whereas alteration at high temperature produces depleted $\delta^{18}O$ values (<5.7‰) compared to mantle values (e.g. Gregory and Taylor, 1981). Strontium isotopic composition can be strongly modified by seawater-rock interactions: altered abyssal peridotite yields $^{87}Sr/^{86}Sr$ ranging from typical mantle values (0.703) to crustal values (0.710) (e.g., Snow et al., 1994; Hattori and Guillot, 2007; Salters and Stracke 2004; Harvey et al., 2014). Even if the pervasiveness of the alteration generally decreases with depth in the ophiolite pile and the average bulk composition may remain unaffected, these heterogeneities may contribute to fluids or partial melts derived from the crust by metamorphic reactions (Staudigel et al., 1995; Kawahata et al., 2001). Further complexities are added by the fact that these isotopic ratios also vary due to radiogenic growth and temporal isotopic variation in seawater for $^{87}Sr/^{86}Sr$ (Fig. 7.1a,b), and due to temperature exchange for $\delta^{18}O$. Therefore, without knowing the original signature of the protolith rock, it is often difficult to establish the contribution of metamorphic fluids to the final isotopic signature. On the other hand, Nd isotopes are largely insensitive to seawater alteration (e.g., Michard et al., 1983; Michard and Albarède, 1986; Snow and Dick, 1995). Even if Nd

isotopic composition of peridotite shows a large range of values, i.e. εNd[1] ranges from minimum value of -3 to maximum value of 20 (Rampone and Hofmann, 2012), most of the values range within an interval between 5 and 12 (εNd). The MORB εNd major frequency (>90%; Rampone and Hofmann, 2012) also falls in this interval.

Nd isotopic signature in granitoids also displays a large variability, which is mainly linked to their origin (i.e., geodynamical context, nature of reservoir, petrogenetic processes undergone) and age (Fig. 1c; Allègre and Ben Othman, 1980). Hercynian granites formed in collisional setting (e.g., Himalaya and Alps) have been extensively studied from chronological, isotopic, and petrological point of view (e.g., Michard and Allègre, 1975; Allègre and Ben Othman, 1980; Cocherie et al., 1994; Roberts et al., 2000; Denele et al., 2012). Nd (and Sr) isotopic composition of granitoids has been often used in order to provide strong constraints on their origin and evolution (e.g. mantle derivation vs. continental crust recycling, processes registered). In the Pyrenean, the group of granites with younger age (280 My) always has negative εNd_i, ranging from -0.7 to -8.9 (Querigut group in Fig. 7.1c), and initial $^{87}Sr/^{86}Sr_i$ ranging from 0.70633 to 0.7153. The usefulness of Nd isotopes is due to the intrinsic chemical properties of rare-earth group elements (REEs) and in particular medium REE: (i) they are mostly not mobile; (ii) a large geochemical fractionation of the Sm/Nd parent/daughter ratio is difficult. Therefore, also for the continental crust Nd can be considered as a mostly immobile chemical element.

Altogether, great caution must be exercised in assigning the cause of the observed isotopic reset to metamorphic processes or to pre-metamorphic events, e.g. natural heterogeneities.

[1] εNd is the standard epsilon notation relative to a Chondrite Unifrom Reservoir (CHUR):

$$\varepsilon Nd = \left[\frac{^{143}Nd/^{144}Nd_{sample}}{^{143}Nd/^{144}Nd_{CHUR}} - 1\right] \times 10^4$$

with $^{143}Nd/^{144}Nd_{CHUR}$ = 0.512638 (Jacobsen and Wasserburg, 1980).

Nevertheless, coupling different isotopic systematic like O-C, Sr-Nd and O-Sr can help distinguishing between metamorphic and pre-metamorphic events and also can inform on the source of fluids that interacted with the rocks.

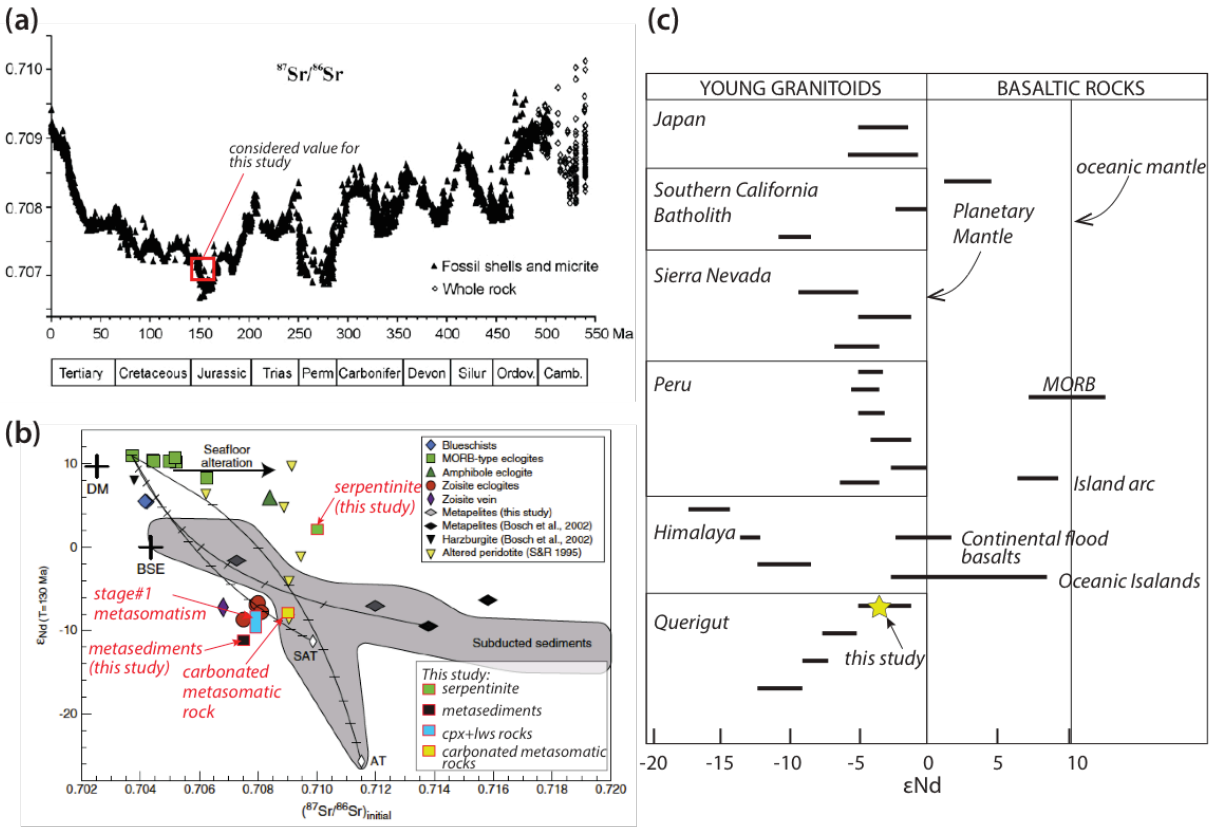

Fig. 7.1: a) Seawater Sr isotopic composition variation through time (modified from Prokopih et al., 2008; time-scale GTS2004, Gradstein et al., 2004). The red box indicates the value considered, for comparison, in this study. b) Sr-Nd diagram (Halama et al., 2011) reporting the isotopic values for different lithologies from the HP Raspas complex (Ecuador), and showing the effect of seawater alteration. Blue, black, yellow and green boxes indicate, in comparison, where the samples from the present study are located. c) Compilation of Nd isotopes variation in young granitoids and basaltic rocks from different geological setting (from Cocherie et al., 1994). Yellow star indicates the Nd isotopic composition of metagranite analyzed during this study.

7.2 Oxygen and carbon stable isotopes in metamorphic carbonate-bearing rocks

Oxygen and carbon isotope ratios are commonly used as monitors of fluid flow and fluid-rock interactions because the isotopic signature of these systems may reflect the extent of chemical exchange between fluid and rocks. Coupled oxygen-carbon isotope variations are seen in many metamorphic systems involving carbonate rocks (e.g., Bickle et al., 1992; Gerdes et al., 1999; Bowman et al., 2009; Beinlich et al., 2012). Six factors contribute to the isotopic composition of a metamorphic rock (Baumgartner and Valley, 2001): (1) the composition and

concentration in oxygen and carbon of the pre-metamorphic protolith; (2) devolatilization reactions (batch and Rayleigh volatilization, dehydration and mixed volatile reactions; Ruble, 1982; Valley, 1986); (3) the temperature of exchange; (4) exchange kinetics; (5) fluid composition and concentration, and (6) fluid fluxes. In a closed-system, the magnitude of the variation of $\delta^{18}O$ and $\delta^{13}C$ is directly linked and can be calculated if reaction stoichiometry is known. In open system, fluid-rock interaction is modeled by considering the stable isotope mass balance between fluid and rock, following the flow direction (Bear, 1972). The shape of the predicted isotope front, as well as its speed of propagation, depends on the mechanism of stable isotope transport (advection, diffusion, hydrodynamic dispersion, see Chapter 6, Section 6.1), the isotope kinetics, and the composition of the fluid and the rock (e.g., Bickle et al., 1997; Skelton et al., 2000; Baumgartner and Valley, 2001). Oxygen isotope system is also widely used to distinguish between external and internal fluid sources (e.g., Bebout and Barton, 1993; Barnicoat and Cartwright, 1995; Bickle et al., 1997; Zheng et al., 2003). Carbon isotopes might also be very useful since different reservoir have clearly distinct isotopic signature. Carbon signature of carbonates in subducted sediments of marine source and oceanic crust usually is around 0‰ in $\delta^{13}C$ (PeeDee Belemnite standard -PDB), whereas marine biogenic organic matter typically has values ranging from -25 to -10‰ (e.g. Cartwright and Barnicoat, 1999; Cook-Kollars et al., 2014; Collins et al., 2015).

Taking into account all the factors that contribute to the final isotopic signature of the rock, oxygen and carbon isotopes geochemistry can nevertheless be considered as an efficient and widely used tool for studying HP-LT metasomatic processes involving carbonates (e.g. Valley 1986; Wang & Rumble 1999; Ague and Nicolescu, 2014; Galvez et al., 2013a,b). For example, this approach was of pivotal importance for Galvez and co-workers to demonstrate that the graphite found in reaction zones along serpentinite-metasediments interfaces was actually derived from carbonate reduction reaction (Galvez et al., 2013a,b).

7.2.1 Oxygen and carbon stable isotopes in the HP-LT Corsican ophiolite

Stable isotope geochemistry of the Corsican ophiolite was extensively investigated by Miller et al. (2001) over a wide range of P-T conditions. The major conclusions of this work are: (1) variation of the isotopic signature of the ophiolite (when present) do not correlate with metamorphic grade; (2) oxygen and carbon isotopes of carbonates in the ophiolite are not in equilibrium with the mafic/ultramafic host rocks at HP conditions, but preserve the marine signature; (3) based on hydrogen isotopes, they concluded that serpentinization occurred during seafloor hydrothermal alteration and during the tectonic emplacement of the ophiolite; (4) fluids produced during metamorphic dehydration must be highly channelized or exit the slab relatively quickly so as to not interact with it. Figure 7.2 reports the oxygen isotopic values from Miller et al. (2001) together with the analyses of metasomatic rocks and minerals from this study. As it will be discussed in the following sections, the analyses of oxygen isotopes proved the existence of an isotopic front in rocks along major lithological boundaries.

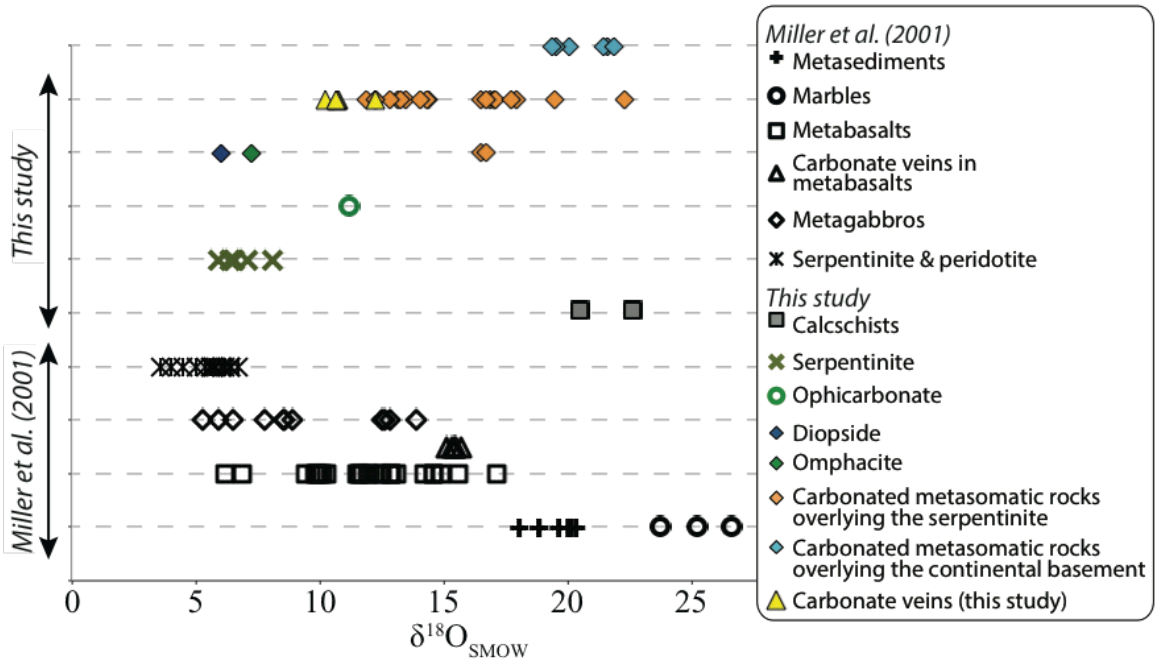

Fig. 7.2: Diagram reporting the $\delta^{18}O$ composition for different lithologies in the HP metamorphic ophiolite of Alpine Corsica (Miller et al., 2001) together with the samples from this study.

7.3 Strontium and neodymium isotopes in metamorphic carbonate-bearing rocks

Sr and/or Nd isotope geochemistry has been used to unveil the effects of metamorphic fluids in mélange rocks and eclogite unit (e.g. King et al., 2006; van der Straaten et al., 2012) or to recognize pre-metamorphic seafloor alteration in ophiolitic units (Barbieri et al., 1979; Miller and Stosch, 1988; Bickle and Teagle, 1992). This technique has also been widely used to constrain fluid flow during regional metamorphism in carbonate-bearing system (e.g., Bickle et al., 1997), since Ca-bearing minerals can host significant amount of Sr due to the behavior of bivalent metal cations (such as Mn, Fe, Sr) to substitute for Ca and Mg. Therefore, the investigation of Sr-Nd signature of carbonated metasomatic rock might give insights on fluid sources and nature of protolith rocks. Moreover, combination of different isotopic systems, i.e. O-C and Sr-Nd, can then better constraint the isotopic front (e.g., Abart et al., 2002).

7.4 Results

7.4.1 Oxygen, carbon stable isotopes of carbonated metasomatic rocks and carbonate veins

We analyzed O and C isotopes of calcite and O isotopes of clinopyroxene and antigorite. We decided to do not analyze a bulk isotopic composition for silicate carbonate-free rocks because it is of difficult interpretation due to the observed only partial equilibration of multiple parageneses and mineral zoning, thus we prefer to test single equilibria between phases. Part of these results have been discusses in Chapter 4, thus, here we will only recall the most important aspects.

Stable isotopes analyses (oxygen and carbon) were performed on 32 samples of carbonated metasomatic rocks, as well as on unaltered rocks (Table 7.1). As a whole, carbonated metasomatic rocks display a characteristic trend of decreasing oxygen signature, from 20‰ toward 10‰ (Standard Mean Ocean Water-SMOW; 7.3 and see also Fig. 7c in Piccoli et al., 2016), trend that is not correlated to the carbonate content (Fig. 7.b in Piccoli et al., 2016

Chapter 4). Carbon has a classical marine metasediment signature with values spanning from -2 to 4‰ (PDB) (Fig. 7.3). Carbonate (± omphacite, ± lawsonite) in HP veins cutting across the metasomatic rind has light values of 10.7‰, even lighter than carbonate veins in metabasalts reported by Miller et al. (2001)(ca. 15‰, Fig. 7.2). An exception exists for carbonated metasomatic rocks overlaying the continental crust: these rocks systematically display heavier $\delta^{18}O$ signature that falls in the range of metasediments (between 20 and 25‰; Figs. 7.2 and 7.3). Among the carbonated metasomatic rocks sampled along the contact with the serpentinite, only sample 1cor14-10g yields heavy $\delta^{18}O$ signature. As described in the previous section (Section 5.1) this sample escaped Stage#1 metasomatism and is interpreted as the metasomatic transformation of a leucocratic jadeite-bearing dyke. This trend of decreasing oxygen and stable carbon isotopic signature is evidence for the precipitation of carbonates from fluid equilibrated with a mafic or ultramafic rock (Fig. 7.3, see also the discussion in Chapter 4.1, Section 8.2).

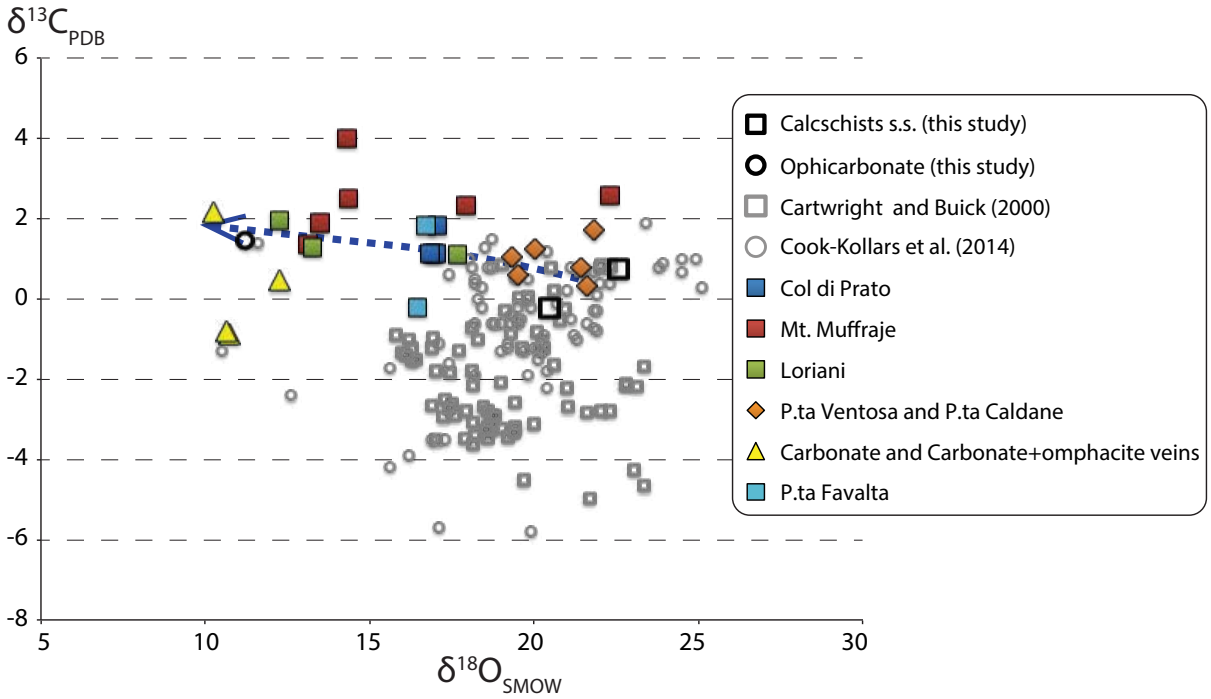

Fig. 7.3: Plot of $\delta^{18}O$ vs. $\delta^{13}C$ of analyzed carbonated metasomatic rocks and unaltered Mesozoic metasediments. The blue arrow indicates the trend of decreasing $\delta^{18}O$. Compilation of eclogite facies metasedimentary carbonates from Alpine Corsica (Cartwright and Buick, 2000) and Western Alps (Cook-Kollars et al., 2014) are also reported for comparison.

In order to better understand the significance of the results from oxygen and carbon isotopes of calcite, we wanted to test the isotopic equilibrium between the silicate paragenesis and the carbonates. We selected a sample of omphacite+calcite vein hosted in a lawsonite+diopside rock (Fig. 3 in Piccoli et al., 2016; see also Fig. 7.11). Indeed, in such a context clinopyroxene can be extracted by handpicking without risk of contamination (i.e. coronitic reaction or rims of omphacite on diopside would give a mixed results). Omphacite and diopside were analyzed using laser-assisted fluorination at IPGP (Paris, France). Lawsonite was not analyzed because of its content in OH groups and water which will unable the measurements. Diopside has $\delta^{18}O$ values of ~6‰. Vein infill omphacite has heavier $\delta^{18}O$ of ~7‰. In the range of geological interest conditions, oxygen isotope geothermometers are essentially independent of pressure (Taylor and Coleman, 1968). Thus, using fractionation factors available from literature data ($\Delta_{cc\text{-}cpx}$), we estimated a T of equilibration of 494°C (±30°) for the omphacite-carbonate assemblage (based on Hoffbauer et al., 1994) and 426°C (±20°) for diopside-carbonate using the same database (Hoffbauer et al., 1994). These different temperatures are consistent with textural disequilibrium between the three minerals (carbonate, diopside and omphacite). The omphacite-calcite thermometer yields T closer to the estimated peak T conditions of the metamorphic unit (490-530°C). This observation suggests the equilibrium for the omphacite + carbonate paragenesis and confirms the microstructural observations. Equilibrium was likely reached by fluid-mediated reactions. These results are discussed in the paper of Piccoli et al. (2016) published in Earth and Planetary Science letters (see Chapter 4).

7.4.2 Oxygen stable isotopes of serpentinite

As described in Section 5.1, the serpentinized basement does not show any macroscopic evidence for fluid infiltration. However, as it will be described in the following, the two analyzed samples of serpentinite for Sr and Nd isotopes give Sr values extremely high and

significantly different from typical mantle values (e.g. Salters and Stracke, 2004). Variation in Sr and O composition during seawater alteration usually correlates well and often defines a linear trend (e.g. Staudigel et al., 1995). Thus, we performed oxygen isotopic composition of 6 antigorite samples from the San Petrone unit (Table 7.2): three from nearby the contact with the metasomatic rind (1cor12-11a and 1cor12-11b, from Aja Rossa, cor13-14a from Mt Muffraje area; Fig 7.4a,b), two from deeper position, ca. 30-50 m from the lithological boundary (cor16-23a and cor16-23b, from Punta Caldane area; Fig. 7.4b), and one sampled nearby a non metasomatized contact between the serpentinite and the continental sliver (sample cor13-10a near Punta Ventosa area; Figs. 5.2a). Results are reported in Table 7.2.

Location	***Sample***	***distance from the contact***	***Average $\delta 18O_{SMOW}$***	***1σ***
Aja Rossa	**1cor12-11a**	2 m	5,94	--
	1cor12-11b	20 cm	6,40	0,21
P.ta Ventosa	**cor13-10a**	3m	7,09	0,10
Mt. Muffraje	**cor13-14a**	20 cm	8,08	0,00
P.ta di Caldane	**cor16-23a**	30 m	6,40	0,30
	cor16-23b	50 m	6,58	0,06

Table 7.2: Stable oxygen isotopes of antigorite

Considering the low number of analyzed samples and the natural high variability in $\delta^{18}O$ signature of the ocean floor serpentinites (e.g., Agrinier et al., 1995; Skelton and Valley; 2000) a unique trend cannot be defined. However, the consistency of measures on sample cor16-23a and cor16-23b points to a more homogeneous isotopic signature in the serpentinite far from the lithological boundaries. Other isotopic studies on serpentine from HP unit in Alpine-Corsica area yield generally quite homogeneous values around 6-6.5‰ (e.g. Miller et al., 2001; Galvez et al., 2013b) with no variation correlated to distance from lithological contacts (Galvez et al., 2013b). However, comparing our results with these values from previous works requires cautions. Actually, samples from Miller et al. (2001) are not associated to a specific tectonostratigraphic position (i.e., sampling were not performed along

profiles), whereas the study unit in Galvez et al. (2013b) reached lower metamorphic conditions compared to the San Petrone unit, of ca. 100°C less. This difference in temperature is significant when considering oxygen mineral-fluid equilibria.

Woks in HP metamorphic units from the Western Alps interpreted as coherent portions of OCT (e.g., Barnes et al., 2014) reported geochemical and isotopic front in the serpentinite juxtaposed to metasediment. Barnes et al. (2014) explains the high $\delta^{18}O$ values of serpentinite near the contact with metasediments by the interaction with a metasediment-derived fluid, possibly during the transition from lizardite to antigorite during subduction. The isotopic profile with decreasing $\delta^{18}O$ from the contact toward deeper structural positions was explained by higher fluid/rock ratio along the lithological boundary with metasediments.

7.4.3 Sr-Nd isotopes of carbonated metasomatic rocks and carbonate veins

Sr and Nd isotopic analyses were performed on a total of 24 samples, including carbonated metasomatic rocks, HP carbonate-bearing veins, Stage#1 metasomatic rocks, and unaltered rocks representative of different lithologies of the San Petrone unit (Table 7.3). In details, the following samples were analyzed: 8 carbonated metasomatic rocks, 2 carbonate-omphacite vein, 1 carbonate vein, 2 samples of serpentinite, 3 samples of lawsonite-clinopyroxene metasomatic rock (metasomatism Stage#1), 3 Mesozoic metasediments (2 calcschists and 1 metachert), 1 orthogneiss, 2 ophicarbonates, one from HP unit, the other one from a low-grade unit. All samples except the low-grade ophicarbonate were sampled in the lawsonite-eclogite unit of San Petrone (Fig. 5.2). The low-grade ophicarbonate was sampled in the low-grade blueschist unit, nearby Bigorno Pass (Vitale Brovarone et al., 2014b).

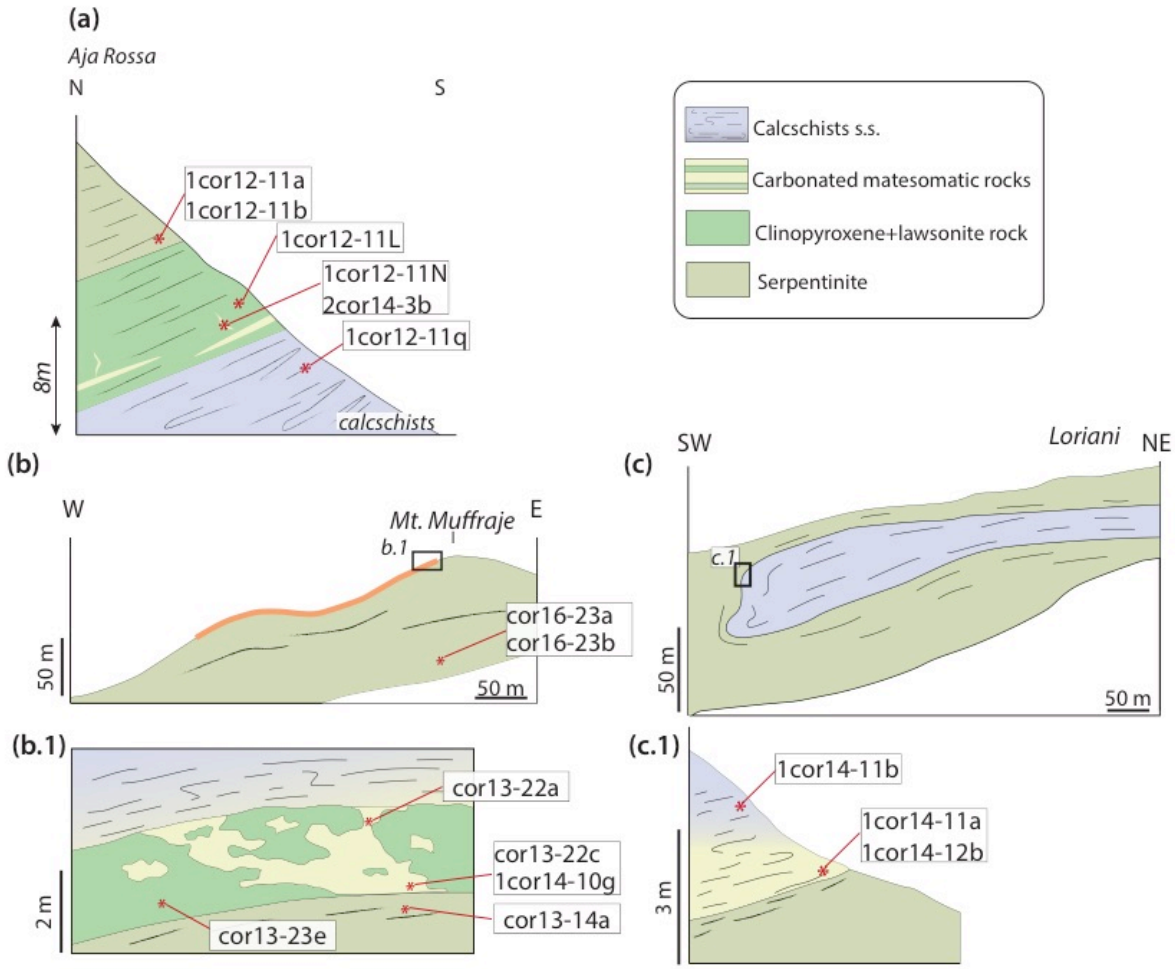

Fig. 7.4: Geological cross sections and location of samples analyzed for O-C and Sr-Nd isotopes. **a)** Geological cross section of the Aja Rossa outcrop. **b)** Geological cross section of Mt. Muffraje area. In this area the cover thickness is out of scale and its location is marked by the orange line. Note that sample location wants to be indicative. The two samples cor16-23a and cor16-23b were sampled in this structural position, but southern toward P.ta Caldane. b-1) Simplified cross section of the metasomatic rind and relative sample location. **c)** Geological cross section of the area of Loriani. Metasediments are in the core of a tight, recumbent fold. c-1) Geological cross section of the forelimb of the fold depicted in (c) displaying the up-right contact between the serpentinite and Mesozoic cover. The first 3 m are of the cover are intensely metasomatized.

The chosen carbonated metasomatic rocks are all from the metasomatic rind forming along the contact with the serpentinite. This choice is based on the following reasons: (i) the HP metasomatic origin of the sample is better constrained by the relationship with the surrounding rocks and by petrological observations, i.e. carbonates precipitated from HP fluids and are not a product of oceanic hydrothermal alteration; (ii) the mineral assemblages are thoroughly described and mineral compositions well known; (iii) oxygen-carbon isotope geochemistry clearly shows a reset of carbonate oxygen isotopic composition by the

interaction with a fluid (Piccoli et al., 2016; Fig. 7.3); (iv) metasomatic rinds forming along the contact with the serpentinite are more widespread compared to those along the continental basement-metasediments contact. Therefore, the selected samples are more likely to be representative of metasomatism induced by regional scale fluid flow, rather than locally produced fluids; (v) In three localities, Aja Rossa, Mt Muffraje and Loriani, it was possible to sample along a profile with increasing distance from the lithological boundary (Fig. 7.4). In the Mt Muffraje area (Fig. 7.4b), one sample close to the serpentinite (ca. 0.5-1 m, cor13-22c) and one at ca. 3 m (sample cor13-22a) were analyzed. Sample 1cor14-10g also comes from the Mt Muffraje area, near the contact (ca. 0.5-1 m), but it displays a different mineralogy, notably clinopyroxene is jadeite (see Section 5.1 for petrographic details). In Loriani (Fig. 7.4c), one sample adjacent to the serpentinite (1cor14-11a) and one ca. 3 m from the contact (1cor14-11b) were analyzed (for O, C, Sr, and Nd). All samples were analyzed for their bulk rock isotopic composition, except for the veins where the carbonate portion was separated from the omphacite crystals. Highly clean omphacite crystals were separated by handpicking under binocular microscope and then leached twice for 30 min at 120°C with 2.5 N HCl and 6 NHCl, respectively, rinsed several times with ultrapure water between each leaching step, and finally put in the ultrasonic bath during 15 min in 2 N HNO_3 before several steps of ultrapure water rinses. For few selected samples (see Table 7.3), we also performed leaching experiments in order to analyze the residues, following the procedures described by Bosch (1991). Results are reported in Figure 7.5a and Table 7.3.

Unaltered metasediments: the two samples of calcschists have slight different $^{87}Sr/^{86}Sr_i$ composition (0.707746 and 0.708482) but nearly identical $^{143}Nd/^{144}Nd_i$ (0.512052 and 0.512035). These Sr isotopic signatures are slightly higher than the Jurassic seawater pole (values range between 0.7070 and 0.7075; Burke et al., 1982; Veizer et al., 1999; Prokoph et

al., 2008; Fig. 7.5a). The difference of $^{87}Sr/^{86}Sr_i$ ratios between the two samples can be explained by various quantity of detrital component with continental affinity, present in the samples (e.g. micas). This interpretation is supported by the leaching experiments: in both cases, the leached fraction yields higher $^{87}Sr/^{86}Sr$ ratio than unleached whole rock. This supports the fact that the rock was not completely homogenized during metamorphism and that hydrochloric acid has preferentially removed the carbonated phase present in different proportion in the two studied samples. The radiolarian metachert analyzed shows a $^{87}Sr/^{86}Sr_i$ signature at 0.708091 in the same range than studied calcschists, but yields slightly higher $^{143}Nd/^{144}Nd_i$ (0.512190).

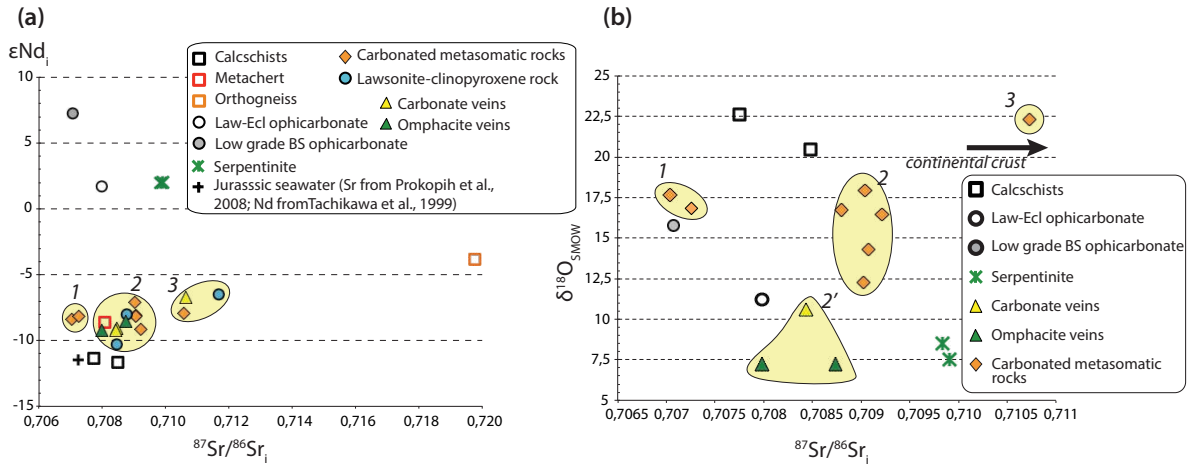

Fig. 7.5: Diagram of $^{87}Sr/^{86}Sr_i$ vs. $^{144}Nd/^{143}Nd_i$ **(a)** and $^{87}Sr/^{86}Sr_i$ vs. $\delta^{18}O$ **(b)** for the analyzed samples. Blue arrows indicate possible mixing lines to explain the measured isotopic composition of carbonated metasomatic rocks. Shaded area group sample by their isotopic composition. Samples grouping coincide in both (a) and (b), but note that not all samples have been analyzed for O and also Sr-Nd isotopes. See text for the definition and the details of each group.

Gneiss: only one continental crustal rock was analyzed during this study. It was sampled from an orthogneiss sliver in contact with the serpentinite basement (Fig. 5.2e). The basal portion of the continental sliver is intensely metasomatized during Stage#1 and then affected by pervasive carbonate veining. The sample selected for Sr-Nd analyses was sampled far from the metasomatic rind (ca. 2.5 m). It yields isotopic ratios of 0.719761 and 0.512438 (εNd_i -3.81) for $^{87}Sr/^{86}Sr_i$ and $^{143}Nd/^{144}Nd_i$, respectively. These values are consistent with the isotopic signature of Hercynian granite from the Pyrenean (Fig. 7.1). Moreover, whole rock

trace elements ratios of this sample shows that it falls in the range of leuco-granites from Corsica (Fig. 7.6).

Ultramafic rocks: during this study, two types of ultramafic rocks were analyzed: serpentinite and ophicarbonate. The serpentinites samples (cor13-14a and 1cor12-11b) have relatively homogeneous isotopic signatures with higher $^{87}Sr/^{86}Sr_i$ and relatively lower $^{143}Nd/^{144}Nd_i$ than typical mantle values, i.e. 0.709841-0.709908 and 0.512736-0.512739, respectively. Nevertheless, the relatively low $^{143}Nd/^{144}Nd$ value (Fig. 7.5a) falls in the range of orogenic peridotite as reported for example by Rampone and Hofmann (2012) and Marchesi et al. (2017), whereas $^{87}Sr/^{86}Sr$ ratio is significantly higher than seawater composition or marine metasediments. This unusual Sr composition can be explained by infiltration of seawater bearing suspended detrital, continent-derived, particulates like clays during the seafloor alteration (e.g., Snow et al., 1993).

The ophicarbonate sample yields comparable $^{143}Nd/^{144}Nd_i$ (0.512723), but lower $^{87}Sr/^{86}Sr_i$ (0.707983), buffered at the same values than those of analyzed metasediments. Moreover, in the leaching experiment, silicate and carbonate fractions yield almost the same $^{87}Sr/^{86}Sr_i$ values (0.708110 and 0.707944, respectively), suggesting that almost complete homogenization was reached during seafloor alteration and/or metamorphism.

Lastly, the low-grade ophicarbonate from the Bigorno pass displays a bulk $^{87}Sr/^{86}Sr$ almost identical to that of the carbonate fraction (0.707073 and 0.707072, respectively), in prefect equilibrium with the Jurassic seawater composition (values range between 0.7070 and 0.7075; Burke et al., 1982; Veizer et al., 1999; Prokoph et al., 2008). The silicate fraction yields a slightly lower $^{87}Sr/^{86}Sr_i$ (0.706462), suggesting that complete equilibrium with seawater was not achieved during seafloor alteration nor during metamorphism. The $^{143}Nd/^{144}Nd_i$ signature (0.513007) falls in the range of typical mantle-derived rocks (e.g., Salters and Stracke 2004; Rampone and Hofmann, 2012; Marchesi et al., 2017).

Lawsonite-clinopyroxene rocks

The three lawsonite-diopside rocks (Stage#1 metasomatic rocks) were sampled along the contact with serpentinite (Fig. 7.4). Field observations unequivocally attests that sample cor16-50 forms at the expense of an orthogneiss. In the area of sampling of the other two samples (1cor12-11L from Aja Rossa and cor13-23e from Monte Muffraje) the metasomatic rind overprint the continental crust and the overlaying metasediments in such a way that the original contact between the serpentinite and the overlying rocks is not longer visible (see Section 5.1). Sample 1cor12-11L was sampled in the most external portion of the metasomatic rind, moving away from the contact with the serpentinite (Fig. 7.4a). This part of the metasomatic rind has been interpreted as the metasomatic transformation of Mesozoic metasediment by previous studies (Vitale Brovarone et al., 2014a). Conversely, sample cor13-23e was sampled in the metasomatic rind near the contact with the serpentinite in Mt Muffraje area (Fig. 7.4b). The funding of pre-Alpine HT garnet in the metasomatic rind rocks (Section 5.1) makes us propose that the Stage#1 rock was a mafic paragneiss, by analogy with the conclusion of previous studies in the same unit (Martin et al., 2011). Samples 1cor12-11L and cor13-23e have very close $^{87}Sr/^{86}Sr_i$, i.e. 0.708458 and

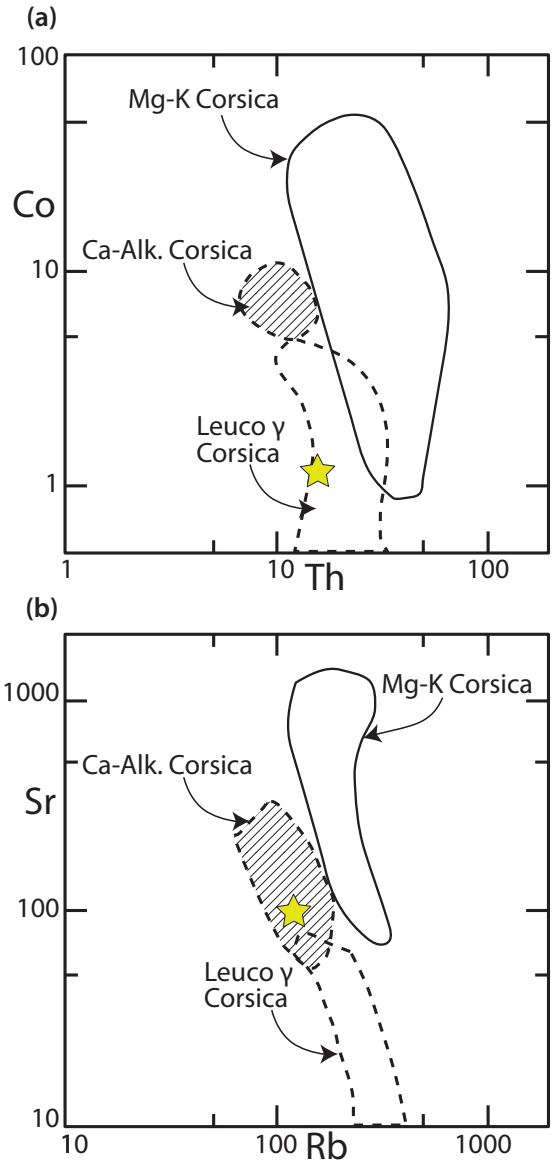

Fig. 7.6: a) Logarithmic plot of Th (ppm) vs. Co (ppm) concentration and-b) logarithmic plot of Rb (ppm) vs. Sr (ppm) concentration for the classification of Corsican batholith. The star indicates the composition of the orthogneiss from this study (Fig. adapted from Cocherie et al., 1994).

0.708750, respectively, but different $^{143}Nd/^{144}Nd_i$, i.e. 0.512106 and 0.512223, respectively. These $^{87}Sr/^{86}Sr_i$ are in the range of those measured for Mesozoic metasediments, but $^{144}Nd/^{143}Nd_i$ values are significantly higher. Sample cor13-50 clearly yields distinct Sr-Nd isotopic compositions than other lawsonite-diopside samples, with significantly higher $^{87}Sr/^{86}Sr$ and $^{143}Nd/^{144}Nd$ ratios, i.e., (0.711696 and 0.512300, respectively).

Carbonated metasomatic rocks

Carbonated metasomatic rocks are characterized by a quite homogenous $^{143}Nd/^{144}Nd_i$ composition (εNd_i ranging from -7.06 to -9.14), whereas the Sr isotopic compositions are more dispersed with values ranging from 0.70726 to 0.710733 (Fig. 7.5a, Table 7.3). Three groups can be distinguished based on the $^{87}Sr/^{86}Sr$ value (Fig. 7.5a): (i) samples 1cor12-20d and sample 1cor14-11d in total equilibrium with Jurassic seawater composition and providing an average value of 0.707148 (± 0.000158, n=2; Group 1, Fig. 7.5a); (ii) all the other samples have more radiogenic $^{87}Sr/^{86}Sr_i$ ratio, higher compared to both to the metasediments and the lawsonite-clinopyroxene rocks (Group 2, Fig. 7.5a). For one sample of Group (2) (sample cor13-22c) we performed leaching experiments, and carbonate (liquid extracted) and silicate fraction (residue) yield similar Sr isotopic signatures. (iii) Sample 1cor14-10g is atypical among the carbonated metasomatic rock samples due to its significantly higher $^{87}Sr/^{86}Sr_i$ (0.710591) and falls in a third group (Group 3, Fig. 7.5a) together with the lawsonite-clinopyroxene rock formed on the orthogneiss in P.ta Caldane and the carbonate vein from this same outcrop.

Vein material

Two different kinds of vein were analyzed: vein composed of omphacite + carbonate (1cor12-11N and 2cor14-3b; Fig. 7.4a) and vein with only carbonate (cor16-49a). In omphacite +

carbonate vein both the carbonate and the omphacite fractions have close to similar $^{143}Nd/^{144}Nd_i$ (Table 7.3), but show different Sr isotopic compositions. The carbonate fractions are buffered to the same value of 0.708445 (± 0.000021, n=2), whereas the omphacite parts have different $^{87}Sr/^{86}Sr_i$ of 0.707985 and 0.708737. The Sr isotopic signature of the carbonate fractions is buffered to the same isotopic composition than the lawsonite-clinopyroxene host-rock (Fig. 7.5a, 1cor12-11L). Omphacite + carbonate veins, thus, fall in the previously defined Group (2). The carbonate vein (cor16-49a) that cut across the lawsonite-clinopyroxene rock and which has been formed at the expense of the orthogneiss has $^{87}Sr/^{86}Sr_i$ partly buffered by its host-rock (Stage#1, cor16-50) with a value at 0.710624. Its εNd value of -6.09 is also very close to the Nd isotopic signature of sample cor16-50 (εNd_i = -6.50). These two samples, together with sample 1cor14-10g, form a third group in the plot $^{87}Sr/^{86}Sr_i$ vs. εNd_i (Fig. 7.5).

7.4.4 Mixing curve models

Understanding of the isotopic signature significance is of great importance to better understand mass transfer processes and chemical fractionation at convergent margins that contribute to the geochemical heterogeneity of the mantle, but also for the understanding of characteristic of volcanic arc magmatism and, at a larger scale, related earthquake and eruption hazard (e.g., Bebout, 2007; Nielsen and Marschall, 2017).

Three main processes may contribute to changes in isotopic composition during subduction: diffusion, mechanical mixing, and metasomatic infiltration. The results in terms of isotopic signature will be different depending on the dominating process. The scale of diffusion, however, is on the order of a decimeter or less (Fletcher and Hofmann, 1974; Rumble, 1978; Rumble and Spear, 1983, Kohn and Valley, 1994). We have demonstrated so far that carbonated metasomatic rocks are found along km contacts within metasomatic rind that

range from 3 to 10 m widths and estimated time-integrated fluid fluxes point to open system metasomatism with dominant advection transport mechanism. Therefore, we will thus focus on the two mechanisms: mechanical mixing and fluid infiltration.

In the previous section, based on the $^{87}Sr/^{86}Sr_i$ vs. εNd_i composition, metasomatic rocks and HP veins have been divided in three groups. To summarize what previously outlined: a first group (Group 1) is composed by two samples: 1cor12-20d and 1cor14-11d. In both cases the Sr isotopic composition is buffered at the value of Jurassic marine seawater, but the two samples show higher Nd_i values, comparable to that of the analyzed metachert. Group (2) is composed by 8 samples with $^{87}Sr/^{86}Sr_i$ ranges from 0.708737 to 0.70921, and εNd_i ranges from -7.06 to -9.18. Samples from Group 2 are from different structural positions (metasediments-serpentinite contact and continental crust-serpentinite contact) and compose of: 4 carbonated metasomatic rocks, 2 omphacite fractions and 2 carbonate fractions separated from the veins. Sample 1cor14-11a belongs to Group 2, even if it was sampled in the same area of 1cor14-11d (Group 1). The two samples do not display significant different mineralogy (see Table 5.4), but sample 1cor14-11a was adjacent to the serpentinite, whereas 1cor14-11b was ca. 3 m from the contact with the serpentinite (Fig. 7.4, see also Section 5.2). The two samples from the Mt. Muffraje area, cor13-22a and cor13-22c, have identical values even if the first one was sampled 3 m from the serpentinite and the second ca. 50 cm from the contact. Two Stage#1 rocks, i.e. 1cor12-11L and cor13-23e, also fall in this group. Lastly, Group (3) includes 3 samples, with $^{87}Sr/^{86}Sr_i$ ranging from 0.710591 to 0.711696, and εNd_i ranging from -7.93 to -6.5. The three samples are: Stage#1 rock (cor16-50), the carbonate vein from the same outcrop (cor16-49a, P.ta Caldane area) and sample 1cor14-10g from Mt Muffraje area. The possible felsic origin of this latter is discussed in Section 5.1. Figure 7.5b shows the plot of $^{87}Sr/^{86}Sr_i$ vs. $\delta^{18}O_{SMOW}$ for the carbonated metasomatic rocks. It can be seen that the different groups also have distinct $\delta^{18}O_{SMOW}$ signature, and the subdivision in three

groups is maintained (i.e., samples fall in the same group in Fig. 7.5a and 7.5b). Samples 1cor12-20d and 1cor14-11d are clustered together, with $\delta^{18}O$ of 17 and 17.6‰, respectively. Sample 1cor14-10g yields a significantly distinct oxygen and strontium signature, with oxygen isotopic ration higher than the other samples from the same outcrop, at 22.3‰ (note that $\delta^{18}O$ for sample cor16-50 and cor16-49a are not available). Carbonated metasomatic rocks from Group (2) yield very similar $^{87}Sr/^{86}Sr_i$, with an average value of 0.709086 (n=4, $1\sigma = 8.8 \cdot 10^{-5}$), but display a significant dispersion in $\delta^{18}O$, with values ranging from 11.9 to 14‰. From Figure 7.5b it can be seen the omphacite + carbonate veins cluster together with the lower $\delta^{18}O$ signature (average for calcite 10.7‰, n=2; omphacite $\delta^{18}O$ = 7‰, n=1; Group 2'). Therefore, bases on Figure 7.5b, Group (2) can be subdivided in two groups: carbonated metasomatic rocks (Group (2)) and HP veins (Group(2')). Considering both Figure 7.5a and 7.5b, it turns out that carbonated metasomatic rocks from Group (2) and (3) isotopic signature falls in between tree poles: the Mesozoic metasediments (calcschists), the serpentinite and the granitic continental basement. In contrast, samples from Group (1) display a composition that falls in an area defined by different pole: calcschists, serpentinite and mantle values. In the following, we will use the identified poles (depleted mantle, serpentinite, calcschists and orthogneiss) for the different mixing models. In order to explore these hypotheses and evaluate the contribution of mantle component, i.e. the serpentinite and/or the continental crust, we performed geochemical modeling using two different approaches: mechanical mixing and fluid rock interactions. Only in the second case, a partition coefficient between fluid and rocks is considered.

7.4.4.1 Mechanical mixing

Geochemical and isotopic changes due to combination of infiltrative and diffusional metasomatism and mechanical mixing have been widely reported in the Catalina Schist (e.g.,

Bebout and Barton, 1993; 2002). Microstructures (Section 5.1) do not point to juxtaposition of adjacent lithologies, except for sample 1cor14-11a, where chlorite rich layers are observed (Section 5.2). However, the advantage of simple, linear mixing models, is the possibility to model 3 poles of mélange (e.g., two mixing: A+B and A'+C, where A' is a combination of A and B with variable proportion). It is particularly important to stress that even if the mechanical mixing models fit the data, this must not be interpreted as a genetic process because field, petrological and geochemical considerations clearly point to infiltration metasomatism (Chapter 5) with fluid strong participation. For example, field and microtextural evidence allows to formally exclude that sample cor16-50 (Stage#1 rock with the highest $^{87}Sr/^{86}Sr_i$ composition) could be formed by mechanical mixing. Nevertheless, these results inform on the different contribution to the composition of the HP fluids and can guide the choice of considered poles in the mixing modeling using equations that consider partition coefficients.

We decided to test different mixing hypotheses considering three poles: the serpentinite (i.e. the mantle-derived component, sample 1cor12-11b, see Table 7.3), the calcschist (the carbonate component, sample 1cor12-11q, see Table 7.3) and the orthogneiss (i.e. the crustal component, sample cor16-16k, see Table 7.3). Figure 7.7 reports the results of various tests using binary model mixings between metasediments and serpentinite and between metasediments and orthogneiss. The mixing modeling between serpentinite and calcschists reported in Figure 7.7a partly reproduces the composition of two Stage#1 rocks (sample 1cor12-11L and cor13-23e) and the carbonate + omphacite veins.

Sample	*lithology*	*distance from the contact*	$^{87}Sr/^{86}Sr_m$	$^{87}Sr/^{86}Sr_{i\ (34My)}$	$^{143}Nd/^{144}Nd_m$	$^{143}Nd/^{144}Nd_{i\ (34My)}$	εNd_i
1cor12-11q	calcschists	10 m	0,708561	0,708482	0,512063	0,512035	-11,69
1cor12-11q*	silicate fraction		0,709478	0,709399	0,512062	0,512033	-11,71
cor13-32	calcschists	50 m	0,707770	0,707746	0,512081	0,512052	-11,35
cor13-32*	carbonate fraction		0,707740	0,707715	--	--	--
cor13-32*	silicate fraction		0,713598	0,713574	0,512081	0,512052	-11,34
cor16-42d	quartzite	1.5-2 m	0,711033	0,708091	0,512216	0,512190	-8,65
cor12-16k	orthogneiss	2.5 m	0,722245	0,719761	0,512473	0,512438	-3,81
cor13-14a	serpentinite	0.2 m	0,710098	0,709841	0,512785	0,512736	2,00
1cor12-11b	serpentinite	0.2 m	0,710131	0,709908	0,512787	0,512739	2,06
BIGORNO	carbonated peridotite	--	0,707073	0,707073	0,513036	0,513007	7,29
BIGORNO*	carbonate fraction		0,707072	0,707072	--	--	--
BIGORNO*	silicate fraction		0,706462	0,706462	0,513046	0,513018	7,49
cor13-30a	ophicarbonate	--	0,707983	0,707983	0,512765	0,512723	1,75
cor13-23e	lawsonite+diopside	1.5 m	0,710105	0,708750	0,512245	0,512223	-8,01
1cor12-11L	lawsonite+diopside	6 m	0,708464	0,708458	0,512133	0,512106	-10,30
cor16-50	lawsonite+diopside	1 m	0,711715	0,711696	0,512323	0,512300	-6,50
cor14-11a	carbonated metasomatic rock	0.5 m	0,709018	0,709017	0,512300	0,512272	-7,06
cor14-11d	carbonated metasomatic rock	3 m	0,707049	0,707037	0,512232	0,512204	-8,38
cor13-22a	carbonated metasomatic rock	3 m	0,709042	0,709042	0,512244	0,512219	-8,09
cor13-22c	carbonated metasomatic rock	0.5-1 m	0,709074	0,709072	0,512242	0,512215	-8,16
cor13-22c*	carbonate fraction		0,709087	0,709085			
cor13-22c*	silicate fraction		0,709033	0,709031	--	--	--
1cor14-10g	carbonated metasomatic rock	0.5-1 m	0,710972	0,710733	0,512255	0,512227	-7,93
1cor14-10g*	silicate fraction		--	--	0,512239	0,512211	-8,24
1cor14-6a	carbonated metasomatic rock	--	0,709226	0,709214	0,512194	0,512165	-9,14
1cor14-6c	carbonated metasomatic rock	--	0,708801	0,708799	< d.l.	--	--
1cor12-20d	carbonated metasomatic rock	1.5 m	0,707265	0,707260	0,512242	0,512215	-8,16
1cor12-11No	omphacite vein	6 m	0,707986	0,707985	0,512270	0,512163	-9,18
2cor14-3bo	omphacite vein	6 m	0,708739	0,708737	0,512240	0,512193	-8,60
2cor14-3b	carbonate vein	6 m	0,708460	0,708460	0,512222	0,512169	-9,06
1cor12-11N	carbonate vein	6 m	0,708430	0,708430	0,512215	0,512163	-9,19
cor16-49a	carbonate vein	1 m	0,710624	0,710624	0,512326	0,512273	-6,09

*leaching experiments analyses of carbonate and residue fractions

Table 7.3: Sr-Nd isotopes values of analyzed samples

The calcschists-orthogneiss mixing (Fig. 7.7a) fits with the composition of Group (2) samples, but fails in modeling the composition of sample of Group (3). In Figure 7.7b, 3 poles mixing are tested implying a first step where two "main" mixing poles (i.e., metasediments and orthogneiss) have interacted to create one new mixing pole (A'). The results of this first step are then used for modeling mixing with the serpentinite pole (C). Satisfying results can be obtained when mixing the serpentinite with the pole A' with different proportion of orthogneiss vs. calcschists (5:95, 30:70, 20:80).

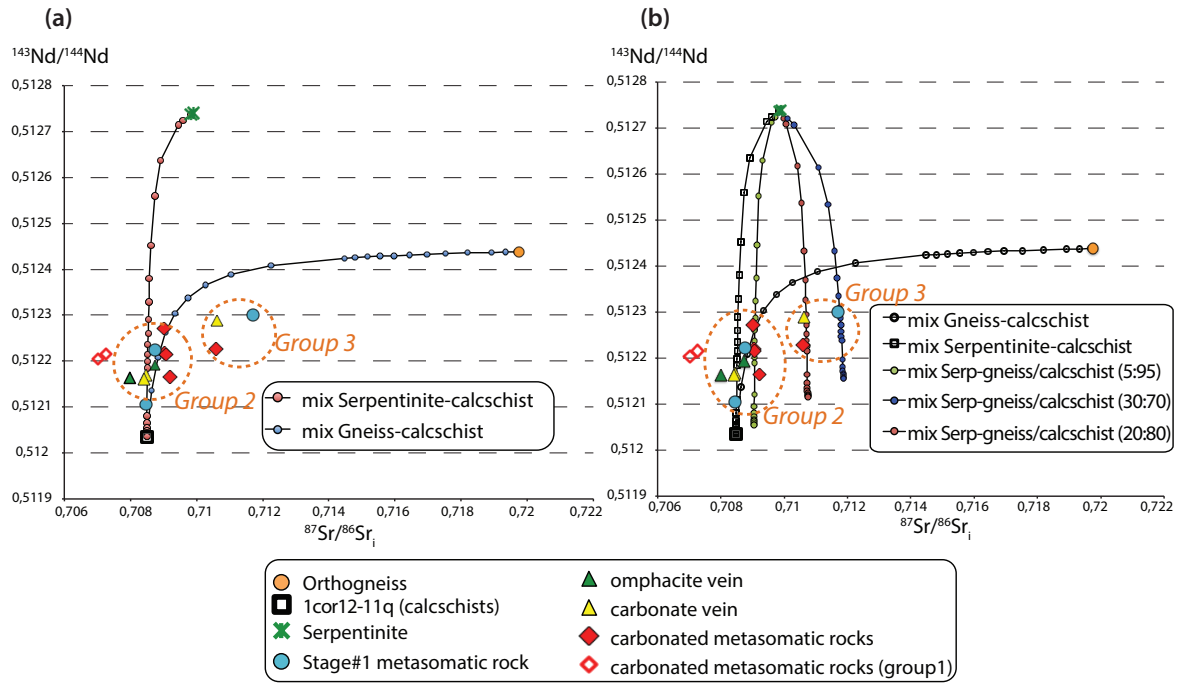

Fig. 7.7: Models for mechanical mixing. a) Simple linear mixing between serpentinite and metasediment (sample 1cor12-11q); b) Simple linear mixing between orthogneiss (sample cor16-16k) and metasediment (sample 1cor12-11q) together with 3 pole mixing.

7.4.4.2 Mixing models with K_d

When using mixing models that include partition coefficient, great care must be exercised because these values are subjected to rather large uncertainties and may change significantly depending on the chemical system and P-T conditions. Moreover, one of the limitations is that only one K_d can be introduced, while to have more realistic modeling we should have at least two K_d: one for the fluid production, one for successive fluid-rock interaction. The other strong limit will be that we consider a natural system, which is an "open-system", suggesting continuous change of the K_d values during interaction. In this work, two different experimentally determined K_d for Sr and Nd have been tested: one from Johnson and Plank (1999) from diamond trap experiments on dehydration and melting of metasediments, the second from Tsay et al. (2017) that performed piston cylinder experiments and fluid entrapment technique into evaluate the mobility of major and trace elements fluids equilibrated with eclogite (clinopyroxene + garnet + allanite). In this section, only results with

the partition coefficient from Johnson and Plank (1999) are presented since they gave the best fit. It is important to point out that, even if in both cases (K_d from both Johnson and Plank, 1999 and Tsay et al., 2017) experimental P for the determination of K_d are comparable to metamorphic peak P reached in the San Petrone unit, temperatures are higher than peak T which has been determined at 530°C (Vitale Brovarone et al., 2011b). This has a significant effect on the results since Sr has a peak in solubility after 600°C in both systems (metasedimentary and mafic) and thus it might results in an overestimation of the water/rock ratio.

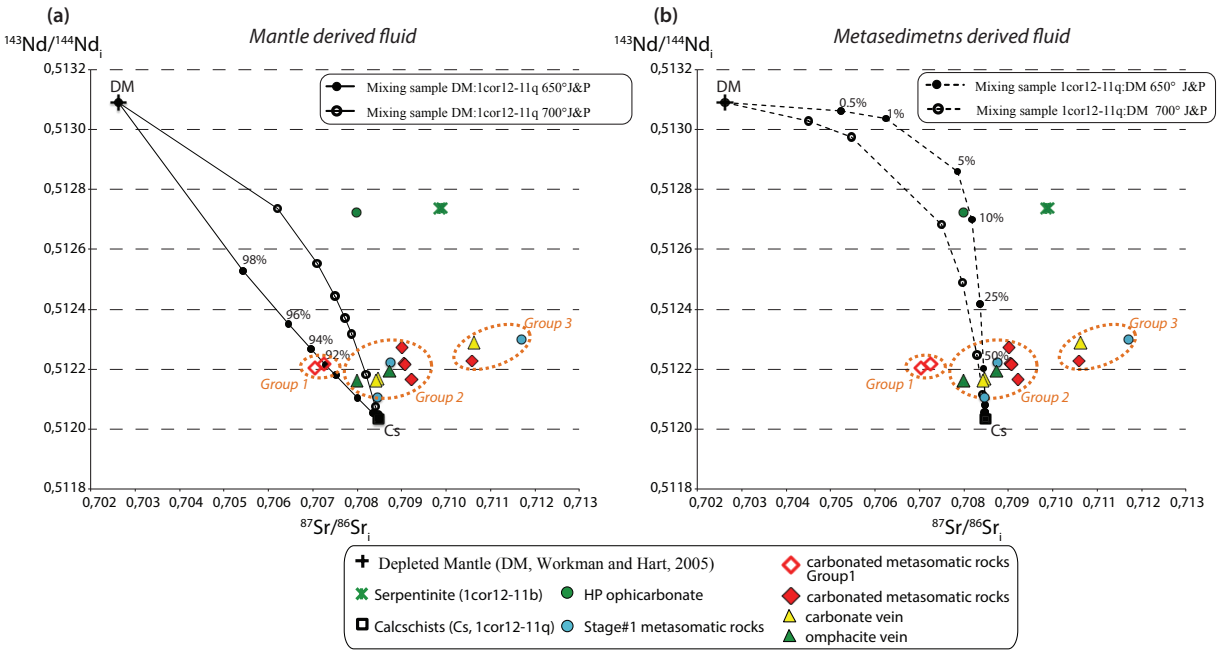

Fig. 7.8: Models for infiltration metasomatism using equation with integrated K_d. a) Mixing between depleted mantel and metasediment (sample 1cor12-11q), with fluid derived from the mantellic pole. b) Mixing between metasediment (sample 1cor12-11q) and depleted mantel (Workman and Hart, 2005), with fluid derived from the metasedimentary pole.

Considering O, Sr and Nd composition, Group (1) rocks signature likely derives from a mixing between metasedimentary and mantle fluid signatures. Figure 7.8a reports the mixing model between a depleted mantle pole ($^{87}Sr/^{86}Sr_i$ 0.70262 and $^{143}Nd/^{144}Nd_i$ 0.513089; Salters and Stracke, 2004; Workman and Hart, 2005) and the metasediment (this study). Using the 650°C K_d from Johnson and Plank (1999), a fluid with the 92% mantle contribution would fit the measured values in the metasomatic rocks (samples 1cor12-20d and 1cor14-11d). In

contrast, using the metasediments as fluid source, the data are not fitted. Interestingly, the ophicarbonate (sample cor13-30a) is fitted with a metasediments contribution to the fluid of ca. 10% (Fig. 7.8b).

Figure 7.9 reports the mixing modeling between different poles: metasediments-serpentinite (7.9a); Stage#1 rocks-serpentinite (7.9b); metasediments-orthogneiss (7.9c), and Stage#1 rocks-orthogneiss (7.9d). As in the mechanical mixing model, simple mixing between metasediments and serpentinite fails to reproduce the isotopic signature of carbonated metasomatic rocks, but models quite well the composition of Stage#1 metasomatic rocks and carbonate + omphacite veins. The carbonate fraction and Stage#1 lawsonite-diopside rock (cor13-11L) are better modeled by mixing serpentinite-metasediments, with 94% and 85-90% respectively, of serpentinite component in the fluid, and using a K_d for a fluid at 700°C (Fig. 7.9a). The modeling with K_d at 650°, better reproduces one of the omphacite sample (2cor14-3b), and one Stage#1 lawsonite-diopside rock (cor13-23e), with serpentinite component in the fluid at ca. 97-98% (Fig. 7.9a). Carbonated metasomatic rocks of Group (2) are better modeled using the Stage#1 rock and the serpentinite as mixing poles (Fig. 7.9b). In both cases, more than 80% of serpentinite component in the fluid is needed to fit the data. Both models, however, fail modeling samples from Group (3), suggesting that a crustal component contributes to their final isotopic signature. Therefore, we modeled a mixing between metasediment and continental crust (Fig. 7.9c) and between Stage#1 rocks and continental crust (Fig. 7.9d). Mixing between metasedimentary and crustal component gives good results only with the high T K_d for sample in Group (2) (Fig. 7.9c). Conversely, mixing crustal component with metasediments reproduces quite well the carbonated metasomatic rock 1cor14-10g (the jadeite-bearing rock) and Stage#1 metasomatic rocks forming at the expense of orthogneiss (cor16-50), with 50 and 60-70% of crustal component in the fluid respectively. The carbonate vein (cor16-49a) falls in between the mixing line for K_d at 650 and 700°. A

better fit for sample of Group (2) is obtained by substituting the metasedimentary component, with Stage#1 rocks (Fig. 7.9d). Notably, mixing sample 1cor12-11L with the orthogneiss reproduces quite well the signature of carbonate veins and omphacite from sample 2cor14-3b.

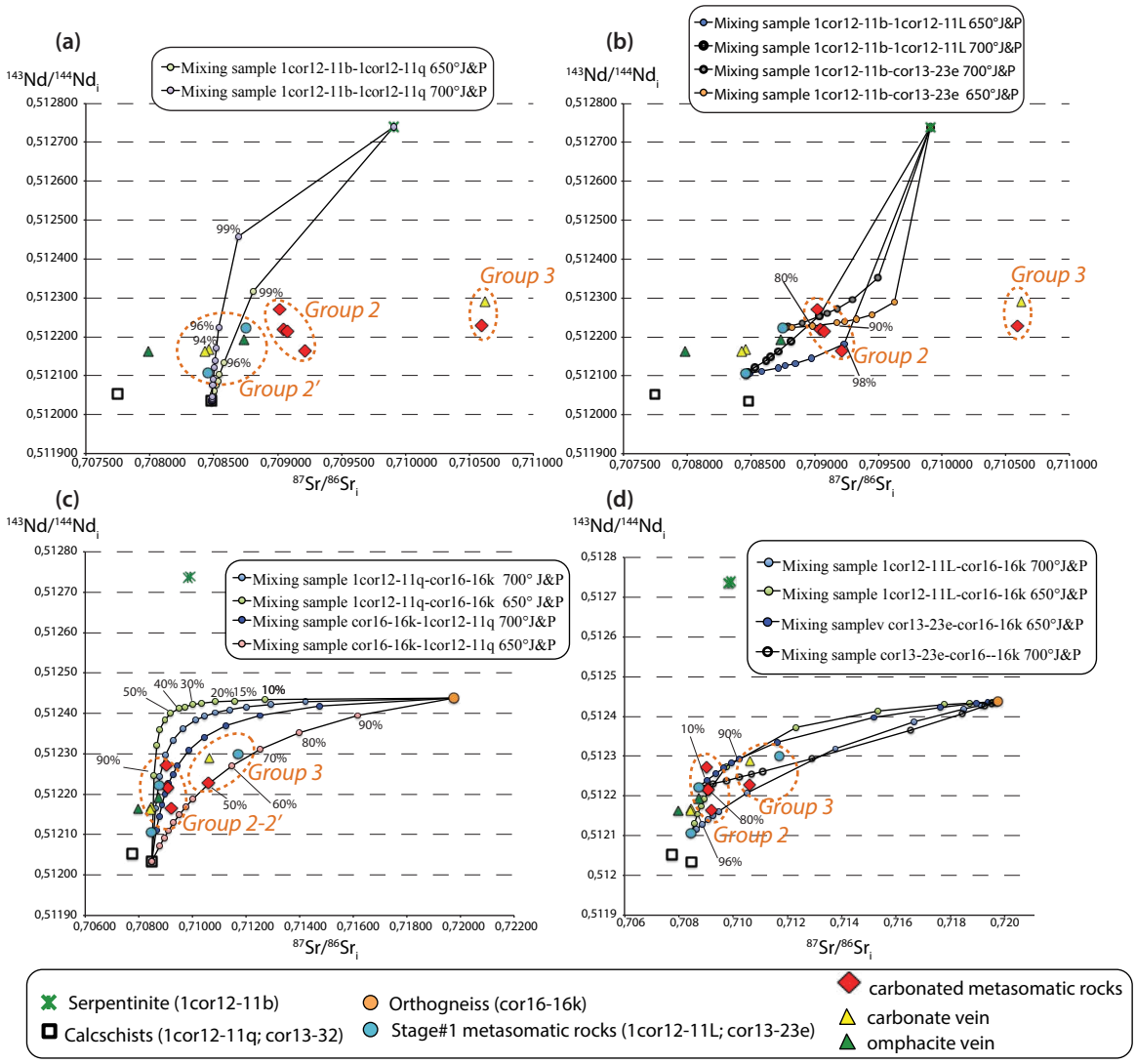

Fig. 7.9: Models for infiltration metasomatism using equation with integrated K_d. a) Mixing between serpentinite and metasediment (sample 1cor12-11q). b) Mixing between Stage#1 rocks (sample 1cor1211L; cor13-23e) and orthogneiss (sample cor16-16k). c) Mixing between metasediment (sample 1cor12-11q) and orthogneiss (sample cor16-16k). d) Mixing between Stage#1 rocks (sample 1cor1211L; cor13-23e) and orthogneiss (sample cor16-16k).

7.5 Discussion

7.5.1 Fluid oxygen isotopes composition

Even if we do not have direct access to primary HP fluid composition, we can use compilations of theoretical and experimental works on mineral-fluid equilibria to find the fluid oxygen isotopic composition in equilibrium with a considered mineral at a given temperature. When dealing with isotopic equilibrium, the effect of P can be neglected since isotopic exchanges imply negligible crystal volume change (Taylor and Coleman, 1968). Mineral-fluid oxygen equilibrium depends on a fractionation factor (α), which in turns depends on T. The equation that describes the dependence of α from T can be determined both experimentally and theoretically. Here we report only the equation for the antigorite-fluid equilibrium because the experimental database does not reach the temperature of interest and we used the equation for the extrapolation of α at higher T.

Based on the theoretical and experimental works of Golyshev et al. (1981) on fractionation of stable isotopes in carbonate systems, the fractionation between calcite and water $\Delta_{cc\text{-}H2O}$ (at 520°, peak metamorphic temperature) has a value of -0.48 or 1.31. Considering the average $\delta^{18}O$ of 10.7‰ for carbonate vein infilling, it gives a $\delta^{18}O$ a fluid composition ranging from 11.2 to 9.4‰ respectively. Following the same line of reasoning for the serpentinite, we used the experimental equation from Saccocia et al. (2009) to calculate $\delta^{18}O_{fluid}$ at peak T conditions (Table 7.4) by extrapolating the oxygen fractionation factor until 550°C, following the equation:

$$1000 \ln \alpha_{serp-water}^{^{18}O/^{16}O} = 3.49 \times \frac{10^6}{T^2} - 9.48 \quad (7.1)$$

where T is the temperature in Kelvin and α is the fractionation factor, defined as:

$$\alpha_{min-fluid} = \frac{1 + \frac{\delta_{min}}{1000}}{1 + \frac{\delta_{fluid}}{1000}} \quad (7.2)$$

At metamorphic peak temperature of 520°C, depending on the serpentinite isotopic composition, the fluid in equilibrium with antigorite has $\delta^{18}O$ ranging from 10 to 13 (Table 7.4). Therefore, from these calculations it results that a fluid in equilibrium with the carbonated metasomatic rocks is also in equilibrium with the serpentinite basement, thus strongly support the interpretation of the oxygen isotopic signature of carbonated metasomatic rocks as the result of carbonated precipitation from aqueous fluids equilibrated with ultramafic rocks.

T °C	measured $\delta^{18}O$ of serpentinite						
	9	**8,5**	**8**	**7,5**	**7**	**6,5**	**6**
250	5,7	5,2	4,7	4,2	3,7	3,2	2,7
300	7,8	7,3	6,8	6,3	5,8	5,3	4,8
350	9,5	9,0	8,5	8,0	7,5	7,0	6,5
400	10,8	10,3	9,8	9,3	8,8	8,3	7,8
450	11,8	11,3	10,8	10,3	9,8	9,3	8,8
500	12,7	12,2	11,7	11,2	10,7	10,2	9,7
520	13,0	12,5	12,0	11,5	11,0	10,5	10,0
550	13,4	12,9	12,4	11,9	11,4	10,9	10,4

Table 7.4: Calculated $\delta^{18}O$ values for a fluid in equilibrium with the serpentinite at different temperatures.

7.5.2 Modeling oxygen isotopes profiles in the serpentinite

A detailed isotopic study of the serpentinite basement is beyond the scope of this study, however, some first order consideration can be outlined. As mentioned in section 7.1, variation in serpentinite isotopic signature along a profile can be inherited from the oceanic stage or can be linked to fluid-rock interactions during metamorphism. Barnes et al. (2014) recognized the presence of a geochemical and isotopic solute front of ca. 20 m (*d*, equation 6.11). Figure 7.10 reports different fluid concentration profiles modeled following Eq. *(6.10)*. The equation is applicable to isotopic system if the change in ratio during alteration is small or if the concentration of the tracer isotopes is small, like is the case for $\delta^{18}O$ (e.g. Lassey and Blatter, 1988; Bickle, 1992). One possible pitfall with oxygen isotope profiles is the temperature sensitive mineral-fluid fractionation. However, since there are no significant T variations in the 50 m profiles of this case study, we consider legitimate to use a fixed K_v

value of 0.6 (Bickle, 1992). Moreover, in this case, this equation for mass transfer is applicable since the isotopic front affects a homogenous lithology where fluid infiltration did not lead to change in mineral assemblage, therefore, a unique *Kv* can be fixed. Here, we will adopt a diffusion coefficient (*D*) of 10^{-8} m^2 s^{-1}, which is a valid assumption in most metamorphic conditions. Tortuosity typically ranges from 0.3 to 0.7 (Bear, 1988). We will use 0.5 as a representative value.

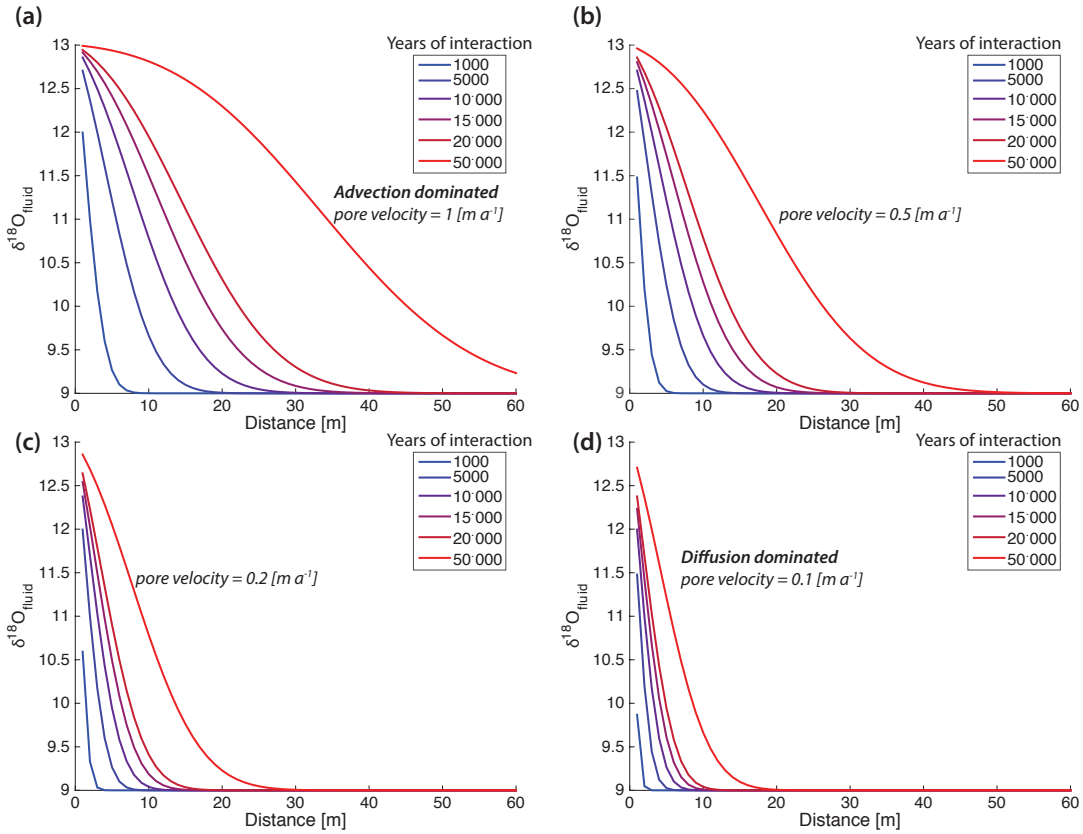

Fig. 7.10: Fluid concentration profiles resulting from advection and hydrodynamic dispersion of heavier oxygen isotopes during interaction with the serpentinite. Oxygen isotopes concentration profiles in the serpentinite should have the same shape. The corresponding $\delta^{18}O$ of the serpentinite would range from 6 to 9‰ (Table 7.4).

Values of dispersivity (α_L) can vary over orders of magnitude (Garven and Freeze, 1984). Considering that the metasomatic rind ranges between 3 and 8 m, we will adopt the representative value of 5 m (Ague, 2000).

These reconnaissance models show that in case of dominant advection transport mechanism (Fig. 7.10a), solute front of ~20 m would be produced for a relative short interaction time

period (10'000 to 20'000 years). In contrast, with a diffusion-dominated transport (Fig. 7.10d), it would take 50'000 years to produce a solute front of 20 m. In order to solve this problem a detailed geochemical and isotopic (stable and radiogenic) study along a number of profiles and better constraints on the duration of fluid infiltration are needed. However, the fact that diffusion dominated model seems to be more reliable supports the proposed model for which that the serpentinite did not undergone fluid infiltration because less permeable than the juxtaposed rocks (Chapter 5). Considering the model of Figure 7.10c, for ca. ~20 m of propagation of the solute front, estimated time-integrated fluid fluxes with Eq. *(6.12)* give ca. 17 m^3_{fluid} m^{-2}_{rock}. Such low fluid fluxes suggest that much of the flow was diverted from the serpentinite, likely parallel to the contact with the overlying lithologies. However, it is important to keep in mind that very heterogeneous isotopic signature of the first meters of the serpentinized mantle might also be inherited from the sea-floor alteration. For example, Figure 7.11 reports the section of the Iberian passive margin together with two oxygen profiles from ODP drill hole in the exhumed mantle. The Iberian exhumed mantle domain might be considered as a present day analogue of the paleogeographic position of the San Petrone unit (see also Fig. 2.3; Vitale Brovarone et al., 2013; Beltrando et al., 2014a). Skelton and Valley (2000) performed an oxygen isotopic study of two drill holes (sites 1068 and 1070) showing that the exhumed mantle underwent two infiltration events, pre and post exhumation, with significant lateral and depth variation in oxygen isotopes signature (Fig. 7.11c,d). The possible retention of pre-subduction vestiges of fluid-rock interactions has to be taken into account before making interpretation of the studied metasomatic rocks.

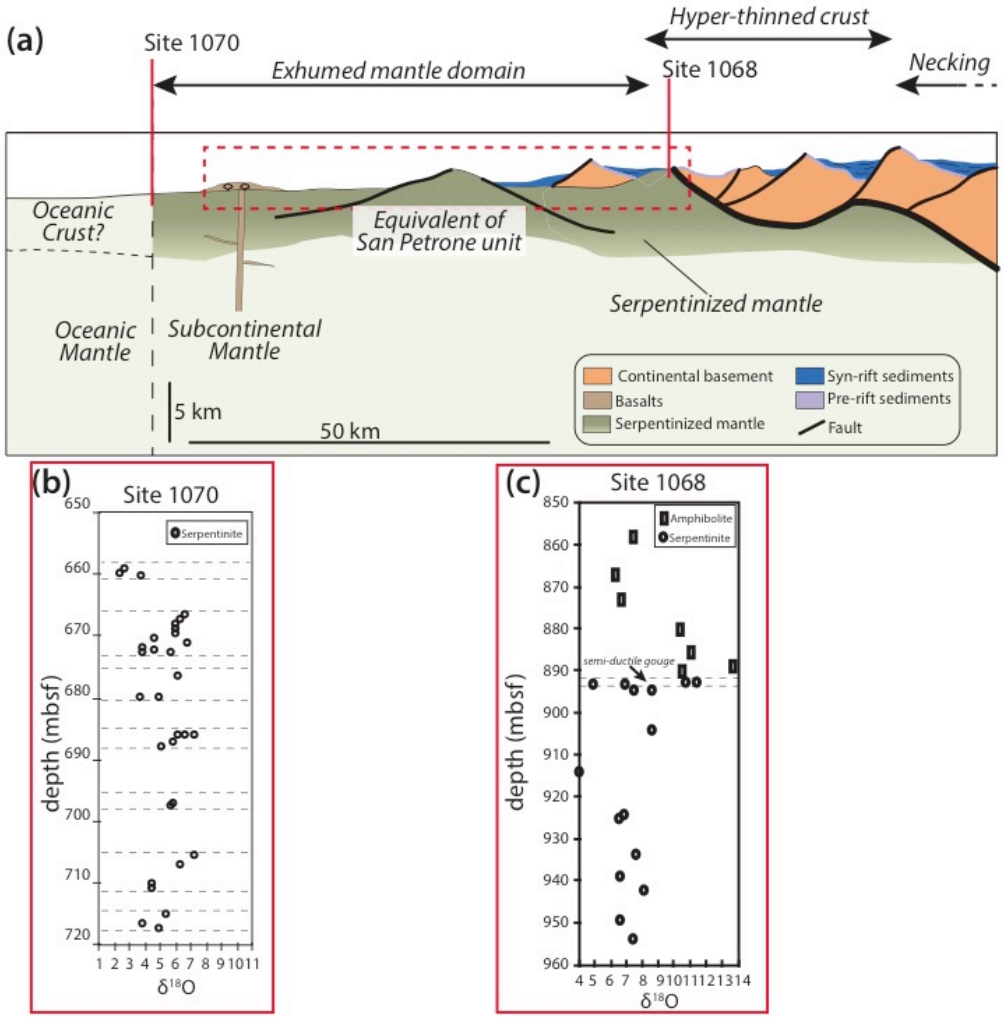

Fig. 7.11: a) Interpreted section across the distal Iberian rifted margin along the TGS/Lusigal 12 seismic reflection lines, based on all available geophysical and ODP drill hole data. The red lines indicate the position of ODP drill hole 1068 and 1070 in the serpentinite basement. The red box indicates the equivalent paleogeographic position of the San Petrone unit (modified after Sutra et al., 2013 and Beltrando et al., 2014). **b-c)** Oxygen isotopes profiles in drill hole 1068 and 1070 showing the large $\delta^{18}O$ variability in the exhumed serpentinized mantle due to hydrothermal alteration (Fig. from Skelton and Valley, 2000).

7.5.3 Possible interpretations of the meaning of O-Sr signature of the serpentinite

The isotopic composition of the serpentinite is of difficult interpretation considering the limited number of samples and the significant variability. The data collected so far show that the two samples of serpentinite basement near metasomatized contacts have different oxygen isotopes composition, but almost identical Sr-Nd isotopes signature. Considering very low Sr concentration in the serpentinite, the infiltration of fluids equilibrated with continental crust might change and homogenized the Sr-isotopic composition increasing Sr isotopic ratio to

value significantly higher than seawater composition. Figure 7.12a,b shows the mixing model for fluid infiltration considering two poles by the time: the "typical" depleted mantle pole ($^{87}Sr/^{86}Sr_i$ 0.70262 and $^{143}Nd/^{144}Nd_i$ 0.513089; Salters and Stracke, 2004; Workman and Hart, 2005) and the continental crust (i.e., the orthogneiss cor16-16k) (Fig. 7.12a), and, then, the depleted mantle with lower Nd ($^{143}Nd/^{144}Nd_i$ 0.512752; Halama et al., 2011) and the continental crust (Fig. 7.12b). Both models show that with only ca. 5% of continental crust component in the fluid, the Sr isotopes would be shifted to the measured value. This corresponds to very low W/R (0.005). However, if the changes (and homogenization) in Sr isotopic composition were linked to HP fluid infiltration, homogenization of oxygen isotopes would be expected as well. Actually, different length of O and Sr isotopic front can be explained considering the different K_v, with the K_v of oxygen being much larger than that of Sr (Bickle, 1992). This implies that, under local equilibrium conditions, oxygen isotopic front will propagate farther than Sr isotopic front for a given q_{TI}. Therefore, considering a very low fluid infiltration, only the oxygen isotopic signature would be modified during HP metasomatism, whereas the pre-subduction Sr signature would remain unchanged.

Altogether, two scenarios can be envisaged: i) the isotopic signature (O-Sr-Nd) of the serpentinite basement is inherited from the sea-floor metamorphism/hydrothermal alteration; ii) Sr-Nd isotopic signature is inherited from the oceanic stage (see sections 7.4.3, 7.5.2, Snow et al., 1993), whereas local oxygen isotopes metasomatism can be explained by HP fluids infiltration. Notably, the results clearly point to an oceanic origin of the Sr-Nd signature, whereas O signature might result from either sea-floor alteration or HP metamorphic fluid infiltration. Our results, therefore, are consistent with the results presented by Miller et al. (2001) that point to sea-floor serpentinization of the exhumed mantle, but also highlight that, potentially, subduction metasomatism can modified the oceanic signature of the serpentinite.

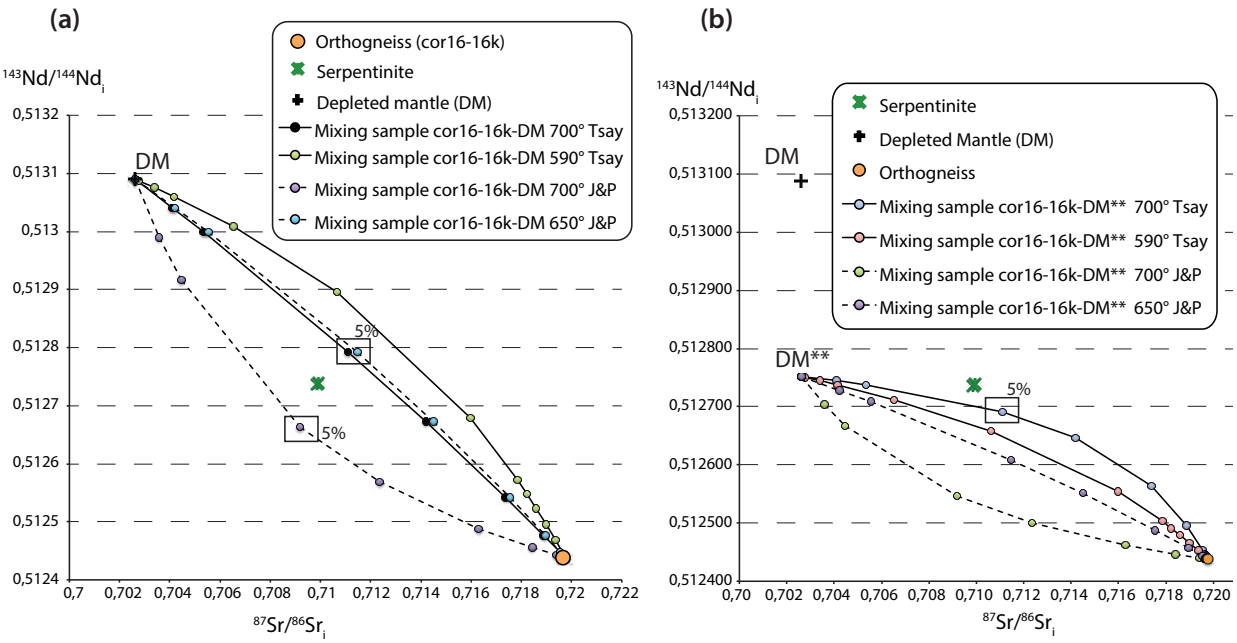

Fig. 7.12: Models for infiltration metasomatism using equation with integrated K_d. a) Mixing between depleted mantle (Sr and Nd values from Workman and Hart, 2005; Salters and Stracke, 2004) and orthogneiss (sample cor16-16k). b) Mixing between depleted mantle (Sr value from Workman and Hart, 2005; Salters and Stracke, 2004; Nd value from Halama et al., 2011) and orthogneiss (sample cor16-16k)

7.5.4 Significance of isotopic signature of carbonated metasomatic rocks

The results of O-C and Sr-Nd isotopic study of carbonated metasomatic rocks (Figs. 7.3, 7.5) allow proposing a general overview on isotopic characteristic signature of carbonate metasomatism. Figure 7.13 depicts the ensemble of the data, unifying field and petrological observations with isotopic signatures. Carbonates in carbonated metasomatic rocks are characterized by generally low $\delta^{18}O$ values, especially when approaching the contact with the serpentinite (Fig. 7.13a). HP carbonates veins always have very low $\delta^{18}O$ values, independently from the distance from the serpentinite basement (Fig. 7.13b). A non sedimentary origin is also strongly supported by Sr isotopic signature that attest to the contribution in variable proportion of ultramafic and crustal isotopes reservoirs (Fig. 7.13c).

More work is needed to thoroughly understand the significance of the isotopic composition of carbonated metasomatic rocks. Though we can outline some preliminary observations. Sr and O isotopic signature of samples from Group (1) could partly result from two different possible mechanisms: 1) interaction with fluid equilibrated with a mafic/ultramafic rock as oxygen

should point out; 2) recycling of marine carbonates as Sr isotopes seem to suggest. As pointed out in section 5.2 sample 1cor12-20d underwent a third metasomatic event (albitization) during exhumation. This late stage of metasomatism induced by, likely, crustal fluid circulation, has a strong effect on trace element composition (see Section 6.5.1) suggesting also possible modifications of isotopic signatures. The age of this late stage metasomatism is still unknown, thus Sr, Nd values cannot be corrected for this latest event and only the peak metamorphic age is considered for the corrections (i.e., 34 My). Also for sample 1cor14-11d, the petrographic study shows evidence of dynamic recrystallization, with new carbonate grains forming by buldging around the old ones (Fig. 5.16a,b). Moreover, late phengite crystallization is observed. Phengite crystallization should increase the $^{87}Sr/^{86}Sr_i$ value, but this is not the case for the study samples. Therefore, samples of Group 1 are of difficult interpretation and the here presented results need more work for a robust interpretation.

Samples classified in Group (2) display a very homogeneous $^{87}Sr/^{86}Sr_i$, but $\delta^{18}O$ values are more dispersed. Samples close to the serpentinite and HP veins systematically display lower oxygen isotopes ratio values (Fig. 7.13a). Considering the Sr mass gain (Chapter 6), and that $^{87}Sr/86Sr_i$ signature is higher than that of the host-rocks (1cor12-11L and cor13-23e), it is plausible that $^{87}Sr/86Sr_i$ was buffered by the fluid. With increasing distance from the contact, fluid fluxes are expected to decrease (Fig. 5.12c in Chapter 5), therefore, relatively higher $\delta^{18}O$ might be related to partial contribution of the metasediments by diffusion through fluid-filled porosity.

The oxygen composition of the carbonate vein from Group (3) (sample cor16-49a) is not available, but $^{87}Sr/86Sr_i$ ratio is lower than that of the host rock (sample cor16-50). Again in this case, a contribution a serpentinite or metasediments-derived fluids might explain the measured values. All together, results point to an isotopic signature due to a combination of parameters: i) initial isotopic composition of the precursor rock (pre-carbonation), especially

for Nd isotopes, which signature is inherited from the protolith rock, prior any metasomatism; ii) multi-source external fluids infiltration, better recorded by O-C and Sr isotopes. At this stage, a quantitative evaluation of the contribution of each pole is hampered by limitation intrinsic to the mixing modeling. Moreover, mass balance estimation attest to the strong Sr mass gain in carbonated metasomatic rocks, thus the assumption for W/R estimation that Sr and Nd concentrations are not modified during fluid-rock interaction is not met, thus W/R estimation would lead to meaningless results (Albarède et al., 1981). Another limit to the comprehension of the whole problem is the impossibility to attest the existence of an O and/or Sr isotopic alteration in the first meters of the serpentinite basement. Actually, in modeling the data, we used the serpentinite values as representative of a mixing pole, but we cannot say that this value is actually representative of the bulk isotopic composition for the serpentinized basement in the San Petrone unit. If it is the case, the analysis is representative of the serpentinite signature prior dehydration. In this case, the models proposed here would be reliable: carbonated metasomatic rocks results from a serpentinite derived fluid that interacts with the Stage#1 rock (Fig. 7.10b). In the other case, if the bulk isotopic composition of the serpentinized basement is close to more typical mantle values (i.e., 0.702), the contribution of the continental crust to the fluid composition would be much larger than expected.

7.5.5 *Preliminary considerations on fluid sources*

In the model proposed in Chapter 5, deeply produced fluids are channelized along the slab lithological interfaces and the flow path along a P-T gradient and the lithological contrast enables a reactive fluid flow. The contribution of fluid equilibrated with ultramafic rocks is strongly suggested by the oxygen isotopes signatures. Actually, serpentinite dehydration releases large amount of water, thus it is tempting to propose that the fluid oxygen isotopic signature is buffered by the water derived from the serpentinite dehydration. Conversely,

considering the very low Sr content of the serpentinite, Sr isotopes are more likely to reequilibrate during reactive flow with different reservoirs (metasediments, continental crust). The relative dispersion in Sr signature of carbonated metasomatic rocks (Groups 1, 2 and 3) points to this interpretation. It can be argued that when the San Petrone unit reached the peak metamorphic condition, the deeper portion of the slab, where fluid are produced by dehydration reactions, the slab was composed by oceanic crust with probably few or none continental sliver (metamorphic equivalent of distal margins). Without a larger dataset on the serpentinite basement, we cannot conclude with good certainty that both low $\delta^{18}O$ and high $^{87}Sr/^{86}Sr$ (higher than metasediments) characterizing the carbonated metasomatic rocks are exclusively due to the serpentinite contribution. Thus, the hypothesis of fluid composition derived from multiple equilibrations (i.e., serpentinite derived fluids that interact with high $^{87}Sr/^{86}Sr$ reservoirs like the continental crust rocks) is still valid.

Altogether, the studied carbonated metasomatic rocks strongly suggest that isotopes can record the contribution of a multi source fluid. Moreover, the complexity of isotopic metasomatism suggests that deeply produced fluids circulate within the slab and equilibrate their isotopic composition with the slab-forming rocks. The record of this long reactive flow is today found in metasomatic system preserved in exhumed HP units. Lastly, it has been shown that late stage deformation and fluid infiltration can also further modify to geochemical and isotopic signature of the rocks.

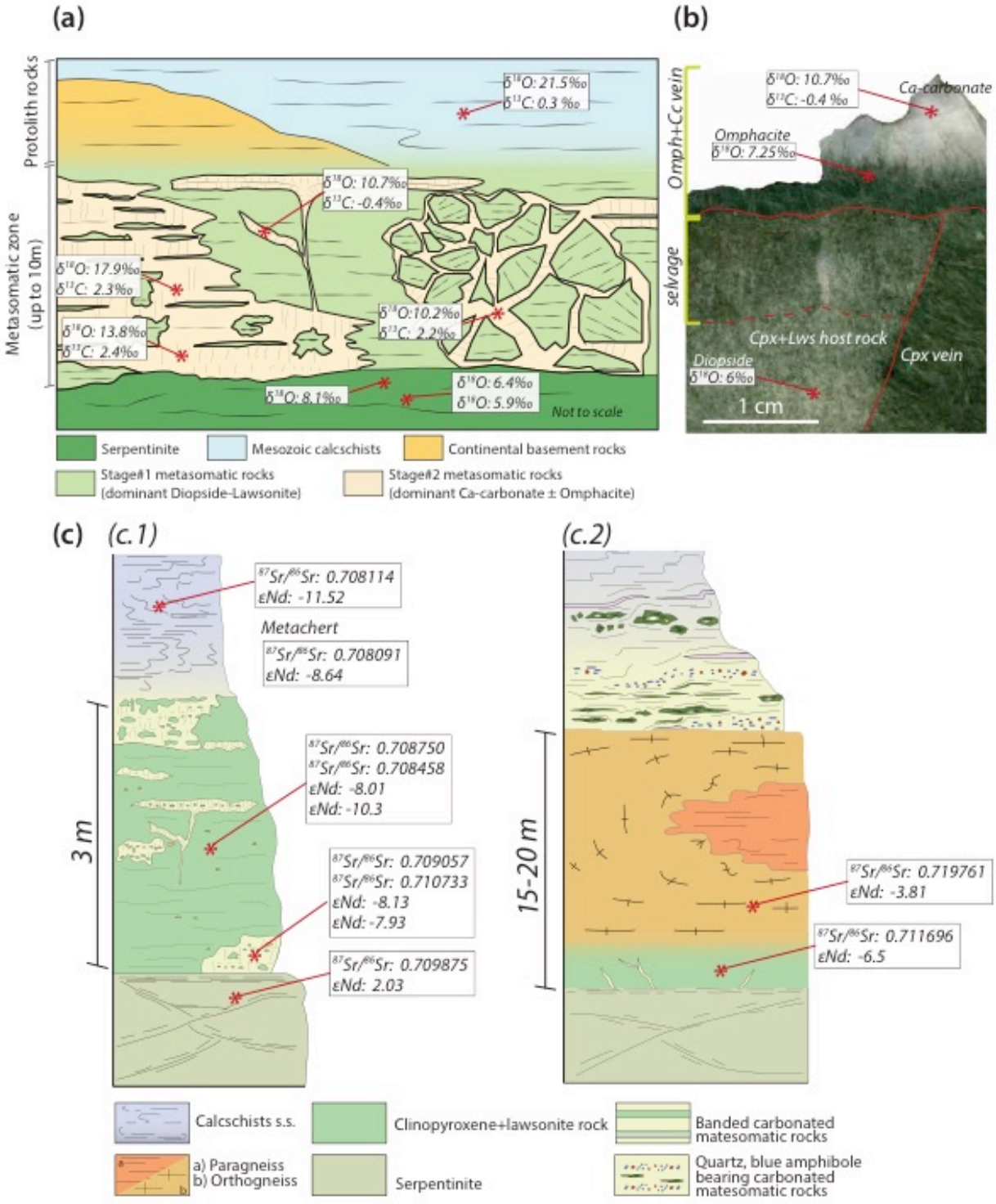

Fig. 7.13: Images reporting an overview of the O-C, and Sr-Nd isotopes analyses relative to various analyzed sample and structural position. **a)** Oxygen and Carbon stable isotopes of carbonated metasomatic rocks and serpentinized basement. **b)** Image of omphacite + carbonate vein cutting across diopside + lawsonite Stage#1 metasomatic rocks and a diopside vein. **c)** Interpretative logs of the metasomatized lithological contact: *c.1* serpentinite-thin continental sliver; *c.2* serpentinite-thick continental sliver.

CHAPTER 8
Discussion

The petrological and geochemical study of high-pressure carbonation has required a multi-technique approach. We integrate a considerable number of techniques passing from field observations, to petrography, mineral chemistry, thermodynamic modeling, geochemistry, isotopes geochemistry and geochemical modeling. Even if not without pitfalls, this multi-technique approach turns out to be suitable for the study of a newly discovered process starting from natural samples that, obviously, display natural heterogeneities due to a long evolution with multiple episode of alteration and deformation. Despite these difficulties, the study of carbon cycle in subduction zone from natural samples gives the unique possibility to investigate the wide set of parameters that, ultimately, control the evolution of the fluid-rock system as well as the geochemical carbon cycle. Results have been thoroughly discussed in the previous chapters. The aim of this chapter is to give an overview of the ensemble of the results and to outline a bigger picture about HP carbonation process.

8.1 Recognition of the metasomatic origin of carbonates in high-pressure metamorphic units

Our understanding of processes that occur in subduction zones at depth of ~70-100 km is based on geological studies of metamorphic and igneous rocks brought to the surface from great depth, and on indirect methods of investigation including experimental petrology, numerical modeling and geophysical techniques. The role of fluids and volatile-bearing minerals in the geodynamic evolution of subduction zones has been addressed by an increasing number of studies by mean of all the above reported methods. The evolution of carbonate and carbon-bearing fluid has long been a topic of interest and has been investigated

with different approaches. The finding of evidences in natural samples of carbonate dissolution during HP-LT metamorphism, overturned older paradigms on carbonate stability with respect to carbon mobility in subduction zones (Frezzotti et al., 2011; Ague and Nicolescu, 2014). However, owing to the recent discovery of this process, much remains to be learned about the ultimate fate of carbon-bearing fluids and their interaction with slab- and mantle-forming rocks.

This work represents the first field-based study that aims to better constrain the origin and composition of carbon-bearing HP fluids and how their interaction with rocks can lead to HP rock carbonation. High-pressure rock carbonation in eclogitic metamorphic rocks has almost never been described before, thus, the first effort was to proof that the observed carbonated metasomatic rocks formed by fluid-rock interactions (Piccoli et al., 2016). Actually, the occurrence of carbonate in metasedimentary rock is very common, and in most cases reflects the primary composition of the subducted rocks. The discovery of carbonated metasomatic rocks in the San Petrone unit opened a number of questions: how common are HP carbonated metasomatic rocks? What is the fluid source, and its composition? What are the chemical/physical parameters that allow fluid-mineral reactions? To address these questions, fieldwork, petrology, mineral chemistry, and geochemistry has been combined.

Impure marbles with peak assemblage comparable to that of observed in the Corsican rocks have been described in many HP belts, for examples, Western Alps (e.g., Castelli, 1991; Reineke, 1998; Castelli et al., 2007); Cyclades (Brady et al., 2004; Schumacker et al., 2008), Sivrihisar belt (Turkey; Seaton et al., 2009), Tianshan (e.g., Lü et al., 2013; Li et al., 2014), and Dabie-SuLu (Proyer et al., 2013). In some cases, structural features and field relationship attested to the former presence of carbonate in the rock prior metamorphism (e.g., dykes cutting across the carbonate bearing metamorphic rocks; Castelli, 1991), or mineral compositional zoning revealing HP prograde, UHP peak, and UHP early retrograde evolution

(Li et al., 2014; Ferrando et al., 2017). We demonstrated that in carbonate-bearing system a detailed petrological characterization coupled with isotopic study can be used to distinguish between pre-metamorphic and metasomatic carbonates. Moreover, careful petrographic and geochemical observations can be used to qualitatively evaluate major (and trace) element mobility.

One of the innovative contributions in this work is the recognition of mineral phases, notably clinopyroxene, that preferentially react with carbon-bearing fluids. One direct implication is the extension of the potential applicability of HP carbonation to mantle wedge-forming rocks, along the slab-mantle interface, where other minerals like olive could undergo carbonation during fluid-infiltration (Scambelluri et al., 2016). Nevertheless, rheological factors should be also considered. It is plausible that clinopyroxene-rich domain were weaker compared to lawsonite-rich ones, thus facilitating deformation, fracturing and fluid-flow. Shear zone development associated with fluid-rock interactions is commonly reported in metagranite (from Central and Eastern Alps, e.g., Mancktelow and Pennacchioni, 2005; Goncalves et al., 2012; and in the Western Alp, e.g., Rolland et al., 2008; Boutoux et al., 2014; Rolland and Rossi, 2016). Altogether, we cannot exclude that both factor (chemical and rheological) interplayed facilitating rock carbonation.

8.2 Extremely high carbon-bearing fluid fluxes: implications for carbon inventory in subduction zones

Carbon fluxes in subduction zones are controlled by carbon solubility in aqueous fluids and hydrous melts. A first order evaluation of how much rock carbonation is relevant on the subduction zone carbon cycle can be done by comparing our results in terms of CO_2 mass gain (wt.%) with CO_2 loss by dissolution/devolatilization reactions in other geological settings (Fig. 8.1). John et al. (2008) report almost complete decarbonation during fluid-rock

interaction at HP conditions. Even if the authors do not explicitly talk about carbonate dissolution, their study focus on eclogite facies transport veins in blueschist terrains (Tianshan), where the fluid source was proved to be external. They estimated that 75% of the total carbon was released to the fluid phase. Even if the initial total carbon was not very high (LOI ~4 wt.%) and thus the absolute amount of CO_2 released into the fluid is quite low, their results already indicated that aqueous fluids can efficiently mobilize carbon. Ague and Nicolescu (2014) studied fluid-mediated reactions in marble rocks adjacent to fluid conduits. They gave evidence for carbonate dissolution during fluid-rock interactions, accompanied by silicate mineral precipitation. They also estimated that almost 60 to 90 wt.% of the initial CO_2 was lost during the interaction (20 to 35 g of CO_2 per 100 g of rock). In Chapter 6, through mass balance calculation, we estimated CO_2 mass gain ranging from a minimum of 50g per 100g of precursor rock to a maximum 175g per 100g of precursor rock (Table 6.2), and we estimated time-integrated CO_2 flux of ca. 300 t m^{-2} (using a CO_2 concentration in HP fluids of 0.05 wt.%, Kelemen and Manning, 2015). It is worth noting that our lower estimation of carbon uptake is in the same order of magnitude of the estimation of carbon loss of Ague and Nicolescu (2014), whereas the upper value is one order of magnitude higher (Fig. 8.1). Considering that HP fluids are very diluted, very large fluid fluxes are needed to account for such a mass gain. It can be argued, that fluid fluxes (10^6 m^3 m^{-2}) might be overestimated because of the low concentration of carbon in the fluid composition used in the calculation, even if it is based on the most recent estimations. Actually, in different setting (from the Himalaya to the Western Alps and Scandinavian Caledonides) estimated time-integrated fluid fluxes are generally very low from almost 0 (<5 m^3 m^{-2}; Philippot and Rumble, 2000) to values as high as 10^2 m^3 m^{-2} in fractured deep crust (Bergen islands; Austrheim, 1990; Jamtveit et al., 1990). However, our estimation of time-integrated fluid fluxes of 10^6 m^3 m^{-2} is

in the range of values predicted in case of channelized fluid flow, for example in fracture zones (DePaolo 2006; Zack and John, 2007; Ague, 2014).

So far, HP carbonation has been reported in only two localities worldwide (Alpine Corsica and Voltri Massif; Piccoli et al., 2016; Scambelluri et al., 2016). The overall good preservation of peak metamorphic mineral paragenesis in the San Petrone unit likely is the reason for the exceptional preservation of metasomatic systems (both Stage#1 and #2).

This suggests that analogous rocks and processes may have occurred in more retrogressed HP belts, along the Alp-Himalaya suture zone. Moreover, HP carbonation might also be happening today in present-day subduction zones. The results of this study represent the first quantification of this newly discovered process. Further work is needed to refine these results and improve our understanding of HP carbonation, with its implications on carbon fluxes in subduction zones. In light of the above, HP carbonation should now on taken into account for the subduction zone carbon inventory as efficient process for carbon storage in the subducting slab.

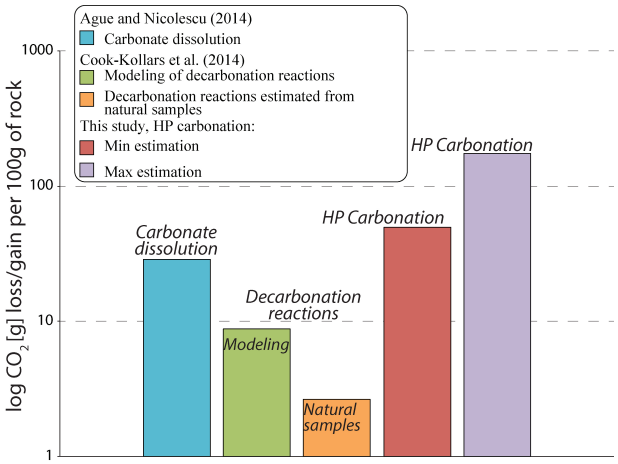

Fig. 8.1: Carbon fluxes during subduction metamorphism. The bar diagram reports the estimation for CO_2 wt.% loss during carbonate dissolution (Ague and Nicolescu, 2014) and decarbonation reactions (Cook-Kollars et al., 2014) together with CO_2 wt.% gain for HP carbonation (this study). Figure updated from Piccoli et al. (2016) with values from Table 6.2.

8.3 Chemical and physical parameters controlling carbonation reaction progress

8.3.1 Evaluation of rock reactivity with carbon-bearing fluids

Deformation, metamorphism, and intense metasomatism in some cases make the identification of protolith rocks challenging, especially when the metasomatic rinds affected a laterally and vertically variable column of rocks including siliceous metasedimentary, mafic,

ultramafic, and also felsic lithologies. Our tectonostratigraphic reconstruction of carbonated metasomatic rocks facilitates inferences regarding the nature of the protolith rock and we gave large petrological and geochemical evidence for complete transformation and carbonation of metafelsic, mafic and ultramafic rocks. Petrographic microstructures presented in this work display striking analogies with shallow and seafloor rock carbonation processes and experimental works (e.g., Spooner and Fyfe, 1973; Bonatti et al., 1974; Lemoine, 1980; Lagabrielle and Cannat, 1980; Kelement and Matter, 2008; Kelemen et al., 2011; Beinlich et al., 2010; Daval et al., 2009a,b, 2010; Clerc et al., 2014). At the shallow conditions, the carbon uptake reactions have been described as (i) dissolution of silicates, (ii) precipitation of carbonates, and (iii) CO_2 capture, that is a sum of the previous two (Guyot et al., 2011):

i) $MSiO_3 + H_2O + 2CO_2 \rightarrow M^{2+} + 2HCO^{3-} + SiO_2$

ii) $M^{2+} + 2HCO^{3-} \rightarrow MCO_3 + H_2O + CO_2$

iii) $MSiO_3 + CO_2 \rightarrow MCO_3 + SiO_2$.

In the reactions reported above, only silicates with divalent M cations such as Ca^{2+} and Mg^{2+} are represented. Dissolution reactions for silicate with monovalent cations, like Na^{+} and K^{+}, exist, but are considered to be rarely involved in solid carbonate precipitation (Oelkers et al., 2008). For these reasons, mafic and ultramafic rocks containing silicates with divalent cations (i.e., diopside, olivine) have been object of a large number of experimental studies for carbon storage through rock carbonation. A direct comparison with HP carbonation is not possible since the simple extrapolation of the reaction thermodynamic properties to higher P and T might be illegitimate, and we have no access to chemical parameters like pH, nor we have knowledge of reaction kinetics. Nevertheless, our petrological study point to silicate dissolution and carbonate precipitation (reaction (iii)) as a mechanism for carbon uptake during HP carbonation. Other analogy with the LP carbonation reaction is the observed reactivity of diopside (silicate with divalent M cations Ca^{2+} and Mg^{2+}) with carbon-bearing

fluids. Clinopyroxene + lawsonite metasomatic rocks have a mafic bulk composition. However, in the San Petrone unit, it can be found evidence for the reactivity of ultramafic rocks with such a fluids as well. For example, ultramafic-carbonated chaotic sequences are found along the contact juxtaposing the continental basement sliver and the metasediments. Considering the tectonostratigraphic position, our favored interpretation of these rocks is that they represent an oceanic sedimentary breccia composed by ultramafic clast. Nevertheless, metasomatic products like chlorite, actinolite and lawsonite pseudomorph are observed, thus suggesting interaction and transformation of ultramafic clasts by COH fluids. Figure 8.2 reports a PT-X_{CO2} pseudosection for modeled serpentinite (bulk composition from sample Lor16-5, Table 6.1). The pseudosection shows that carbonate-free assemblages are restricted to very low X_{CO2}, ranging from 0 to 0.002. Carbonate is stable even at very low X_{CO2}, with relatively high abundance. In the pseudosection for the modeled serpentinite, the first carbonate-bearing field contains 20 wt.% of carbonates, thus high enough to be observed in thin section. It is worth noting that the modeled carbonate is Mg-Fe rich, consistently with the modeled bulk composition. Such a result would be consistent with the observation in the Voltri Massif, where dolomite replaces diopside, but it does not apply to the Corsican case, where only Ca-carbonate is found. In the Voltri case, relatively closed system might explain the formation of Mg-carbonates. For the Corsican case, in Chapter 6 it has been shown that massive Ca mass gain occurred, thus the carbonate composition might be buffered by the fluid. Although speculative, it is also plausible to propose that kinetic factors might favor Ca-carbonate precipitation against Mg-rich composition, analogously to what is observed in experiments at low P and T (e.g., Berner, 1975; Deleuze and Brantley, 1997; Davis et al., 2000; Davis et al., 2011). Chlorite is overall stable, whereas calcic-amphibole (tremolite and actinolite) are restricted to T lower than 500°C and very low X_{CO2}. Clinopyroxene crystallization is predicted and also observed in our samples. Talc crystallization is predicted,

but it is never observed in samples from the San Petrone unit. However, talc, chlorite metasomatic product are reported in the blueschist unit (Vitale Brovarone et al., 2011a). Altogether, petrographic observations and pseudosection modeling attest to the reactivity of ultramafic/mafic lithologies with carbon-bearing fluid. More work is needed to better evaluate the effect of fluid infiltration on phase relations in different system (ultramafic/mafic) and the different reactivity of mineral phase, i.e. antigorite, clinopyroxene, amphibole.

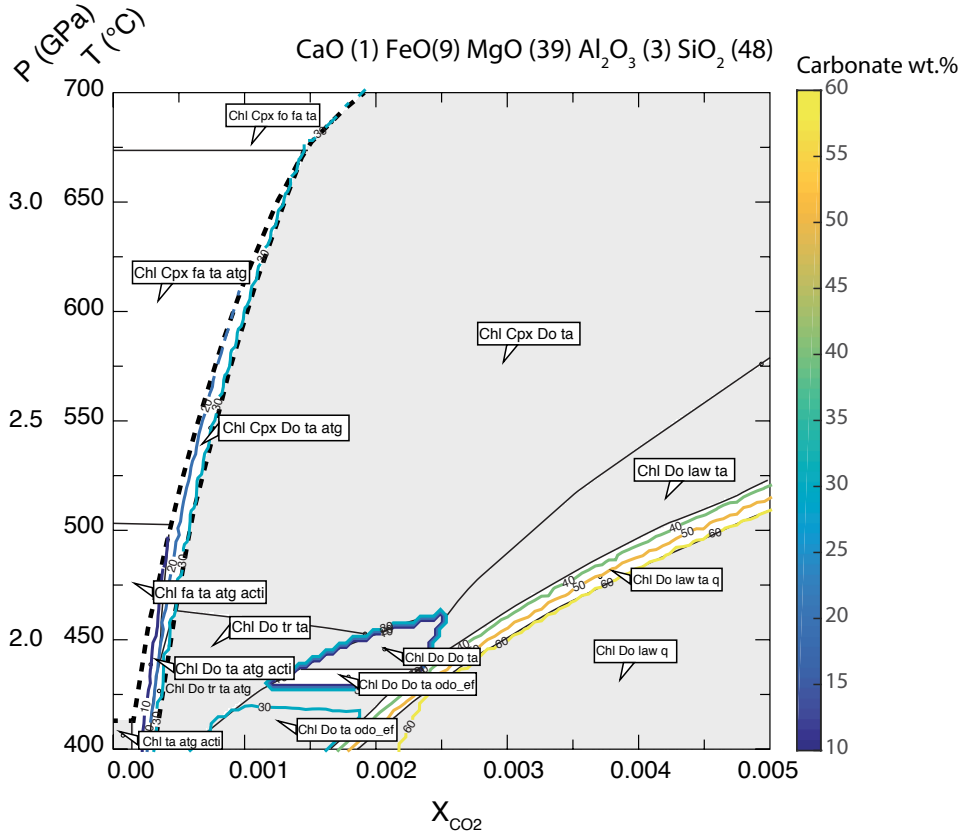

Fig. 8.2: PT-X_{CO2} pseudosection for the bulk composition of serpentinite calculated with Perple_X software. Carbonate absolute abundance isocontours are also reported (abundance in weight per cent). The thermodynamic data file used is hp02. Solid solutions are used for chlorite (Chl), clinopyroxene (Cpx), and carbonate (Do).

In Chapter 5, carbonation affecting other clinopyroxene than diopside, like jadeite, has been reported. This finding opens new perspective on the evaluation of metafelsic rocks as possible reactive lithology with COH fluids. This might be particularly relevant in collisional setting during continental crust subduction. Actually, metamorphic degassing from active collisional orogens supplies a significant amount of CO_2 (Becker et al., 2008; Gaillardet and Galy, 2008;

Perrier et al., 2009; Evans, 2011; Skelton, 2011; Groppo et al., 2013; Girault et al., 2014) and carbon fluxes have been estimated at 0.5-1.5 Mt a^{-1} (Groppo et al., 2017). Potential carbon-source rocks in collisional orogens are calc-silicate rocks and impure marbles that undergo decarbonation reactions (Groppo et al., 2013; Rolfo et al., 2017). Moreover, large carbon fluxes should be facilitated by magmatic intrusion-induced hydrothermal flow (Kerrick and Caldeira, 1998).

If carbon fluxes due to decarbonation might be important along warm geotherms (e.g., Gorman et al., 2006), in deep and cold subduction such that underwent by Alpine Corsica and the Western Alps, carbonate dissolution is a relevant mechanism for carbon transfer also in deeply subducted continental crust (Ferrando et al., 2016). Ferrrando et al. (2016) investigated the UHP impure calcite-dolomite marbles for the Dora Maira Massif and found evidence for dolomite growth during prograde metamorphism by dissolution/precipitation processes, enhanced by increasing P-T conditions as well as by the high salinity in aqueous fluid and low pH conditions. In that case study, the system was closed, thus carbon-bearing fluids could not migrate. However, evidences for fluid flow within the subducting continental crust, along inherited heterogeneities have been brought, for example by Angiboust et al. (2017). The finding of carbonated metafelsic rocks in Alpine Corsica, plus the fieldwork campaign in the Eclogitic Micaschists Complex in the Sesia Lanzo zone (summer 2015; see the Perspective Chapter 10), are promising starting point for a future study on the evolution of carbon-bearing fluids in the subducted continental crust.

8.3.2 Possible physical factors controlling reaction progress

The study of the rate of carbonation reaction at shallow condition in natural analogues and by experimental technique has received increasing attention for its implications on the development of technique for enhanced, in situ CO_2 capture (e.g., Kelemen and Matter, 2008;

Kelemen et al., 2011; Daval, 2009a,b, 2010; Guyot et al., 2011). Beside the industrial and societal interest, near-surface carbonation reaction has been extensively investigated also for its relevance for the global carbon cycle, and for the understanding of the physical-chemical interaction during retrograde metamorphism. Even if a direct extrapolation to higher P and T is not possible, it is interesting to recall some general concepts on parameters that control the overall retrograde reaction rate. One common feature of volume-increasing retrograde reaction is porosity reduction that will ultimately stop the reaction by impeding fluid flow. The porosity reduction during retrograde reaction can be decomposed in: net absorption of the fluid into the rock, and incremental volume occupied by the solid phase converted from the fluid (Tian and Ague, 2014). In contrast, reaction induced fracturing during replacement may be the mechanical mechanism that accelerates the reaction rate by generating new reactive surface area (e.g., Jamtveit et al., 2009; Plümper et al., 2011). Carbonation, like serpentinization and spheroidal weathering, are reactions that involve volume expansion. Fluid-rock interactions that increase the solid volume are often self-limiting because they fill porosity and create reaction rims (e.g., Aharonov et al., 1998; Milsch et al., 2009, Morrow et al., 2001; Tenthorey et al., 1998). Decreasing permeability (cementation of grain boundaries) and reaction rims (amorphous silica layers around carbonated minerals) have been frequently observed in basalt carbonation (e.g., Alt and Tigle, 1999) and experimental studies (e.g., Daval et al., 2009a). The presence of reaction rims coating the grains and clogging the nanoscale porosity are observable only at micro- to nanometer length scale by, for example by TEM observations. Nevertheless, our field observation of pervasive hydrofracturing and microstructures attesting to mineral replacement support the interpretation that in the studied HP carbonation, the reaction was not self-limiting. As proposed by Rudge et al. (2010), permeability and reactive surface are probably maintained by a feedback between volume change (that we estimated increasing of a minimum of ~100% and a maximum ~400%,

Chapter 6), stress increase, and fracturing. Actually, other natural studies on olivine carbonation reactions (e.g., Kelemen and Hirth, 2012) and listwanites (e.g., Hansen et al., 2005; Rudge et al., 2010; Beinlich et al., 2012) arrived to the same conclusions. For example, listwanites often display brecciated textures in the outcrop, as well as hierarchical fracture networks, filled by syn-kinematic carbonate and quartz veins.

Another physical parameter that might exert a control on the rate of fluid rock interaction is the fluid transport mechanism. Tian and Ague (2014) explored chemical reaction systematics for carbonation reactions during retrogression at P-T conditions corresponding to ~13-20 km. In their model they compared reaction progress in case of Darcinian flow and porosity wave transport. Their conclusion is that the overall reaction progress is mainly controlled by the time-integrated fluid fluxes. Nevertheless, they point out that porosity waves might play a crucial role in preventing the porosity to become clogged and, thus, sustaining fluid-flow. At this stage, we cannot definitively conclude on the mechanism of fluid transport along the slab interfaces and how porosity was maintained to allow such large reaction front. However, we gave evidence of very large fluid fluxes of the order of 10^6 m^3 m^{-2}, hydrofracturing and fluid-mineral reaction. Porosity waves model is thus our favored model since it can explain long-range, large-scale upslope fluid flow, high reaction rates and high fluid fluxes. Altogether, geochemical and isotopic signature of carbonated metasomatic rocks coupled with the estimated time-integrated fluid fluxes strongly support models for reactive fluid flow along lithospheric boundaries.

8.4 New insights on the geochemistry of deep carbon-bearing fluids

Metasomatic products may form by fluids from internal source (e.g., dehydration veins) or by externally derived fluids. These two different mechanisms have profound consequence on models for mass transfer in the subducting slab since the first one indicates short-distance (cm

to m) transport, whereas the second one indicates long-distance (km) mass transport. Both kind of metasomatic product yield important information about the composition and behavior of subduction zone fluids. Several lines of evidence outlined in this study on carbonated metasomatic rocks indicate that fluids were actually externally derived (Chapters 5, 6 and 7). Moreover, the geochemical signature of these HP fluids attests to the multi source composition, which suggests that when channelized in the slabs, fluid chemistry change along the fluid path by successive interactions with rocks (hereafter, reactive fluid flow).

Reliable geochemical modeling for element mobility is hindered by unavailable fluid-rock partition coefficients for complex mineral assemblages, such those in the metasomatic systems of the San Petrone unit. Nevertheless, mineral replacement by dissolution and reprecipitation mechanism can inform on the fluid composition. Every contribution to improve the knowledge of subduction zone chemistry is extremely valuable. Actually, direct sampling was realized during the ODP campaign in Costa Rica and in the Izu-Bonin/Mariana margin, but it was restricted to shallow depth (~10-25 km) and had no constrain on reaction-flow history prior sampling (Fryer et al., 1990; Kimura et al., 1997; Fryer et al., 1999). Fluid inclusions in exhumed blueschist and eclogite-facies metamorphic rocks are the most direct way to investigate deep fluids (e.g., Philippot and Selverstone, 1991; Philippot et al., 1995; Cartwright and Barnicoat, 1999; Scambelluri and Philippot, 2001; Frezzotti and Ferrando, 2015). A reconnaissance study on fluid inclusions in omphacite + carbonate veins and carbonated metasomatic rocks has been conducted (see Perspectives, Chapter 10). Results are of difficult interpretation and considering the problems concerning the study of fluid inclusions in carbonates (i.e., possible loss of primary inclusions during aragonite-calcite transition) we chose to focus on estimations from mineralogical phase relations and stable isotope geochemistry.

8.4.1 Carbon transport in high-pressure fluids

Knowledge of the fluid chemistry is essential to determine the transport properties of fluids. Fluid inclusions studies show that diverse fluid compositions are preserved in prograde and peak metamorphic minerals: water dominated C-O-H-N mixtures, brines, N_2-CO_2/CH_4 fluids, and aluminosilicate-rich aqueous fluid phases (see Frezzotti and Ferrando, 2015 for review). All together, the high concentrations of dissolved carbon species proved a mechanism to transport large amounts of carbon between subduction zone reservoirs. Moreover, the ionic carbon speciation may influence the oxidation state of the mantle wedge (Sverjensky et al., 2014). Even if we could not directly measure or predict the carbon speciation in the fluid responsible for the observed carbonation, petrological and geochemical results reported in this work contribute substantially to the understanding of the carbon sources in HP fluids circulating during metamorphism. The systematic of carbon stable isotopes of metasomatic carbonates clearly points to an inorganic source, likely marine metasediments. Moreover, the results of mass balance calculation show a stoichiometric mass gain of CaO and CO_2. This result strongly supports the interpretation of carbon isotopes, identifying dissolved carbonate as the major source of carbon in the HP fluids, for our study area. Carbon speciation in the fluid will depend on many parameters, notably P-T, pH, fO_2 conditions and silicate environment (Sverjensky et al., 2014). Moreover, Sverjensky et al. (2014) pointed out that if at low pressure (i.e. 0.5GPa), only CH_4 and CO_2 forms of aqueous carbon are stable, at HP conditions, things get more complex, with acetic acid and acetate field lying in between the

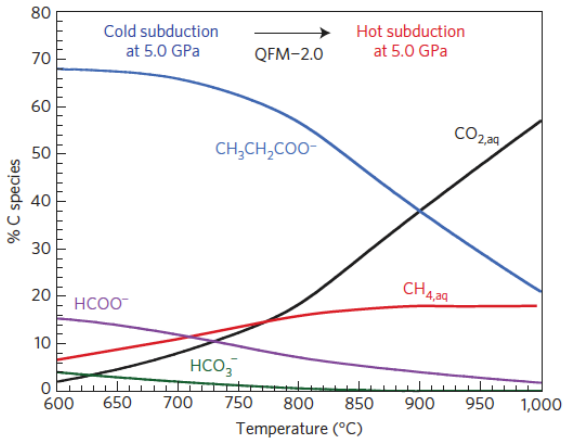

Fig. 8.3: Aqueous C-bearing speciation in equilibrium with a model metasedimentary eclogite containing diamond, jadeite, pyrope, kyanite and coesite at 5GPa and fO_2 condition of QFM -2. Figure from Sverjensky et al. (2014).

QFM and IW redox buffer at near neutral pH. Thus all the above reported species can coexist in equilibrium. These observations are particularly relevant for eclogitic fluid in cold subduction zones where the lower T and the alkaline pH strongly favor ionic carbon-bearing species (Fig. 8.3). In this work, we provided constrains on the fO_2 conditions at which carbonation occurs. For the modeled rock, we used the hematite forming reaction to estimate fO_2 conditions and obtained oxidized conditions (ΔQFM=3). Nevertheless, it is worth stressing that oxidized condition might have been buffered by the rock, therefore, it is not directly linked to the redox state of the fluid (Ague, 1998). Knowledge of fluid redox conditions is relevant for its implications for the relative abundance of carbon-species. More work is needed to better constrain the redox condition of HP fluids and its role in HP carbonation.

8.4.2 Non-volatile element transport in high-pressure, COH fluids

Molecular carbon-bearing species in fluids have no or low dipole moment, thus have very low solvent property (e.g., Deul and Franck, 1991; Walther and Schott, 1988; Walther, 1992). However, fluids also contain dissolved solutes that might play a role in complexing and transporting elements. Fluid speciation, redox state and pH are among the parameters that can control that fluid capability to mobilize elements. Field-based works on HP veins and experimental studies on fluids composition at HP conditions (Becker et al., 1999; Gao and Klemd, 2001; Manning, 2004) conclude that oceanic-slab derived fluids, a part for major component C-O-H, may also be enriched in Na, Ca, Al, Si rich, but with low Mg and Fe. As general trend, Manning (2004) pointed out that total dissolved solids (TDS) increase with depth. Moreover, trace element pattern of low-Cl fluids is comparable to that of island-arc basalt with enrichment in LILE and Pb and depletions in HFSE (Fig. 8.4). Hermann et al. (2006) also propose that aqueous fluids liberated at the blueschist to eclogite facies transition

are dilute and contain only a moderate amounts of LILE, Sr, and Pb. Manning (2004) also pointed out the need of a reactive flow model that accounts for changes of fluid composition during flow.

Mass balance calculation enabled the evaluation of trace element transport during carbonation. Firstly, it has demonstrated that Ca metasomatism (Stage#1 and Stage#1) goes with a general trend of enrichment in alkaline, alkaline earth, LILE (Sr, Pb, ±Th, ±U, ±Ba), permanent loss of LILE hosted by micas (K, Rb, Cs, ± Ba) and mass gain in HREE.

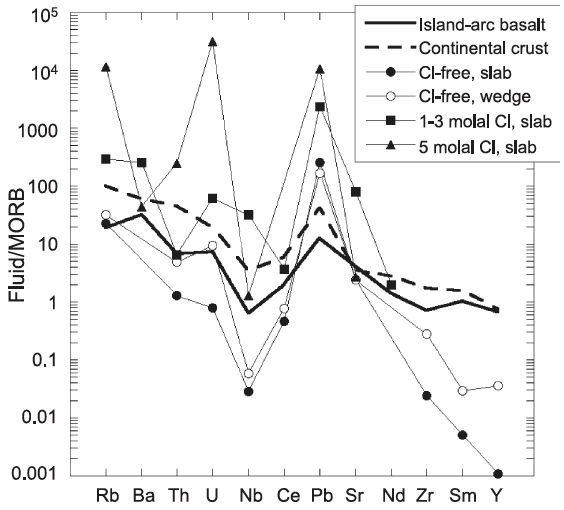

Fig. 8.4: Experimental determination of trace element pattern in slab derived low-Cl aqueous fluids. Figure from Manning (2004).

LREE enrichment is observed during Stage#1, but no systematic mass change occurs during carbonation. This might be related to: i) mineralogical control; ii) fluid composition; iii) a combination of the two. LREE during lawsonite metasomatism is easily explained by the high affinity of this mineral for LREE. Carbonation mainly affects clinopyroxene that are much less rich in trace element than lawsonite. Therefore, the overall preservation of lawsonite might explain the lack of LREE mass loss. Secondly, both Stage#1 and Stage#2 display MREE and HREE + Y mass gain. An increase in more compatible REE is generally related to garnet crystallization. This might be the case for carbonate metasomatism. However, preliminary results on in-situ trace element composition of metasomatic carbonates (by LA-ICP-MS) seem to indicate that carbonate precipitating from HP fluids are enriched in MREE (see the Perspectives in Chapter 10). Our finding on the mobility of MREE and HREE in HP fluids might mean that negative anomalies of these more compatible elements reported in

other studies might be related also to a fractionation during fluid flow and not only to an overall immobility.

8.5 Fluid sources and geodynamic implications

The ensemble of geochemical and isotopic characteristics of metasomatic carbonates requires a fluid which final composition is given by the input of different rock source. Oxygen isotopes signature confirmed that the main water sources are mafic/ultramafic rocks. Conversely, carbon isotopes and the stoichiometric mass gain of CaO and CO_2 is a robust evidence that Ca-C source was external, but derived from previous metasedimentary carbonates dissolution during fluid flow. Other possible metasediments derived fluid tracer is the extremely high Sr enrichment. Actually, carbonates are one of the major Sr reservoirs in subducted rocks. Carbonate dissolution by water-rich-serpentinite derived fluids infiltration, would likely mobilize high quantity of Sr. However, Sr and LILE enrichment might also originate from serpentinite-derived fluids, which can become enriched in incompatible elements in the fore-arc and accretionary prism settings (Deschamps et al., 2012; Kodolányi et al., 2012). Sr isotopic signature revealed the complexity in determining different contribution into the fluids. Isotopic data of carbonated metasomatic rocks fall along mixing curves between metasediments, serpentinite and continental crust. Moreover, it has been shown that simple linear mixing is found inappropriate to model the measured isotopic composition.

We provide, together with previous studies, robust evidences that the metasomatic rind developing along major lithological boundaries in the San Petrone unit, represents a fossil intra-slab fluid channel responsible for long-distance mass transport (externally derived fluids). This channel was likely active from the prograde to peak and early retrograde stage. The time gap between lawsonite metasomatism (Stage#1) and carbonate metasomatism

(Stage#2) remains unsolved, and, for the moment, we can give only relative time constrains. Considering the field observations (metasomatism along slab-parallel interface), the isotopic data, and the high time-integrated fluid fluxes (10^6 m^3 m^{-2}), we interpret these results as the evidence for long-range, large-scale upslope fluid flow along porosity channel within the slab (Fig. 8.5). The collected data allow proposing a model for fluid composition evolution by reactive fluid flow along disparate lithologies. The driving forces for mineral-fluid reaction and chemical exchange were both P-T and chemical gradient (Bebout and Barton, 1989, 1993; Bebout and Penniston-Dorland, 2016). Considering that major serpentinite dehydration (i.e., antigorite breakdown) occurs at ca. 100 km depth, and a slab angle of 45°, it means that fluids percolate 40km upslope, along a down-P, down-T gradient.

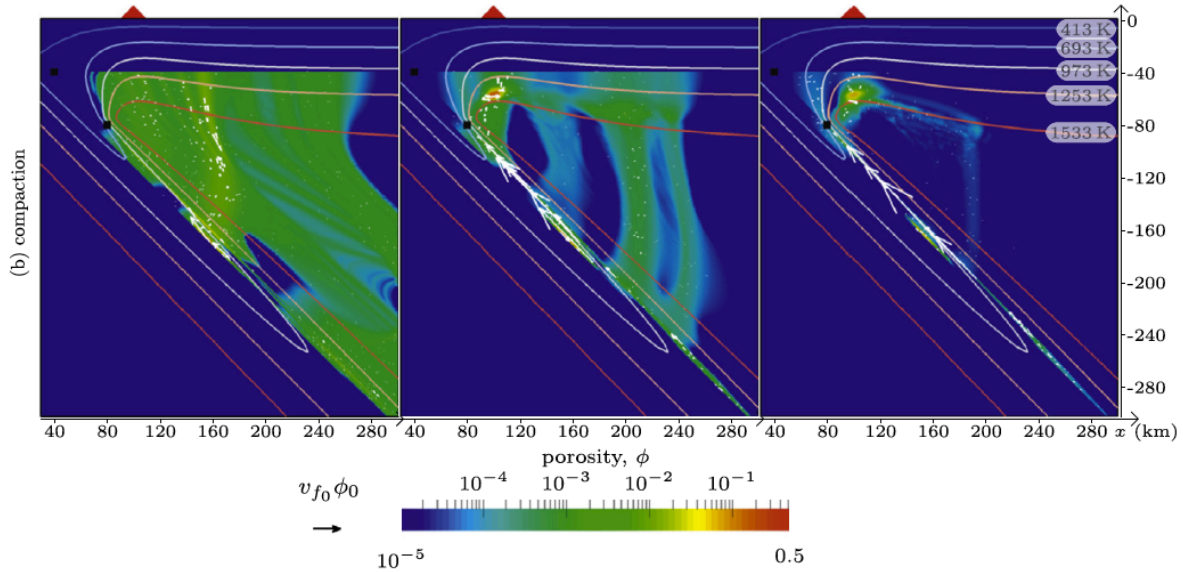

Fig. 8.5: Time-averaged porosity and fluid fluxes when effects of compaction pressure gradients (porosity waves) are included in numerical models. White arrows indicate the upslope flow of fluids produced by dehydration reactions. Figure from Wilson et al., 2014.

CHAPTER 9
Conclusions

The study of the long-term, global carbon cycle must take into consideration important processes occurring in subduction zones that are able to modulate the residence time of carbon in different reservoirs, modify the isotopic composition of subducted vs. recycled carbon, and, in a long time-scale perspective, influence the fluctuation of CO_2 emissions at volcanic arcs and thereby the fluctuation of atmospheric CO_2 over geological time scales. Fluids have pivotal role in the evolution of carbon-bearing rocks during metamorphism and, therefore, they determine the ultimate fate of carbon during subduction. For this reason, special attention should be paid to preserved metasomatic systems in exhumed HP and UHP metamorphic terrains, because they represents a unique opportunity to directly investigate deep processes involving fluid-rock interactions.

The field survey, the petrological, geochemical and isotopic study conducted in this work is among the first reports of HP carbonation process and contributes to answer some of the major questions that arose after this discovery. The composition and source of the HP fluids involved are elucidated, as well as the mechanism of mass transfer through fluid flow and the flow direction. The results presented in the previous chapters allow coming to the following conclusions about HP rock carbonation process:

- Reactive fluid flow and carbonate precipitation from HP fluids along major lithospheric lithological interfaces of the subducting slab is evidenced by field evidence for fluid overpressure, like hydraulic breccias and crack-seal veining, and by the development reaction rinds between disparate lithologies. The necessary chemical

potential for reaction is given by the down-T, down-P geothermal gradient and by the juxtaposition of contrasting lithologies.

- Carbon-bearing fluid-rock interactions are recorded by microstructures (e.g. atoll-like minerals or embayed crystal rims), mineral zoning, and isotopic changes. In most of the cases, HP carbonation reactions results are recognizable by structural and microstructural relationships that give corrosion-like textures, notably with heterogeneous consumption and segmentation of silicate-rich domains.
- Stable isotopes thermometry and thermodynamic modeling indicates that rock carbonation occurred near peak conditions at 2-2.3 GPa and ~500°. Moreover, it has been shown that carbonation occurs in oxidized lithologies. Rocks from Alpine Corsica display evidence for oxidized conditions like increase in Fe^{3+} content in clinopyroxene and hematite-bearing mineral assemblages. Moreover, petrogenetic grids attest to the oxidized conditions of the modeled rock ($\Delta FQM = 3$). Other studies show that ultramafic and more reduced lithologies like serpentinite can be carbonated during HP metamorphism as well. All together, the data suggest that oxygen fugacity might not be a limiting factor for the progress of carbonation reaction.
- It has been demonstrated that a large variety of rocks, ranging from ultramafic/mafic lithologies to metafelsic, are reactive with carbon-bearing fluids. This finding potentially has implication for fluid-rock interactions processes occurring during continental crust subduction in collisional settings. Carbonation of metafelsic rocks might be particularly relevant for orogenic CO_2 cycling during continental subduction in active collisional settings like the Himalaya.
- Carbonates precipitated from HP fluids have a characteristic isotopic signature with low $\delta^{18}O$, $\delta^{13}C$ at ~0, and $^{87}Sr/^{86}Sr$ signature that reflects the multi source origin of the

fluid. Therefore, carbonation can potential modify the oxygen and carbon isotopic signature of carbonates during oceanic subduction.

- The stoichiometric CaO and CO_2 mass gain strongly suggests that previously dissolved carbonates are the main source of Ca and C in HP fluids.
- Estimated time-integrated fluid fluxes of 10^6 m^3 m^{-2} indicates that extremely high fluid fluxes are not restricted to shallower environment or to fractured deep crust. The Alpine Corsica case well shown that inherited lithospheric interfaces may play a crucial role in channelizing fluid flow during subduction that, ultimately will contribute to determine the petrological evolution of the subducting slab by driving metasomatic reactions.
- Estimated time-integrated CO_2 fluxes of ca. 300 t m^{-2} indicate that carbon is extremely mobile during subduction metamorphism if fluids infiltration occurs. However, our estimation of carbon uptake during carbonation of 175 g per 100 g of rocks also suggests that the same amount of carbon that is released during carbonate dissolution can be uptake again during carbonation.

In conclusion, carbon sequestration from fluids by HP rock carbonation can affect carbon fluxes between subduction zones reservoir and, potentially, this process may have consequences for the residence time of carbon in the subducting slab. This implies that rock carbonation may modulate the emission of CO_2 at volcanic arcs over geological times.

CHAPTER 10
Perspectives

High-pressure carbonation and, more generally, processes of carbon-bearing fluid-rock interaction at HP condition have yet to be thoroughly understood. This thesis represents the first field-based study on HP carbonation, and opens to several possible long-term researches. As an example thermo-chemical modeling may help to better constrain the details of carbonation reactions at HP conditions in terms of physico-chemical parameters like pH, fO_2 and fluid speciation. Many others perspectives are opened (field-work in different geological settings, detailed isotopic study, microstructural study by transmitted electron microscope, experiments on mineral carbonation etc.). Research on carbon-bearing fluid-rock interactions is a new exciting field that has draw attention of several research groups. For examples, works on natural samples of carbonated metasomatic rocks from other geological settings (Betic Cordillera, South Spain; Menzel et al., 2016) and exerpimental studies of HP carbonation (Sieber et al., 2016;) are on going.

In this last chapter, preliminary results of other research activities have been done during my PhD will be presented, notably: results of trace element analyses by LA-ICP-MS, fluid-inclusions study by micro-Raman spectrometry and microthermometry, together with some considerations on thermodynamic modeling. Lastly, the last section will be dedicated to some promising finding from the fieldwork in the Sesia Lanzo zone (Western Alps). These results are preliminary, but still deserve consideration as useful indicators of the direction of future research projecets.

10.1 Trace element data of metasomatic carbonates by LA-ICP-MS

Eclogite-facies minerals garnet and omphacite have limited role in hosting trace elements. Conversely, accessory minerals have been a topic of interest in the last decades since they may host many traces elements in the slab (e.g., Hermann, 2002; Rubatto and Hermann, 2003; Spandler et al., 2003; Miller et al., 2007; Klimm et al., 2008).

Fluid-rock interactions are critical to the stability of trace element-rich phases and, thus, can determine the fate of these elements during metamorphism. By consequence, processes occurring in HP alteration/mélange zones have a pivotal role in the redistribution of trace elements between metamorphic minerals and fluids. The interpretation of fluid composition responsible for vein formation and metasomatism, however, is challenging because rocks undergo complex fluid-rock interactions and dissolution/precipitation processes that are yet to fully understand (Spandler and Pirrard, 2013). Petrography, geochemistry and mass balance calculation can give us constrains on the overall element mobility and/or redistribution.

For a thorough understanding of fluid-rock exchange process, a detailed study of mineral trace-element data is fundamental for the thoroughly understanding of whole rock analysis and mass balance estimations. Preliminary LA-ICP-MS data will be presented here, with focus on carbonate, clinopyroxene and lawsonite trace element data. Data on garnet, epidote, and sphene were also acquired, but will not be discussed here. Carbonates crystals from four different calcschist samples, and 22 carbonated metasomatic rocks and carbonate (± omphacite, ± lawsonite) veins were analyzed by LA-ICP-MS. Clinopyroxene has been analyzed in 4 carbonated metasomatic rocks and one carbonate + omphacite vein. the aim of this set of analyses was to highlight geochemical differences between unaltered metasedimentary carbonates and carbonated precipitated from HP fluids. Also, the analysis of HP carbonate veins vs. carbonated metasomatic rocks aims to investigated the geochemical effects of fluid-rock interactions and evaluates the element mobility during silicate

dissolution/carbonate precipitation process. Analyses were performed at the University of Montpellier in collaboration with Olivier Alard and Olivier Bruguier. Analytical methods and conditions are reported in Chapter 3.

10.1.1 Sampling and analysis strategy

Analyses for trace element data of carbonated metasomatic rocks by LA-ICP-MS were performed in 2014 and 2016. After that first set of data was acquired, preliminary data seem to indicate that a difference in trace element composition between carbonated metasomatic rocks and carbonate (± omphacite, ± lawsonite) veins exist (Fig. 10.1a). Therefore, in order to get a higher statistic, we collected new samples from study different outcrops in the San Petrone unit and separate more massive carbonate from vein material. Fragments of carbonates were successively mounted in epoxy (Fig. 10.1b). Epoxy was successively polished and carbon coated. Carbonate fragments were observed at SEM to ensure that crystals were clear of inclusion and, then, analyzed by LA-ICP-MS. SEM observations were performed after LA-ICP-MS to ensure that no contamination occurred during the analysis.

(a) **(b)**

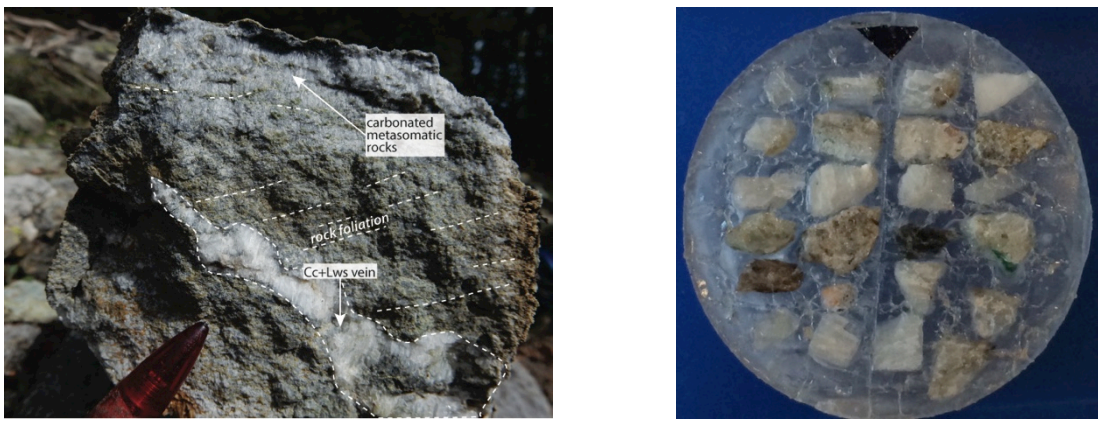

Fig. 10.1: a) Fresh cut of a carbonated metasomatic rock from Mt Muffraje area cut across by a carbonate + lawsonite vein. Dashed white lines underline the vein wall and the rock foliation. **b)** Carbonate fragments incorporate in epoxy.

10.1.2 Results

Primitive mantle normalized trace elements in carbonates from both unaltered and carbonated metasomatic rocks display flat pattern, with positive anomaly in Pb and Sr. Only sample 1cor12-11N (carbonate + omphacite vein) display an enrichment in MREE and Y with value 10 times higher than the primitive mantle. In contrast, chondrite normalized REE patterns for unaltered and metasomatic rocks display different trends. These latter will thus presented in the following.

Carbonate from pristine metasediments:

Analyzed carbonate crystals display very homogenous trends, with negative slope (Fig. 10.2). La/Sm_N ratio ranges from 0.59 to 1.8, whereas Ce/Yb_N ranges from 1.5 to 5.15. All samples display a negative Eu anomaly (Eu*= Eu/((Sm+Gd)/2))) with an average value of 0.43 (±0.04).

Carbonate from carbonated metasomatic rocks:

Carbonates from carbonated metasomatic rocks display a characteristic bell-shaped pattern with a relative enrichment of MREE over LREE and HREE. In most cases, they are more depleted compared to the average metasediments (Fig. 10.2). An exception is constituted by carbonate from carbonate + omphacite veins from Aja Rossa are more enriched in MREE than the average metasediment. Carbonate in carbonate and carbonate + lawsonite veins from the Mt Muffraje area vein display a Eu* positive anomaly (max value 1.7; Fig. 10.1). Samples from carbonated metasomatic rocks in the Mt Muffraje display different trends: carbonate from carbonated portion of the rock displays a negative slope, and is more enriched in LREE compared to carbonate from unaltered rock: La/Sm_N ratio range from 0.38 to 5.84, whereas Ce/Yb_N ranges from 1.84 to 9.04. In contrast, carbonate in veins has a bell-shape pattern like veins from Aja Rossa, Col di Prato and Loriani.

Clinopyroxene and lawsonite from carbonated metasomatic rocks

Chondrite normalized patterns of clinopyroxene display a positive to flat pattern, with MREE and HREE more enriched compared to LREE (Fig. 10.3). Diopside (Cpx1) is generally more depleted in REE than omphacite (Cpx2), and patterns are less homogeneous. Conversely, omphacite (Cpx2) are very homogeneous over all analyzed samples from different localities and REE content is always above the detection limit. Moreover, Cpx2 displays higher Li content than Cpx1 (Fig. 10.4). Omphacite from omphacite + carbonate veins (Aja Rossa) display a positive Eu* anomaly (minimum 1.34 and maximum value 2.5), whereas Cpx2 from Mt Muffraje display a negative Eu* anomaly. Lawsonite displays a characteristic pattern with negative slope (La/Sm_N ratio ranging from 0.58 to 7.25 and Ce/Yb_N ranging from 0.72 to 29.65) and positive Eu* anomaly. However, lawsonite from Mt Muffraje displays a rather flat pattern with an average La/Sm_N of 1.73 and Ce/Yb_N of 0.74.

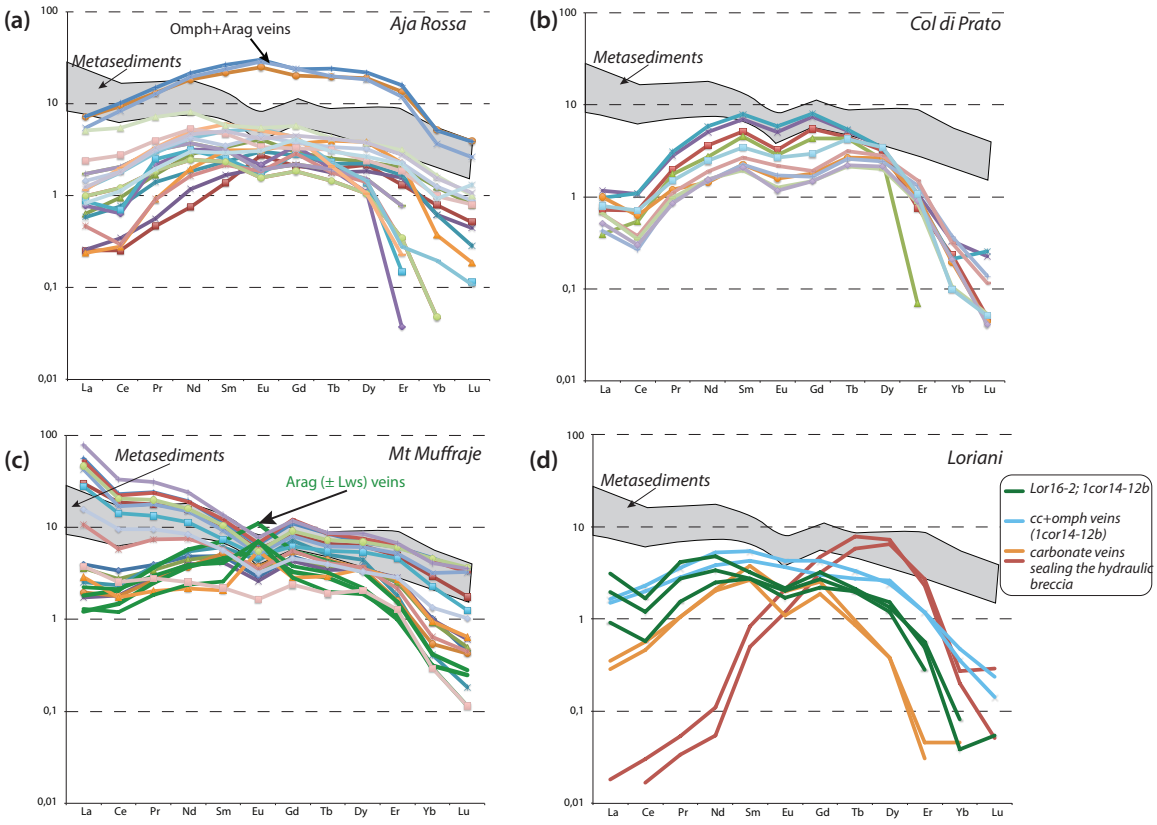

Fig. 10.2: Chondrite normalized REE patterns for metasomatic carbonates. Shaded area corresponds to the field of compositions of analyzed unaltered metasediments. In (c) green lines corresponds to analyses of carbonate veins.

10.1.3 Preliminary discussion

Two intriguing observation can be outlined about the analyzed metasomatic carbonates.

i) Carbonate in HP veins are overall homogeneous, in the entire investigated area, with a bell-shaped pattern enriched in MEE over LREE and HREE. This homogeneity suggests that these patterns are representative of the partitioning between the HP fluid and the carbonate, thus providing information on the composition of the fluid. Carbonate in carbonate + lawsonite vein displays a positive anomaly in Eu, which suggests that they might be representative of a different fluid pulse, richer in Eu..

ii) Carbonate in carbonated metasomatic rocks display a wide range of pattern from bell-shape to pattern with enrichment in LREE over HREE. Microstructurally, carbonates that display a LREE-enriched pattern are in portion of the rock were corrosion-like texture are observed.

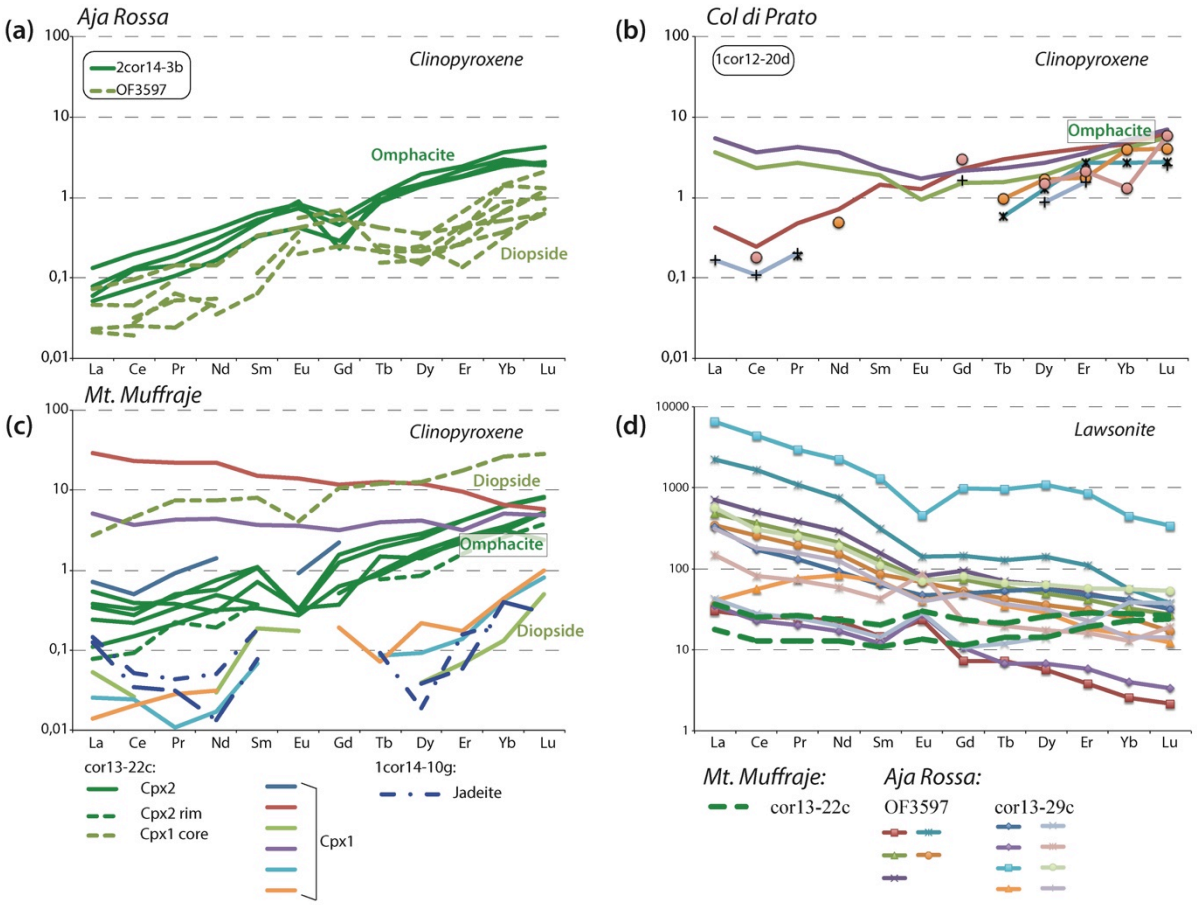

Fig. 10.3: a-c) Chondrite normalized REE patterns for clinopyroxenes (Cpx1 and Cpx2) in carbonated metasomatic rocks. d) Chondrite normalized REE patterns for lawsonite in carbonates metasomatic rocks.

It is tempting to propose that this different trend between carbonate in veins and those found in the rock matrix as the effect of silicate dissolution and trace element redistribution in the precipitating carbonate. In particular, the local enrichment in LREE and MREE might be linked to the dissolution of high LREE/HREE phases, in this case Cpx1. This hypothesis is also supported by the measured REE content in Cpx1, that display pattern with negative to flat slope. In contrast, Cpx2 always display a positive slope. This latter observation might mean that LREE are either fractionated into the carbonate or bring out of the system by fluids.

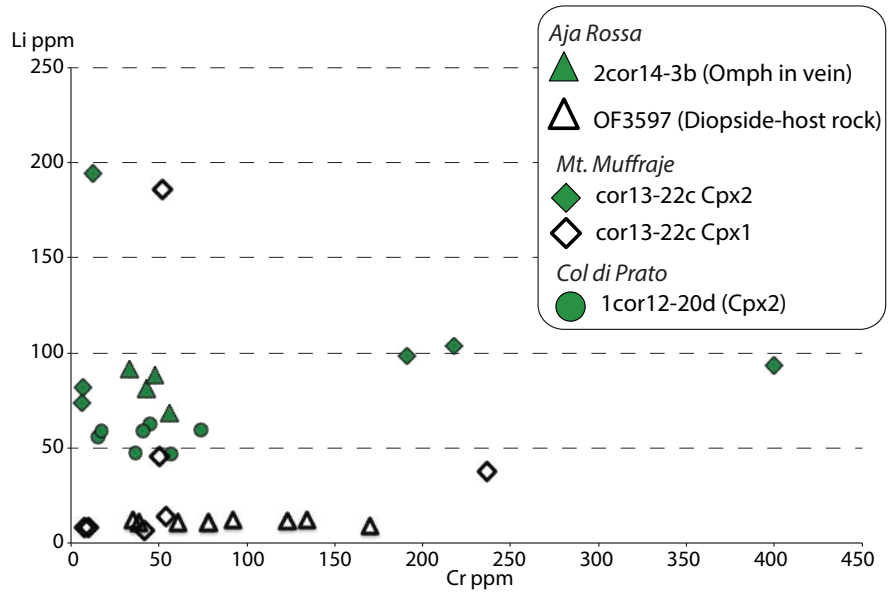

Fig. 10.4: Plot of Cr vs. Li concentration (values in part per million) of analyzed clinopyroxenes (Cpx1 and Cpx2) from different outcrops. Clinopyroxene from the same outcrop have same symbol, and the generation is distinguishable by open (Cpx1) or shaded symbol (Cpx2).

Lastly, the analyses of lawsonite (Fig. 10.3d) well show how different trace element content can be found in mineral phases, even if ascribed to the same stage of metasomatism. This observation calls for further investigation to determine the contribution of each phase to the whole rock trace element composition, also taking in consideration the local initial heterogeneities. This approach may represent an useful tool for the study of metasomatic rocks where deformation and retrogression make the distinction between primary and secondary carbonates more complex.

10.2 Fluid inclusions study by micro-Raman spectrometry and microthermometry

Fluid inclusions are a type of inclusion composed of a fluid phase coexisting with the host mineral during crystallization (primary inclusion) or later, trapped along healed microfractures (secondary incl.). As long as no leakage has occurred, fluid inclusions usually behave as closed systems, provided that no reaction takes place between the inclusion and the mineral host. The study of fluid inclusions constitutes a special topic of petrology/geochemistry, described in specialized literature (e.g. Roedder, 1984; Hurai et al., 2015). As the fluid phase disappears as soon as the inclusion is opened, it is essential to determine its main characteristics (composition and density) by non-destructive techniques, first of all microthermometry (temperatures of phase transitions, i.e. T of homogenization-T_h and T of melting-T_m, during freezing-heating experiments) or micro-Raman spectrometry. Alternatively, the unopened inclusion is an isochoric (constant density) system, provided that solid volume variations (compressibility or dilatancy) are neglected and that no leakage has occurred at changing P and T. In relatively simple systems (unary or binary), which fortunately are present in most inclusions, final melting temperature T_m gives the composition (e.g. salinity in H_2O-NaCl fluids), and T_h gives the density of the fluid. Raman micro-spectroscopy, much used in recent years, allows the characterization of solid, liquid and vapor phases for Raman-active substances (e.g., Touret and Frezzotti, 2003; Hurai et al., 2015). Modern Raman confocal systems can operate at a lateral resolution of ~1μm and depth resolution of about ±2μm, resulting in an effective volume resolution of ~5μm^3 (Hurai et al., 2015). It means that even tiny fluid inclusions can be analyzed by Raman spectroscopy. Common compounds in gas phases detectable by Raman spectrometry are: CO_2, CH_4, CO, N_2, H_2, H_2S, SO_2. Dissolved anions like HCO_3^- are also detectable. Monoatomic ions, such as Na^+, K^+, $Ca^{2+,}$ and Cl^-, are Raman inactive. Moreover, after previous calibration, it is possible to have a quantitative chemical analysis of the studied inclusions. In short, fluid inclusions

provide a unique opportunity to have a direct access to the chemical and physical properties of a fluid that interacted with rocks at great depth or in the most remote past. The difficulty of this type of study and the possible causes of errors must however be constantly kept in mind and discussed step by step. In metamorphic rocks, these are notably:

i) The small size (difficulty of observation) but great number of inclusions in any rock sample, requiring an extremely careful description of the inclusions to be studied.

ii) Possible modifications of the fluid composition and/or density during peak conditions, at which most rock-forming minerals have crystallized, and the surface. High-pressure metamorphic rocks are especially complicated in this respect, as the distance of transportation may represent 10's km. As any possible modification of the inclusion or its fluid content depends from the pressure difference between the fluid and the mineral host, much attention must be given on the relation between the fluid isochores and the rock P-T path (Isochoric principle)(Touret, 2001). Actually, after the formation at HP conditions of a fluid inclusion, P and T are no longer independent variable, because they are related to the equation of state of the enclosed fluid. During the retrograde path, when the strength of the host mineral is no longer able to accommodate to the pressure difference, inclusion may be ruptured, either by implosion, or by explosion (decrepitation). In order to have reliable measurements of fluid physical properties, only primary inclusions have to be analyzed because they did not record any volume changes that cause variations in parameters like density. However, it must be note that, if the system keeps closed, a decrepitated primary fluid inclusion still preserves its chemical composition.

iii) Finally, the interpretation of fluid inclusion data must be done at the light of mineral data, a model of fluid-mineral interaction at changing P-T conditions, or any other variable of state of the fluid-rock system (e.g. fO_2, etc.).

10.2.1 Results

Fluid inclusions in three samples have been studied by micro-Raman and microthermometry: 2 omphacite + carbonate veins (1cor12-11N and 2cor14-3b) and one silicate-bearing marble (cor13-22d). Host minerals were calcite and omphacite in the veins and apatite and garnet in the silicate-bearing marble. I will give here a brief petrographic description of the different fluid inclusions for each host mineral and their relative composition determined by micro-Raman spectrometry.

10.2.1.1 Petrography and composition of fluid inclusions

Omphacite (samples 1cor12-11N and 2cor14-3b): all fluid inclusions in omphacite are bi-phase (liquid+vapor) and primary. Crystals usually host fluid inclusions along cleavage planes, and the most of them are thus decrepitated or too tiny to be analyzed. However, few preserved fluid inclusions have been identified. Unfortunately, each crystal contains no more than one preserved fluid inclusion so that fluid-changes during crystal growth could not be tested. Inclusions display characteristic negative crystal shape and homogeneous vapor-liquid ratio ranging fro 1:3 to 1:4 (Fig. 10.5a). Furthermore, most of preserved primary inclusions display a tail. This feature points to a partial decrepitation of the inclusion. From a chemical point of view, all inclusions are composed by water + H_2O_{vap} (data acquired by micro-Raman spectrometry) and no daughter minerals have been observed (e.g. halite is Raman inactive, but cubic crystals can be easily recognized by optical microscopy).

Calcite (samples 1cor12-11N and 2cor14-3b): all fluid inclusions in calcite are bi-phase (liquid + vapor) with no daughter minerals. Two different generations of inclusions can be distinguished: (i) trails of small inclusions (usually <10μm) cutting across calcite and omphacite crystals (Fig. 10.5b), and oriented parallel to the vein wall; (ii) cluster of primary inclusions within single crystal (Fig. 10.5c). Trail forming inclusions have variable vapor-liquid ratio (ranging from 1:2 to 1:6) and they are composed by water and H_2O_{vap}.

Interestingly, inclusion size decreases nearby crystal twinning. Primary inclusions often occur in calcite crystals nearby omphacite. Large variations in inclusion size are observed (size ranging from 10 to 50 μm) but the vapor-liquid ratio is quite homogeneous (ranging from 1:4 to 1:6). Bigger inclusions are composed by water + gas mixture of H_2O_{vap}+CH_4. In one case, the gas phase was: H_2O_{vap}+CH_4+H_2. Secondary fluid inclusions (trails) are composed by water+ H_2O_{vap}.

Apatite (sample cor13-22d): fluid inclusions are bi-phase (liquid + vapor) and primary (Fig. 10.5d). Shape is often rectangular and size around 10 μm. Bigger inclusions have more irregular shape, probably linked to a partial decrepitation. The vapor-liquid ratio ranges from 1:3 to 1:5. Sometimes, clusters of smaller inclusions occur around bigger ones. Inclusions are composed by water + gas mixture H_2O_{vap}+CH_4. The smaller inclusions are composed by water+ H_2O_{vap}.

Garnet (sample cor13-22d): fluid inclusions are bi-phase (water + H_2O_{vap}). Shape is quite irregular and vapor-liquid ratio ranges from 1:3 to 1:5.

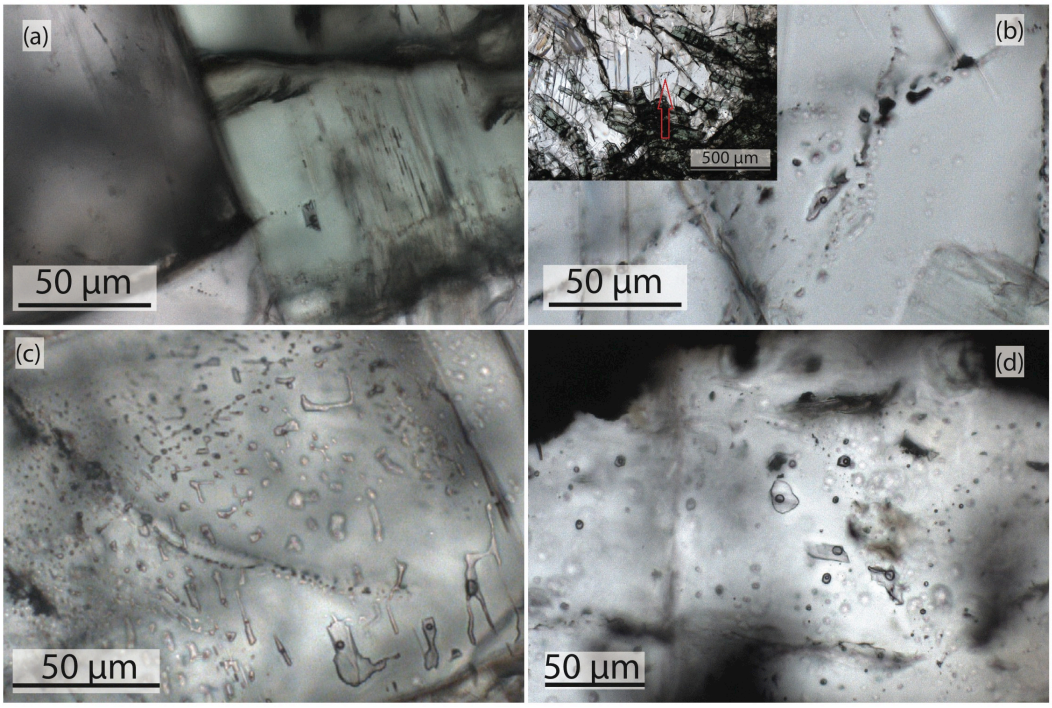

Fig. 10.5: Fluid inclusions in host minerals. (a) Primary fluid inclusions in omphacite; (b) trail of fluid inclusions calcite; (c) cluster of fluid inclusion in calcite; (d) primary fluid inclusions in apatite.

10.2.1.2 Microthermometry on fluid inclusions

Temperature of homogenization and final melting were measured by microthermometry on fluid inclusions in carbonate (from omphacite + carbonate vein and carbonated metasomatic rock), omphacite and apatite. Fluid inclusions in garnet were also measured, but T of final melting could not be determined. Results are reported as histogram for T_h and T_m in Figure 10.6, whereas results for inclusions where both T_h and T_m were determined are reported in the plot T_h vs. T_m in Figure 10.7

The plot T_h vs. T_m (Fig. 10.7) shows that calcite and omphacite can be distinguished into two separate groups (group1 and group3), whereas among inclusions in apatite two differnt groups are distiguished (group 2 and 2'). This is better depicted in the histogram (Fig. 10.6) where the distribution points out the different groups. T_h for cluster inclusions in calcite is quite dispersed between 180 and 210°, but display an overall unimodal distribution with the 195° class of temperature with the highest frequency of measurements. Modal distribution for T_h in trail inclusions cannot be determined because of the low number of measurements. However, they clearly display lower T_h compared to cluster inclusion. Conversely, in the T_m histogram, all inclusion in calcite display a unimodal distribution (T ranging from -3 to -2°; Fig. 10.6.2b,d) and the distinction between cluster and trails is no visible. T_h for inclusions in omphacite is quite dispersed. The distribution of T_h seems to be bi-modal around the class of temperature 170 and 200° (Fig. 10.6c). T_h distribution in fluid inclusions in apatite is quite homogeneous (Fig. 10.6c), whereas T_m is bi-modal. We can thus distiguish two groups: one with higher salinity (lower T_m, group 2) and one with T_m falling in between that of group 1 and 3 (Fig. 10.7). An intermediate group resulting from mixing fluids from group 2 and 2' was not identified. Plotting the isochores on a P-T diagram (Fig. 10.8), it can be seen that all isochores have low slope and they cluster together quite well (Fig. 10.8d). Furthermore, all isochores are lower than the aragonite-calcite transition.

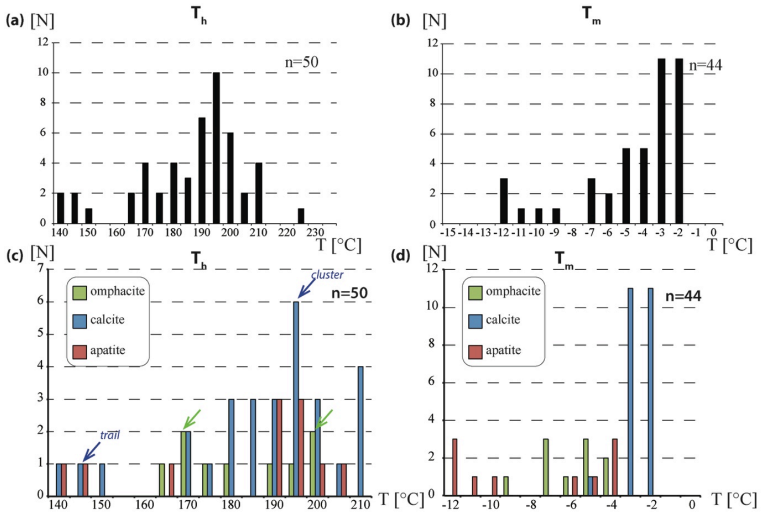

Fig. 10.6: histogram of measured Th and Tm in calcite, omphacite and apatite. Blue and green arrows indicate selected inclusions in calcite and omphacite for isochores plot in Figure X.5.

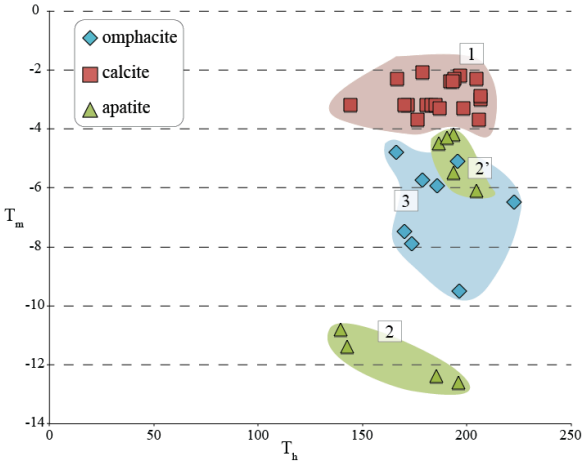

Fig. 10.7: plot T_h vs. T_m for analyses on fluid inclusions where both T_h and T_m could be measured.

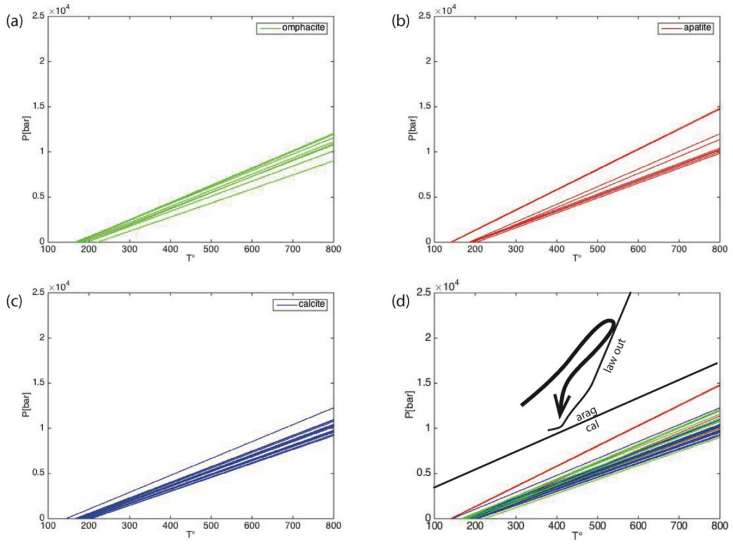

Fig. 10.8: Calculated isochores for inclusions in omphacite (a), apatite (b) and calcite (c). d) P-T diagramme reporting isochores and corsica P-T path, together with the reaction curve for calcite-aragonite transition and the lawsonite-out reaction.

10.2.2 Preliminary interpretation

Similar T_h and different T_m indicate that the composition of the fluid inclusions varies from one grain to another; thus densities must vary also. This compositional variation may be either primary or secondary in origin. On the other hand the quite constant values of T_h points to similar temperature of entrapment. Raman spectroscopy on fluid inclusions in omphacite, calcite and apatite shows that omphacite biphase L+V inclusion are composed by H_2O_{liq} and H_2O_{vap}, while calcite and apatite have gas phase composed by $H_2O_{vap} + CH_4$. No ions such HCO_3^- has been detected. Notably, inclusions in omphacite and calcite in veins have different chemistry, but similar T_h and T_m.

The simplest explanation is a local equilibrium within carbonate inclusions. Indeed, carbonate precipitation lower pH by producing protons H^+:

$$\text{(i) } Ca^{2+} + 2HCO_3^- \rightarrow CaCO_3 + HCO_3^- + H^+$$

Therefore, it is tempting to propose that the new, more acid, fluid entrapped during carbonate crystallization can react with the mineral wall and dissolve some carbonate to form methane.

$$\text{(ii) } CaCO_3 + 4H_2 \rightarrow CH_4 + Ca(OH)_2 + H_2O$$

Differences in density can also be observed plotting selected isochores on a P-T diagram. In Figure 10.9, selected isochores for cluster and trail fluid inclusion in calcite have been plotted together with the two selected isochores for omphacite (170 and 200°). The observed differences in T_h and T_m may correspond to different time of entrapment: a first one, corresponding to the formation of cluster inclusions in calcite and primary inclusion in omphacite, occurring during a first stage of almost isothermic decompression, a second one during later stage decompression and cooling. Isochores of fluid inclusions in apatite fall have the same slope of inclusions from the omphacite + carbonate vein. It is plausible that they formed at the same time. However, data are not enough to interpret the presence of CH_4. Actually, more catholuminescence observation revealed that apatite and carbonate in the

carbonated metasomatic rock are zoned (Fig. 10.10). Therefore, a more detailed study on fluid inclusions of different generations (primary, secondary) and from different zone is needed toe elucidate the evolution of the chemistry of infiltrating fluids.

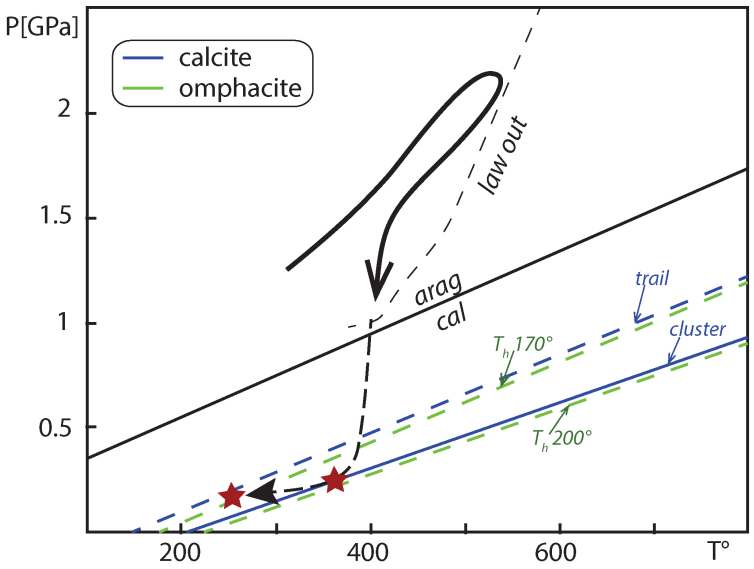

Fig. 10.9: selected isochores for calcite and omphacite. This diagramme point to a re-equilibration of primary and secondary inclusion during later stage of exhumation and after the aragonite-calcite transition.

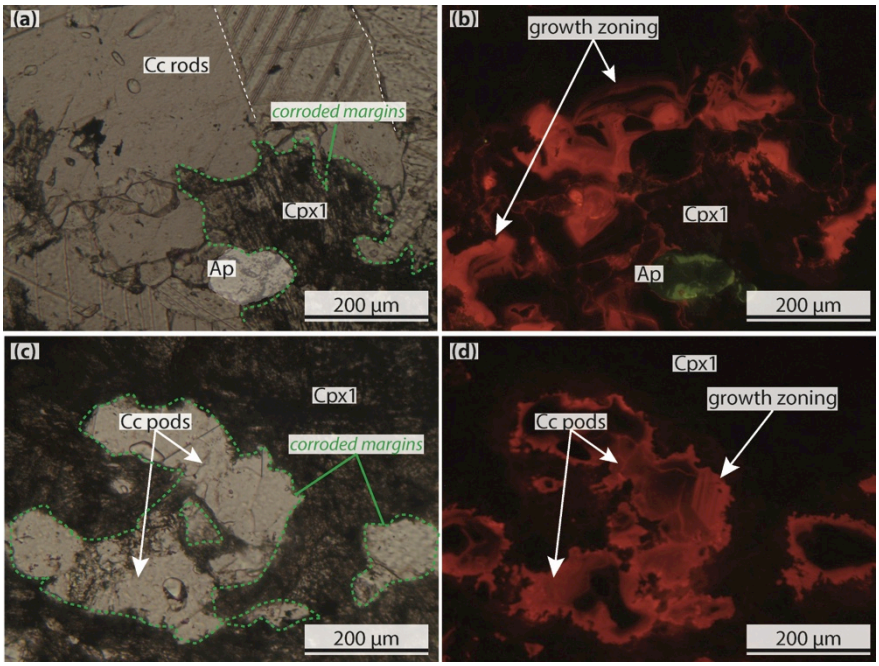

Fig. 10.10: Photomicrographs and relative optical cathodoluminescence image of carbonates from carbonated metasomatic rocks from Mt Muffraje area. Calcite crystals display concentric and sectoral zoning. Luminescence color passes from dark-brown, to dark orange and bright orange/yellow. Note that apatite is also zoned. Note that apatite is also luminescent and zoned. a-b) sample cor13-22e; c-d) Sample cor13-22d.

10.3. Thermodynamic modeling and thermobarometry

The determination of P-T conditions at which metasomatism takes place is crucial since it can inform on the physical conditions at which fluid-rock interactions take place (Goncalves et al., 2013). Phase diagram sections computed for specific bulk composition as a function of intensive parameters, like P, T and fluid composition (i.e., pseudosections) have been widely used in the last decades for the study metamorphic reactions and to achieve thermobarometry estimations (Connolly and Petrini, 2002; Powell and Holland, 2008). However, pseudosection modeling requires: i) the assumption that "local equilibrium" is achieved (Thompson, 1959; Carmichael, 1969; Korzhinskii, 1970), and ii) the precise estimation of the equilibrium volume and effective bulk composition. These assumptions are commonly not hold in metasomatic rocks, as attested by reaction textures and complex mineral zoning (Powell and Holland, 2008). Successful application of pseudosection modeling requires: i) detailed mineralogical and textural investigation to identify the paragenesis that is in equilibrium during the fluid-rock interaction; ii) mass balance calculation; iii) knowledge on the effects of mass transfer on phase relations (Goncalves et al., 2013). For the study of carbonated metasomatic rocks from Alpine Corsica, other major issues are i) the choice of carbonate solid solutions, ii) the unknown fluid composition, and iii) the role of different carbon species dissolved in the fluid. Reconnaissance calculations have been run for carbonated metasomatic rocks in order to test mineral equilibria. One of the first results is that given the most recent thermodynamic model for carbonate solid solution (Franzolin et al., 2011), carbonates are overall stable in the P-T range of interest and carbonate-free metasomatic rocks should not exist even at very low X_{CO2}. Moreover, carbonate in the metasomatic system of Alpine Corsica is always pure Ca-carbonate. In contrast, the thermodynamic solid solution model for ternary Ca-Fe-Mg carbonates predicts the co-stability of dolomite and Mg-poor calcite in the entire P-T range investigated (between 400-800 °C and 15-25 kbar). For example, Figure

10.11 reports the pseudosection for the modeled bulk composition of the omphacite + carbonate vein. Two major observations can be done from this simple model. 1) Pseudosections do not reproduce the measured mineral composition. Omphacite has too high Al content, and compositionally pure Ca-carbonate is never modeled. 2) Slight increase in fluid X_{CO2} lead to a significant expansion of the two carbonates field.

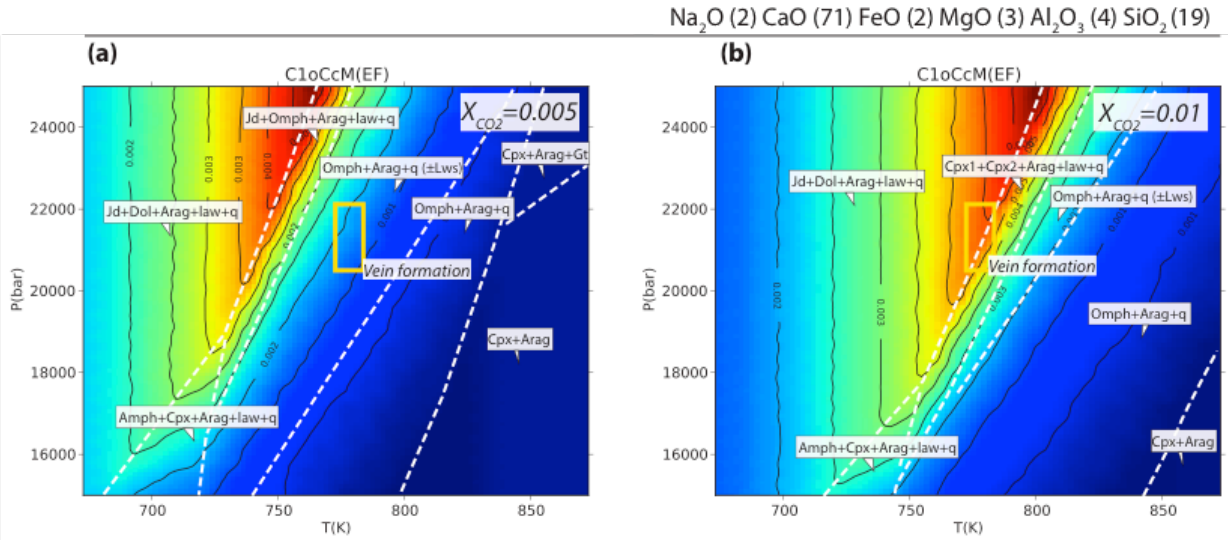

Fig. 10.11: Variation of Mg component in the carbonate solid solution (Mg/Ca+Mg+Fe) for pseudosections run with X_{CO2}=0.005 **(a)** and 0.01 **(b)**. Dashed white lines mark the phase stability field. The yellow box indicates the estimated P-T conditions for vein formation based on petrogenetic grids (Chapter 5) and stable isotopes thermometry (Chapter 7).

The results presented in this work (petrology and mass balance) are a robust framework for future work on thermodynamic modeling on high-pressure carbonation: mineral reactions and assemblages driven by metasomatism are clearly identified, and mass and volume changes are defined by mass balance calculation. Nevertheless, the question that arises is if "classic" software packages like Perple_X are suitable for modeling high-pressure carbonation processes. In other words, what is the impact of neglecting fluid chemistry as a phase, which participates to the mineral equilibria? (Putnis and Austrheim, 2010). Dissolved components in fluids play a pivotal role with respect to phase relations and mass transfer (Goncalves et al., 2013). Moreover, the results of this work attest to a long and complex evolution of the fluid composition during reactive fluid flow. At present, all these variables are ignored in most thermobarometric estimation applied to metasomatic rocks. The development of the Deep

Earth Water (DEW) provided great advances in research on quantitative evaluation of water-rock interactions at high-pressure (up to 6 GPa) and temperature (1200°) (Sverjensky et al., 2014). Works for the integration of the DEW model into software for the calculation of pseudosections and phase diagrams are ongoing, and represents an exciting future advances in research on metasomatic systems.

In conclusion, considering the obtained results and all the new possibility for the evaluation of mineral solubility in high-pressure fluids, thermodynamic modeling applied to high-pressure rock carbonation represents a promising perspective that deserves to be further investigated in the future.

10.3 Fieldwork in the Eclogitic Micaschists Complex (Sesia Lanzo, Western Alps)

Better understanding the behavior of carbonates during subduction demands to explore different scenarios, that is to say understanding the evolution of both the oceanic and the continental crust during subduction. Impure, silicate rich, marbles are reported within the Eclogite Micaschists Complex in the internal Sesia-Lanzo zone (Western Alps). This carbonate bearing system has been object of previous tectono-stratigraphic, petrological and geochemical studies (Castelli, 1987; Venturini et al., 1994, 1995; Regis et al., 2014). We studied some known outcrops (Castelli, 1987) together with new ones. Particular attention was given to outcrops showing the contact between mafic rocks and eclogitic micaschists. Moreover, one slice of serpentinized peridotite was reported within the Eclogitic Micaschists unit by Ferraris and Compagnoni (2003). This slice derives from the Alpine Tethys and has been tectonically emplaced into the continental crust of Sesia zone (Ferraris and Compagnoni, 2003). Thus, it was interesting to observe an object with a long and complex tectonic evolution. Altogether, the observations made in the Eclogitic Micaschists Complex are promising, but deserve an accurate regional survey in the Sesia Lanzo zone as well as in the

Austroalpine outliers like Mt Emilius, coupled with a detailed petrological and geochemical study.

10.3.1 Geological setting

The Sesia-Lanzo Zone (SLZ) of the Western Alps is a continental crust fragment (100 x 10 km-sized) involved in the Alpine subduction and collision (Zucali and Spalla, 2011). It crops out from the Stura creek until the town of Locarno with a N-E direction (Compagnoni et al., 1977) (Fig. 10.12). Its internal margin is delimited by the Periadriatic Line, that here is named Canavese line, that divides the SLZ from the Canavese Zone and the Ivrea Zone.

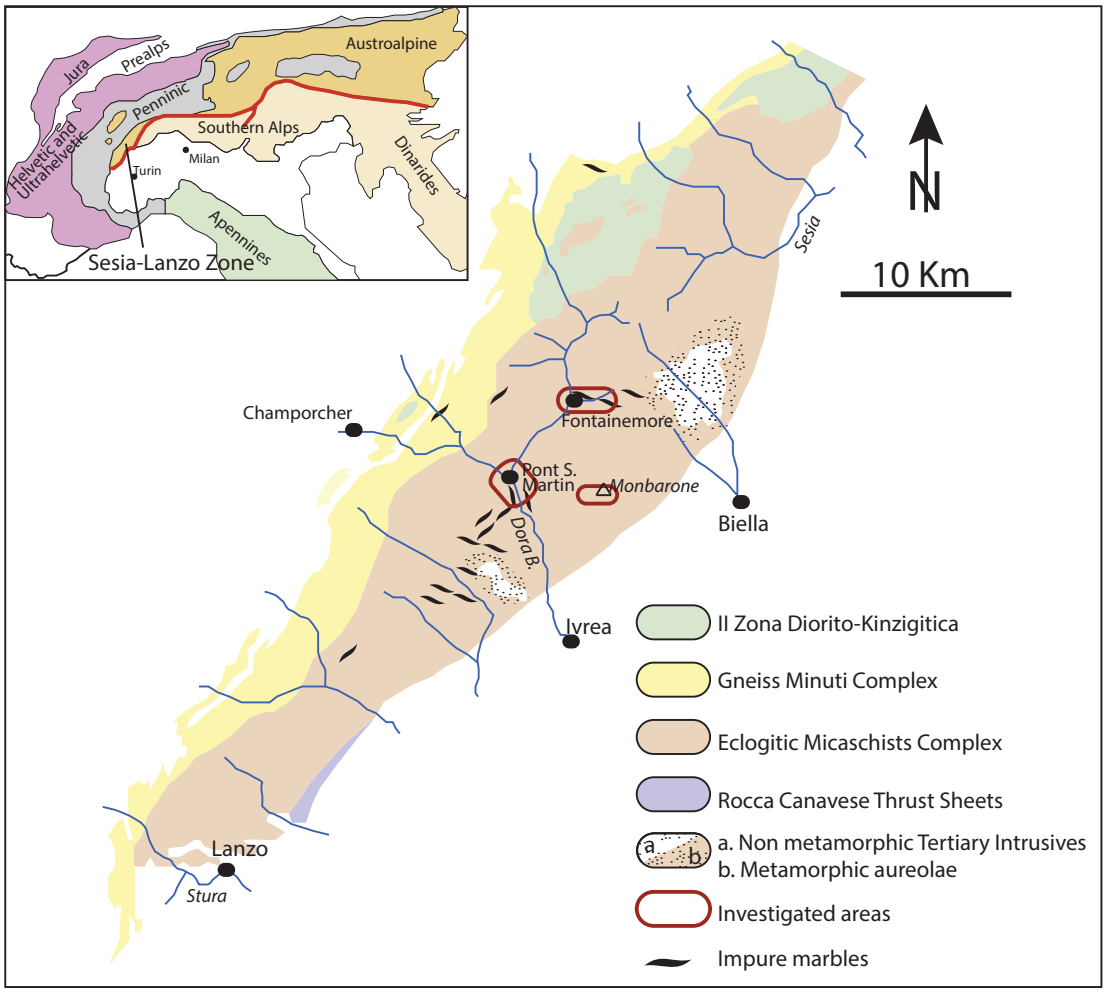

Fig. 10.12: simplified geological map of the Sesia-Lanzo Zone. Modified after Zucali and Spalla, 2011.

The external margin is partially overthrusted on the Piemonte Zone (Dal Piaz et al., 1972; Compagnoni et al., 1977). The SLZ is the most internal part of the Austroalpine system of the Western Alps, composed by the SLZ, the Dent-Blanche nappe, the Monte Emilius nappe and other smaller outliers. As a whole, this tectonic system is considered the austroalpine continental margin and it is composed by both polymetamorphic and monometamorphic rocks overthrusted on the Penninic unit during the Alpine orogenesis. The SLZ (Fig. 10.12) consists of two elements (Dal Piaz et al., 1972; Compagnoni et al., 1977): i) the upper element, "the II Zona Diorito-Kinzigitica"; composed by metapelites and metabasites that display a pre-Alpine high grade metamorphic imprint (amphibolite to granulite facies); ii) the lower element, consisting of metapelites, metagranitoids, and metabasites. This later one is further divided into two metamorphic complexes: the "Gneiss Minuti Complex", mainly displaying an Alpine low grade (greenschist) metamorphic imprint, and the "Eclogitic Micaschists Compex" (EMC), showing HP Alpine imprint. The EMC, where the study areas are located, consists of quartz-feldspar rich micashists intercalated with lens of mafic and ultramafic rocks as well as carbonate bearing rocks in lens or levels of variable thickness. P-T estimates from the impure marble HP assemblages have been calculated (Castelli, 1991) and give results consistent within the range obtained from the surrounding lithologies (T=575°C and P=1.5 GPa). Geochronological estimates attribute an eclogitic peak age between 60 and 70 Myr (Reddy et al., 1996; Rubatto et al., 1999).

4.1.1 Outcrops description

Sesia Lanzo Zone

Three well-studied localities in the EMC have been chosen for investigate carbonate systems in subducted continental crust. The common characteristic is the presence of rocks with strongly different composition in contact since the early stage of Alpine orogenesis.

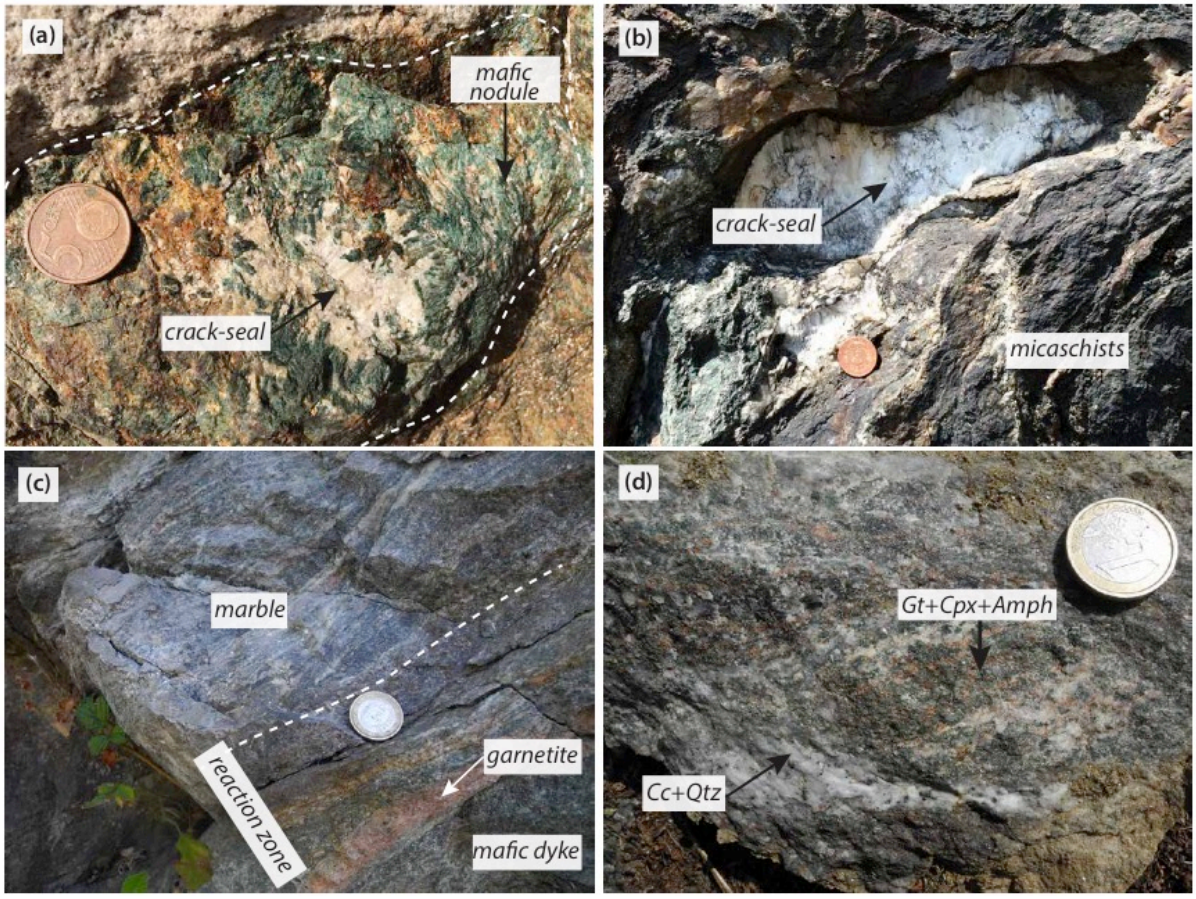

Fig. 10.13: Photos of the outcrops. a) Outcrop of Pont Saint Martin. The eclogitic metabasite boudin embedded in the micaschists is fractured and fractures are filled by prismatic Ca-carbonate. b) Outcrop of Pont Saint Martin. Carbonate crack-seal within the micaschists. c) Outcrop of Fontainemore. Reaction zone between silicate-bearing marble and metamafic dyke. Note the garnetite level forming along the contact. d) Outcrop of Passé (near Croix Courma). The margins of the mafic dyke are corroded and dismembered resulting in rocks with microstructures comparable to carbonated metasomatic rocks of Alpine Corsica.

Pont Saint Martin (Fig. 10.13a,b). Here, levels of silicate-bearing marbles are folded within the quartz rich eclogitic micaschists country rock and may include eclogitic metabasites boudins (cm-sized). Locally, late-Hercynian granitoids dikes cut across the silicate-bearing marbles (Castelli, 1987), therefore carbonate were present in the system prior to the Alpine metamorphism. Carbonate-rich levels and veins concentrate around and penetrate inside the metabasite boudins.

Fontainemore and Croix Courma (Fig. 10.13c,d). In the Gressoney Valley, small, m-thick, carbonate lenses within the eclogitic micaschists are reported. These small lenses are

connected to a bigger lens-shape body cropping out NNE of Fontainemore. Eclogitic metabasite boudins and dykes are presemt in both the micaschists and the bigger marble body. The later one had been exploited as a quarry and the fresh cut allows unique observations of the contacts between the metabasites and the surrounding marble. Here, the contact between metabasite boudins and marbles is characterized by a cm-thick reaction zone, with abundant chlorite forming at the expense of the metabasite and carbonate veins opening in between. Micaschists and metabasite dykes near Fontainemore underwent less pervasive deformation compared to the outcrop of Pont Saint Martin. They metamafic dyke are either in direct contact with micaschists or they are surrounded by a carbonate-rich aureole. These aureoles around metabasites also contain omphacite and garnet. Altogether, observed textures like veins and carbonate-bearing aureoles around metabasites suggest a potential chemical reactivity of carbon-bearing fluids in contact with mafic rocks during subduction and deserve a more detailed petrological and geochemical investigation.

Colma di Mombarone A slice of partly serpentinized upper mantle peridotite is exposed on the left side of Val d'Aosta, within the EMC (Ferraris and Compagnoni, 2003). This ultramafic body is interpreted as an ophiolitic slice, derived from the Tethys Ocean floor and tectonically inserted into the continental crust of the SLZ during early stage of Alpine orogeny. A layer of quartzite characterizes the contact between the ultramafic and the surrounding rocks; no carbonate bearing rocks has been observed.

The finding of carbonated metafelsic rocks in Alpine Corsica and the widespread observation of carbonate mobilization in deeply subducted continental units open to new questions about the role of fluids and possibly, the role of rock carbonation, in regulating the metamorphic CO_2 degassing in collisional orogens. A detailed study of these rocks represents a promising perspective for future studies

References

A

Abart, R., Badertscher, N., Burkhard, M., Povoden, E., 2002. Oxygen, carbon and strontium isotope systematics in two profiles across the Glarus thrust: implications for fluid flow. Contributions to Mineralogy and Petrology 143, 192–208.

Agrinier, P., Laverne, C., Tartarotti, P., 1995. Stable isotope ratios (oxygen, hydrogen) and petrology of hydrothermally altered dolerites at the bottom of the sheeted dike complex of Hole 504B. Presented at the Proceedings of the Ocean Drilling Program, Scientific Results, p. 140.

Ague, J.J., 2014. Fluid Flow in the Deep Crust, in: Turekian, K.K. (Ed.), Treatise on Geochemistry (Second Edition). Elsevier, Oxford, pp. 203–247. doi:10.1016/B978-0-08-095975-7.00306-5

Ague, J.J., 2007. Models of permeability contrasts in subduction zone mélange: Implications for gradients in fluid fluxes, Syros and Tinos Islands, Greece. Chemical Geology 239, 217–227. doi:10.1016/j.chemgeo.2006.08.012

Ague, J.J., 2003. Fluid flow in the deep crust. Treatise on geochemistry 3, 659.

Ague, J.J., 2000. Release of CO_2 from carbonate rocks during regional metamorphism of lithologically heterogeneous crust. Geology 28, 1123–1126.

Ague, J.J., 1998. Simple models of coupled fluid infiltration and redox reactions in the crust. Contributions to Mineralogy and Petrology 132, 180–197.

Ague, J.J., 1994a. Mass transfer during Barrovian metamorphism of pelites, south-central Connecticut; I, Evidence for changes in composition and volume. American Journal of Science 294, 989–1057.

Ague, J.J., 2003a. Fluid infiltration and transport of major, minor, and trace elements during regional metamorphism of carbonate rocks, Wepawaug Schist, Connecticut, USA. American Journal of Science 303, 753–816.

Ague, J.J., novembre 1, 1994b. Mass transfer during Barrovian metamorphism of pelites, south-central Connecticut; II, Channelized fluid flow and the growth of staurolite and kyanite. American Journal of Science 294, 1061–1134. doi:10.2475/ajs.294.9.1061

Ague, J.J., Carlson, W.D., 2013. Metamorphism as Garnet Sees It: The Kinetics of Nucleation and Growth, Equilibration, and Diffusional Relaxation. Elements 9, 439. doi:10.2113/gselements.9.6.439

Ague, J.J., Nicolescu, S., 2014. Carbon dioxide released from subduction zones by fluid-mediated reactions. Nature Geoscience 7, 355.

Ague, J.J., Van Haren, J.L., 1996. Assessing metasomatic mass and volume changes using the bootstrap, with application to deep crustal hydrothermal alteration of marble. Economic Geology 91, 1169–1182.

Aitchison, J., 1986. The statistical analysis of compositional data.

Albarède, F., 1996. Introduction to geochemical modeling. Cambridge University Press.

Albarède, F., Michard, A., Minster, J., Michard, G., 1981. $^{87}Sr/^{86}Sr$ ratios in hydrothermal waters and deposits from the East Pacific Rise at 21 N. Earth and Planetary Science Letters 55, 229–236.

Allègre, C.J., Othman, D.B., 1980. Nd–Sr isotopic relationship in granitoid rocks and continental crust development: a chemical approach to orogenesis. Nature 286, 335–342.

Alt, J.C., Garrido, C.J., Shanks, W., Turchyn, A., Padrón-Navarta, J.A., Sánchez-Vizcaíno, V.L., Pugnaire, M.T.G., Marchesi, C., 2012. Recycling of water, carbon, and sulfur

during subduction of serpentinites: A stable isotope study of Cerro del Almirez, Spain. Earth and Planetary Science Letters 327, 50–60.

Alt, J.C., Schwarzenbach, E.M., Früh-Green, G.L., Shanks III, W.C., Bernasconi, S.M., Garrido, C.J., Crispini, L., Gaggero, L., Padrón-Navarta, J.A., Marchesi, C., 2013. The role of serpentinites in cycling of carbon and sulfur: Seafloor serpentinization and subduction metamorphism. Lithos, Serpentinites from mid-oceanic ridges to subduction 178, 40–54. doi:10.1016/j.lithos.2012.12.006

Alt, J.C., Teagle, D.A.H., 1999. The uptake of carbon during alteration of ocean crust. Geochimica et Cosmochimica Acta 63, 1527–1535. doi:10.1016/S0016-7037(99)00123-4

Amato, J.M., Johnson, C.M., Baumgartner, L.P., Beard, B.L., 1999. Rapid exhumation of the Zermatt-Saas ophiolite deduced from high-precision Sm-Nd and Rb-Sr geochronology. Earth and Planetary Science Letters 171, 425–438.

Angiboust, S., Langdon, R., Agard, P., Waters, D., Chopin, C., 2012. Eclogitization of the Monviso ophiolite (W. Alps) and implications on subduction dynamics. Journal of Metamorphic Geology 30, 37–61. doi:10.1111/j.1525-1314.2011.00951.x

Angiboust, S., Pettke, T., De Hoog, J.C.M., Caron, B., Oncken, O., 2014. Channelized Fluid Flow and Eclogite-facies Metasomatism along the Subduction Shear Zone. Journal of Petrology 55, 883–916. doi:10.1093/petrology/egu010

Angiboust, S., Yamato, P., Hertgen, S., Hyppolito, T., Bebout, G.E., Morales, L., 2017. Fluid pathways and high-P metasomatism in a subducted continental slice (Mt. Emilius klippe, W. Alps). Journal of Metamorphic Geology.

Argnani, A., 2009. Plate tectonics and the boundary between Alps and Apennines. Bollettino della Societa Geologica Italiana 128, 317–330.

Austrheim, H., 1990. The granulite-eclogite facies transition: A comparison of experimental work and a natural occurrence in the Bergen Arcs, western Norway. Lithos 25, 163–169.

B

Bach, W., Jöns, N., Klein, F., 2013. Metasomatism within the ocean crust, in: Metasomatism and the Chemical Transformation of Rock. Springer, pp. 253–288.

Bach, W., Rosner, M., Jöns, N., Rausch, S., Robinson, L.F., Paulick, H., Erzinger, J., 2011. Carbonate veins trace seawater circulation during exhumation and uplift of mantle rock: Results from ODP Leg 209. Earth and Planetary Science Letters 311, 242–252. doi:10.1016/j.epsl.2011.09.021

Barbieri, M., Masi, U., Tolomeo, L., 1979. Stable isotope evidence for a marine origin of ophicalcites from the north-central Apennines (Italy). Marine Geology 30, 193–204.

Barnes, J.D., Beltrando, M., Lee, C.-T.A., Cisneros, M., Loewy, S., Chin, E., 2014. Geochemistry of Alpine serpentinites from rifting to subduction: A view across paleogeographic domains and metamorphic grade. Chemical Geology 389, 29–47.

Barnicoat, A., Cartwright, I., 1995. Focused fluid flow during subduction: oxygen isotope data from high-pressure ophiolites of the western Alps. Earth and Planetary Science Letters 132, 53–61.

Barnola, J.-M., Raynaud, D., Korotkevich, Y.S., Lorius, C., 1987. Vostok ice core provides 160,000-year record of atmospheric CO_2. Nature 329, 408–414.

Baumgartner, L.P., Olsen, S.N., 1995. A least-squares approach to mass transport calculations using the isocon method. Economic Geology 90, 1261–1270.

Baumgartner, L.P., Valley, J.W., 2001. Stable isotope transport and contact metamorphic fluid flow. Reviews in Mineralogy and Geochemistry 43, 415–467.

Bayrakci, G., Minshull, T., Sawyer, D., Reston, T.J., Klaeschen, D., Papenberg, C., Ranero, C., Bull, J., Davy, R., Shillington, D., 2016. Fault-controlled hydration of the upper mantle during continental rifting. Nature Geoscience 9, 384–388.

Bear, J., 2013. Dynamics of fluids in porous media. Courier Corporation.

Bebout, G.E., 2007. Metamorphic chemical geodynamics of subduction zones. Earth and Planetary Science Letters 260, 373–393.

Bebout, G.E., Barton, M.D., 2002. Tectonic and metasomatic mixing in a high-T, subduction-zone mélange—insights into the geochemical evolution of the slab–mantle interface. Chemical Geology 187, 79–106.

Bebout, G.E., Barton, M.D., 1993. Metasomatism during subduction: products and possible paths in the Catalina Schist, California. Chemical Geology 108, 61–92.

Bebout, G.E., Barton, M.D., 1989. Fluid flow and metasomatism in a subduction zone hydrothermal system: Catalina Schist terrane, California. Geology 17, 976–980.

Bebout, G.E., Penniston-Dorland, S.C., 2016. Fluid and mass transfer at subduction interfaces—The field metamorphic record. Lithos 240–243, 228–258. doi:10.1016/j.lithos.2015.10.007

Becker, H., Jochum, K.P., Carlson, R.W., 1999. Constraints from high-pressure veins in eclogites on the composition of hydrous fluids in subduction zones. Chemical Geology 160, 291–308. doi:10.1016/S0009-2541(99)00104-7

Becker, J.A., Bickle, M.J., Galy, A., Holland, T.J., 2008. Himalayan metamorphic CO_2 fluxes: Quantitative constraints from hydrothermal springs. Earth and Planetary Science Letters 265, 616–629.

Beinlich, A., Klemd, R., John, T., Gao, J., 2010. Trace-element mobilization during Ca-metasomatism along a major fluid conduit: Eclogitization of blueschist as a consequence of fluid–rock interaction. Geochimica et Cosmochimica Acta 74, 1892–1922. doi:10.1016/j.gca.2009.12.011

Beinlich, A., Plümper, O., Hövelmann, J., Austrheim, H., Jamtveit, B., 2012. Massive serpentinite carbonation at Linnajavri, N–Norway. Terra Nova 24, 446–455.

Bell, D.R., Rossman, G.R., 1992. Water in Earth's Mantle: The Role of Nominally Anhydrous Minerals. Science 255, 1391. doi:10.1126/science.255.5050.1391

Beltrando, M., Frasca, G., Compagnoni, R., Vitale-Brovarone, A., 2012. The Valaisan controversy revisited: Multi-stage folding of a Mesozoic hyper-extended margin in the Petit St. Bernard pass area (Western Alps). Tectonophysics 579, 17–36.

Beltrando, M., Manatschal, G., Mohn, G., Dal Piaz, G.V., Brovarone, A.V., Masini, E., 2014. Recognizing remnants of magma-poor rifted margins in high-pressure orogenic belts: The Alpine case study. Earth-Science Reviews 131, 88–115.

Beltrando, M., Rubatto, D., Manatschal, G., 2010. From passive margins to orogens: The link between ocean-continent transition zones and (ultra) high-pressure metamorphism. Geology 38, 559–562.

Berner, R., 1975. The role of magnesium in the crystal growth of calcite and aragonite from sea water. Geochimica et Cosmochimica Acta 39, 489IN3495-494504.

Berner, R.A., 1991. A model for atmospheric CO_2 over phanerozoic time. American Journal of Science;(United States) 291.

Berner, R.A., Kothavala, Z., 2001. GEOCARB III: a revised model of atmospheric CO_2 over Phanerozoic time. American Journal of Science 301, 182–204.

Berner, R.A., Lasaga, A.C., 1989. Modeling the geochemical carbon cycle. Scientific American;(USA) 260.

Bickle, M., 1992. Transport mechanisms by fluid-flow in metamorphic rocks; oxygen and strontium decoupling in the Trois Seigneurs Massif; a consequence of kinetic dispersion? American Journal of Science 292, 289–316.

Bickle, M., Chapman, H., Ferry, J., Rumble III, D., Fallick, A., 1997. Fluid Flow and Diffusion in the Waterville Limestone, South—Central Maine: Constraints from Strontium, Oxygen and Carbon Isotope Profiles. Journal of Petrology 38, 1489–1512.

Bickle, M., McKenzie, D., 1987. The transport of heat and matter by fluids during metamorphism. Contributions to Mineralogy and Petrology 95, 384–392.

Bickle, M.J., Baker, J., 1990. Advective-diffusive transport of isotopic fronts: An example from Naxos, Greece. Earth and Planetary Science Letters 97, 78–93. doi:10.1016/0012-821X(90)90100-C

Bickle, M.J., Teagle, D.A., 1992. Strontium alteration in the Troodos ophiolite: implications for fluid fluxes and geochemical transport in mid-ocean ridge hydrothermal systems. Earth and Planetary Science Letters 113, 219–237.

Bodinier, J.L., Menzies, M.A., Thirlwall, M.F., others, 1991. Continental to oceanic mantle transition-REE and Sr–Nd isotopic geochemistry of the Lanzo lherzolite massif. J. Petrol 32, 191–210.

Bonatti, E., Emiliani, C., Ferrara, G., Honnorez, J., Rydell, H., 1974. Ultramafic-carbonate breccias from the equatorial Mid Atlantic Ridge. Marine Geology 16, 83–102.

Bottinga, Y., Javoy, M., 1973. Comments on oxygen isotope geothermometry. Earth and Planetary Science Letters 20, 250–265.

Boulard, E., Gloter, A., Corgne, A., Antonangeli, D., Auzende, A.-L., Perrillat, J.-P., Guyot, F., Fiquet, G., 2011. New host for carbon in the deep Earth. Proceedings of the National Academy of Sciences 108, 5184–5187.

Boundy, T.M., Donohue, C.L., Essene, E.J., Mezger, K., Austrheim, H., 2002. Discovery of eclogite facies carbonate rocks from the Lindås Nappe, Caledonides, Western Norway. Journal of Metamorphic Geology 20, 649–667.

Boutoux, A., Verlaguet, A., Bellahsen, N., Lacombe, O., Villemant, B., Caron, B., Martin, E., Assayag, N., Cartigny, P., 2014. Fluid systems above basement shear zones during inversion of pre-orogenic sedimentary basins (External Crystalline Massifs, Western Alps). Lithos 206, 435–453.

Bowman, J.R., Valley, J.W., Kita, N.T., 2009. Mechanisms of oxygen isotopic exchange and isotopic evolution of $^{18}O/^{16}O$-depleted periclase zone marbles in the Alta aureole, Utah: insights from ion microprobe analysis of calcite. Contributions to Mineralogy and Petrology 157, 77–93. doi:10.1007/s00410-008-0321-1

Bowtell, S., Cliff, R., Barnicoat, A., 1994. Sm-Nd isotopic evidence on the age of eclogitization in the Zermatt-Saas ophiolite. Journal of Metamorphic Geology 12, 187–196.

Brady, J.B., Markley, M.J., Schumacher, J.C., Cheney, J.T., Bianciardi, G.A., 2004. Aragonite pseudomorphs in high-pressure marbles of Syros, Greece. Journal of Structural Geology 26, 3–9. doi:10.1016/S0191-8141(03)00099-3

Bröcker, M., Enders, M., 2001. Unusual bulk-rock compositions in eclogite-facies rocks from Syros and Tinos (Cyclades, Greece): implications for U–Pb zircon geochronology. Chemical Geology 175, 581–603.

Busigny, V., Cartigny, P., Philippot, P., Ader, M., Javoy, M., 2003. Massive recycling of nitrogen and other fluid-mobile elements (K, Rb, Cs, H) in a cold slab environment: evidence from HP to UHP oceanic metasediments of the Schistes Lustrés nappe (western Alps, Europe). Earth and Planetary Science Letters 215, 27–42. doi:10.1016/S0012-821X(03)00453-9

C

Caciagli, N.C., Manning, C.E., 2003. The solubility of calcite in water at 6-16 kbar and 500-800°C. Contributions to Mineralogy and Petrology 146, 275–285. doi:10.1007/s00410-003-0501-y

Cannat, M., Fontaine, F., Escartin, J., 2010. Serpentinization and associated hydrogen and methane fluxes at slow spreading ridges. Diversity of hydrothermal systems on slow spreading ocean ridges 241–264.

Carignan, J., Hild, P., Mevelle, G., Morel, J., Yeghicheyan, D., 2001. Routine Analyses of Trace Elements in Geological Samples using Flow Injection and Low Pressure On-Line Liquid Chromatography Coupled to ICP-MS: A Study of Geochemical Reference Materials BR, DR-N, UB-N, AN-G and GH. Geostandards Newsletter 25, 187–198. doi:10.1111/j.1751-908X.2001.tb00595.x

Caron, J., Delcey, R., 1979. Lithostratigraphie des schistes lustrés corses: diversité des séries post-ophiolitiques. Compte Rendu Académies des Sci, Paris 208, 1525–1528.

Caron, J., Delcey, R., Scius, H., Essein, J., Fraipont, P. de, Mawhin, B., Reuber, I., 1979. Répartition cartographique des principaux types des séries dans les Schistes Lustrés de Corse. Comptes Rendus de l'Académie des Sciences Paris 288, 1363–1366.

Caron, J.M., 1977. Lithostratigraphie et tectonique des Schistes lustrés dans les Alpes cottiennes septentrionales et en Corse orientale.

Caron, J.-M., Kienast, J.-R., Triboulet, C., 1981. High-pressure-low-temperature metamorphism and polyphase Alpine deformation at Sant'Andrea di Cotone (eastern Corsica, France). Tectonophysics 78, 419–451.

Cartwright, I., Barnicoat, C.A., 1999. Stable isotope geochemistry of Alpine ophiolites: a window to ocean-floor hydrothermal alteration and constraints on fluid–rock interaction during high-pressure metamorphism. International Journal of Earth Sciences 88, 219–235. doi:10.1007/s005310050261

Cartwright, I., Buick, I.S., 2000. Fluid generation, vein formation and the degree of fluid–rock interaction during decompression of high-pressure terranes: the Schistes Lustrés, Alpine Corsica, France. Journal of Metamorphic Geology 18, 607–624.

Castelli, D., 1991. Eclogitic metamorphism in carbonate rocks: the example of impure marbles from the Sesia-Lanzo Zone, Italian Western Alps. Journal of Metamorphic Geology 9, 61–77.

Castelli, D., 1987. Il metamorfismo alpino delle rocce carbonatiche della zona Sesia Lanzo (Alpi Occidentali). Ph.D.

Chamberlain, C.P., Conrad, M.E., 1991. The relative permeabilities of quartzites and schists during active metamorphism at mid-crustal levels. Geophysical Research Letters 18, 959–962.

Chauvel, C., Blichert-Toft, J., 2001. A hafnium isotope and trace element perspective on melting of the depleted mantle. Earth and Planetary Science Letters 190, 137–151. doi:10.1016/S0012-821X(01)00379-X

Chemenda, A., Matte, P., Sokolov, V., 1997. A model of Palaeozoic obduction and exhumation of high-pressure/low-temperature rocks in the southern Urals. Tectonophysics 276, 217–227.

Chopin, C., 1984. Coesite and pure pyrope in high-grade blueschists of the Western Alps: a first record and some consequences. Contributions to Mineralogy and Petrology 86, 107–118. doi:10.1007/BF00381838

Chopin, C., Beyssac, O., Bernard, S., Malavieille, J., 2008. Aragonite–grossular intergrowths in eclogite-facies marble, Alpine Corsica. European Journal of Mineralogy 20, 857–865.

Clayton, R.N., Mayeda, T.K., 1963. The use of bromine pentafluoride in the extraction of oxygen from oxides and silicates for isotopic analysis. Geochimica et cosmochimica acta 27, 43–52.

Clerc, C., Boulvais, P., Lagabrielle, Y., Blanquat, M. de S., 2013. Ophicalcites from the northern Pyrenean belt: a field, petrographic and stable isotope study. Int J Earth Sci (Geol Rundsch) 103, 141–163. doi:10.1007/s00531-013-0927-z

Cocherie, A., Rossi, P., Fouillac, A., Vidal, P., 1994. Crust and mantle contributions to granite genesis—An example from the Variscan batholith of Corsica, France, studied by trace-element and Nd Sr O-isotope systematics. Chemical Geology 115, 173–211.

Collins, N.C., Bebout, G.E., Angiboust, S., Agard, P., Scambelluri, M., Crispini, L., John, T., 2015. Subduction zone metamorphic pathway for deep carbon cycling: II. Evidence from HP/UHP metabasaltic rocks and ophicarbonates. Chemical Geology 412, 132–150.

Compagnoni, R., 1977. The Sesia-Lanzo Zone: high pressure-low temperature metamorphism in the Austroalpine continental margin. Rend. Soc. Ital. Mineral. Petrol 33, 335–374.

Compagnoni, R., Rolfo, F., Castelli, D., 2012. Jadeitite from the Monviso meta-ophiolite, western Alps: occurrence and genesis. European Journal of Mineralogy 24, 333. doi:10.1127/0935-1221/2011/0023-2164

Connolly, J., Petrini, K., 2002. An automated strategy for calculation of phase diagram sections and retrieval of rock properties as a function of physical conditions. Journal of Metamorphic Geology 20, 697–708.

Connolly, J.A.D., 2005. Computation of phase equilibria by linear programming: A tool for geodynamic modeling and its application to subduction zone decarbonation. Earth and Planetary Science Letters 236, 524–541. doi:10.1016/j.epsl.2005.04.033

Coogan, L.A., Dosso, S.E., 2015. Alteration of ocean crust provides a strong temperature dependent feedback on the geological carbon cycle and is a primary driver of the Sr-isotopic composition of seawater. Earth and Planetary Science Letters 415, 38–46. doi:10.1016/j.epsl.2015.01.027

Coogan, L.A., Parrish, R.R., Roberts, N.M.W., 2016. Early hydrothermal carbon uptake by the upper oceanic crust: Insight from in situ U-Pb dating. Geology 44, 147–150. doi:10.1130/G37212.1

Cook-Kollars, J., Bebout, G.E., Collins, N.C., Angiboust, S., Agard, P., 2014. Subduction zone metamorphic pathway for deep carbon cycling: I. Evidence from HP/UHP metasedimentary rocks, Italian Alps. Chemical Geology 386, 31–48. doi:10.1016/j.chemgeo.2014.07.013

Créon, L., Rouchon, V., Youssef, S., Rosenberg, E., Delpech, G., Szabó, C., Remusat, L., Mostefaoui, S., Asimow, P.D., Antoshechkina, P.M., 2016. Highly CO 2-supersaturated melts in the Pannonian lithospheric mantle–A transient carbon reservoir? Lithos.

D

Dal Piaz, G.V., 2001. History of tectonic interpretations of the Alps. Journal of Geodynamics 32, 99–114. doi:10.1016/S0264-3707(01)00019-9

Dal Piaz, G.V., 1972. La Zona Sesia-Lanzo e l'evoluzione tettonico-metamorfica delle Alpi nordoccidentali interne. Memoirs of the Geological Society of Italy 11, 433–460.

Dalton, J.A., Presnall, D.C., 1998. Carbonatitic melts along the solidus of model lherzolite in the system CaO-MgO-Al_2O_3-SiO_2-CO_2 from 3 to 7 GPa. Contributions to Mineralogy and Petrology 131, 123–135.

Dasgupta, R., 2013. Ingassing, storage, and outgassing of terrestrial carbon through geologic time. Reviews in Mineralogy and Geochemistry 75, 183–229.

Dasgupta, R., Hirschmann, M.M., 2007. A modified iterative sandwich method for determination of near-solidus partial melt compositions. II. Application to determination of near-solidus melt compositions of carbonated peridotite. Contributions to Mineralogy and Petrology 154, 647–661.

Dasgupta, R., Hirschmann, M.M., 2006. Melting in the Earth's deep upper mantle caused by carbon dioxide. Nature 440, 659.

Dasgupta, R., Hirschmann, M.M., Dellas, N., 2005. The effect of bulk composition on the solidus of carbonated eclogite from partial melting experiments at 3 GPa. Contributions to Mineralogy and Petrology 149, 288–305.

Dasgupta, R., Hirschmann, M.M., Smith, N.D., 2007. Water follows carbon: CO_2 incites deep silicate melting and dehydration beneath mid-ocean ridges. Geology 35, 135–138.

Dasgupta, R., Hirschmann, M.M., Withers, A.C., 2004. Deep global cycling of carbon constrained by the solidus of anhydrous, carbonated eclogite under upper mantle conditions. Earth and Planetary Science Letters 227, 73–85.

Dasgupta, R., Mallik, A., Tsuno, K., Withers, A.C., Hirth, G., Hirschmann, M.M., 2013. Carbon-dioxide-rich silicate melt in the Earth's upper mantle. Nature 493, 211.

Daval, D., Hellmann, R., Corvisier, J., Tisserand, D., Martinez, I., Guyot, F., 2010. Dissolution kinetics of diopside as a function of solution saturation state: Macroscopic measurements and implications for modeling of geological storage of CO_2. Geochimica et Cosmochimica Acta 74, 2615–2633. doi:10.1016/j.gca.2010.02.003

Daval, D., Martinez, I., Corvisier, J., Findling, N., Goffé, B., Guyot, F., 2009b. Carbonation of Ca-bearing silicates, the case of wollastonite: Experimental investigations and kinetic modeling. Chemical Geology 265, 63–78. doi:10.1016/j.chemgeo.2009.01.022

Daval, D., Martinez, I., Guigner, J.-M., Hellmann, R., Corvisier, J., Findling, N., Dominici, C., Goffé, B., Guyot, F., 2009a. Mechanism of wollastonite carbonation deduced from micro-to nanometer length scale observations. American Mineralogist 94, 1707–1726.

Davis, A.C., Bickle, M.J., Teagle, D.A., 2003. Imbalance in the oceanic strontium budget. Earth and Planetary Science Letters 211, 173–187.

Davis, K.J., Dove, P.M., De Yoreo, J.J., 2000. The role of Mg2+ as an impurity in calcite growth. Science 290, 1134–1137.

Davis, N., Newman, J., Wheelock, P., Kronenberg, A., 2011. Grain growth kinetics of dolomite, magnesite and calcite: a comparative study. Physics and Chemistry of Minerals 38, 123–138.

Debret, B., Andreani, M., Muñoz, M., Bolfan-Casanova, N., Carlut, J., Nicollet, C., Schwartz, S., Trcera, N., 2014. Evolution of Fe redox state in serpentine during subduction. Earth and Planetary Science Letters 400, 206–218. doi:10.1016/j.epsl.2014.05.038

Delcey, R., 1974. Données sur deux nouvelles sèries litostratigraphiques de la zone des schistes lustrés de la Corse nord-orientale. Comptes Rendus de l'Académie des Sciences Paris D 279, 1693–1696.

Deleuze, M., Brantley, S.L., 1997. Inhibition of calcite crystal growth by Mg2+ at 100 C and 100 bars: Influence of growth regime. Geochimica et Cosmochimica Acta 61, 1475–1485.

Denèle, Y., Paquette, J., Olivier, P., Barbey, P., 2012. Permian granites in the Pyrenees: the Aya pluton (Basque Country). Terra Nova 24, 105–113.

DePaolo, D.J., 2015. Sustainable carbon emissions: The geologic perspective. MRS Energy & Sustainability-A Review Journal 2.

DePaolo, D.J., 2006. Isotopic effects in fracture-dominated reactive fluid–rock systems. Geochimica et Cosmochimica Acta 70, 1077–1096.

Deschamps, F., Godard, M., Guillot, S., Hattori, K., 2013. Geochemistry of subduction zone serpentinites: A review. Lithos 178, 96–127. doi:10.1016/j.lithos.2013.05.019

Deul, R., Franck, E., 1991. The Static Dielectric Constant of the Water-Benzene Mixture System to 400°C and 2800 bar. Berichte der Bunsengesellschaft für physikalische Chemie 95, 847–853.

Duchêne, S., Blichert-Toft, J., Luais, B., Télouk, P., 1997. The Lu-Hf dating of garnets and the ages of the Alpine high-pressure metamorphism. Nature 387, 586.

Durand Delga, M., 1986. Principaux traits de la Corse alpine et correlations avec les Alpes Ligures. Memorie della Societa Geologica Italiana 28, 285–329.

E

Egal, E., 1992. Structures and tectonic evolution of the external zone of Alpine Corsica. Journal of Structural Geology 14, 1215–1228.

Eggler, D.H., 1976. Does CO_2 cause partial melting in the low-velocity layer of the mantle? Geology 4, 69–72.

Engstrom, A., Skelton, A., Grassineau, N., 2007. Isotopic and petrological evidence of fluid–rock interaction at a Tethyan ocean–continent transition in the Alps: implications for tectonic processes and carbon transfer during early ocean formation. Geofluids 7, 401–414. doi:10.1111/j.1468-8123.2007.00194.x

Ernst, W., 2006. Preservation/exhumation of ultrahigh-pressure subduction complexes. Lithos 92, 321–335.

Ernst, W.G., 1971. Metamorphic zonations on presumably subducted lithospheric plates from Japan, California and the Alps. Contributions to Mineralogy and Petrology 34, 43–59. doi:10.1007/BF00376030

Evans, K., 2011. Metamorphic carbon fluxes: how much and how fast? Geology 39, 95–96.

F

Faccenda, M., 2014. Water in the slab: A trilogy. Tectonophysics 614, 1–30. doi:10.1016/j.tecto.2013.12.020

Facq, S., Daniel, I., Montagnac, G., Cardon, H., Sverjensky, D.A., 2014. In situ Raman study and thermodynamic model of aqueous carbonate speciation in equilibrium with aragonite under subduction zone conditions. Geochimica et Cosmochimica Acta 132, 375–390. doi:10.1016/j.gca.2014.01.030

Federico, L., Crispini, L., Scambelluri, M., Capponi, G., 2007. Ophiolite mélange zone records exhumation in a fossil subduction channel. Geology 35, 499–502.

Fein, J., Walther, J., 1989. Calcite solubility and speciation in supercritical NaCl-HCl aqueous fluids. Contr. Mineral. and Petrol. 103, 317–324. doi:10.1007/BF00402918

Fernandez, L., Bosch, D., Bruguier, O., Hammor, D., Caby, R., Monié, P., Arnaud, N., Toubal, A., Galland, B., Douchet, C., 2016. Permo-carboniferous and early miocene geological evolution of the internal zones of the Maghrebides–new insights on the western Mediterranean evolution. Journal of Geodynamics 96, 146–173.

Ferrando, S., Groppo, C., Frezzotti, M.L., Castelli, D., Proyer, A., 2017. Dissolving dolomite in a stable UHP mineral assemblage: Evidence from Cal-Dol marbles of the Dora-Maira Massif (Italian Western Alps). American Mineralogist 102, 42–60.

Ferraris, C., Compagnoni, R., 2003. Metamorphic evolution and significance of a serpentinized peridotite slice within the Eclogitic Micaschist Complex of the Sesia-Zone (Western Alps–Italy). Swiss Bulletin of Mineralogy and Petrology 83, 3–13.

Ferry, J.M., 1994. A historical review of metamorphic fluid flow. Journal of Geophysical Research: Solid Earth 99, 15487–15498.
Ferry, J.M., Gerdes, M.L., 1998. Chemically reactive fluid flow during metamorphism. Annual Review of Earth and Planetary Sciences 26, 255–287.
Fletcher, R., Hofmann, A., 1974. Simple models of diffusion and combined diffusion-infiltration metasomatism. Geochemical transport and kinetics 634, 243–259.
Fournier, M., Jolivet, L., Goffé, B., Dubois, R., 1991. Alpine Corsica metamorphic core complex. Tectonics 10, 1173–1186.
Franz, G., Liebscher, A., 2004. Physical and Chemical Properties of the Epidote Minerals–An Introduction–. Reviews in Mineralogy and Geochemistry 56, 1. doi:10.2138/gsrmg.56.1.1
Franzolin, E., Schmidt, M.W., Poli, S., 2011. Ternary Ca–Fe–Mg carbonates: subsolidus phase relations at 3.5 GPa and a thermodynamic solid solution model including order/disorder. Contributions to Mineralogy and Petrology 161, 213–227. doi:10.1007/s00410-010-0527-x
Frezzotti, M.L., Andersen, T., Neumann, E.-R., Simonsen, S.L., 2002. Carbonatite melt–CO_2 fluid inclusions in mantle xenoliths from Tenerife, Canary Islands: a story of trapping, immiscibility and fluid–rock interaction in the upper mantle. Lithos 64, 77–96.
Frezzotti, M.L., Ferrando, S., 2015. The chemical behavior of fluids released during deep subduction based on fluid inclusions. American Mineralogist 100, 352–377. doi:10.2138/am-2015-4933
Frezzotti, M.L., Selverstone, J., Sharp, Z.D., Compagnoni, R., 2011. Carbonate dissolution during subduction revealed by diamond-bearing rocks from the Alps. Nature Geoscience 4, 703–706. doi:10.1038/ngeo1246
Fryer, P., Pearce, J.A., Stokking, L.B., Ali, J., Arculus, R., Ballotti, D., Burke, M., Ciampo, G., Haggerty, J., Haston, R., 1990. Bonin/Mariana region, covering Leg 125 of the cruises of the drilling vessel JOIDES Resolution, Apra Harbor, Guam, to Tokyo, Japan, sites 778-786. Presented at the Proceedings of the Ocean Drilling Program.
Fryer, P., Pearce, J.A., Stokking, L.B., others, 1992. 36. A synthesis of Leg 125 drilling of serpentine seamounts on the Mariana and Izu–Bonin forearcs, in: Proceedings of the Ocean Drilling Program, Scientific Results. pp. 593–614.
Fryer, P., Wheat, C., Mottl, M., 1999. Mariana blueschist mud volcanism: Implications for conditions within the subduction zone. Geology 27, 103–106.
Fu, B., Touret, J.L., Zheng, Y.-F., Jahn, B., 2003. Fluid inclusions in granulites, granulitized eclogites and garnet clinopyroxenites from the Dabie–Sulu terranes, eastern China. Lithos 70, 293–319.
Fyfe, W., Price, N., Thompson, A., 1978. Fluids in the earth's crust. Developments in Geochemistry 1. Elsevier 1, 3–4.

G

Gaillardet, J., Galy, A., 2008. Himalaya-carbon sink or source? SCIENCE-NEW YORK THEN WASHINGTON- 320, 1727.
Galvez, M.E., Beyssac, O., Martinez, I., Benzerara, K., Chaduteau, C., Malvoisin, B., Malavieille, J., 2013a. Graphite formation by carbonate reduction during subduction. Nature Geoscience 6, 473–477. doi:10.1038/ngeo1827
Galvez, M.E., Martinez, I., Beyssac, O., Benzerara, K., Agrinier, P., Assayag, N., 2013b. Metasomatism and graphite formation at a lithological interface in Malaspina (Alpine Corsica, France). Contributions to Mineralogy and Petrology 166, 1687–1708. doi:10.1007/s00410-013-0949-3

Gao, J., John, T., Klemd, R., Xiong, X., 2007. Mobilization of Ti–Nb–Ta during subduction: evidence from rutile-bearing dehydration segregations and veins hosted in eclogite, Tianshan, NW China. Geochimica et Cosmochimica Acta 71, 4974–4996.

Gao, J., Klemd, R., 2001. Primary fluids entrapped at blueschist to eclogite transition: evidence from the Tianshan meta-subduction complex in northwestern China. Contributions to Mineralogy and Petrology 142, 1–14. doi:10.1007/s004100100275

Gao, S., Liu, X., Yuan, H., Hattendorf, B., Günther, D., Chen, L., Hu, S., 2002. Determination of Forty Two Major and Trace Elements in USGS and NIST SRM Glasses by Laser Ablation-Inductively Coupled Plasma-Mass Spectrometry. Geostandards Newsletter 26, 181–196. doi:10.1111/j.1751-908X.2002.tb00886.x

Garrido, C., Alt, J., Sanks, W., Turchyn, A., Padrón-Navarta, J., López-Sánchez-Vizcaíno, V., Gómez-Pugnaire, M., Marchesi, C., 2012. Tracing the Recycling of Water, Carbon, and Sulfur during Subduction Metamorphism of Seafloor Serpentinites. Presented at the EGU General Assembly Conference Abstracts, p. 8798.

Garven, G., Freeze, R.A., 1984. Theoretical analysis of the role of groundwater flow in the genesis of stratabound ore deposits; 1, Mathematical and numerical model. American Journal of Science 284, 1085–1124.

Gerdes, M.L., Baumgartner, L.P., Person, M., Rumble, D., 1995. One-and two-dimensional models of fluid flow and stable isotope exchange at an outcrop in the Adamello contact aureole, Southern Alps, Italy. American Mineralogist 80, 1004–1019.

Gerdes, M.L., Baumgartner, L.P., Valley, J.W., 1999. Stable isotopic evidence for limited fluid flow through dolomitic marble in the Adamello contact aureole, Cima Uzza, Italy. Journal of Petrology 40, 853–872.

Gerya, T.V., Perchuk, L.L., Maresch, W.V., Willner, A.P., Van Reenen, D.D., Smit, C.A., 2002a. Thermal regime and gravitational instability of multi-layered continental crust. European Journal of Mineralogy 14, 687–699.

Gerya, T.V., Stöckhert, B., Perchuk, A.L., 2002b. Exhumation of high-pressure metamorphic rocks in a subduction channel: A numerical simulation. Tectonics 21.

Giglia, G., Capponi, G., Crispini, L., Piazza, M., 1996. Dynamics and seismotectonics of the West-Alpine arc. Tectonophysics 267, 143–175.

Gillis, K., Coogan, L., 2011. Secular variation in carbon uptake into the ocean crust. Earth and Planetary Science Letters 302, 385–392.

Girault, F., Perrier, F., Crockett, R., Bhattarai, M., Koirala, B.P., France-Lanord, C., Agrinier, P., Ader, M., Fluteau, F., Gréau, C., 2014. The Syabru-Bensi hydrothermal system in central Nepal: 1. Characterization of carbon dioxide and radon fluxes. Journal of Geophysical Research: Solid Earth 119, 4017–4055.

Glodny, J., Austrheim, H., Molina, J.F., Rusin, A.I., Seward, D., 2003. Rb/Sr record of fluid-rock interaction in eclogites: The Marun-Keu complex, Polar Urals, Russia. Geochimica et Cosmochimica Acta 67, 4353–4371.

Glodny, J., Kühn, A., Austrheim, H., 2008. Diffusion versus recrystallization processes in Rb–Sr geochronology: isotopic relics in eclogite facies rocks, Western Gneiss Region, Norway. Geochimica et Cosmochimica Acta 72, 506–525.

Golyshev, S., 1981. Fractionation of stable oxygen and carbon isotopes in carbonate systems. Geokhimiya 10, 1427–1441.

Goncalves, P., Marquer, D., Oliot, E., Durand, C., 2013. Thermodynamic modeling and thermobarometry of metasomatized rocks, in: Metasomatism and the Chemical Transformation of Rock. Springer, pp. 53–91.

Goncalves, P., Oliot, E., Marquer, D., Connolly, J., 2012. Role of chemical processes on shear zone formation: an example from the Grimsel metagranodiorite (Aar massif, Central Alps). Journal of Metamorphic Geology 30, 703–722.

Gorman, P.J., Kerrick, D.M., Connolly, J.A.D., 2006. Modeling open system metamorphic decarbonation of subducting slabs. Geochemistry, Geophysics, Geosystems 7, n/a-n/a. doi:10.1029/2005GC001125

Gradstein, F.M., Ogg, J.G., Smith, A.G., Bleeker, W., Lourens, L.J., 2004. A new geologic time scale, with special reference to Precambrian and Neogene. Episodes 27, 83–100.

Grant, J.A., 1986. The isocon diagram; a simple solution to Gresens' equation for metasomatic alteration. Economic Geology 81, 1976–1982.

Green, T.H., Adam, J., 2003. Experimentally-determined trace element characteristics of aqueous fluid from partially dehydrated mafic oceanic crust at 3.0 GPa, 650–700°C. European Journal of Mineralogy 15, 815. doi:10.1127/0935-1221/2003/0015-0815

Gregory, R.T., Taylor, H.P., 1981. An oxygen isotope profile in a section of Cretaceous oceanic crust, Samail Ophiolite, Oman: Evidence for $\delta^{18}O$ buffering of the oceans by deep (> 5 km) seawater-hydrothermal circulation at mid-ocean ridges. Journal of Geophysical Research: Solid Earth 86, 2737–2755.

Gresens, R.L., 1967. Composition-volume relationships of metasomatism. Chemical geology 2, 47–65.

Griffin, W., Powell, W., Pearson, N., O'reilly, S., 2008. GLITTER: data reduction software for laser ablation ICP-MS. Laser Ablation-ICP-MS in the earth sciences. Mineralogical association of Canada short course series 40, 204–207.

Groppo, C., Rolfo, F., Castelli, D., Connolly, J.A., 2013. Metamorphic CO_2 production from calc-silicate rocks via garnet-forming reactions in the CFAS–H_2O–CO_2 system. Contributions to Mineralogy and Petrology 166, 1655–1675.

Groppo, C., Rolfo, F., Castelli, D., Mosca, P., 2017. Metamorphic CO_2 Production in Collisional Orogens: Petrological Constraints from Phase Diagram Modeling of Himalayan, Scapolite-bearing, Calc-silicate Rocks in the NKC(F)MAS(T)-HC system. Journal of Petrology 58, 53–83.

Guevara, V.E., Caddick, M.J., 2016. Shooting at a moving target: phase equilibria modelling of high-temperature metamorphism. Journal of Metamorphic Geology 34, 209–235. doi:10.1111/jmg.12179

Guyot, F., Daval, D., Dupraz, S., Martinez, I., Ménez, B., Sissmann, O., 2011. CO_2 geological storage: The environmental mineralogy perspective. Comptes Rendus Geoscience 343, 246–259. doi:10.1016/j.crte.2010.12.007

H

Habermann, D., Neuser, R.D., Richter, D.K., 1998. Low limit of Mn2+-activated cathodoluminescence of calcite: state of the art. Sedimentary Geology 116, 13–24.

Habermann, D., Neuser, R.D., Richter, D.K., 1996. REE-activated cathodoluminescence of calcite and dolomite: high-resolution spectrometric analysis of CL emission (HRS-CL). Sedimentary Geology 101, 1–7.

Halama, R., John, T., Herms, P., Hauff, F., Schenk, V., 2011. A stable (Li, O) and radiogenic (Sr, Nd) isotope perspective on metasomatic processes in a subducting slab. Chemical Geology 281, 151–166.

Hammouda, T., 2003. High-pressure melting of carbonated eclogite and experimental constraints on carbon recycling and storage in the mantle. Earth and Planetary Science Letters 214, 357–368. doi:10.1016/S0012-821X(03)00361-3

Handy, M.R., Schmid, S.M., Bousquet, R., Kissling, E., Bernoulli, D., 2010. Reconciling plate-tectonic reconstructions of Alpine Tethys with the geological–geophysical record of spreading and subduction in the Alps. Earth-Science Reviews 102, 121–158.

Hansen, L.D., Dipple, G.M., Gordon, T.M., Kellett, D.A., 2005. Carbonated serpentinite (listwanite) at Atlin, British Columbia: A geological analogue to carbon dioxide sequestration. The Canadian Mineralogist 43, 225–239.

Harvey, J., Savov, I.P., Agostini, S., Cliff, R.A., Walshaw, R., 2014. Si-metasomatism in serpentinized peridotite: The effects of talc-alteration on strontium and boron isotopes in abyssal serpentinites from Hole 1268a, ODP Leg 209. Geochimica et Cosmochimica Acta 126, 30–48.

Hattori, K.H., Guillot, S., 2007. Geochemical character of serpentinites associated with high-to ultrahigh-pressure metamorphic rocks in the Alps, Cuba, and the Himalayas: Recycling of elements in subduction zones. Geochemistry, Geophysics, Geosystems 8.

Hazen, R.M., Schiffries, C.M., 2013. Why Deep Carbon? Reviews in Mineralogy and Geochemistry 75, 1–6. doi:10.2138/rmg.2013.75.1

Healy, D., Reddy, S.M., Timms, N.E., Gray, E.M., Brovarone, A.V., 2009. Trench-parallel fast axes of seismic anisotropy due to fluid-filled cracks in subducting slabs. Earth and Planetary Science Letters 283, 75–86. doi:10.1016/j.epsl.2009.03.037

Hermann, J., Spandler, C., Hack, A., Korsakov, A.V., 2006. Aqueous fluids and hydrous melts in high-pressure and ultra-high pressure rocks: Implications for element transfer in subduction zones. Lithos 92, 399–417. doi:10.1016/j.lithos.2006.03.055

Herms, P., John, T., Bakker, R.J., Schenk, V., 2012. Evidence for channelized external fluid flow and element transfer in subducting slabs (Raspas Complex, Ecuador). Chemical Geology 310–311, 79–96. doi:10.1016/j.chemgeo.2012.03.023

Hickmott, D.D., Shimizu, N., Spear, F.S., Selverstone, J., 1987. Trace-element zoning in a metamorphic garnet. Geology 15, 573–576. doi:10.1130/0091-7613(1987)15<573:TZIAMG>2.0.CO;2

Hoefs, J., 2013. Stable isotope geochemistry. Springer Science & Business Media.

Hoffbauer, R., Hoernes, S., Fiorentini, E., 1994. Oxygen isotope thermometry based on a refined increment method and its application to granulite-grade rocks from Sri Lanka. Precambrian Research 66, 199–220. doi:10.1016/0301-9268(94)90051-5

Holland, T.J.B., Powell, R., 1998. An internally consistent thermodynamic data set for phases of petrological interest. Journal of Metamorphic Geology 16, 309–343. doi:10.1111/j.1525-1314.1998.00140.x

Hollister, L.S., 1966. Garnet Zoning: An Interpretation Based on the Rayleigh Fractionation Model. Science 154, 1647. doi:10.1126/science.154.3757.1647

Houghton, R.A., 2007. Balancing the Global Carbon Budget. Annual Review of Earth and Planetary Sciences 35, 313–347. doi:10.1146/annurev.earth.35.031306.140057

Hurai, V., Huraiová, M., Slobodník, M., Thomas, R., 2015. Geofluids: Developments in Microthermometry, Spectroscopy, Thermodynamics, and Stable Isotopes. Elsevier.

J

Jacobsen, S.B., Wasserburg, G., 1980. Sm-Nd isotopic evolution of chondrites. Earth and Planetary Science Letters 50, 139–155.

Jamtveit, B., Bucher-Nurminen, K., Austrheim, H., 1990. Fluid controlled eclogitization of granulites in deep crustal shear zones, Bergen arcs, Western Norway. Contributions to Mineralogy and Petrology 104, 184–193.

Jamtveit, B., Putnis, C.V., Malthe-Sørenssen, A., 2009. Reaction induced fracturing during replacement processes. Contributions to Mineralogy and Petrology 157, 127–133.

Jarc, S., Zupancic, N., 2009. A cathodoluminescence and petrographical study of marbles from the Pohorje area in Slovenia. Chemie der Erde-Geochemistry 69, 75–80.

Jarrard, R.D., 2003. Subduction fluxes of water, carbon dioxide, chlorine, and potassium. Geochem. Geophys. Geosyst. 4, 8905. doi:10.1029/2002GC000392

Javoy, M., 1977. Stable isotopes and geothermometry. Journal of the Geological Society 133, 609–636.

Jébrak, M., 1997. Hydrothermal breccias in vein-type ore deposits: A review of mechanisms, morphology and size distribution. Ore Geology Reviews 12, 111–134. doi:10.1016/S0169-1368(97)00009-7

John, T., Klemd, R., Gao, J., Garbe-Schönberg, C.-D., 2008. Trace-element mobilization in slabs due to non steady-state fluid–rock interaction: constraints from an eclogite-facies transport vein in blueschist (Tianshan, China). Lithos 103, 1–24.

Johnson, M.C., Plank, T., 2000. Dehydration and melting experiments constrain the fate of subducted sediments. Geochemistry, Geophysics, Geosystems 1.

Jolivet, L., Daniel, J.-M., Fournier, M., 1991. Geometry and kinematics of extension in Alpine Corsica. Earth and Planetary Science Letters 104, 278–291. doi:10.1016/0012-821X(91)90209-Z

Jolivet, L., Dubois, R., Fournier, M., Goffé, B., Michard, A., Jourdan, C., 1990. Ductile extension in alpine Corsica. Geology 18, 1007–1010. doi:10.1130/0091-7613(1990)018<1007:DEIAC>2.3.CO;2

K

Kawahata, H., Nohara, M., Ishizuka, H., Hasebe, S., Chiba, H., 2001. Sr isotope geochemistry and hydrothermal alteration of the Oman ophiolite. Journal of Geophysical Research: Solid Earth 106, 11083–11099.

Kelemen, P.B., Hirth, G., 2012. Reaction-driven cracking during retrograde metamorphism: Olivine hydration and carbonation. Earth and Planetary Science Letters 345, 81–89. doi:10.1016/j.epsl.2012.06.018

Kelemen, P.B., Manning, C.E., 2015. Reevaluating carbon fluxes in subduction zones, what goes down, mostly comes up. Proceedings of the National Academy of Sciences 112, E3997–E4006. doi:10.1073/pnas.1507889112

Kelemen, P.B., Matter, J., 2008. In situ carbonation of peridotite for CO_2 storage. Proceedings of the National Academy of Sciences 105, 17295–17300. doi:10.1073/pnas.0805794105

Kelemen, P.B., Matter, J., Streit, E.E., Rudge, J.F., Curry, W.B., Blusztajn, J., 2011. Rates and mechanisms of mineral carbonation in peridotite: natural processes and recipes for enhanced, in situ CO_2 capture and storage. Annual Review of Earth and Planetary Sciences 39, 545–576.

Kerrick, D., Connolly, J., 1998. Subduction of ophicarbonates and recycling of CO_2 and H_2O. Geology 26, 375–378.

Kerrick, D.M., Caldeira, K., 1998. Metamorphic CO_2 degassing from orogenic belts. Chemical Geology 145, 213–232.

Kerrick, D.M., Connolly, J.A.D., 2001a. Metamorphic devolatilization of subducted marine sediments and the transport of volatiles into the Earth's mantle. Nature 411, 293–296.

Kerrick, D.M., Connolly, J.A.D., 2001b. Metamorphic devolatilization of subducted oceanic metabasalts: implications for seismicity, arc magmatism and volatile recycling. Earth and Planetary Science Letters 189, 19–29. doi:10.1016/S0012-821X(01)00347-8

Kimura, G., Silver, E., Blum, P., 1997. Costa Rica accretionary wedge, Sites 1039–1043. Proc. Ocean Drilling Program, Init. Repts 170, 1–247.

King, R.L., Bebout, G.E., Moriguti, T., Nakamura, E., 2006. Elemental mixing systematics and Sr–Nd isotope geochemistry of mélange formation: obstacles to identification of fluid sources to arc volcanics. Earth and Planetary Science Letters 246, 288–304.

Kleine, B.I., Skelton, A.D.L., Huet, B., Pitcairn, I.K., 2014. Preservation of Blueschist-facies Minerals along a Shear Zone by Coupled Metasomatism and Fast-flowing CO_2-bearing Fluids. Journal of Petrology 55, 1905–1939. doi:10.1093/petrology/egu045

Kleine, B.I., Zhao, Z., Skelton, A.D.L., 2016. Rapid fluid flow along fractures at greenschist facies conditions on Syros, Greece. American Journal of Science 316, 169–201. doi:10.2475/02.2016.03

Klimm, K., Blundy, J.D., Green, T.H., 2008. Trace element partitioning and accessory phase saturation during H_2O-saturated melting of basalt with implications for subduction zone chemical fluxes. Journal of Petrology 49, 523–553.

Knoche, R., Sweeney, R.J., Luth, R.W., 1999. Carbonation and decarbonation of eclogites: the role of garnet. Contributions to Mineralogy and Petrology 135, 332–339.

Kodolanyi, J., Pettke, T., Spandler, C., Kamber, B.S., Gmeling, K., 2012. Geochemistry of Ocean Floor and Fore-arc Serpentinites: Constraints on the Ultramafic Input to Subduction Zones. Journal of Petrology 53, 235–270. doi:10.1093/petrology/egr058

Kogarko, L., Kurat, G., Ntaflos, T., 2001. Carbonate metasomatism of the oceanic mantle beneath Fernando de Noronha Island, Brazil. Contributions to Mineralogy and Petrology 140, 577–587.

Kogiso, T., Tatsumi, Y., Nakano, S., 1997. Trace element transport during dehydration processes in the subducted oceanic crust: 1. Experiments and implications for the origin of ocean island basalts. Earth and Planetary Science Letters 148, 193–205. doi:10.1016/S0012-821X(97)00018-6

Kohn, M.J., 2014. 4.7 - Geochemical Zoning in Metamorphic Minerals A2 - Holland, Heinrich D., in: Turekian, K.K. (Ed.), Treatise on Geochemistry (Second Edition). Elsevier, Oxford, pp. 249–280.

Kohn, M.J., Spear, F., 2000. Retrograde net transfer reaction insurance for pressure-temperature estimates. Geology 28, 1127–1130. doi:10.1130/0091-7613(2000)28<1127:RNTRIF>2.0.CO;2

Kohn, M.J., Valley, J.W., 1994. Oxygen isotope constraints on metamorphic fluid flow, Townshend Dam, Vermont, USA. Geochimica et Cosmochimica Acta 58, 5551–5566.

Korsakov, A.V., Hermann, J., 2006. Silicate and carbonate melt inclusions associated with diamonds in deeply subducted carbonate rocks. Earth and Planetary Science Letters 241, 104–118.

Kretz, R., 1983. Symbols for rock-forming mineralsl. American Mineralogist 68, 277–279.

Kump, L.R., Brantley, S.L., Arthur, M.A., 2000. Chemical weathering, atmospheric CO_2, and climate. Annual Review of Earth and Planetary Sciences 28, 611–667.

L

Lacombe, O., Jolivet, L., 2005. Structural and kinematic relationships between Corsica and the Pyrenees-Provence domain at the time of the Pyrenean orogeny. Tectonics 24.

Lagabrielle, Y., Bodinier, J., 2008. Submarine reworking of exhumed subcontinental mantle rocks: field evidence from the Lherz peridotites, French Pyrenees. Terra Nova 20, 11–21.

Lagabrielle, Y., Cannat, M., 1990. Alpine Jurassic ophiolites resemble the modern central Atlantic basement. Geology 18, 319–322. doi:10.1130/0091-7613(1990)018<0319:AJORTM>2.3.CO;2

Lagabrielle, Y., Lemoine, M., 1997. Alpine, Corsican and Apennine ophiolites: the slow-spreading ridge model. Comptes Rendus de l'Académie des Sciences - Series IIA - Earth and Planetary Science 325, 909–920. doi:10.1016/S1251-8050(97)82369-5

Lagabrielle, Y., Vitale Brovarone, A., Ildefonse, B., 2015. Fossil oceanic core complexes recognized in the blueschist metaophiolites of Western Alps and Corsica. Earth-Science Reviews 141, 1–26. doi:10.1016/j.earscirev.2014.11.004

Lahondère, D., 1996. Les schistes bleus et les éclogites à lawsonite des unités continentales et océaniques de la Corse alpine: nouvelles données pétrologiques et structurales.

Lahondere, D., 1988. Le métamorphisme éclogitique dans les orthogneiss et les métabasites ophiolitiques de la région de Farinole (Corse). Bulletin de la Société géologique de France 4, 579–585.

Lahondère, D., Caby, R., 1989. Les méta-conglomérats polygéniques des «Schistes lustrés» de la vallée du Golo (Corse alpine): signification paléogéographique et conséquences tectoniques. Comptes rendus de l'Académie des sciences. Série 2, Mécanique, Physique, Chimie, Sciences de l'univers, Sciences de la Terre 309, 727–732.

Lanari, P., Vidal, O., De Andrade, V., Dubacq, B., Lewin, E., Grosch, E.G., Schwartz, S., 2014. XMapTools: A MATLAB©-based program for electron microprobe X-ray image processing and geothermobarometry. Computers & Geosciences 62, 227–240. doi:10.1016/j.cageo.2013.08.010

Lassey, K.R., Blattner, P., 1988. Kinetically controlled oxygen isotope exchange between fluid and rock in one-dimensional advective flow. Geochimica et Cosmochimica Acta 52, 2169–2175.

Lazar, C., Zhang, C., Manning, C.E., Mysen, B.O., 2014. Redox effects on calcite-portlandite-fluid equilibria at forearc conditions: Carbon mobility, methanogenesis, and reduction melting of calcite. American Mineralogist 99, 1604–1615. doi:10.2138/am.2014.4696

Leake, B.E., Woolley, A.R., Birch, W.D., Burke, E.A.J., Ferraris, G., Grice, J.D., Hawthorne, F.C., Kisch, H.J., Krivovichev, V.G., Schumacher, J.C., Stephenson, N.C.N., Whittaker, E.J.W., 2004. Nomenclature of amphiboles: additions and revisions to the International Mineralogical Association's amphibole nomenclature. Mineralogical Magazine 68, 209–215. doi:10.1180/0026461046810182

Lemoine, M., 1980. Serpentinites, gabbros and ophicalcites in the Piemont-Ligurian domain of the Western Alps: possible indicators of oceanic fracture zones and of associated serpentinite protrusions in the Jurassic-Cretaceous Tethys. Archives des Sciences, Genève 33, 103–116.

Lemoine, M., Tricart, P., Boillot, G., 1987. Ultramafic and gabbroic ocean floor of the Ligurian Tethys (Alps, Corsica, Apennines): In search of a genetic imodel. Geology 15, 622–625. doi:10.1130/0091-7613(1987)15<622:UAGOFO>2.0.CO;2

Levi, N., Malasoma, A., Marroni, M., Pandolfi, L., Paperini, M., 2007. Tectono-metamorphic history of the ophiolitic Lento unit (northern Corsica): evidences for the complexity of accretion-exhumation processes in a fossil subduction system. Geodinamica Acta 20, 99–118.

Li, J.-L., Klemd, R., Gao, J., Meyer, M., 2014. Compositional zoning in dolomite from lawsonite-bearing eclogite (SW Tianshan, China): Evidence for prograde metamorphism during subduction of oceanic crust. American Mineralogist 99, 206–217.

Lombardo, B., Rubatto, D., Castelli, D., 2002. Ion microprobe U-Pb dating of zircon from a Monviso metaplagiogranite: implications for the evolution of the Piedmont-Ligura Tethys in the Western Alps. Ofioliti 27, 109–117. doi:10.4454/ofioliti.v27i2.181

Lü, Z., Bucher, K., Zhang, L., 2013. Omphacite-bearing calcite marble and associated coesite-bearing pelitic schist from the meta-ophiolitic belt of Chinese western Tianshan. Journal of Asian Earth Sciences 76, 37–47.

Lundin, E.R., Doré, A.G., 2011. Hyperextension, serpentinization, and weakening: A new paradigm for rifted margin compressional deformation. Geology 39, 347–350.

M

Malatesta, C., Gerya, T., Scambelluri, M., Federico, L., Crispini, L., Capponi, G., 2012. Intraoceanic subduction of "heterogeneous" oceanic lithosphere in narrow basins: 2D numerical modeling. Lithos 140, 234–251.

Malavieille, Chemenda, Larroque, 1998. Evolutionary model for Alpine Corsica: mechanism for ophiolite emplacement and exhumation of high-pressure rocks. Terra Nova 10, 317–322. doi:10.1046/j.1365-3121.1998.00208.x

Malavieille, J., Chemenda, A., Larroque, C., 1998. Evolutionary model for Alpine Corsica: mechanism for ophiolite emplacement and exhumation of high-pressure rocks. Terra Nova-Oxford - 10, 317–322.

Malvoisin, B., Chopin, C., Brunet, F., Galvez, M.E., 2012. Low-temperature Wollastonite Formed by Carbonate Reduction: a Marker of Serpentinite Redox Conditions. Journal of Petrology 53, 159–176. doi:10.1093/petrology/egr060

Manatschal, G., 2004. New models for evolution of magma-poor rifted margins based on a review of data and concepts from West Iberia and the Alps. International Journal of Earth Sciences 93, 432–466.

Manatschal, G., 1999. Fluid- and reaction-assisted low-angle normal faulting: evidence from rift-related brittle fault rocks in the Alps (Err Nappe, eastern Switzerland). Journal of Structural Geology 21, 777–793. doi:10.1016/S0191-8141(99)00069-3

Manatschal, G., Marquer, D., Früh-Green, G.L., 2000. Channelized fluid flow and mass transfer along a rift-related detachment fault (Eastern Alps, southeast Switzerland). Geological Society of America Bulletin 112, 21–33. doi:10.1130/0016-7606(2000)112<21:CFFAMT>2.0.CO;2

Manatschal, G., Müntener, O., 2009. A type sequence across an ancient magma-poor ocean–continent transition: the example of the western Alpine Tethys ophiolites. Tectonophysics 473, 4–19.

Mancktelow, N.S., Pennacchioni, G., 2005. The control of precursor brittle fracture and fluid–rock interaction on the development of single and paired ductile shear zones. Journal of Structural Geology 27, 645–661.

Manning, C., 2004. The chemistry of subduction-zone fluids. Earth and Planetary Science Letters 223, 1–16. doi:10.1016/j.epsl.2004.04.030

Manning, C.E., Shock, E.L., Sverjensky, D.A., 2013. The Chemistry of Carbon in Aqueous Fluids at Crustal and Upper-Mantle Conditions: Experimental and Theoretical Constraints. Reviews in Mineralogy and Geochemistry 75, 109–148. doi:10.2138/rmg.2013.75.5

Marschall, H.R., Schumacher, J.C., 2012. Arc magmas sourced from melange diapirs in subduction zones. Nature Geosci 5, 862–867. doi:10.1038/ngeo1634

Martin, L.A.J., Rubatto, D., Crépisson, C., Hermann, J., Putlitz, B., Vitale-Brovarone, A., 2014. Garnet oxygen analysis by SHRIMP-SI: Matrix corrections and application to high-pressure metasomatic rocks from Alpine Corsica. Chemical Geology 374–375, 25–36. doi:10.1016/j.chemgeo.2014.02.010

Martin, L.A.J., Rubatto, D., Vitale Brovarone, A., Hermann, J., 2011. Late Eocene lawsonite-eclogite facies metasomatism of a granulite sliver associated to ophiolites in Alpine Corsica. Lithos 125, 620–640. doi:10.1016/j.lithos.2011.03.015

Mattauer, M., Faure, M., Malavieille, J., 1981. Transverse lineation and large-scale structures related to Alpine obduction in Corsica. Journal of Structural Geology 3, 401–409.

Matter, J.M., Kelemen, P.B., 2009. Permanent storage of carbon dioxide in geological reservoirs by mineral carbonation. Nature Geosci 2, 837–841. doi:10.1038/ngeo683

Mayer, A., Abouchami, W., Dal Piaz, G., 1999. Eocene Sm-Nd age for the eclogitic metamorphism of the Zermatt-Saas ophiolite in Ayas Valley, western Alps. Eur Union Geosci 10, 809.

Mayer, L., Pisias, N., Janecek, T., 1992. Proceeding of the Ocean Drilling Program, Initial Reports (Ocean Drill Program, College Station, TX) 138.

McCrea, J.M., 1950. On the isotopic chemistry of carbonates and a paleotemperature scale. The Journal of Chemical Physics 18, 849–857.

Menzel, M.D., Garrido, C.J., López Sánchez-Vizcaíno, V., Marchesi, C., Hidas, K., 2016. The fate of carbon and CO_2-fluid-rock interaction during subduction metamorphism of serpentinites. Presented at the EGU General Assembly Conference Abstracts, p. 13863.

Meresse, F., Lagabrielle, Y., Malavieille, J., Ildefonse, B., 2012. A fossil Ocean–Continent Transition of the Mesozoic Tethys preserved in the Schistes Lustrés nappe of northern Corsica. Tectonophysics 579, 4–16. doi:10.1016/j.tecto.2012.06.013

Merlini, M., Crichton, W.A., Hanfland, M., Gemmi, M., Müller, H., Kupenko, I., Dubrovinsky, L., 2012. Structures of dolomite at ultrahigh pressure and their influence on the deep carbon cycle. Proceedings of the National Academy of Sciences 109, 13509–13514.

Michard, A., Albarède, F., 1986. The REE content of some hydrothermal fluids. Chemical Geology 55, 51–60.

Michard, A., Albarede, F., Michard, G., Minster, J., Charlou, J., 1983. Rare-earth elements and uranium in high-temperature solutions from East Pacific Rise hydrothermal vent field (13 N). Nature 303, 795–797.

Mikhail, S., Sverjensky, D.A., 2014. Nitrogen speciation in upper mantle fluids and the origin of Earth's nitrogen-rich atmosphere. Nature Geoscience 7, 816.

Miller, C., Stosch, H.-G., 1988. Geochemistry and origin of eclogites from the type locality Koralpe and Saualpe, Eastern Alps, Austria. Chemical geology 67, 103–118.

Miller, C., Zanetti, A., Thöni, M., Konzett, J., 2007. Eclogitisation of gabbroic rocks: Redistribution of trace elements and Zr in rutile thermometry in an Eo-Alpine subduction zone (Eastern Alps). Chemical Geology 239, 96–123. doi:10.1016/j.chemgeo.2007.01.001

Miller, J., Buick, I., Cartwright, I., 2000. Textural implications of high-pressure fluid flow controlled by pre-subduction deformation and alteration patterns. Journal of Geochemical Exploration 69, 551–555.

Miller, J.A., Cartwright, I., Buick, I.S., Barnicoat, A.C., 2001. An O-isotope profile through the HP–LT Corsican ophiolite, France and its implications for fluid flow during subduction. Chemical Geology 178, 43–69.

Mohn, G., Manatschal, G., Beltrando, M., Masini, E., Kusznir, N., 2012. Necking of continental crust in magma-poor rifted margins: Evidence from the fossil Alpine Tethys margins. Tectonics 31, n/a-n/a. doi:10.1029/2011TC002961

Mohn, G., Manatschal, G., Masini, E., Müntener, O., 2011. Rift-related inheritance in orogens: a case study from the Austroalpine nappes in Central Alps (SE-Switzerland and N-Italy). International Journal of Earth Sciences 100, 937–961.

Mohn, G., Manatschal, G., Müntener, O., Beltrando, M., Masini, E., 2010. Unravelling the interaction between tectonic and sedimentary processes during lithospheric thinning in the Alpine Tethys margins. International Journal of Earth Sciences 99, 75–101.

Molina, J.F., Poli, S., 2000. Carbonate stability and fluid composition in subducted oceanic crust: an experimental study on H_2O–CO_2-bearing basalts. Earth and Planetary Science Letters 176, 295–310. doi:10.1016/S0012-821X(00)00021-2

Molli, G., 2008. Northern Apennine–Corsica orogenic system: an updated overview. Geological Society, London, Special Publications 298, 413–442.

Molli, G., Malavieille, J., 2011. Orogenic processes and the Corsica/Apennines geodynamic evolution: insights from Taiwan. Int J Earth Sci (Geol Rundsch) 100, 1207–1224. doi:10.1007/s00531-010-0598-y

Morimoto, N., 1989. Nomenclature of Pyroxenes. Mineralogy and Petrology 39, 55–76. doi:10.1007/BF01226262

Mosca, P., Polino, R., Rogledi, S., Rossi, M., 2010. New data for the kinematic interpretation of the Alps–Apennines junction (Northwestern Italy). International Journal of Earth Sciences 99, 833–849.

N

Newton, R.C., Manning, C.E., 2002. Experimental determination of calcite solubility in H_2O-NaCl solutions at deep crust/upper mantle pressures and temperatures: Implications for metasomatic processes in shear zones. American Mineralogist 87, 1401–1409.

Nielsen, S.G., Marschall, H.R., 2017. Geochemical evidence for mélange melting in global arcs. Science Advances 3, e1602402.

Nishiyama, T., 1990. CO_2-metasomatism of a metabasite block in a serpentine melange from the Nishisonogi metamorphic rocks, southwest Japan. Contributions to Mineralogy and Petrology 104, 35–46.

Nitsch, K., 1972. The PT-X_{CO2} stability held of lawsonite. Contrib Min Petrol 25, 116–134.

O

Oelkers, E.H., Gislason, S.R., Matter, J., 2008. Mineral carbonation of CO 2. Elements 4, 333–337.

Oliver, N.H.S., 1996. Review and classification of structural controls on fluid flow during regional metamorphism. Journal of Metamorphic Geology 14, 477–492. doi:10.1046/j.1525-1314.1996.00347.x

Oliver, N.H.S., Bons, P.D., 2001. Mechanisms of fluid flow and fluid–rock interaction in fossil metamorphic hydrothermal systems inferred from vein–wallrock patterns, geometry and microstructure. Geofluids 1, 137–162. doi:10.1046/j.1468-8123.2001.00013.x

Ota, T., Kaneko, Y., 2010. Blueschists, eclogites, and subduction zone tectonics: Insights from a review of Late Miocene blueschists and eclogites, and related young high-pressure metamorphic rocks. Gondwana Research 18, 167–188. doi:10.1016/j.gr.2010.02.013

P

Passchier, C., Trouw, R., 1987. J. 2005. microtectonics.

Peacock, S.M., 2001. Are the lower planes of double seismic zones caused by serpentine dehydration in subducting oceanic mantle? Geology 29, 299–302.

Pearce, N.J.G., Perkins, W.T., Westgate, J.A., Gorton, M.P., Jackson, S.E., Neal, C.R., Chenery, S.P., 1997. A Compilation of New and Published Major and Trace Element Data for NIST SRM 610 and NIST SRM 612 Glass Reference Materials. Geostandards Newsletter 21, 115–144. doi:10.1111/j.1751-908X.1997.tb00538.x

Péquignot, G., Potdevin, J.-L., Caron, J.-M., Ohnenstetter, M., 1984. Detritisme ophiolitique dans les schistes lustres corses et paleogeographie du domaine piemontais. Bulletin de la Société Géologique de France 7, 913–920.

Peretti, A., Dubessy, J., Mullis, J., Frost, B.R., Trommsdorff, V., 1992. Highly reducing conditions during Alpine metamorphism of the Malenco peridotite (Sondrio, northern Italy) indicated by mineral paragenesis and H 2 in fluid inclusions. Contributions to Mineralogy and Petrology 112, 329–340.

Perrier, F., Richon, P., Byrdina, S., France-Lanord, C., Rajaure, S., Koirala, B.P., Shrestha, P.L., Gautam, U.P., Tiwari, D.R., Revil, A., 2009. A direct evidence for high carbon dioxide and radon-222 discharge in Central Nepal. Earth and Planetary Science Letters 278, 198–207.

Philippot, P., Chevallier, P., Chopin, C., Dubessy, J., 1995. Fluid composition and evolution in coesite-bearing rocks (Dora-Maira massif, Western Alps): implications for element recycling during subduction. Contributions to Mineralogy and Petrology 121, 29. doi:10.1007/s004100050088

Philippot, P., Selverstone, J., 1991. Trace-element-rich brines in eclogitic veins: implications for fluid composition and transport during subduction. Contributions to Mineralogy and Petrology 106, 417–430.

Philpotts, A., Ague, J., 2009. Principles of igneous and metamorphic petrology. Cambridge University Press.

Piana, F., Polino, R., 1995. Tertiary structural relationships between Alps and Apennines: the critical Torino Hill and Monferrato area. Northwestern Italy. Terra Nova 7, 138–143.

Piccoli, F., Vitale Brovarone, A., Beyssac, O., Martinez, I., Ague, J.J., Chaduteau, C., 2016. Carbonation by fluid–rock interactions at high-pressure conditions: Implications for carbon cycling in subduction zones. Earth and Planetary Science Letters 445, 146–159. doi:10.1016/j.epsl.2016.03.045

Pin, C., Briot, D., Bassin, C., Poitrasson, F., 1994. Concomitant separation of strontium and samarium-neodymium for isotopic analysis in silicate samples, based on specific extraction chromatography. Analytica Chimica Acta 298, 209–217. doi:10.1016/0003-2670(94)00274-6

Pin, C., Telouk, P., Imbert, J.-L., 1995. Direct determination of the samarium: neodymium ratio in geological materials by inductively coupled plasma quadrupole mass spectrometry with cryogenic desolvation. Comparison with isotope dilution thermal ionization mass spectrometry. J. Anal. At. Spectrom. 10, 93–98. doi:10.1039/JA9951000093

Pinto, V.H.G., Manatschal, G., Karpoff, A.M., Viana, A., 2015. Tracing mantle-reacted fluids in magma-poor rifted margins: The example of Alpine Tethyan rifted margins. Geochemistry, Geophysics, Geosystems 16, 3271–3308.

Plank, T., 2014. The chemical composition of subducting sediments. Treatise on geochemistry 4, 607–629.

Plank, T., Langmuir, C.H., 1998. The chemical composition of subducting sediment and its consequences for the crust and mantle. Chemical Geology 145, 325–394. doi:10.1016/S0009-2541(97)00150-2

Plümper, O., Røyne, A., Magrasó, A., Jamtveit, B., 2012. The interface-scale mechanism of reaction-induced fracturing during serpentinization. Geology 40, 1103–1106.
Poli, S., 2015. Carbon mobilized at shallow depths in subduction zones by carbonatitic liquids. Nature Geosci 8, 633–636.
Poli, S., Franzolin, E., Fumagalli, P., Crottini, A., 2009. The transport of carbon and hydrogen in subducted oceanic crust: An experimental study to 5 GPa. Earth and Planetary Science Letters 278, 350–360. doi:10.1016/j.epsl.2008.12.022
Poli, S., Schmidt, M.W., 2004. Experimental Subsolidus Studies on Epidote Minerals. Reviews in Mineralogy and Geochemistry 56, 171. doi:10.2138/gsrmg.56.1.171
Poli, S., Schmidt, M.W., 2002. Petrology of Subducted Slabs. Annu. Rev. Earth Planet. Sci. 30, 207–235. doi:10.1146/annurev.earth.30.091201.140550
Powell, R., Holland, T.J.B., 2008. On thermobarometry. Journal of Metamorphic Geology 26, 155–179. doi:10.1111/j.1525-1314.2007.00756.x
Prokoph, A., Shields, G., Veizer, J., 2008. Compilation and time-series analysis of a marine carbonate δ 18 O, δ 13 C, 87 Sr/86 Sr and δ 34 S database through Earth history. Earth-Science Reviews 87, 113–133.
Putnis, A., 2009. Mineral Replacement Reactions. Reviews in Mineralogy and Geochemistry 70, 87–124. doi:10.2138/rmg.2009.70.3
Putnis, A., John, T., 2010. Replacement Processes in the Earth's Crust. Elements 6, 159–164. doi:10.2113/gselements.6.3.159

R

Rampone, E., Hofmann, A.W., 2012. A global overview of isotopic heterogeneities in the oceanic mantle. Lithos 148, 247–261.
Ramsay, J.G., 1980. The crack-seal mechanism of rock deformation. Nature 284, 135–139. doi:10.1038/284135a0
Ranero, C., Sallares, V., 2004. Geophysical evidence for hydration of the crust and mantle of the Nazca plate during bending at the north Chile trench. Geology 32, 549–552.
Ranero, C.R., Morgan, J.P., McIntosh, K., Reichert, C., 2003. Bending-related faulting and mantle serpentinization at the Middle America trench. Nature 425, 367.
Ravna, E.J.K., Andersen, T.B., Jolivet, L., De Capitani, C., 2010. Cold subduction and the formation of lawsonite eclogite – constraints from prograde evolution of eclogitized pillow lava from Corsica. Journal of Metamorphic Geology 28, 381–395. doi:10.1111/j.1525-1314.2010.00870.x
Rea, D.K., Ruff, L.J., 1996. Composition and mass flux of sediment entering the world's subduction zones: implications for global sediment budgets, great earthquakes, and volcanism. Earth and Planetary Science Letters 140, 1–12.
Reddy, S.M., Kelley, S.P., Wheeler, J., 1996. A $^{40}Ar/^{39}Ar$ laser probe study of micas from the Sesia Zone, Italian Alps: implications for metamorphic and deformation histories. Journal of Metamorphic Geology 14, 493–508. doi:10.1046/j.1525-1314.1996.00338.x
Reinecke, T., 1991. Very-high-pressure metamorphism and uplift of coesite-bearing metasediments from the Zermatt-Saas zone, Western Alps. European Journal of Mineralogy 7–18.
Roberts, M.P., Pin, C., Clemens, J.D., Paquette, J.-L., 2000. Petrogenesis of mafic to felsic plutonic rock associations: the calc-alkaline Quérigut complex, French Pyrenees. Journal of Petrology 41, 809–844.
Roedder, E., 1984. Volume 12: Fluid inclusions. Mineralogical.

Rolfo, F., Groppo, C., Mosca, P., 2017. Metamorphic CO 2 production in calc-silicate rocks from the eastern Himalaya. Italian Journal of Geosciences 136, 28–38.

Rolland, Y., Rossi, M., 2016. Two-stage fluid flow and element transfers in shear zones during collision burial-exhumation cycle: Insights from the Mont Blanc Crystalline Massif (Western Alps). Journal of Geodynamics 101, 88–108.

Rolland, Y., Rossi, M., Cox, S., Corsini, M., Mancktelow, N., Pennacchioni, G., Fornari, M., Boullier, A.-M., 2008. 40Ar/39Ar dating of synkinematic white mica: insights from fluid-rock reaction in low-grade shear zones (Mont Blanc Massif) and constraints on timing of deformation in the NW external Alps. Geological Society, London, Special Publications 299, 293–315.

Rubatto, D., Gebauer, D., Fanning, M., 1998. Jurassic formation and Eocene subduction of the Zermatt–Saas-Fee ophiolites: implications for the geodynamic evolution of the Central and Western Alps. Contributions to Mineralogy and Petrology 132, 269–287. doi:10.1007/s004100050421

Rubatto, D., Hermann, J., 2003. Zircon formation during fluid circulation in eclogites (Monviso, Western Alps): implications for Zr and Hf budget in subduction zones. Geochimica et Cosmochimica Acta 67, 2173–2187.

Rudge, J.F., Kelemen, P.B., Spiegelman, M., 2010. A simple model of reaction-induced cracking applied to serpentinization and carbonation of peridotite. Earth and Planetary Science Letters 291, 215–227. doi:10.1016/j.epsl.2010.01.016

Rumble, D., 1998. Stable Isotope Geochemistry of Ultrahigh-Pressure Rocks, in: Hacker, B.R., Liou, J.G. (Eds.), When Continents Collide: Geodynamics and Geochemistry of Ultrahigh-Pressure Rocks. Springer Netherlands, Dordrecht, pp. 241–259.

Rumble, D., 1982. Stable isotope fractionation during metamorphic devolatilization reactions. Reviews in Mineralogy and Geochemistry 10, 327–353.

Rumble, D., Spear, F.S., 1983. Oxygen-isotope equilibration and permeability enhancement during regional metamorphism. Journal of the Geological Society 140, 619–628.

Rumble, D., Yui, T.-F., 1998. The Qinglongshan oxygen and hydrogen isotope anomaly near Donghai in Jiangsu Province, China. Geochimica et Cosmochimica Acta 62, 3307–3321.

Rumble III, D., 1978. Mineralogy, petrology, and oxygen isotopic geochemistry of the Clough Formation, Black Mountain, western New Hampshire, USA. Journal of Petrology 19, 317–340.

Rumble III, D., Farquhar, J., Young, E.D., Christensen, C.P., 1997. In situ oxygen isotope analysis with an excimer laser using F2 and BrF5 reagents and O2 gas as analyte. Geochimica et Cosmochimica Acta 61, 4229–4234. doi:10.1016/S0016-7037(97)00232-9

Rüpke, L.H., Morgan, J.P., Hort, M., Connolly, J.A.., 2004. Serpentine and the subduction zone water cycle. Earth and Planetary Science Letters 223, 17–34. doi:10.1016/j.epsl.2004.04.018

Rye, R.O., Schuiling, R.D., Rye, D.M., Jansen, J.B.H., 1976. Carbon, hydrogen, and oxygen isotope studies of the regional metamorphic complex at Naxos, Greece. Geochimica et Cosmochimica Acta 40, 1031–1049. doi:10.1016/0016-7037(76)90045-4

S

Saccocia, P.J., Seewald, J.S., Shanks, W.C., 2009. Oxygen and hydrogen isotope fractionation in serpentine–water and talc–water systems from 250 to 450 C, 50MPa. Geochimica et Cosmochimica Acta 73, 6789–6804.

Salters, V.J., Stracke, A., 2004. Composition of the depleted mantle. Geochemistry, Geophysics, Geosystems 5.
Sano, Y., Marty, B., 1995. Origin of carbon in fumarolic gas from island arcs. Chemical Geology 119, 265–274.
Scambelluri, M., Bebout, G.E., Belmonte, D., Gilio, M., Campomenosi, N., Collins, N., Crispini, L., 2016. Carbonation of subduction-zone serpentinite (high-pressure ophicarbonate; Ligurian Western Alps) and implications for the deep carbon cycling. Earth and Planetary Science Letters 441, 155–166. doi:10.1016/j.epsl.2016.02.034
Scambelluri, M., Piccardo, G.B., Philippot, P., Robbiano, A., Negretti, L., 1997. High salinity fluid inclusions formed from recycled seawater in deeply subducted alpine serpentinite. Earth and Planetary Science Letters 148, 485–499. doi:10.1016/S0012-821X(97)00043-5
Scambelluri, M., Tonarini, S., 2012. Boron isotope evidence for shallow fluid transfer across subduction zones by serpentinized mantle. Geology 40, 907–910.
Schertl, H.-P., Neuser, R.D., Nikolai, V., Shatsky, V.S., 2004. UHP-metamorphic rocks from Dora Maira/Western Alps and Kokchetav/Kazakhstan. European Journal of Mineralogy 16, 49–57.
Schiano, P., Clocchiatti, R., Shimizu, N., Weis, D., Mattielli, N., 1994. Cogenetic silica-rich and carbonate-rich melts trapped in mantle minerals in Kerguelen ultramafic xenoliths: implications for metasomatism in the oceanic upper mantle. Earth and Planetary Science Letters 123, 167–178.
Schmidt, M., Poli, S., 2014. Devolatilization during subduction. The Crust, Treatise on Geochemistry (eds. HD Holland and KK Turekian, Second Edition), Elsevier-Pergamon, Oxford 669–701.
Schmidt, M.W., Poli, S., 1998. Experimentally based water budgets for dehydrating slabs and consequences for arc magma generation. Earth and Planetary Science Letters 163, 361–379. doi:10.1016/S0012-821X(98)00142-3
Schneider, J., Boni, M., Laukamp, C., Bechstädt, T., Petzel, V., 2008. Willemite (Zn 2 SiO 4) as a possible Rb–Sr geochronometer for dating nonsulfide Zn–Pb mineralization: examples from the Otavi Mountainland (Namibia). Ore Geology Reviews 33, 152–167.
Schneider, J., Melcher, F., Brauns, M., 2007. Concordant ages for the giant Kipushi base metal deposit (DR Congo) from direct Rb–Sr and Re–Os dating of sulfides. Mineralium Deposita 42, 791–797.
Schumacher, M., Laubscher, H., 1996. 3D crustal architecture of the Alps-Apennines join—a new view on seismic data. Tectonophysics 260, 349–363.
Seaton, N.C.A., Whitney, D.L., Teyssier, C., Toraman, E., Heizler, M.T., 2009. Recrystallization of high-pressure marble (Sivrihisar, Turkey). Tectonophysics 479, 241–253. doi:10.1016/j.tecto.2009.08.015
Selverstone, J., Franz, G., Thomas, S., Getty, S., 1992. Fluid variability in 2 GPa eclogites as an indicator of fluid behavior during subduction. Contributions to Mineralogy and Petrology 112, 341–357. doi:10.1007/BF00310465
Séranne, M., 1999. The Gulf of Lion continental margin (NW Mediterranean) revisited by IBS: an overview. Geological Society, London, Special Publications 156, 15–36.
Shi, G.U., Tropper, P., Cui, W., Tan, J., Wang, C., 2005. Methane (CH4)-bearing fluid inclusions in the Myanmar jadeitite. Geochemical Journal 39, 503–516.
Shieh, Y., Taylor Jr, H., 1969. Oxygen and carbon isotope studies of contact metamorphism of carbonate rocks. Journal of Petrology 10, 307–331.
Siebe, M., Yaxley, G., Hermann, J. 2016. Carbonation of serpentinite and spinel peridotite under forarc conditions-an experimental study. Goldschmidt, abstract.

Skelton, A., 2011. Flux rates for water and carbon during greenschist facies metamorphism. Geology 39, 43–46.
Skelton, A.D., Graham, C.M., Bickle, M.J., 1995. Lithological and structural controls on regional 3-D fluid flow patterns during greenschist facies metamorphism of the Dalradian of the SW Scottish Highlands. Journal of Petrology 36, 563–586.
Skelton, A.D., Valley, J.W., 2000. The relative timing of serpentinisation and mantle exhumation at the ocean–continent transition, Iberia: constraints from oxygen isotopes. Earth and Planetary Science Letters 178, 327–338.
Skelton, A.D.L., Bickle, M.J., Graham, C.M., 1997. Fluid-flux and reaction rate from advective-diffusive carbonation of mafic sill margins in the Dalradian, southwest Scottish Highlands. Earth and Planetary Science Letters 146, 527–539. doi:10.1016/S0012-821X(96)00248-8
Snow, J.E., Dick, H.J., 1995. Pervasive magnesium loss by marine weathering of peridotite. Geochimica et Cosmochimica Acta 59, 4219–4235.
Snow, J.E., Hart, S.R., Dick, H.J., 1994. Nd and Sr isotope evidence linking mid-ocean-ridge basalts and abyssal peridotites. Nature 371, 57–60.
Snow, J.E., Hart, S.R., Dick, H.J., 1993. Orphan strontium-87 in abyssal peridotites: daddy was a granite. Science-AAAS-Weekly Paper Edition-including Guide to Scientific Information 262, 1861–1863.
Spandler, C., Hermann, J., 2006. High-pressure veins in eclogite from New Caledonia and their significance for fluid migration in subduction zones. Lithos 89, 135–153. doi:10.1016/j.lithos.2005.12.003
Spandler, C., Hermann, J., Arculus, R., Mavrogenes, J., 2003. Redistribution of trace elements during prograde metamorphism from lawsonite blueschist to eclogite facies; implications for deep subduction-zone processes. Contributions to Mineralogy and Petrology 146, 205–222. doi:10.1007/s00410-003-0495-5
Spandler, C., Pettke, T., Rubatto, D., 2011. Internal and External Fluid Sources for Eclogite-facies Veins in the Monviso Meta-ophiolite, Western Alps: Implications for Fluid Flow in Subduction Zones. Journal of Petrology 52, 1207–1236. doi:10.1093/petrology/egr025
Spandler, C., Pirard, C., 2013. Element recycling from subducting slabs to arc crust: A review. Lithos 170–171, 208–223. doi:10.1016/j.lithos.2013.02.016
Spear, F.S., 1991. On the interpretation of peak metamorphic temperatures in light of garnet diffusion during cooling. Journal of Metamorphic Geology 9, 379–388. doi:10.1111/j.1525-1314.1991.tb00533.x
Spear, F.S., Selverstone, J., 1983. Quantitative P-T paths from zoned minerals: Theory and tectonic applications. Contributions to Mineralogy and Petrology 83, 348–357. doi:10.1007/BF00371203
Speranza, F., Villa, I.M., Sagnotti, L., Florindo, F., Cosentino, D., Cipollari, P., Mattei, M., 2002. Age of the Corsica–Sardinia rotation and Liguro–Provençal Basin spreading: new paleomagnetic and Ar/Ar evidence. Tectonophysics 347, 231–251.
Spooner, E., Chapman, H., Smewing, J., 1977. Strontium isotopic contamination and oxidation during ocean floor hydrothermal metamorphism of the ophiolitic rocks of the Troodos Massif, Cyprus. Geochimica et Cosmochimica Acta 41, 873879–877890.
Spooner, E.T.C., Fyfe, W.S., 1973. Sub-sea-floor metamorphism, heat and mass transfer. Contributions to Mineralogy and Petrology 42, 287–304. doi:10.1007/BF00372607
Staudigel, H., 2014. Chemical fluxes from hydrothermal alteration of the oceanic crust.
Staudigel, H., Hart, S.R., Schmincke, H.-U., Smith, B.M., 1989. Cretaceous ocean crust at DSDP Sites 417 and 418: Carbon uptake from weathering versus loss by magmatic outgassing. Geochimica et Cosmochimica Acta 53, 3091–3094.

Staudigel, H., Plank, T., White, B., Schmincke, H., 1996. Geochemical fluxes during seafloor alteration of the basaltic upper oceanic crust: DSDP Sites 417 and 418. Subduction top to bottom 19–38.

Stüwe, K., 1997. Effective bulk composition changes due to cooling: a model predicting complexities in retrograde reaction textures. Contributions to Mineralogy and Petrology 129, 43–52. doi:10.1007/s004100050322

Sun, S. -s., McDonough, W.F., 1989. Chemical and isotopic systematics of oceanic basalts: implications for mantle composition and processes. Geological Society, London, Special Publications 42, 313–345. doi:10.1144/GSL.SP.1989.042.01.19

Sutra, E., Manatschal, G., Mohn, G., Unternehr, P., 2013. Quantification and restoration of extensional deformation along the Western Iberia and Newfoundland rifted margins. Geochemistry, Geophysics, Geosystems 14, 2575–2597.

Sverjensky, D.A., Stagno, V., Huang, F., 2014. Important role for organic carbon in subduction-zone fluids in the deep carbon cycle. Nature Geoscience 7, 909.

Syracuse, E.M., van Keken, P.E., Abers, G.A., 2010. The global range of subduction zone thermal models. Physics of the Earth and Planetary Interiors 183, 73–90. doi:10.1016/j.pepi.2010.02.004

T

Tachikawa, K., Jeandel, C., Roy-Barman, M., 1999. A new approach to the Nd residence time in the ocean: the role of atmospheric inputs. Earth and Planetary Science Letters 170, 433–446.

Taetz, S., John, T., Bröcker, M., Spandler, C., 2016. Fluid–rock interaction and evolution of a high-pressure/low-temperature vein system in eclogite from New Caledonia: insights into intraslab fluid flow processes. Contributions to Mineralogy and Petrology 171, 90. doi:10.1007/s00410-016-1295-z

Taylor, H.P., 1977. Water/rock interactions and the origin of H_2O in granitic batholiths Thirtieth William Smith lecture. Journal of the Geological Society 133, 509–558.

Taylor, H.P., Coleman, R.G., 1968. O18/O16 ratios of coexisting minerals in glaucophane-bearing metamorphic rocks. Geological Society of America Bulletin 79, 1727–1756.

Tera, F., Brown, L., Morris, J., Sacks, I.S., Klein, J., Middleton, R., 1986. Sediment incorporation in island-arc magmas: Inferences from ^{10}Be. Geochimica et Cosmochimica Acta 50, 535–550. doi:10.1016/0016-7037(86)90103-1

Tian, M., Ague, J.J., 2014. The impact of porosity waves on crustal reaction progress and CO 2 mass transfer. Earth and Planetary Science Letters 390, 80–92.

Touret, J.L., 2001. Fluids in metamorphic rocks. Lithos 55, 1–25. doi:10.1016/S0024-4937(00)00036-0

Touret, J.L., Frezzotti, M.-L., 2003. Fluid inclusions in high pressure and ultrahigh pressure metamorphic rocks. Ultrahigh-pressure Metamorphism. European Mineralogical Union Notes in Mineralogy 5, 467–487.

Tracy, R.J., 1982. Compositional zoning and inclusions in metamorphic minerals. Reviews in Mineralogy and Geochemistry 10, 355–397.

Tracy, R.J., Robinson, P., Thompson, A.B., 1976. Garnet composition and zoning in the determination of temperature and pressure of metamorphism, central Massachusetts. American Mineralogist 61, 762–775.

Tsay, A., Zajacz, Z., Ulmer, P., Sanchez-Valle, C., 2017. Mobility of major and trace elements in the eclogite-fluid system and element fluxes upon slab dehydration. Geochimica et Cosmochimica Acta 198, 70–91.

Tsujimori, T., Ernst, W.G., 2014. Lawsonite blueschists and lawsonite eclogites as proxies for palaeo-subduction zone processes: a review. J. Meta. Geol. 32, 437–454. doi:10.1111/jmg.12057

Tsujimori, T., Sisson, V.B., Liou, J.G., Harlow, G.E., Sorensen, S.S., 2006. Very-low-temperature record of the subduction process: A review of worldwide lawsonite eclogites. Lithos 92, 609–624. doi:10.1016/j.lithos.2006.03.054

Tumiati, S., Fumagalli, P., Tiraboschi, C., Poli, S., 2012. An experimental study on COH-bearing peridotite up to 3· 2 GPa and implications for crust–mantle recycling. Journal of Petrology 54, 453–479.

U

Ulmer, P., Trommsdorff, V., 1995. Serpentine Stability to Mantle Depths and Subduction-Related Magmatism. Science 268, 858. doi:10.1126/science.268.5212.858

Urey, H.C., 1947. The thermodynamic properties of isotopic substances. Journal of the Chemical Society (Resumed) 562–581.

V

Valley, J.W., 2001. Stable isotope thermometry at high temperatures. Reviews in mineralogy and geochemistry 43, 365–413.

Van Achterbergh, E., Ryan, C., Jackson, S., Griffin, W., 2001. Data reduction software for LA-ICP-MS. Laser-Ablation-ICPMS in the earth sciences—principles and applications. Miner Assoc Can (short course series) 29, 239–243.

van Daalen, M., Heilbronner, R., Kunze, K., 1999. Orientation analysis of localized shear deformation in quartz fibres at the brittle–ductile transition. Tectonophysics 303, 83–107.

van der Straaten, F., Halama, R., John, T., Schenk, V., Hauff, F., Andersen, N., 2012. Tracing the effects of high-pressure metasomatic fluids and seawater alteration in blueschist-facies overprinted eclogites: Implications for subduction channel processes. Chemical Geology 292–293, 69–87. doi:10.1016/j.chemgeo.2011.11.008

Venturini, G., Martinotti, G., Armando, G., Barbero, M., Hunziker, J., 1994. The central Sesia Lanzo Zone (Western Italian Alps): new field observations and lithostratigraphic subdivisions. Schweizerische Mineralogische und Petrographische Mitteilungen 74, 115–125.

Vernié, P., Kienast, J.R., Mével, C., 1986. The occurrence of deerite in highly oxidizing conditions within the ‘schistes lustrés’of eastern Corsica. Journal of Metamorphic Geology 4, 385–399. doi:10.1111/j.1525-1314.1986.tb00359.x

Vernooij, M.G., den Brok, B., Kunze, K., 2006. Development of crystallographic preferred orientations by nucleation and growth of new grains in experimentally deformed quartz single crystals. Tectonophysics 427, 35–53.

Vitale Brovarone, A., Alard, O., Beyssac, O., Martin, L., Picatto, M., 2014a. Lawsonite metasomatism and trace element recycling in subduction zones. Journal of Metamorphic Geology 32, 489–514. doi:10.1111/jmg.12074

Vitale Brovarone, A., Beltrando, M., Malavieille, J., Giuntoli, F., Tondella, E., Groppo, C., Beyssac, O., Compagnoni, R., 2011a. Inherited Ocean–Continent Transition zones in deeply subducted terranes: Insights from Alpine Corsica. Lithos 124, 273–290. doi:10.1016/j.lithos.2011.02.013

Vitale Brovarone, A., Beyssac, O., 2014. Lawsonite metasomatism: A new route for water to the deep Earth. Earth and Planetary Science Letters 393, 275–284. doi:10.1016/j.epsl.2014.03.001

Vitale Brovarone, A., Beyssac, O., Malavieille, J., Molli, G., Beltrando, M., Compagnoni, R., 2013. Stacking and metamorphism of continuous segments of subducted lithosphere in a high-pressure wedge: The example of Alpine Corsica (France). Earth-Science Reviews 116, 35–56. doi:10.1016/j.earscirev.2012.10.003

Vitale Brovarone, A., Groppo, C., HetéNyi, G., Compagnoni, R., Malavieille, J., 2011b. Coexistence of lawsonite-bearing eclogite and blueschist: phase equilibria modelling of Alpine Corsica metabasalts and petrological evolution of subducting slabs. Journal of Metamorphic Geology 29, 583–600. doi:10.1111/j.1525-1314.2011.00931.x

Vitale Brovarone, A., Picatto, M., Beyssac, O., Lagabrielle, Y., Castelli, D., 2014b. The blueschist–eclogite transition in the Alpine chain: P–T paths and the role of slow-spreading extensional structures in the evolution of HP–LT mountain belts. Tectonophysics 615–616, 96–121. doi:10.1016/j.tecto.2014.01.001

Vitale Brovarone, A.V., Herwartz, D., 2013. Timing of HP metamorphism in the Schistes Lustrés of Alpine Corsica: New Lu–Hf garnet and lawsonite ages. Lithos 172, 175–191.

W

Walker, J.C., Hays, P., Kasting, J.F., 1981. A negative feedback mechanism for the long-term stabilization of Earth's surface temperature. Journal of Geophysical Research: Oceans 86, 9776–9782.

Walther, J., 1992. Ionic association in H_2O–CO_2 fluids at mid-crustal conditions. Journal of Metamorphic Geology 10, 789–797.

Walther, J.V., Schott, J., 1988. The dielectric constant approach to speciation and ion pairing at high temperature and pressure. Nature 332, 635–638.

Wang, Q., Rumble, D., 1999. Oxygen and carbon isotope composition from the UHP Shuanghe marbles, Dabie Mountains, China. Science in China Series D: Earth Sciences 42, 88–96.

White, J., White, S., 1981. On the structure of grain boundaries in tectonites. Tectonophysics 78, 613–628.

Wilson, C.R., Spiegelman, M., van Keken, P.E., Hacker, B.R., 2014. Fluid flow in subduction zones: The role of solid rheology and compaction pressure. Earth and Planetary Science Letters 401, 261–274. doi:10.1016/j.epsl.2014.05.052

Wood, R.M., 1979. The iron-rich blueschist facies minerals: I, Deerite. Mineral Mag 43, 251.

Workman, R.K., Hart, S.R., 2005. Major and trace element composition of the depleted MORB mantle (DMM). Earth and Planetary Science Letters 231, 53–72.

Wyllie, P.J., 1977. Peridotite–CO_2–H_2O, and carbonatitic liquids in the upper asthenosphere. Nature 266, 45–47.

Y

Yamato, P., Brun, J.-P., 2017. Metamorphic record of catastrophic pressure drops in subduction zones. Nature Geoscience 10, 46–50.

Yang, P., Rivers, T., 2001. Chromium and manganese zoning in pelitic garnet and kyanite: Spiral, overprint, and oscillatory (?) zoning patterns and the role of growth rate.

Journal of Metamorphic Geology 19, 455–474. doi:10.1046/j.0263-4929.2001.00323.x
Yardley, B.W., Lloyd, G.E., 1995. Why metasomatic fronts are really metasomatic sides. Geology 23, 53–56.
Yaxley, G.M., Brey, G.P., 2004. Phase relations of carbonate-bearing eclogite assemblages from 2.5 to 5.5 GPa: implications for petrogenesis of carbonatites. Contributions to Mineralogy and Petrology 146, 606–619.
Yaxley, G.M., Green, D.H., 1994. Experimental demonstration of refractory carbonate-bearing eclogite and siliceous melt in the subduction regime. Earth and Planetary Science Letters 128, 313–325.
Yui, T.-F., Rumble, D., Lo, C.-H., 1995. Unusually low δ18O ultra-high-pressure metamorphic rocks from the Sulu Terrain, eastern China. Geochimica et Cosmochimica Acta 59, 2859–2864.

Z

Zack, T., John, T., 2007. An evaluation of reactive fluid flow and trace element mobility in subducting slabs. Chemical Geology 239, 199–216. doi:10.1016/j.chemgeo.2006.10.020
Zeitler, P.K., Barreiro, B., Chamberlain, C.P., Rumble, D., 1990. Ion-microprobe dating of zircon from quartz-graphite veins at the Bristol, New Hampshire, metamorphic hot spot. Geology 18, 626–629.
Zhang, L., Chu, X., Zhang, L., Du, J., n.d. Phase equilibria modelling using major and trace element compositions of zoned garnet and clinopyroxene from southwestern Tianshan eclogites, China. Journal of Asian Earth Sciences. doi:10.1016/j.jseaes.2017.05.002
Zheng, Y.-F., 1993. Calculation of oxygen isotope fractionation in anhydrous silicate minerals. Geochimica et Cosmochimica Acta 57, 1079–1091. doi:10.1016/0016-7037(93)90042-U
Zheng, Y.-F., Fu, B., Gong, B., Li, L., 2003. Stable isotope geochemistry of ultrahigh pressure metamorphic rocks from the Dabie–Sulu orogen in China: implications for geodynamics and fluid regime. Earth-Science Reviews 62, 105–161.
Zucali, M., Spalla, M.I., 2011. Prograde lawsonite during the flow of continental crust in the Alpine subduction: Strain vs. metamorphism partitioning, a field-analysis approach to infer tectonometamorphic evolutions (Sesia-Lanzo Zone, Western Italian Alps). Journal of Structural Geology 33, 381–398.

Table 4.2: Whole rock composition of study samples (major and selected trace elements). Analyses below the lower detection limit are labeled "<d.l.". Values in wt.%.

Sample	COR13-32 reference calcschist	COR13-30a reference ophicarbonate	COR13-21b metasomatic marble	COR13-21d ultramafic sample	COR13-27e metasomatic marble	COR13-17c metasomatic marble	COR13-22c metasomatic marble	COR13-28c metasomatic marble	1COR12-20d marble layer Stage#2	1COR12-20d silicate layer Stage#1	COR13-29c marble layer Stage#2	COR13-29c silicate layer Stage#1
Corg	0,08	0,03	<d.l.	0,02	<d.l.	0,02	0,25	<d.l.	<d.l.	<d.l.	<d.l.	0,02
CO_2 total	32,54	23,25	32,51	11,69	27,36	33,7	23,45	18,68	38,3	5,64	36,32	2,87
H_2O+	0,59	3,23	0,6	2,9	0,57	0,76	0,32	3,33	0,51	0,88	1,71	6,06
SiO_2	23,20	20,50	16,44	36,54	31,47	12,46	28,11	24,95	6,34	47,88	7,18	43,19
Al_2O_3	1,78	1,56	2,13	3,81	2,37	1,82	5,08	8,38	1,57	8,19	4,81	15,31
Fe_2O_3	1,11	4,75	3,14	7,54	1,69	2,08	2,44	4,86	1,73	9,21	0,41	6,27
MnO	0,02	0,16	0,13	0,45	0,18	0,05	0,19	0,18	0,43	0,58	0,01	0,13
MgO	0,66	12,69	1,26	13,66	0,69	2,51	3,61	6,37	0,56	5,11	0,50	7,47
CaO	40,23	33,93	42,42	22,16	35,46	47,43	36,21	31,86	50,56	17,93	49,58	17,41
Na_2O	0,09	0,02	1,06	1,28	0,34	0,20	1,60	0,15	0,59	5,84	0,03	0,28
K_2O	0,45	0,00	0,44	0,03	0,81	0,00	0,09	0,10	0,08	0,03	0,02	0,13
TiO_2	0,12	0,06	0,09	0,13	0,11	0,10	0,13	0,33	0,10	0,14	0,14	0,64
P_2O_5	0,10	0,00	0,07	0,00	0,06	0,06	0,05	0,11	0,13	0,08	0,13	0,19
LOI	32,25	25,54	32,45	13,93	27,41	33,32	21,38	21,56	38,16	6,09	36,47	8,44
Total	100,00	99,20	99,61	99,53	100,58	100,01	98,88	98,85	100,24	101,08	99,27	99,45

Table 4.2 (continue)

Sample	COR13-32 reference calcschist	COR13-30a reference ophicarbonate	COR13-21b metasomatic marble	COR13-21d ultramafic sample	COR13-27e metasomatic marble	COR13-17c metasomatic marble	COR13-22c metasomatic marble	COR13-28c metasomatic marble	1COR12-20d marble layer Stage#2	1COR12-20d silicate level Stage#1	COR13-29c marble layer Stage#2	COR13-29c silicate layer Stage#1
Sb	31,27	0,00	51,84	5,29	0,83	3,00	5,31	1,45	0,00	7,77	1,34	3,20
Sn	5,66	3,09	6,85	6,56	2,12	1,29	4,56	4,31	3,08	5,63	2,68	3,23
Ti	737,39	779,35	353,71	125,90	1960,37	587,51	677,44	575,52	857,29	809,33	3842,80	0,00
V	15,15	42,17	31,90	74,73	16,25	14,65	27,01	72,11	15,82	122,80	33,01	113,00
Co	3,17	65,70	9,31	74,60	6,77	2,99	9,32	33,82	7,26	32,67	3,17	35,13
Ni	0,00	1042,00	53,21	1022,00	21,86	0,00	34,08	381,00	0,00	121,40	0,00	107,50
Cr	29,81	1625,00	22,39	2114,00	22,11	24,23	51,25	807,30	21,86	62,31	57,14	93,90
Sc	1,84	8,34	2,25	14,93	2,78	1,93	3,33	10,23	3,28	7,99	2,20	17,26
As	2,41	0,00	0,00	0,00	2,68	0,00	0,00	2,86	4,81	4,42	0,00	0,00
Cs	1,12	0,12	1,09	0,19	3,04	0,00	0,18	0,12	0,33	31,21	0,00	0,00
Rb	19,95	0,00	23,66	0,72	38,49	0,00	2,83	3,62	4,34	3,39	0,00	3,38
Sr	1134,00	362,90	265,80	97,98	219,30	1150,00	1820,00	601,20	1087,00	139,40	761,60	135,90
Y	9,32	3,00	10,99	5,70	11,75	6,69	16,73	19,81	24,90	15,84	20,57	39,92
Zr	48,79	2,33	21,96	14,32	20,14	22,12	45,67	61,57	23,40	9,22	26,59	109,80
Nb	2,01	0,00	1,74	0,59	2,01	1,97	3,45	5,69	1,71	2,52	2,35	10,24
Ba	43,54	3,36	41,37	3,85	91,06	2,36	17,07	14,04	7,47	6,99	2,15	8,66
La	6,10	0,60	9,30	0,74	9,35	5,42	15,58	20,79	15,49	5,92	17,39	34,81
Ce	11,51	0,49	13,01	0,92	14,57	8,65	24,29	34,30	17,57	9,45	31,95	64,57
Pr	1,71	0,13	2,24	0,25	2,22	1,30	3,40	4,99	3,85	1,53	4,76	8,69
Nd	6,94	0,67	8,96	1,29	8,79	5,15	12,99	19,56	16,04	6,57	19,71	33,84
Sm	1,49	0,21	1,80	0,42	1,82	1,03	2,59	3,89	3,27	1,61	4,22	7,18
Eu	0,32	0,10	0,41	0,13	0,40	0,59	0,51	0,99	0,74	0,36	1,18	1,91
Gd	1,37	0,27	1,71	0,53	1,68	0,99	2,36	3,41	3,08	1,50	3,89	6,33
Tb	0,21	0,05	0,25	0,10	0,26	0,15	0,37	0,52	0,48	0,26	0,56	0,98
Dy	1,35	0,38	1,51	0,71	1,60	0,96	2,29	3,06	3,14	1,90	3,27	6,10
Ho	0,29	0,09	0,32	0,17	0,36	0,21	0,49	0,64	0,73	0,49	0,65	1,32
Er	0,80	0,25	0,83	0,48	0,95	0,53	1,27	1,70	1,98	1,48	1,62	3,55
Tm	0,11	0,04	0,11	0,07	0,14	0,08	0,18	0,24	0,28	0,23	0,21	0,54
Yb	0,74	0,23	0,75	0,48	0,91	0,49	1,20	1,61	1,84	1,62	1,30	3,55
Lu	0,11	0,04	0,12	0,07	0,13	0,07	0,19	0,24	0,27	0,27	0,19	0,53
Hf	1,37	0,08	0,64	0,37	0,62	0,64	1,42	1,86	0,72	0,42	0,82	3,35
Ta	0,19	0,00	0,17	0,03	0,22	0,16	0,39	0,57	0,20	0,16	0,21	0,96
Pb	18,56	5,14	18,43	11,38	19,22	7,39	16,45	16,42	40,26	14,18	21,40	11,45
Th	1,45	0,00	1,90	0,10	2,29	1,54	4,20	4,97	2,33	0,90	3,19	9,93
U	0,91	0,09	0,76	0,46	0,69	1,37	1,12	1,18	0,60	0,73	0,95	2,34

Table 4.3: Stable isotopes analyses of calcite.Analyses made in duplicate.

	$\delta^{13}C$ PDB	$\delta^{18}O$ SMOW	sample notes
	Silicate-bearing marble sampled at Serpentinite/Metasediments (Permian or Mesozoic) contact		
1COR12-20d**	1,14	16,93	
A814	1,83	17,08	
1COR14-10b	2,50	14,34	
1COR14-10g	2,59	22,29	
1COR14-10i	1,35	13,13	
1COR14-11a	1,96	12,25	
1COR14-11d	1,13	17,69	
1COR14-12b	1,28	13,27	
1COR14-12b	2,19	10,24	vein
1COR14-6a	-0,20	16,47	
1COR14-6c	1,84	16,70	
1COR14-2b	1,42	19,44	
2COR14-4i	-0,90	10,69	vein
COR1317c	0,48	12,84	
COR13-17	-0,87	10,74	vein
1COR12-11N	-0,80	10,63	vein
1COR12-11P2	0,47	12,25	
1COR12-20d	1,14	16,83	
COR13-22a	2,32	17,92	
COR13-22b	1,90	13,48	
COR13-22c	4,03	14,31	
COR13-29c	0,17	10,70	
COR13-28d	1,67	14,04	
COR13-28c	0,06	11,89	
	Silicate-bearing marble sampled at continental sliver/Mesozoic metasediments contact		
COR13-27e*	0,32	21,59	vein
COR413-27e*	0,80	21,43	
COR13-27c	1,24	20,04	
COR13-21a	1,71	21,84	
COR13-21b*	0,60	19,50	
COR13-21d*	1,06	19,33	ultramafic sample
	Metacarbonate rocks far-removed from veins or lithological contacts		
1COR12-11Q	-0,20	20,48	calcschist
COR13-32	0,75	22,57	calcschist
COR13-30a	1,48	11,19	ophicarbonate

*=analysis non duplicated

**=analysis made in quadrupliacate

Table 4.4: Representative clinopyroxene analyses

	COR13-22c				COR13-22a	OF3597 clast in marble		1COR12-11N vein selvage	
	atoll-like core	atoll-like rim				core	rim	core	rim
SiO_2	51,88	56,40	53,57	56,06	53,70	53,30	52,44	52,56	54,94
TiO_2	0,05	0,11	0,00	0,12	0,04	0,03	0,00	0,03	0,05
Al_2O_3	0,23	10,81	0,43	12,15	1,91	0,68	0,89	0,43	8,37
Cr_2O_3	0,05	0,11	0,00	0,12	0,00	0,03	0,00	0,00	0,02
FeO	12,12	5,75	7,66	4,49	4,46	9,85	10,12	9,25	6,70
MnO	0,68	0,47	0,48	0,39	3,12	0,24	0,23	0,48	0,25
MgO	10,49	7,53	13,08	6,67	12,11	11,89	11,52	12,03	8,26
CaO	24,93	13,93	26,20	13,84	22,94	23,27	23,03	24,53	15,72
Na_2O	0,31	7,72	0,22	7,78	1,55	0,48	0,77	0,51	5,82
K_2O	0,00	0,00	0,00	0,00	0,00	0,02	0,00	0,00	0,00
Total	100,69	102,71	101,65	101,57	99,83	99,76	99,04	99,82	100,12
No. Ox.	6	6	6	6	6	6	6	6	6
Structural formula									
Si	1,96	1,95	1,97	1,96	1,99	2,01	1,99	1,98	1,98
Ti	0,00	0,00	0,00	0,00	0,00	0,00	0,00	0,00	0,00
Al	0,05	0,11	0,00	0,12	0,04	0,03	0,00	0,00	11,89
Cr	0,00	0,00	0,00	0,00	0,00	0,00	0,00	0,00	0,00
Fe	10,49	7,53	13,08	6,67	12,11	11,89	11,52	0,00	0,01
Mn	0,02	0,01	0,01	0,01	0,10	0,01	0,01	0,02	0,01
Mg	0,59	0,39	0,72	0,35	0,67	0,67	0,65	0,67	0,44
Ca	1,01	0,52	1,03	0,52	0,91	0,94	0,94	0,99	0,61
Na	0,02	0,52	0,02	0,53	0,11	0,04	0,06	0,04	0,41
K	0,00	0,00	0,00	0,00	0,00	0,00	0,00	0,00	0,00
$X_{QUAD\%}$	96,58	44,69	97,66	44,35	78,60	96,52	93,00	96,51	57,67
$X_{Ae\%}$	3,42	16,00	2,34	9,66	14,16	0,45	4,21	3,49	8,99
$X_{Jd\%}$	0,00	39,31	0,00	45,99	7,24	3,03	2,80	0,00	33,35

Table 4.5: Representative garnet analyses

Sample	**1COR12-20d**					**COR13-22a**	**COR13-22c**
	rim	core	rim	skeletal	skeletal	anhedral	vein
SiO_2	37,35	37,69	36,97	37,63	37,34	38,18	39,94
TiO_2	0,27	0,23	0,14	0,07	1,85	0,20	0,57
$Al2O_3$	20,40	19,96	20,42	20,13	12,76	21,36	21,65
FeO	13,53	22,46	13,56	25,17	11,45	9,40	1,82
MnO	20,80	9,86	21,01	8,58	1,79	19,76	0,55
MgO	0,12	0,57	0,11	0,54	0,00	0,90	0,00
CaO	7,79	9,38	8,07	8,91	33,95	10,73	34,57
Na_2O	0,01	0,02	0,03	0,01	0,02	-	0,00
K_2O	0,01	0,01	0,00	0,01	0,01	-	0,00
Cr_2O_3	0,02	0,01	0,00	0,02	0,06	0,00	0,02
Total	100,71	99,76	100,85	101,08	99,22	100,52	99,12
No. Ox.	12	12	12	12	12	12	12
Structural formula							
Si	3,02	3,01	3,03	3,01	2,96	3,01	3,03
Al tot	1,92	1,94	1,91	1,90	1,22	1,99	1,94
Ti	0,01	0,02	0,02	0,00	0,11	0,01	0,03
Cr	0,00	0,00	0,00	0,00	0,00	0,00	0,00
Fe tot	0,94	0,91	0,68	1,68	0,76	0,64	0,12
Mn	1,35	1,42	1,42	0,58	0,12	1,32	0,04
Mg	0,01	0,01	0,01	0,06	0,00	0,11	0,00
Ca	0,73	0,67	0,91	0,76	2,88	0,91	2,81
Total	7,99	8,90	8,66	8,01	8,82	8,62	7,97
X_{Alm}	29,59	29,07	20,21	55,73	0,00	22,89	2,07
X_{Sps}	47,12	49,10	49,69	20,90	4,46	46,19	1,21
X_{Gr}	23,30	21,83	30,10	23,37	61,77	30,92	96,72
X_{Adr}	-	-	-	-	33,77	-	-

Table 4.6: Representative amphibole, lawsonite, phengite, epidote, pumpellyite analyses

Mineral	**Amphibole**				**Lawsonite**		**Phengite**		**Epidote**		**Pumpellyite**
Sample	**COR13-21b**		**COR13-27e**		**COR13-29c**	**OF3597**	**COR13-22c**		**COR13-22c**		**COR13-28c**
	core	rim	core	rim	Cr-rich	Ti-rich					
SiO_2	55,05	55,52	55,14	57,39	38,44	38,57	54,68	51,37	39,35	39,40	37,41
TiO_2	0,02	0,00	0,04	0,00	0,87	0,66	0,16	0,13	0,09	0,03	0,08
Al_2O_3	7,01	6,90	4,21	6,38	28,86	32,16	23,12	25,43	30,16	29,50	26,24
FeO	21,37	21,45	25,28	16,07	0,37	0,63	1,03	3,21	3,52	3,47	3,97
MnO	0,20	0,14	0,17	0,21	0,00	0,00	0,01	0,10	0,15	0,15	0,54
MgO	6,25	5,84	5,22	9,35	0,00	0,00	6,01	5,09	0,00	0,51	2,77
CaO	0,44	0,46	0,17	1,06	16,92	17,17	0,00	0,45	25,79	25,62	22,66
Na_2O	7,15	7,08	6,77	6,48	0,03	0,00	0,07	0,09	0,02	0,06	0,07
K_2O	0,04	0,04	0,00	0,04	0,02	0,00	13,04	12,22	0,01	0,01	0,00
Cr_2O_3	0,00	0,04	0,00	0,00	4,28	0,00	-	-	-	-	0,03
Total	97,54	97,47	97,00	96,98	89,79	89,20	98,15	98,11	99,12	98,76	93,78
No. Ox.	23	23	23	23	8	8	14	14	12,5	12,5	24
Structural formula											
Si	7,89	7,98	8,04	8,07	2,01	2,00	3,57	3,39	2,99	3,01	6,09
Al iv	0,11	0,02	0,00	0,00	-	-	-	-	-	-	-
Altot	1,18	1,17	0,72	1,06	1,78	1,97	1,78	1,98	0,01	0,00	5,03
Al vi	1,07	1,15	0,72	1,06	-	-	-	-	-	-	-
Ti	0,00	0,00	0,00	0,00	0,03	0,03	0,01	0,01	0,01	0,00	0,01
Cr	0,00	0,00	0,00	0,00	0,18	0,00	-	-	-	-	0,00
Fe3+	0,90	0,74	1,23	0,72	0,00	0,00	0,00	0,00	0,22	0,22	0,00
Fe2+	1,66	1,84	1,85	1,17	0,02	0,03	0,06	0,18	-	-	0,54
Mn	0,02	0,02	0,02	0,03	0,00	0,00	0,00	0,01	0,01	0,01	0,07
Mg	1,34	1,25	1,13	1,96	0,00	0,00	0,58	0,50	0,00	0,06	0,67
Ca	0,07	0,07	0,03	0,16	0,95	0,96	0,00	0,03	2,10	2,10	3,95
Na	1,99	1,97	1,91	1,77	0,00	0,00	0,01	0,01	0,00	0,01	0,02
OH*	2,00	2,00	2,00	2,00	-	-	-	-	-	-	-
K	-	-	-	-	0,00	0,00	1,08	1,03	0,00	0,00	0,00

Table 5.2: mineral occurrences in analyzed thin sections. Mineral modal volumes percentages are estimated by optical microscopy with the support of the chart for modal volume percentage (Terry and Chilinger, 1955). Lawsonite occurring as pseudomorph is labeled *psm*.

THIN SECTION	Cc	Qtz	Grt	Lws	Cpx	Gln	Act	Ph	Ep	Chl	Accessories
Continental crust-metasediments											
cor13-21b	65%	10%	<5%		10%	<5%		5%			Ep (Aln core), Spn, Rt, Chl, CM, Py
cor13-27e	60%	10%	5%	psm		10%		10%			Ep, Chl, Tour, Zrn, CM
cor13-21c	10%						35%	<5%		45%	opaques, CM
cor13-21d	30%				10%		40%			20%	Spn, opaques CM
cor13-27a	25%		<5%	psm		10%		35%		30%	Spn, Ap, Py
cor13-27c	60%					15%			5%	15%	Qtz, Ph, Ap, Tour, Spn
Vein material											
OF3597	40%			25%	35%						Spn, Rt, Py, CM
2cor14-3b vein	80%				20%						
2cor14-3b selvage				15%	80%			10%			
2cor14-3b wallrock				40%	55%			<5%			
1cor14-RM	40%			35%	25%						CM; Spn
cor13-29c	70%			20%			5%				Rt, Qtz, Spn, Chl
Serpentinite-continental crust											
cor13-22a	65%		<5%	10%	20%						Ap, Wm, Chl, opaques
cor13-22c	55%		5%	<5%	30%			5%			Ep, Spn, Rt, Chl, CM, Zr, opaques
cor13-22d	40%	15%	5%	<5%	30%						Ap, CM, opaques
1cor14-10g	80%				10%			20%			Ab
Serpentinite-Mesozoic metasediments											
1cor12-20d	65%		10%		20%			<5%			Ab, Qtz, Ep (All core), CM
cor13-28a	45%	45%	<5%		<5%	<5%		<5%			Ep (All)
cor13-28c	55%		<5%	<5%			25%			<5%	Pmp 5%, Ep, Spn, Rt, Ap,Py, Wm, Zr, opaques
1cor14-12b	70%		5%		20%			<5%			Qtz, Chl, CM, Lws
1cor14-6a	25%	10%	10%		20%	15%			10%		Hem, Deer
Loose block											
1cor14-2b A	30%	30%	10%			15%			15%		All
1cor14-2b B	<5%		5%	10%	65%	15%					CM
1cor14-2c	5%		15%	30%	45%	5%					CM
Metasomatic rocks with no carbonates											
1cor12-11P				40%	55%						CM
1cor12-11L				40%	50%					10%	CM
Unaltered rcocks											
cor13-30a	50%				10%					35%	opaques
1cor12-11q	40%	40%		psm				14%		5%	CM, opaques
cor13-32	70%	20%		psm				5%		5%	CM, opaques
1cor14-5	40%	30%							5%		Zr, Hem, opaques
1cor12-20c	35%	35%	<5%			<5%		15%	5%	5%	Ap, opaques
cor16-42d		40%	15%			20%		25%			Ep, All, Ap
1cor14-10d		5%	10%	25%		40%		15%			Chl, Sph, opaques

Table 5.3: Representative clinopyrxene analyses.

Sample	1cor14-10g		cor13-22c			1cor14-12b	OF3597		1cor12-11N		cor13-21d		cor13-21b		1cor14-6a	
	Jadeite	Jadeite	Cpx2-rim	Cpx1-core	Cpx2	Cpx2	Cpx1	Cpx1	Cpx2	Cpx2	Cpx2-rim	Cpx1-core	Cpx2	Cpx2	Cpx2	Cpx2
SiO_2	58,71	58,72	56,40	51,88	56,06	51,04	53,72	53,30	54,94	55,56	54,43	50,90	55,19	54,21	52,72	51,53
TiO_2	0,71	0,81	0,11	0,05	0,12	0,00	0,02	0,03	0,05	0,10	0,00	0,82	0,12	0,20	0,04	0,06
Al_2O_3	24,25	23,67	10,81	0,23	12,15	3,85	0,96	0,68	8,37	10,59	1,99	5,18	5,47	4,70	1,32	1,25
Cr_2O_3	0,02	0,00	0,11	0,05	0,12	0,00	0,00	0,03	0,02	0,04	0,59	1,06	0,01	0,04	0,01	0,01
FeO	0,94	1,25	5,75	12,12	4,49	18,80	10,06	9,85	6,70	5,46	12,57	2,94	15,44	15,20	16,70	17,03
MnO	0,05	0,06	0,47	0,68	0,39	2,00	0,19	0,24	0,25	0,23	0,08	0,05	0,42	0,56	0,30	0,19
MgO	0,19	0,14	7,53	10,49	6,67	3,35	11,40	11,89	8,26	7,53	9,83	15,82	5,25	5,32	8,03	8,52
CaO	0,06	0,11	13,93	24,93	13,84	18,20	23,54	23,27	15,72	13,29	13,88	22,87	10,77	11,39	13,65	16,00
Na_2O	15,79	15,93	7,72	0,31	7,78	3,44	0,80	0,48	5,82	7,25	6,34	0,77	8,03	7,69	6,54	5,19
K_2O	0,00	0,01	0,00	0,00	0,00	0,00	0,01	0,02	0,00	0,02	0,00	0,00	0,02	0,03	0,01	0,01
Total	100,73	100,71	102,71	100,69	101,57	100,69	100,70	99,76	100,12	100,06	99,70	100,41	100,71	99,34	99,33	99,79
No. Ox.	6	6	6	6	6	6	6	6	6	6	6	6	6	6	6	6
Structural formula																
Si	1,96	1,96	1,95	1,96	1,96	1,96	2,00	2,01	1,98	1,98	1,99	1,84	2,01	2,00	1,96	1,92
Ti	0,02	0,02	0,00	0,00	0,00	0,00	0,00	0,00	0,00	0,00	0,00	0,02	0,00	0,01	0,00	0,00
Al	0,96	0,93	0,11	0,05	0,12	0,17	0,02	0,03	0,36	0,44	0,09	0,22	0,23	0,20	0,06	0,05
Cr	0,00	0,00	0,00	0,00	0,00	0,00	0,00	0,00	0,00	0,00	0,02	0,03	0,00	0,00	0,00	0,00
Fe	0,03	0,03	7,53	10,49	6,67	0,60	11,40	11,89	0,20	0,16	0,38	0,09	0,47	0,47	0,52	0,53
Mn	0,00	0,00	0,01	0,02	0,01	0,07	0,01	0,01	0,01	0,01	0,00	0,00	0,01	0,02	0,01	0,01
Mg	0,01	0,01	0,39	0,59	0,35	0,19	0,63	0,67	0,44	0,40	0,53	0,85	0,28	0,29	0,44	0,47
Ca	0,00	0,00	0,52	1,01	0,52	0,75	0,94	0,94	0,61	0,51	0,54	0,89	0,42	0,45	0,54	0,64
Na	1,02	1,03	0,52	0,02	0,53	0,26	0,06	0,04	0,41	0,50	0,45	0,05	0,57	0,55	0,47	0,38
K	0,00	0,00	0,00	0,00	0,00	0,00	0,00	0,00	0,00	0,00	0,00	0,00	0,00	0,00	0,00	0,00
X_{QUAD}	0,6	0,5	44,69	96,58	44,35	73,0	94,05	96,52	58,82	49,23	54,80	94,22	42,83	43,72	51,63	60,81
X_{Ae}	10,4	12,6	16,00	3,42	9,66	14,8	1,73	0,45	8,88	9,57	37,98	3,13	33,58	35,67	47,14	35,15
X_{Jd}	89,1	86,9	39,31	0,00	45,99	12,2	4,22	3,03	32,24	41,08	7,23	2,65	23,59	20,61	1,23	4,03

Table 5.3 (continue): Representative garnet analyses

Sample	1COR12-20d		COR13-22a	COR13-22c	1cor14-6a					1cor14-12b				cor13-21b	cor13-27e	1cor14-10d	
	core	rim		vein	core	mantle	rim	/ergrowing	epido	Gt1	Gt1	Gt2	Gt2			core	rim
SiO_2	37,69	37,35	38,18	39,94	36,97	37,58	37,07	37,72	38,00	36,07	36,51	38,14	37,97	37,52	36,67	36,54	37,19
TiO_2	0,23	0,27	0,20	0,57	0,01	0,01	0,08	0,09	0,18	0,45	0,39	0,21	0,20	0,10	0,16	0,08	0,09
$Al2O_3$	19,96	20,40	21,36	21,65	18,95	19,54	19,57	20,48	20,68	19,43	18,95	19,80	19,51	20,32	20,11	21,12	21,04
FeO	22,46	13,53	9,40	1,82	17,01	29,62	20,69	27,95	27,84	10,75	10,44	13,24	9,51	9,89	22,89	27,12	22,96
MnO	9,86	20,80	19,76	0,55	17,16	2,39	11,45	1,19	1,07	23,91	23,79	7,09	9,35	22,86	11,48	8,01	12,30
MgO	0,57	0,12	0,90	0,00	0,41	0,53	0,56	0,51	0,52	0,02	0,01	0,08	0,02	0,54	0,41	2,51	0,44
CaO	9,38	7,79	10,73	34,57	9,63	10,51	11,27	12,29	12,81	8,44	9,10	21,17	22,65	8,97	7,97	3,57	6,75
Na_2O	0,02	0,01	-	0,00	0,00	0,03	0,00	0,04	0,01	0,00	0,02	0,02	0,00	0,03	0,00	0,01	0,03
K_2O	0,01	0,01	-	0,00	0,00	0,00	0,00	0,00	0,02	0,01	0,00	0,00	0,00	0,01	0,00	0,00	0,00
Cr_2O_3	0,01	0,02	0,00	0,02	0,09	0,11	0,06	0,12	0,00	0,03	0,00	0,00	0,00	0,02	0,01	0,06	0,00
Total	99,76	100,71	100,52	99,12	100,28	100,31	100,79	100,43	101,18	99,12	99,22	99,76	99,21	100,26	99,70	99,02	100,80
No. Ox.	12	12	12	12	12	12	12	12	12	12	12	12	12	12	12	12	12
Structural																	
Si	3,01	3,02	3,01	3,03	2,99	3,02	2,97	3,01	3,00	2,96	2,99	3,01	3,00	3,01	2,98	2,97	2,99
Al tot	1,94	1,92	1,99	1,94	1,82	1,86	1,86	1,93	1,93	1,89	1,84	1,85	1,83	1,93	1,93	2,02	2,00
Ti	0,02	0,01	0,01	0,03	0,00	0,00	0,00	0,01	0,01	0,03	0,02	0,01	0,01	0,01	0,01	0,00	0,01
Cr	0,00	0,00	0,00	0,00	0,01	0,01	0,00	0,01	0,00	0,00	0,00	0,00	0,00	0,00	0,00	0,00	0,00
Fe tot	0,91	0,94	0,64	0,12	1,15	1,99	1,39	1,86	1,84	0,74	0,71	0,87	0,63	0,66	1,56	1,85	1,54
Mn	1,42	1,35	1,32	0,04	1,18	0,16	0,78	0,08	0,07	1,66	1,65	0,47	0,63	1,55	0,79	0,55	0,84
Mg	0,01	0,01	0,11	0,00	0,05	0,06	0,07	0,06	0,06	0,00	0,00	0,01	0,00	0,06	0,05	0,30	0,05
Ca	0,67	0,73	0,91	2,81	0,84	0,91	0,97	1,05	1,08	0,74	0,80	1,79	1,92	0,77	0,69	0,31	0,58
Total	8,90	7,99	8,62	7,97	8,03	8,01	9,42	8,00	9,84	8,02	8,73	8,01	8,65	8,00	8,02	8,01	8,00
X_{Alm}	29,07	29,59	22,89	2,07	31,01	63,07	39,99	61,36	60,18	18,69	16,62	22,68	13,23	19,63	49,34	60,84	50,95
X_{Sps}	49,10	47,12	46,19	1,21	40,52	5,68	26,82	2,77	2,47	56,20	56,17	16,18	21,35	53,75	26,98	18,60	28,11
X_{Gr}	21,83	23,30	30,92	96,72	20,16	26,00	25,78	33,45	34,73	19,63	20,53	55,13	58,29	24,12	20,27	10,29	19,17
X_{Adr}	-	-	-	-	8,30	5,25	7,41	2,41	2,62	5,47	6,68	6,01	7,13	2,50	3,42	-	-
X_{Py}	-	-	-	-	-	-	-	-	-	-	-	-	-	-	-	10,26	1,77

Table 5.3 (continue): Representative amphibole, epidote, lawsonite, phengite, pumpellyite, deerite, hematite analyses

Mineral	**Amphibole**								**Epidote**					**Lawsonite**		**Phengite**			**Pumpellyite**	**Deerite**		**Hematite**	
Sample	**cor13-21b**		**cor13-27e**		**cor13-29c**	**1cor14-6a**		**cor13-21d**	**1cor12-20d**	**cor13-28c**		**1cor14-6a**		**cor13-29c**	**OF3597**	**cor13-22c**	**1cor14-10g**	**1cor12-20d**	**cor13-28c**	**1cor14-6a**		**1cor14-6a**	
	core	rim	core	rim										Cr-rich	Ti-rich	Phg1				in qtz	in cc		
SiO_2	55,05	55,52	55,14	57,39	56,37	55,21	55,46	55,67	37,88	37,38	37,04	37,58	36,97	38,18	38,17	54,68	54,35	53,39	37,41	34,16	34,33	0,00	0,01
TiO_2	0,02	0,00	0,04	0,00	0,00	0,00	0,07	0,00	0,50	0,15	0,23	0,08	0,12	1,19	0,78	0,16	0,25	0,30	0,08	1,41	3,55	0,19	0,26
Al_2O_3	7,01	6,90	4,21	6,38	0,63	2,27	1,96	0,43	20,46	19,62	19,52	21,54	19,88	29,44	32,31	23,12	23,06	21,83	26,24	0,11	0,17	0,05	0,01
FeO	21,37	21,45	25,28	16,07	10,73	21,52	20,96	7,74	12,69	14,54	13,54	15,15	14,33	0,24	0,65	1,03	2,39	4,91	3,97	50,86	51,28	89,73	89,01
MnO	0,20	0,14	0,17	0,21	0,33	0,29	0,44	0,93	10,78	21,52	20,26	0,66	0,67	0,00	0,04	0,01	0,11	0,09	0,54	2,96	1,29	0,03	0,03
MgO	6,25	5,84	5,22	9,35	17,44	9,33	9,67	19,19	0,00	0,07	0,14	0,00	0,00	0,00	0,00	6,01	4,71	4,04	2,77	1,91	1,59	0,10	0,08
CaO	0,44	0,46	0,17	1,06	12,65	0,93	1,36	11,44	16,81	7,89	8,36	21,95	22,02	16,93	17,46	0,00	0,03	0,15	22,66	0,02	1,34	0,00	0,01
Na_2O	7,15	7,08	6,77	6,48	0,40	6,73	6,58	0,85	0,02	0,00	0,02	0,00	0,00	0,00	0,01	0,07	0,03	0,10	0,07	0,03	0,05	0,00	0,04
K_2O	0,04	0,04	0,00	0,04	0,07	0,02	0,00	0,05	0,00	0,01	0,01	0,00	0,01	0,00	0,01	13,04	11,56	10,37	0,00	0,00	0,01	0,02	0,01
Cr_2O_3	0,00	0,04	0,00	0,00	0,00	0,00	0,00	0,15	0,02	0,00	0,00	0,02	2,01	3,25	0,00	-	-	-	0,03	0,49	0,09	0,03	0,08
Total	97,54	97,47	97,00	96,98	98,61	96,43	96,59	96,45	99,17	101,19	99,13	97,01	96,03	89,24	89,44	98,15	96,53	95,17	93,78	92,54	94,17	90,17	89,55
No. Ox.	23	23	23	23	23	23	23	23	12.5	12.5	12.5	12.5	12.5	8	8	11	11	11	13.5	22.5	22.5	3	3
Structural formula																							
Si	7,89	7,98	8,04	8,07	7,93	7,97	7,99	7,86	3,15	3,14	3,16	3,04	3,04	2,00	1,98	3,57	3,59	3,61	3,29	6,19	6,07	0,00	0,00
Al iv	0,11	0,02	0,00	0,00	0,07	0,03	0,01	0,07	-	-	-			-	-	-	-	-	-	-	-	-	-
Altot	1,18	1,17	0,72	1,06	0,11	0,39	0,33	0,07	2,00	1,94	1,96	2,05	1,93	1,82	1,98	1,78	1,80	1,74	2,72	0,02	0,04	0,00	0,00
Al vi	1,07	1,15	0,72	1,06	0,04	0,35	0,33	0,00	-	-	-			-	-	-	-	-	-	-	-	-	-
Ti	0,00	0,00	0,00	0,00	0,00	0,00	0,01	0,00	0,03	1,94	1,96	0,00	0,01	0,05	0,03	0,01	0,01	0,02	0,01	0,19	0,47	0,00	0,00
Cr	0,00	0,00	0,00	0,00	0,00	0,00	0,00	0,02	0,00	0,00	0,00	0,00	0,13	0,13	0,00	-	-	-	0,00	0,07	0,01	0,00	0,00
Fe3+	0,90	0,74	1,23	0,72	0,09	1,52	1,41	0,47	0,00	0,00	0,00	0,92	0,89	0,00	0,00	0,00	0,00	0,00	0,00	2,36	2,32	1,99	1,99
Fe2+	1,66	1,84	1,85	1,17	1,17	1,08	1,12	0,39	0,88	1,02	0,97	0,05	0,05	0,01	0,03	0,06	0,13	0,28	0,29	5,09	5,00	0,00	0,00
Mn	0,02	0,02	0,02	0,03	0,04	0,04	0,05	0,06	0,76	1,53	1,46	0,05	0,05	0,00	0,00	0,00	0,01	0,01	0,04	0,45	0,19	0,00	0,00
Mg	1,34	1,25	1,13	1,96	3,66	2,01	2,08	4,13	0,00	0,01	0,02	0,00	0,00	0,00	0,00	0,58	0,46	0,41	0,36	0,52	0,42	0,00	0,00
Ca	0,07	0,07	0,03	0,16	1,91	0,14	0,21	1,73	1,50	0,71	0,76	1,90	1,94	0,95	0,97	0,00	0,00	0,01	2,13	0,00	0,25	0,00	0,00
Na	1,99	1,97	1,91	1,77	0,11	1,88	1,84	0,26	0,00	0,00	0,00	0,00	0,00	0,00	0,00	0,01	0,00	0,01	0,01	0,01	0,02	0,00	0,00
OH*	2,00	2,00	2,00	2,00	2,00	2,00	2,00	2,00	-	-	-	-	-	-	-	-	-	-	-	-	-	-	-
K	-	-	-	-	-	-	-	-	-	-	-	-	-	0,00	0,00	1,08	0,97	0,89	0,00	0,00	0,00	0,00	0,00

Table 6.1 Major and trace element composition of the study samples. Major element are given in weight percent (wt.%), whereas trace elements are in part per million (ppm).

	Locality	*Col di Prato*						*Loriani*										*Pta Caldane*	*Mt Muffraje*	*Aja Rossa*	
Elements	*Sample*	cor16-63a	cor16-63b	cor16-63d	cor16-63f	cor16-63g	cor16-63c	cor16-42d	Lor16-6	Lor16-7	Lor16-1	cor16-4A	cor16-2	cor16-4B	1cor14-12b	cor16-42e	Lor16-5	cor13-32	cor13-22c	cor13-17c	OF3598
*Major el. [wt.%]**		calcschists		Stage#1	Stage#2			metachert	calcschists		Stage#1		Stage#2				serpentinite	calcschists	Stage#2		Stage#1
SiO_2		72,50	19,80	61,30	24,90	8,10	10,60	88,90	29,10	24,50	42,30	37,70	9,16	13,70	11,90	19,30	42,40	23,20	28,11	12,46	45,30
Al_2O_3		1,04	1,20	13,00	5,18	1,54	2,63	2,31	1,92	2,31	13,00	21,00	2,71	8,32	2,29	1,73	2,91	1,78	5,08	1,82	15,11
Fe_2O_3		1,38	2,10	6,76	3,22	1,61	0,50	2,38	1,06	1,88	7,53	7,43	2,08	2,63	4,24	12,40	8,08	1,11	2,44	2,08	5,03
MgO		0,20	0,46	2,49	1,41	0,67	0,27	0,66	0,57	0,73	6,42	2,45	0,85	0,78	0,96	0,43	34,90	0,66	3,61	2,51	6,95
CaO		14,50	42,60	6,43	36,10	50,00	48,00	2,64	37,40	39,00	23,10	23,50	49,10	44,30	46,60	35,40	0,69	40,23	36,21	47,43	20,62
K_2O		0,28	0,27	0,02	<0,01	<0,01	<0,01	0,69	0,37	0,33	<0,01	0,02	0,03	<0,01	0,08	0,03	<0,01	0,45	0,09	0,00	0,01
Na_2O		0,06	0,27	8,27	3,47	0,90	1,51	0,45	0,16	0,17	0,40	0,22	0,21	0,07	0,48	2,39	<0,01	0,09	1,60	0,20	0,47
TiO_2		0,04	0,03	0,24	0,18	0,06	0,04	0,09	0,08	0,09	0,72	0,81	0,09	0,39	0,08	0,04	0,12	0,12	0,09	0,10	0,65
MnO		0,30	0,28	0,36	0,44	0,36	0,12	0,50	0,13	0,14	0,22	0,14	0,30	0,06	0,63	1,67	0,08	0,02	0,13	0,05	0,11
P_2O_5		0,04	0,05	0,10	0,07	0,04	0,03	0,07	0,04	0,08	0,11	0,11	0,03	0,10	0,09	0,04	0,01	0,10	0,05	0,06	0,11
Cr_2O_3		0,01	<0,01	0,02	<0,01	<0,01	<0,01	<0,01	<0,01	<0,01	0,02	0,01	0,03	<0,01	0,01	<0,01	0,40	*0,004*	*0,007*	*0,004*	*0,01*
V_2O_5		<0,01	<0,01	0,02	<0,01	<0,01	<0,01	<0,01	<0,01	<0,01	0,04	0,03	<0,01	<0,01	<0,01	<0,01	0,01	--	--	--	--
LOI		11,30	33,60	1,78	25,80	37,20	36,60	2,58	30,00	31,60	7,60	7,91	35,90	30,30	33,80	27,40	11,60	32,25	21,38	33,32	5,57
Sum		101,60	100,70	100,80	100,80	100,50	100,40	101,30	100,80	100,80	101,40	101,40	100,50	100,70	101,20	100,80	101,20	100,02	98,79	100,01	99,94

Table 6.1 continue

	Locality	*Col di Prato*						*Loriani*										*Pta Caldane*	*Mt Muffraje*	*Aja Rossa*	
Elements	*Sample*	cor16-63a	cor16-63b	cor16-63d	cor16-63f	cor16-63g	cor16-63c	cor16-42d	Lor16-6	Lor16-7	Lor16-1	cor16-4A	cor16-2	cor16-4B	1cor14-12b	cor16-42e	Lor16-5	cor13-32	cor13-22c	cor13-17c	OF3598
Trace el. [ppm]		calcschists		Stage#1	Stage#2			metachert	calcschists		Stage#1		Stage#2				serpentinite	calcschists	Stage#2		Stage#1
Ba		<10	17,00	<10	<10	<10	<10	255,00	26,00	20,00	<10	<10	<10	<10	23,00	24,00	<10	43,54	17,07	2,36	2,48
Nb		<2	<2	7,00	2,00	<2	<2	2,00	<2	<2	14,00	15,00	<2	8,00	<2	<2	<2	2,01	3,45	1,97	10,55
Rb*		16,00	14,00	<2	<2	2,00	2,00	40,00	19,00	18,00	<2	2,00	2,00	3,00	6,00	<2	<2	--	--	--	--
Sr		43,00	105,00	14,00	547,00	643,00	346,00	19,00	511,00	570,00	59,00	489,00	360,00	687,00	532,00	119,00	11,00	1134,00	1820,00	1150,00	177,10
Y*		8,00	10,00	25,00	15,00	15,00	10,00	10,00	9,00	15,00	29,00	29,00	11,00	26,00	17,00	10,00	2,00	--	--	--	--
Zr*		24,00	24,00	69,00	29,00	22,00	14,00	71,00	28,00	29,00	136,00	159,00	28,00	83,00	30,00	24,00	6,00	--	--	--	--
Ag		<1	<1	<1	<1	<1	<1	<1	<1	<1	<1	<1	<1	<1	<1	<1	<1	--	--	--	--
Ce		8,50	8,40	43,00	11,30	11,40	8,30	15,70	13,30	16,70	101,00	83,80	8,70	49,20	13,60	6,50	0,90	11,51	24,29	8,65	57,55
Co		3,70	3,90	21,00	11,00	5,90	2,30	11,70	6,30	4,20	34,70	18,30	6,20	10,60	6,60	9,50	81,60	3,17	9,32	2,99	10,01
Cs		1,40	1,40	<0,1	0,10	<0,1	<0,1	2,60	1,10	0,90	0,10	<0,1	<0,1	<0,1	0,30	1,30	<0,1	1,12	0,18	0,00	<DL
Cr		--	--	--	--	--	--	--	--	--	--	--	--	--	--	--	--	29,81	51,25	24,23	96,65
Cu		7,00	12,00	133,00	7,00	8,00	30,00	233,00	16,00	24,00	147,00	21,00	7,00	81,00	19,00	32,00	<5	43,32	13,65	35,69	48,34
Dy		1,15	1,30	4,03	2,12	1,78	1,33	1,52	1,46	2,21	4,87	5,06	1,31	4,17	2,19	1,09	0,34	1,35	2,29	0,96	4,95
Er		0,67	0,77	2,16	1,22	1,09	0,79	0,84	0,75	1,25	2,89	2,96	0,86	2,24	1,25	0,70	0,25	0,80	1,27	0,53	2,64
Eu		0,21	0,27	0,91	0,44	0,34	0,24	0,40	0,35	0,56	1,81	1,37	0,26	0,98	0,50	0,18	<0,05	0,32	0,51	0,59	2,26
Ga		2,00	2,00	8,00	5,00	2,00	1,00	3,00	3,00	3,00	15,00	29,00	3,00	11,00	3,00	2,00	3,00	2,45	8,03	2,11	16,59
Gd		1,14	1,30	3,85	2,00	1,81	1,29	1,67	1,61	2,62	6,21	5,65	1,30	4,41	2,28	1,14	0,23	1,37	2,36	0,99	5,68
Hf		<1	2,00	2,00	1,00	<1	<1	2,00	<1	<1	4,00	4,00	<1	2,00	1,00	<1	<1	1,37	1,42	0,64	3,32
Ho		0,22	0,27	0,82	0,46	0,35	0,27	0,32	0,26	0,47	0,99	1,05	0,29	0,83	0,44	0,21	0,07	0,29	0,49	0,21	0,96
La		7,40	10,40	23,90	6,90	9,90	7,50	11,60	7,60	12,20	46,10	43,80	9,00	28,70	14,30	7,50	0,80	6,10	15,58	5,42	33,55
Lu		0,06	0,10	0,29	0,21	0,13	0,10	0,12	0,07	0,13	0,40	0,41	0,11	0,27	0,15	0,06	<0,05	0,11	0,19	0,07	0,38
Mo		<2	<2	<2	<2	<2	4,00	<2	<2	<2	<2	<2	<2	<2	<2	<2	<2	<0.5	<0.5	<0.5	<0.5
Nb		1,00	1,00	6,00	2,00	1,00	1,00	2,00	2,00	2,00	12,00	14,00	2,00	8,00	2,00	1,00	<1	2,01	3,45	1,97	10,55
Nd		6,70	7,50	23,30	8,40	7,10	6,40	10,30	8,30	12,80	41,70	39,50	7,10	26,40	11,80	6,10	0,60	6,94	12,99	5,15	29,48
Ni		19,00	21,00	317,00	47,00	28,00	18,00	36,00	41,00	22,00	118,00	69,00	49,00	36,00	36,00	54,00	1869,00	0,00	34,08	0,00	47,80
Pr		1,63	1,89	5,82	2,12	2,06	1,62	2,64	1,97	3,02	10,90	10,50	1,79	6,70	2,93	1,48	0,11	1,71	3,40	1,30	7,75
Rb		15,50	14,20	<0,2	<0,2	<0,2	<0,2	38,30	17,00	15,80	0,30	0,40	0,70	<0,2	3,90	0,90	<0,2	19,95	2,83	0,00	0,81
Sm		1,30	1,40	4,60	1,80	1,70	1,30	2,00	1,80	2,70	8,60	7,60	1,50	5,50	2,50	1,20	0,20	1,49	2,59	1,03	6,18
Sn		<1	<1	2,00	1,00	1,00	<1	<1	<1	<1	3,00	4,00	1,00	2,00	<1	<1	<1	5,66	4,56	1,29	3,33
Ta		<0,5	<0,5	<0,5	<0,5	<0,5	<0,5	<0,5	<0,5	<0,5	0,90	1,00	<0,5	0,50	<0,5	<0,5	<0,5	0,19	0,39	0,16	0,95
Tb		0,19	0,19	0,61	0,36	0,27	0,19	0,29	0,22	0,35	0,84	0,85	0,20	0,66	0,33	0,17	<0,05	0,21	0,37	0,15	0,85
Th		1,30	1,30	5,40	2,00	2,30	1,50	2,10	1,50	2,10	12,50	13,30	2,00	6,90	1,90	1,30	0,10	1,45	4,20	1,54	9,86
Tl		<0,5	<0,5	<0,5	<0,5	<0,5	<0,5	<0,5	<0,5	<0,5	<0,5	<0,5	<0,5	<0,5	<0,5	<0,5	<0,5	--	--	--	--
Tm		0,07	0,11	0,30	0,20	0,13	0,09	0,13	0,09	0,16	0,39	0,40	0,10	0,31	0,16	0,07	<0,05	0,11	0,18	0,08	0,39
U		0,39	0,57	1,08	0,79	0,64	0,49	0,55	0,57	0,73	2,81	2,58	0,49	1,83	0,49	0,61	<0,05	0,91	1,12	1,37	2,64
V		36,00	36,00	100,00	54,00	16,00	14,00	28,00	33,00	29,00	207,00	165,00	24,00	79,00	51,00	64,00	86,00	15,15	27,01	14,65	102,00
W		<1	<1	<1	<1	<1	<1	<1	<1	<1	<1	1,00	<1	<1	<1	<1	<1	0,33	0,00	0,00	<0,25
Y		8,00	11,30	22,80	14,60	14,10	10,50	9,70	8,80	14,70	27,90	27,00	10,80	24,10	15,90	9,20	2,10	9,32	16,73	6,69	30,08
Yb		0,50	0,70	2,00	1,30	1,00	0,60	0,70	0,60	1,00	2,60	2,70	0,70	2,00	1,10	0,60	0,30	0,74	1,20	0,49	2,52
Zr		23,00	24,50	63,80	31,40	28,00	15,00	68,90	32,10	30,40	144,00	158,00	24,70	83,40	29,10	24,50	8,60	48,79	45,67	22,12	122,90

*analysis by XRF method

Table 7.1: oxygen and carbon stable isotopes analyses of calcite

	Sample	$\delta^{13}C$ PDB	average	$\delta^{18}O$ SMOW	average
Col di Prato	1COR12-20d	1,22	1,14	16,79	16,83
	1COR12-20d	1,06		16,88	
	1COR12-20d	1,13	1,14	17,02	17,03
	1COR12-20d	1,14		17,03	
	A814	1,86	1,83	17,17	17,08
	A814	1,80		16,98	
Mt. Muffraje	1COR14-10b	2,50	2,50	14,33	14,34
	1COR14-10b	2,51		14,36	
	1COR14-10g	2,63	2,59	22,31	22,29
	1COR14-10g	2,55		22,27	
	1COR14-10i	1,33	1,35	13,07	13,13
	1COR14-10i	1,36		13,19	
	COR13-22a	2,41	2,32	17,84	17,92
	COR13-22a	2,23		17,99	
	COR13-22b	1,90	1,90	13,46	13,48
	COR13-22b	1,90		13,50	
	COR13-22c	4,14	4,03	14,38	14,31
	COR13-22c	3,92		14,23	
Loriani	1COR14-11a	1,95	1,96	12,26	12,25
	1COR14-11a	1,96		12,24	
	1COR14-11d	1,11	1,13	17,66	17,69
	1COR14-11d	1,14		17,72	
	1COR14-12b	1,32	1,28	13,30	13,27
	1COR14-12b	1,24		13,23	
	1COR14-12b (cc vein)	2,11	2,19	10,17	10,24
	1COR14-12b (cc vein)	2,27		10,31	
P.ta Favalta	1COR14-6a	-0,25	-0,20	16,55	16,47
	1COR14-6a	-0,15		16,38	
	1COR14-6c	1,83	1,84	16,71	16,70
	1COR14-6c	1,85		16,69	
	COR13-30a	1,52	1,48	11,12	11,19
	COR13-30a	1,43		11,26	
loose block	1COR14-2b	1,35	1,42	19,32	19,44
	1COR14-2b	1,49		19,55	
Aja rossa	2COR14-4i (cc+omph vein)	-0,94	-0,90	10,64	10,69
	2COR14-4i (cc+omph vein)	-0,87		10,75	
	COR13-17c (cc vein)	0,45	0,48	12,91	12,84
	COR13-17c (cc vein)	0,50		12,77	
	COR13-17 (cc vein)	-0,86	-0,87	10,76	10,74
	COR13-17c (cc vein)	-0,88		10,71	
	COR13-29c (cc+lws vein)	0,30	0,17	10,66	10,70
	COR13-29c (cc+lws vein)	0,05		10,75	
	COR13-28d	1,72	1,67	13,97	14,04
	COR13-28d	1,62		14,10	
	COR13-28c	0,10	0,06	11,94	11,89
	COR13-28c	0,02		11,84	
	1COR12-11N (cc+omph vein)	-0,72	-0,80	10,61	10,63
	1COR12-11N (cc+omph vein)	-0,88		10,65	
	1COR12-11P2 (cc vein)	0,51	0,47	12,25	12,25
	1COR12-11P2 (cc vein)	0,43		12,25	
Calcschists	1COR12-11q	-0,14	-0,20	20,49	20,48
	1COR12-11q	-0,27		20,47	
	COR13-32	0,75	0,75	22,52	22,57
	COR13-32	0,76		22,61	
P.ta Ventosa and P.ta Caldane	COR13-27e (cc vein)	0,32	0,32	21,59	21,59
	COR413-27e	0,80	0,80	21,43	21,43
	COR13-27c	1,24	1,24	20,04	20,04
	COR13-21a	1,75	1,71	21,91	21,84
	COR13-21a	1,67		21,77	
	COR13-21b	0,68	0,60	19,45	19,50
	COR13-21b	0,53		19,55	
	COR13-21d	1,06	1,06	19,33	19,33

Table 7.3.1: *trace element composition of selected samples for Sr and Nd isotopes analyses*

Sample name	*lithology*	Rb	Sr	Y	Zr	Nb	Cs	Ba	La	Ce	Pr	Nd	Sm	Eu	Gd	Tb	Dy	Ho	Er	Tm	Yb	Lu	Hf	Ta	Pb	Th	U
1cor12-11q	calcschists	36,96	653,22	18,06	10,30	3,72	2,37	97,77	10,93	18,72	2,47	9,95	2,09	0,52	2,23	0,38	2,61	0,59	1,72	0,23	1,31	0,16	0,31	0,24	7,30	2,70	0,55
cor13-32	calcschists	19,95	1134,00	9,32	48,79	2,01	1,12	43,54	6,10	11,51	1,71	6,94	1,49	0,32	1,37	0,21	1,35	0,29	0,80	0,11	0,74	0,11	1,37	0,19	18,56	1,45	0,91
cor16-42d	quartzite	40,00	19,00	10,00	71,00	2,00	2,60	255,00	11,60	15,70	2,64	10,30	2,00	0,40	1,67	0,29	1,52	0,32	0,84	0,13	0,70	0,12	2,00	0,50	--	2,10	0,55
cor13-16k	orthogneiss	145,99	82,24	75,38	7,18	18,60	2,93	227,18	27,10	66,73	7,41	30,15	7,74	0,34	7,15	1,36	9,02	1,48	4,74	1,03	4,61	0,61	0,12	1,65	10,61	18,76	1,13
cor13-14a	serpentinite	0,28	1,55	1,35	1,58	0,14	0,16	5,93	0,22	0,37	0,05	0,30	0,11	0,03	0,16	0,03	0,22	0,05	0,15	0,02	0,16	0,02	0,07	0,00	0,93	0,04	0,10
1cor12-11b	serpentinite	0,17	1,05	0,91	1,21	0,08	0,06	2,60	0,14	0,32	0,04	0,22	0,08	0,02	0,12	0,02	0,16	0,04	0,11	0,02	0,11	0,02	0,05	0,00	2,36	0,03	0,19
BIGORNO	carbonated peridotite	0,00	207,80	6,21	0,00	0,15	0,00	10,97	1,80	6,29	1,18	6,27	1,35	0,18	1,15	0,16	0,91	0,18	0,46	0,06	0,48	0,09	0,00	0,01	6,74	0,00	0,11
cor13-30a	ophicarbonate	0,00	362,90	3,00	2,33	0,00	0,12	3,36	0,60	0,49	0,13	0,67	0,21	0,10	0,27	0,05	0,38	0,09	0,25	0,04	0,23	0,04	0,08	0,00	5,14	0,00	0,09
cor13-23e	lawsonite+diopside	29,99	30,93	10,14	12,44	4,58	0,67	91,57	35,05	48,81	6,21	22,35	3,60	0,37	2,36	0,31	1,65	0,31	0,85	0,14	1,08	0,18	0,40	0,19	1,21	6,23	1,02
1cor12-11L	lawsonite+diopside	0,37	84,20	24,92	9,70	7,74	0,08	7,25	27,96	48,39	6,19	24,18	4,99	1,44	4,71	0,69	4,00	0,78	2,09	0,28	1,67	0,22	0,32	0,51	6,09	6,95	1,48
cor16-50	lawsonite+diopside	4,55	333,95	44,14	11,59	26,51	0,10	12,27	104,50	199,22	22,79	81,42	13,70	2,76	10,23	1,48	8,22	1,58	4,36	0,63	4,13	0,60	0,59	2,10	18,77	43,43	9,22
cor14-11a	carbonated metasomatic rock	0,22	192,22	9,25	2,56	0,94	0,04	6,49	5,80	4,87	1,24	5,39	1,13	0,24	1,22	0,18	1,06	0,22	0,59	0,08	0,51	0,08	0,08	0,07	27,70	0,88	0,22
cor14-11d	carbonated metasomatic rock	7,88	875,11	13,03	0,75	0,68	0,70	39,99	8,94	7,44	1,62	6,62	1,36	0,28	1,44	0,21	1,35	0,30	0,87	0,12	0,79	0,11	0,06	0,05	33,94	1,16	0,43
cor13-22a	carbonated metasomatic rock	0,24	921,57	13,52	4,97	2,43	0,01	5,62	15,94	19,77	2,68	9,94	1,89	0,39	1,75	0,26	1,53	0,32	0,89	0,13	0,80	0,12	0,21	0,16	7,77	2,79	0,59
cor13-22c	carbonated metasomatic rock	2,83	1820,00	16,73	45,67	3,45	0,18	17,07	15,58	24,29	3,40	12,99	2,59	0,51	2,36	0,37	2,29	0,49	1,27	0,18	1,20	0,19	1,42	0,39	16,45	4,20	1,12
1cor14-10g	carbonated metasomatic rock	36,90	135,28	12,98	4,55	1,97	2,23	84,03	8,83	10,71	1,67	6,73	1,38	0,27	1,47	0,22	1,35	0,29	0,81	0,12	0,74	0,11	0,15	0,16	6,85	1,90	0,30
1cor14-6a	carbonated metasomatic rock	1,68	193,58	19,29	2,60	2,56	0,10	13,98	12,26	22,55	3,15	13,59	2,94	0,74	3,25	0,49	3,04	0,62	1,67	0,22	1,41	0,21	0,13	0,12	17,39	0,97	0,50
1cor14-6c	carbonated metasomatic rock	0,13	121,27	6,01	0,45	0,06	0,02	6,83	2,44	0,78	0,33	1,50	0,34	0,11	0,53	0,09	0,61	0,15	0,43	0,06	0,36	0,06	0,03	0,00	28,27	0,01	0,06
1cor12-20d	carbonated metasomatic rock	4,34	1087,00	24,90	23,40	1,71	0,33	7,47	15,49	17,57	3,85	16,04	3,27	0,74	3,08	0,48	3,14	0,73	1,98	0,28	1,84	0,27	0,72	0,20	40,26	2,33	0,60
2cor14-3bo (in situ)	omphacite vein	0,02	13,67	2,99	1,15	0,06		0,34	0,02	0,08	0,02	0,13	0,07	0,04	0,08	0,04	0,38	0,22	0,33	0,06	0,48	0,07	0,14	0,00	0,98	0,03	0,07
1cor12-11No	omphacite vein	--	--	--	--	--	--	--	--	--	--	--	--	--	--	--	--	--	--	--	--	--	--	--	--	--	--
2cor14-3b	carbonate vein	0,18	4044,52	25,48	0,21	0,03	0,01	3,80	1,31	4,44	1,01	7,08	2,82	1,35	4,40	0,65	3,87	0,79	1,79	0,16	0,68	0,08	0,04	0,00	21,31	0,02	0,01
1cor12-11N (in situ)	carbonate vein	0,01	4211,80	30,88	0,00	0,00		2,53	1,43	5,22	1,17	8,23	3,24	1,43	4,20	0,70	4,52	0,91	2,08	0,18	0,73	0,08	0,00	0,00	25,53	0,00	0,00
cor16-49a in situ	carbonate vein	2,23	2121,61	7,11	0,17	0,04	0,04	24,99	1,03	2,82	0,48	2,46	0,68	0,31	0,77	0,15	1,03	0,24	0,63	0,07	0,30	0,03	0,02	0,00	506,37	0,18	0,14